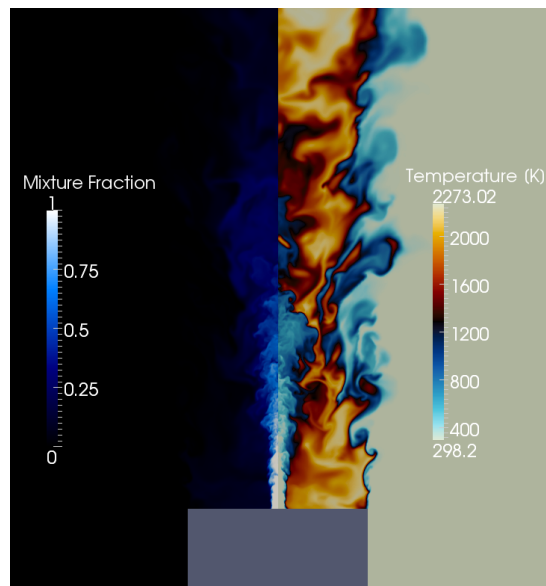


# Numerical simulation of turbulent diffusion flames using flamelet models on unstructured meshes



Centre Tecnològic de Transferència de Calor  
Departament de Màquines i Motors Tèrmics  
Universitat Politècnica de Catalunya

Jordi Ventosa Molina  
Doctoral Thesis



**Numerical simulation of turbulent diffusion flames  
using flamelet models on unstructured meshes**

Jordi Ventosa Molina

TESI DOCTORAL

presentada al

Departament de Màniques i Motors Tèrmics  
E.T.S.E.I.A.T.  
Universitat Politècnica de Catalunya (UPC)

per a l'obtenció del grau de

Doctor per la Universitat Politècnica de Catalunya

Terrassa, Setembre 2015



# **Numerical simulation of turbulent diffusion flames using flamelet models on unstructured meshes**

Jordi Ventosa Molina

## **Directors de la Tesi**

Dr. Assensi Oliva Llena

Dr. Carles David Pérez Segarra

Dr. Oriol Lehmkuhl Barba



*Als meus pares i avis.*

*All right, so it's possible there's an alternate version of myself out there  
that actually understands what the hell you're talking about.*

-Col. O'Neill (Stargate)

Asgard: *Understand this: there was once an alliance of four great races in the galaxy. The Asgard, the Nox, the Furlings and the Ancients, the builders of the Stargates. This alliance was built over many millennium. Your race has much to prove before we may interact at such a level.*

O'Neill: *You folks should understand that we're out there. Now. We might not be ready for a lot of this stuff, but we're doing the best we can. We are a very curious race.*

Asgard: *You have already taken the first steps toward becoming the Fifth Race.*

Stargate, *The Fifth Race*



# Agraïments

Escriure aquestes línies implica tancar un cicle, que n'obre un de nou. Ara bé, per arribar a aquest punt hi ha hagut companys de viatge, tant a nivell professional/acadèmic com personal, als qui m'agradaria agrair l'ajuda i el suport rebuts.

En primer lloc, voldria agrair al Prof. Assensi Oliva, catedràtic del *Centre Tecnològic de Transferència de Calor* (CTTC), per haver-me donat la possibilitat de realitzar el doctorat en aquest departament. També pel suport i la confiança en la feina que s'ha estat realitzant durant el doctorat.

Al Prof. Carles David Pérez Segarra, catedràtic del CTTC, per la seva ajuda durant el doctorat. Sobretot agrair-li l'ajuda i temps dedicat a resoldre tot tipus de qüestions. La seva capacitat de trobar respuestes mitjançant l'anàlisi detallada i rigurosa de les equacions descriuint el fenomen d'interès és una font d'inspiració en la manera de treballar.

Al Dr. Oriol Lehmkuhl, supervisor, mentor i bon amic. La feina que s'ha pogut desenvolupar en aquesta tesi no es pot entendre sense les seves aportacions i la seva capacitat per entendre la dinàmica de fluids. La seva capacitat per entendre la modelització de la turbulència i les seves recomanacions i consells són altament valorats.

Apart de la vessant física, si avui (crec que) puc dir que sé programar en C++ és per haver-ne après del seu exemple. Al començar el doctorat creia saber programar, aquest temps m'ha demostrat el contrari.

I would like to thank Prof. Pedro Martins Coelho for the stay at *Instituto Superior Técnico* of the *Universidade Técnica de Lisboa* (IST-UTL). Furthermore, his help and answers to my questions during my stay are highly valued.

Al Jordi Chiva li voldria agraïr tota l'ajuda en la resolució d'errors de programació i d'optimització de codi. Realment no sé quantes hores de *debugging* m'he estalviat gràcies a la seva ajuda.

Agraïr al Dr. Lluís Jofré l'ajuda rebuda en el desenvolupament de la llibreria de propietats físiques. També per algunes discussions força interessants i per haver estat una mica de guia durant el doctorat, ja que el va començar un any abans. També mencionar l'Aleix Báez, amb el qual vam desenvolupar una llibreria per avaluar termes convectius i difusius. Ambdues llibreries són centrals per aquesta tesi i ara són usades àmpliament en el grup. Tampoc voldria oblidar-me d'en Jordi Muela, el qual ha col·laborat en desenvolupar i millorar diferents aspectes dels algoritmes per combustió.

Donada la naturalesa computacional de la tesi, no voldria oblidar-me els informàtics del grup, passats i actuals, en Dani, el Gabriel, l'Octavi i el Ramiro, per l'ajuda en aspectes de *software* i *hardware*. No voldria deixar-me gent del CTTC, com la Roser Capdevila, die *Deutschmitschülerin*, el Joan Farnós, l'Hector Giráldez,

i Ricard Borrel, i els professors Joaquim Rigola, Carles Oliet i Ivette Rodríguez.

En l'àmbit més personal, voldria fer una menció a tota la colla d'amics de Reus. En part no he acabat del tot "mentally lost" pels bons moments compartits. I a aquelles noves persones que en un moment apareixen i et canvien.

Finalment, no puc deixar d'agraïr a la meva família tot el suport rebut. Especialment al meu pare Joan i la meva mare Carme, per ser-hi sempre i ajudar-me a créixer com a persona. Als meus avis, Jaime, Trinidad, Joan i Pepita pels valors que m'han transmès. I també es mereix una menció especial la meva germana Glòria, tot i que molt sovint siguem com gat i gos.

Jordi V. M.

# Abstract

Combustion is a temporal and spatial multiscale problem characterised by the interaction between chemical reactions and turbulent flow. Furthermore, chemical reactions involve a large number of participating species. Hence, models are required to reduce the dimensionality of the problem. In addition, turbulence is a complex process by itself, whose resolution is computationally demanding and still is a topic of current research. Therefore, modelling is also applied to reduce its computational effort.

The present thesis aims at developing numerical methods and algorithms for the efficient simulation of diffusion flames in the flamelet regime. To tackle turbulent chemically reacting flows a double framework is used in the present thesis. On the one hand, flow description is performed in the context of Large Eddy Simulation (LES) techniques. In LES, by spatially filtering the Navier-Stokes equations, the large scales of the flow are solved and the small scales are modelled, as they present a more universal behaviour. On the other hand, thermochemistry is modelled by means of flamelet models. Chemical reactions occur at the molecular level. Consequently, in many cases of academic and industrial interest, reactions occur at scales smaller than the smallest flow scale, namely the Kolmogorov scale. With this assumption, the flamelet regime is characterised by the split of the combustion process into a flame structure case and flow transport case.

Therefore, to study chemically reacting flows different models and algorithms are required. First, an algorithm for computing variable density flows. Second, a model to describe chemical kinetics. Finally, a procedure to link the transport model with the flame model. In order to accomplish these goals the thesis is divided into five chapters, each one describing and analysing a specific aspect of the required numerical methods.

In first place, in *Chapter 1* the basic formulation for describing chemically reacting flows is detailed. Chemical kinetics are briefly described and transport terms for multicomponent flows are detailed. Then, an introduction to turbulent combustion is performed, where the challenges of simulating these flows using finite rate kinetics are stated. It is then argued that specific models are required.

Before proceeding to describe the combustion model, an algorithm for the simulation of variable density flows is described and studied in *Chapter 2*. Furthermore, the study revolves around the use of unstructured meshes, since one of the focus of the thesis is the capacity of the developed numerical methodology to be applied on complex geometries. A temporal integration scheme, specifically a multi-step scheme, and two spatial discretisation schemes, namely collocated and staggered schemes, are described and studied. Reacting and non-reacting test cases are considered.

In *Chapter 3* a flamelet model for the simulation of diffusion flames is described. First, the flamelet regime is described and the flame equations in composition space,

or mixture fraction space, are presented. Then, a Flamelet/Progress-Variable model is used to fully describe the flame in mixture fraction space. The two main parameters used are the mixture fraction and the progress-variable. Additionally, a finite differences method for the solution of the flamelet equations is presented. Since the target flames are turbulent, assumed probability density functions are introduced in order to restate the flamelet solutions as stochastic quantities. The model allows pre-computing the flame thermochemistry and storing it into a database, which is then accessed during simulations in physical space.

The next two chapters deal with the parameters used to represent the flamelet database. In first place, *Chapter 4* studies the definition of the progress-variable, which is required to unambiguously represent the chemical state. This statement mainly translates into a requirement of monotonic evolution. The definition of this parameter has been reported to be case sensitive. The present work evidences a dependence on the diffusion model. Definitions found valid for Fickian diffusion are shown to result in non-monotonic distributions when differential diffusion is considered. Furthermore, in the chapter two detailed chemical mechanism are considered. Tests include a methane/hydrogen/nitrogen diffusion flame and a self-igniting methane flame, where the fuel issues into a vitiated coflow. In the latter case, chemical mechanisms are shown to play a central role in the prediction of the flame stabilisation distance.

Lastly, when turbulent flames are considered, the flamelet database is stated as a function of stochastic parameters. Among them, the mixture fraction variance, which represents mixing at the subgrid level, is not directly computed and requires modelling. Since chemical reactions in the flamelet regime occur at scales smaller than the Kolmogorov scale, the correct characterisation of subgrid mixing is a critical issue. Hence, in *Chapter 5* different models for the evaluation of the subgrid variance are studied. The study case is the methane/hydrogen/nitrogen diffusion flame. The study shows that correct description of the subgrid mixing is critical in accurately predicting the flame stabilisation.

# Contents

<b>Agraïments</b>	<b>vii</b>
<b>Abstract</b>	<b>ix</b>
<b>1 Introduction</b>	<b>1</b>
1.1 Prologue . . . . .	1
1.2 Combustion modelling . . . . .	3
1.2.1 Chemical kinetics . . . . .	4
1.2.2 Transport equations . . . . .	5
1.2.3 Burning mode . . . . .	10
1.2.4 Turbulence . . . . .	11
1.2.5 LES . . . . .	12
1.2.6 Combustion closure . . . . .	14
1.3 Background at the CTTC . . . . .	17
1.4 Objectives . . . . .	19
1.5 Outline of the thesis . . . . .	21
References . . . . .	22
<b>2 Numerical assessment of conservative unstructured discretisations for Low-Mach flows</b>	<b>27</b>
2.1 Introduction . . . . .	28
2.2 Low-Mach number equations . . . . .	30
2.2.1 Chemically reacting flows . . . . .	31
2.2.2 Thermodynamic pressure . . . . .	32
2.2.3 Momentum projection scheme - Fractional Step method . . . . .	33
2.3 Unstructured discretisation . . . . .	34
2.3.1 Collocated discretisation: . . . . .	36
2.3.2 Staggered discretisation: . . . . .	37
2.3.3 Face interpolation schemes . . . . .	40
2.3.4 Boundaries . . . . .	42
2.4 Temporal Integration Algorithm . . . . .	42
2.4.1 Temporal integration algorithm . . . . .	43
2.5 Numerical Tests . . . . .	45
2.5.1 Test Case 1 - Interpolation schemes accuracy . . . . .	46
2.5.2 Test Case 2 - Analysis of the spatial discretisations . . . . .	48
2.5.3 Test Case 3 - Analysis of the transient behaviour . . . . .	53
2.6 Conclusions . . . . .	56

References . . . . .	58
<b>3 Flamelet modelling of nonpremixed combustion phenomena</b>	<b>63</b>
3.1 Introduction . . . . .	64
3.2 Flamelet model . . . . .	65
3.2.1 Classical Flamelet . . . . .	72
3.2.2 Flamelet/Progress-variable (FPV) model . . . . .	75
3.3 Flamelet database . . . . .	81
3.3.1 Solution of the flamelet equations . . . . .	81
3.3.2 Flamelet solutions . . . . .	90
3.4 Flamelets in turbulent flows . . . . .	90
3.4.1 Radiation and NO <sub>x</sub> in turbulent flows . . . . .	98
3.5 Database for CFD . . . . .	99
3.6 Concluding remarks . . . . .	103
References . . . . .	106
<b>4 Differential diffusion effects in the progress-variable definition for Flamelet/Progress-variable models for non-premixed flames</b>	<b>111</b>
4.1 Introduction . . . . .	113
4.2 Mathematical model . . . . .	115
4.2.1 Flamelet/Progress-variable (FPV) model . . . . .	118
4.2.2 Numerical method . . . . .	123
4.3 Turbulent diffusion CH <sub>4</sub> /H <sub>2</sub> /N <sub>2</sub> flame - DLR A flame . . . . .	124
4.3.1 Flamelet burning region - Fickian vs Differential . . . . .	125
4.3.2 Progress-variable definition - steady . . . . .	125
4.3.3 Progress-variable definition - unsteady . . . . .	129
4.3.4 Progress-variable definition - radiation . . . . .	132
4.3.5 CFD analysis . . . . .	137
4.4 Turbulent auto-igniting diffusion CH <sub>4</sub> flame - Cabra flame . . . . .	142
4.4.1 S-shaped curve . . . . .	143
4.4.2 Progress-variable definition . . . . .	146
4.4.3 CFD analysis . . . . .	150
4.5 Conclusions . . . . .	154
References . . . . .	156
<b>5 Large Eddy Simulation of a shear stabilised turbulent diffusion flame using a Flamelet/Progress-Variable model.</b>	<b>161</b>
5.1 Introduction . . . . .	163
5.2 Mathematical model . . . . .	166
5.2.1 LES model . . . . .	166
5.2.2 Flamelet/Progress-Variable (FPV) model . . . . .	166

5.2.3	Numerical method . . . . .	173
5.3	Turbulent diffusion $CH_4/H_2/N_2$ flame - DLR A flame . . . . .	173
5.4	Results and discussion . . . . .	174
5.4.1	Turbulent fluxes closure . . . . .	174
5.4.2	Flame stabilisation . . . . .	176
5.4.3	Effect of the subgrid mixing closures . . . . .	179
5.5	Conclusions . . . . .	193
	References . . . . .	195
<b>6</b>	<b>Conclusions</b>	<b>201</b>
	References . . . . .	208
<b>A</b>	<b>Projection method in the Fractional Step for Low Mach algorithms</b>	<b>211</b>
<b>B</b>	<b>A note on software development</b>	<b>213</b>
	References . . . . .	214
<b>C</b>	<b>Main publications in the context of this thesis</b>	<b>215</b>



# Introduction

## 1.1 Prologue

From the early times of humankind fire has played a significant role in the development of human society; from its early use as a source of light and heat, and to cook food, thus reducing the amount of energy used in digesting it, up to modern chemical rockets, gas turbines and internal combustion engines. Not only has it been used to progress but also has been an element of destruction. Moreover, the influence of fire in human culture goes beyond that of practical use. In many mythological stories, fairy-tales and different sorts of artistic representations fire is a central element. It has been used as a symbol for both creation and destruction, which also has been interpreted as a purification process.

Besides philosophical considerations, fire, or specifically combustion, has been at the centre of human life. It has been the main energy source during centuries. Although in the last century several new technologies, like nuclear energy and renewable energies, such as solar and wind power, have gained, or are gaining, notoriety, combustion driven machinery still plays a significant role in the amount of produced energy in the world. Furthermore, it is forecast that at least in the following 50 to 80 years, combustion generated energy will still be one of the main energy sources worldwide. Besides, there are other processes related to combustion which are not directly linked to energy generation but are linked to human safety, such as fires in wildland and in buildings. Moreover, in combustion processes, in addition to the energy release, there is a generation of non-desired products, or pollutants. In the last decades, regulations on pollutants is becoming more stringent due to concerns on the effect on human health and on the environment. These pollutants are usually in lower proportions compared to the main combustion products and their dynamics are usually different. Therefore, accurate models are required to correctly characterise pollutant emissions. Then, methods and techniques must be developed in order to reduce their production. Hence, there is a need for understanding how pollutants are created and transported.

Combustion is a conglomeration of different complex processes which interact and

result in a, usually visible, exothermic process. Beginning with the core process, chemical reactions describe how certain reactants, usually a pair of fuel and oxidizer, combine and produce certain products while releasing heat. Then, reactants may be found in different states: as solid fuel, in a liquid bed or spray, or in gas form. The former two require that, prior to combustion, a phase change to the gas state must take place. Concerning the combustion products, they are usually in gas form, since chemical heat released causes a large temperature increase. This last effect introduces two critical aspects of combustion processes, heat transfer and radiation. The former requires describing how heat is transported within a flow field composed of different elements, or species. The latter effect, radiation, is a complex phenomenon by itself, which, due to the coupling with the other described phenomena, becomes even more challenging. A last aspect to remark is that in most designs of technological interest, flows are usually turbulent, mainly due to the increased power output, compared to laminar designs. Turbulence, which lies at the heart of the Navier-Stokes equations, is a challenge which as of today is still unclosed and is considered one of the seven “Millennium problems”, set by the Clay Mathematics Institute [1]. Hence, the combination of chemistry, heat and mass transfer, turbulence, phase change and radiation, among others, pose a significant challenge that requires advanced modelling techniques in order to obtain accurate solutions with finite resources.

Initial works in the combustion field date back to the end of the 19th century by LeChatelier and Arrhenius and in the thirties of the 20th century by Burke-Schumann, among others. Following, during the 20th century the number of studies focused on combustion increased. It was soon realised that the complexity of the investigated phenomena required the use of specific models which would reduce the number of unknowns and interactions. In the process, combustion researchers identified canonical situations with different characteristic behaviours, based on whether the reactants are mixed prior to combustion or not: premixed and non-premixed flames. Initially, fundamental analysis of flames in either regime were mostly based on one-dimensional configurations. For diffusion flames, most models resorted to a flame in a counterflow configuration, where each reactant issues from one different inlet, and the reaction zone separates each stream. For premixed flames, the already mixed reactants undergo a temperature increase while going through a thin reaction zone, where the flame front displaces with a characteristic speed, the laminar flame speed.

The extension to turbulent flames proved challenging due to the coupling between chemistry and turbulence. The challenges found in laminar flames grow significantly when considering turbulent motions. Hence, most models developed for turbulent flames were based on what had been learned from laminar flames. Phenomenological models allowed solving certain cases with good accuracy.

Parallel to the increase in computer power during the 20th century, the capabilities

for numerical simulations of fluid flow increased, and also for combustion. Thanks to this computational power increase, Computational Fluid Dynamics (CFD) emerged as a tool to solve the Navier-Stokes equations numerically. An aspect to bear in mind concerning the research in the combustion field is that performing experimental measurements is specially challenging due to the high temperatures involved and the large number of participating species. Hence, CFD can provide a good understanding of the processes, although the modelling effort is important. However, a large effort was and still is needed to solve these equations. Nonetheless, the information gathered using these techniques has proven invaluable in understanding the laws controlling the physics of flow movement and transport. In recent years, the computational capacity and understanding of combustion processes has allowed researchers and engineers to tackle complex engineering designs such as the combustion process within an aeronautical gas turbine [2–4].

In the following an introduction to the mathematical description of combustion phenomena is presented. Chemistry, transport equations and coefficients are described for the general solution of flames. The extension to turbulent flows is considered and different models are discussed. The following discussion is not intended as an extensive state of the art, rather as an introduction and basis for the rest of the thesis. In each chapter a specific state of the art is conducted.

## 1.2 Combustion modelling

A combustion process is an exothermic chemical reaction taking place within a fluid flow. Therefore, its study requires describing a chemical process and the movement of the flow. The chemical composition of a mixture composed of  $N$  species is described by means of the species mass fractions  $Y_k = m_k/m$ , where  $m_k$  and  $m$  are the  $k$ th-species and mixture mass respectively, both in a given volume. The density of the mixture  $\rho$ , linked to pressure  $P$  and temperature  $T$ , is evaluated through the ideal gas state law

$$P_o = \rho R_g T = \rho \frac{R}{W} T = \rho T R \sum_{k=1}^N \frac{Y_k}{W_k} \quad (1.1)$$

where  $R_g$  and  $R = 8.314 J/(K mol)$  are the specific and ideal gas constants, respectively. The mixture molar mass  $W$  is calculated from the species molar masses  $W_k$

$$\frac{1}{W} = \sum_{k=1}^N \frac{Y_k}{W_k} \quad (1.2)$$

Mass fractions are related to molar fractions  $X_k$  and molar concentrations  $[X_k]$  through the molar mass

$$X_k = \frac{W}{W_k} Y_k \quad (1.3)$$

$$[X_k] = \rho \frac{Y_k}{W_k} = \rho \frac{X_k}{W} \quad (1.4)$$

The thermodynamic state of the mixture can be represented by the enthalpy  $h$ , defined as the sum of its chemical and sensible parts

$$h = \sum_{k=1}^N Y_k h_k = \sum_{k=1}^N Y_k \left( \underbrace{\Delta h_{f,k}^o}_{\text{chemical}} + \underbrace{\int_{T_0}^T c_{p_k}(T) dT}_{\text{sensible}} \right) \quad (1.5)$$

where  $h_k$  is a species enthalpy,  $\Delta h_{f,k}^o$  is a species enthalpy of formation,  $c_{p_k}$  is a species heat capacity and  $T_0 = 298.2K$  is the reference temperature for evaluating thermodynamic data. Both enthalpy and heat capacity of each species are calculated using NASA's polynomials [5, 6] and the mixture heat capacity  $c_p$  and enthalpy  $h$  are evaluated as

$$c_p(T) = \sum_{k=1}^N Y_k c_{p_k}(T) \quad (1.6)$$

$$h(T) = \sum_{k=1}^N Y_k h_k(T) \quad (1.7)$$

### 1.2.1 Chemical kinetics

A chemical process is a series of interactions involving  $N$  different chemical species and is represented by  $N_r$  reactions

$$\sum_{k=1}^N \nu'_{r,k} \mathfrak{Y}_k \rightleftharpoons \sum_{k=1}^N \nu''_{r,k} \mathfrak{Y}_k \quad r = 1 \dots N_r \quad (1.8)$$

where  $\mathfrak{Y}_k$  represents the species involved in reaction  $r$ ,  $\nu'_{r,k}$  and  $\nu''_{r,k}$  are the molar stoichiometric coefficients of the  $k$ th species in reaction  $r$ . The reaction rate for each equation is given by the empirical *rate law*

$$\dot{w}_{k,r} = W_k \nu_{r,k} \mathcal{R}_r \quad (1.9)$$

where  $\nu_{r,k} = \nu''_{r,k} - \nu'_{r,k}$  and  $\mathcal{R}_r$  is the rate of progress of reaction  $r$  given by

$$\mathcal{R}_r = k_r^f \prod_{k=1}^N [X_k]^{\nu'_{r,k}} - k_r^b \prod_{k=1}^N [X_k]^{\nu''_{r,k}} \quad (1.10)$$

where  $k_r^f$  and  $k_r^b$  are the forward and backward kinetic rate constants, which are not constant in the strict sense. Forward rate constants are evaluated using Arrhenius law

$$k_r^f = AT^\beta \exp\left(-\frac{E_{a,r}}{RT}\right) \quad (1.11)$$

where  $A$  is the pre-exponential constant,  $\beta$  the temperature exponential and  $E_{a,r} = RT_{a,r}$  is the activation energy, which can be related to an activation temperature  $T_{a,r}$ . Chemical mechanisms containing sets of reactions and values for these constants can be found in the literature; ranging from detailed mechanisms, such as the GRI mechanism [7] for methane combustion, to reduced mechanisms, for example the Jones and Lindstedt mechanism for methane [8] or the mechanism of Mueller et al. for hydrogen [9], and single-step irreversible mechanisms. Backward constants are usually not included, but are computed through reaction equilibrium constants

$$k_r^b = \frac{k_r^f}{\left(\frac{p_a}{RT}\right)^{\sum_{k=1}^N \nu_{r,k}} \exp\left(\frac{\Delta S_k^0}{R} - \frac{\Delta H_k^0}{RT}\right)} \quad (1.12)$$

where  $p_a = 0.1 \text{ MPa}$  and  $\Delta S_k^0$  and  $\Delta H_k^0$  the standard entropy and enthalpy changes for reaction  $r$ .

The reaction rate for any species is then

$$\dot{w}_k = W_k \sum_{r=1}^{N_r} \nu_{r,k} \mathcal{R}_r \quad (1.13)$$

Summing all reactions rates of all species results in

$$\sum_{k=1}^N \dot{w}_k = \sum_{k=1}^N W_k \left( \sum_{r=1}^{N_r} \nu_{r,k} \mathcal{R}_r \right) = \sum_{r=1}^{N_r} \mathcal{R}_r \left( \sum_{k=1}^N W_k \nu_{r,k} \right) = 0 \quad (1.14)$$

since  $\sum_{k=1}^N W_k \nu_{r,k} = 0$  which shows that mass is conserved.

### 1.2.2 Transport equations

The Navier-Stokes equations can describe a combustion process taking place within a fluid flow. Depending on the characteristic Mach number of the flow, either low Mach formulations or compressible formulations are used to describe the fluid flow. In the current thesis, the study is focused on combustion in low Mach flows. Solving a non-reacting case involves computing six variables, density, pressure, velocity and temperature, whereas a reacting case adds  $N$  more variables. Hence, the computation of reacting cases first entails an increment of the computational effort. In the following it will also be shown that the modelling effort is also increased. The governing

equations, which are presented in detail in Chapter 2 are

$$\frac{\partial \rho}{\partial t} + \frac{\partial \rho u_j}{\partial x_j} = 0 \quad (1.15)$$

$$\frac{\partial \rho u_i}{\partial t} + \frac{\partial \rho u_j u_i}{\partial x_j} = -\frac{\partial p}{\partial x_i} + \frac{\partial \tau_{ij}}{\partial x_j} + \rho g_i \quad (i = 1, 2, 3) \quad (1.16)$$

$$\frac{\partial \rho h}{\partial t} + \frac{\partial \rho u_j h}{\partial x_j} = \frac{dP_o}{dt} + v_i \frac{\partial p_i}{\partial x_i} - \dot{q}^R - \frac{\partial \dot{q}_j}{\partial x_j} + \tau_{ij} \frac{\partial u_i}{\partial x_j} \quad (1.17)$$

$$\frac{\partial \rho Y_k}{\partial t} + \frac{\partial \rho u_j Y_k}{\partial x_j} = -\frac{\partial j_{k,j}}{\partial x_j} + \dot{w}_k \quad (k = 1..N) \quad (1.18)$$

where  $t$  represents time,  $\rho$  the fluid density,  $u$  a mixture averaged velocity,  $\tau$  the shear stress tensor,  $g$  the gravity,  $h$  the specific enthalpy of the mixture,  $\dot{q}_j$  the diffusion heat flux,  $\dot{q}^R$  the radiant heat rate,  $Y_k$  a species mass fraction,  $\dot{w}_k$  a species reaction rate and  $j_k = \rho V_{k,j} Y_k$  a species diffusion mass flux, where the diffusion flux is defined through a diffusion velocity  $V_{k,j}$ . For low Mach flows, the pressure can be split into a hydrodynamic pressure  $p$  and a thermodynamic pressure  $P_o$ . This set of equations involve several transport terms to be modelled, i.e. the shear stress tensor  $\tau_{ij}$ , the heat flux  $\dot{q}_j$  and the mass fluxes  $j_{k,j}$ .

### Momentum equation

In the momentum equation Eq. (1.16) the shear stress tensor is modelled through Stoke's law for Newtonian fluids

$$\tau_{ij} = \mu \left( \frac{\partial u_i}{\partial x_j} + \frac{\partial u_j}{\partial x_i} - \frac{2}{3} \delta_{ij} \frac{\partial u_k}{\partial x_k} \right) \quad (1.19)$$

where  $\delta_{ij}$  is the Kronecker Delta and  $\mu$  is the mixture dynamic viscosity.

### Energy equation

Heat diffusion in multicomponent flows takes place through two mechanisms, thermal heat diffusion described by Fourier's law and heat transport by inter-diffusion of species with different enthalpies

$$\dot{q}_j = -\kappa \frac{\partial T}{\partial x_j} + \sum_{k=1}^N h_k j_{k,j} \quad (1.20)$$

where  $\kappa$  is the mixture thermal conductivity. A further term that could be considered is the flux of energy produced by concentration gradients, namely the Duffour effect. This effect is based on Onsager's reciprocal relations of irreversible thermodynamics. It implies that if temperature gradients give rise to diffusion velocities (thermal diffusion), then concentration gradients must produce a heat flux. However, compared

to the other two terms, the Duffour contribution to the heat flux is small. Thus, it has been neglected in the computations.

### Species mass fraction

Mass fluxes appear in both energy and mass transport equations. Furthermore, their proper definition is critical for conserving mass even at the differential level, since the summation of all species transport equations must add to the continuity equation. Therefore, summing all species equations Eq. (1.18)

$$\sum_{k=1}^N \left( \frac{\partial \rho Y_k}{\partial t} + \frac{\partial \rho u_j Y_k}{\partial x_j} \right) = \sum_{k=1}^N \left( -\frac{\partial j_{k,j}}{\partial x_j} \right) + \sum_{k=1}^N (\dot{w}_k) \quad (1.21)$$

The first two terms in the left hand side add to the continuity equation, since  $\rho_k = \rho Y_k \rightarrow \sum_{k=1}^N \rho Y_k = \rho$  and all mass fraction add to one. Additionally, it has been shown that the summation of all species reaction terms adds to null. Hence, all mass diffusion fluxes summed must cancel out

$$\sum_{k=1}^N \left( -\frac{\partial j_{k,j}}{\partial x_j} \right) = 0 \quad (1.22)$$

A detailed model for diffusion velocities and fluxes can be computed from the kinetic theory [2, 10], which under some approximations reduces to the Stefan-Maxwell equation

$$\frac{\partial X_k}{\partial x_j} = \sum_{\alpha=1}^N \frac{X_{\alpha} X_k}{D_{\alpha k}} (V_{k,j} - V_{\alpha,j}) \quad (1.23)$$

where  $D_{\alpha k}$  is the binary mass diffusivity of species  $\alpha$  into species  $k$ . Solution of this equation is computationally expensive [2]. Therefore, simplified models have been proposed: Fick's law and Hirschfelder and Curtiss approximation. Under the assumption of equal diffusivities for all species, Fick's law is an exact solution to Eq. (1.23). Diffusion fluxes are evaluated as

$$j_{k,j} = -\rho D \frac{\partial Y_k}{\partial x_j} \quad (1.24)$$

where mass diffusivity  $D = D_{\alpha k}$  is equal for all species. When the equal diffusivities assumption is not made, diffusion fluxes are evaluated using Hirschfelder and Curtiss approximation [2], which is a first order approximation to Eq. (1.23)

$$V_{k,j} X_k = -D_k \frac{\partial X_k}{\partial x_j} \rightarrow V_{k,j} Y_k = -D_k \frac{W_k}{W} \frac{\partial X_k}{\partial x_j} \quad (1.25)$$

where Eq. (1.3) has been used to convert molar fractions into mass fractions. However, this approximation does not conserve mass. If Eq. (1.22) is evaluated using Eq. (1.25) to describe the species mass fluxes, there remains a residual. In order to ensure mass conservation, a correction velocity  $V_j^c$  is introduced to the Hirschfelder and Curtiss diffusion velocity

$$V_j^c = \sum_{k=1}^N D_k \frac{W_k}{W} \frac{\partial X_k}{\partial x_j} \quad (1.26)$$

$$V_{k,j} Y_k = -D_k \frac{W_k}{W} \frac{\partial X_k}{\partial x_j} + V_j^c \quad (1.27)$$

This approach can be shown to be equivalent to Fick's law when equal diffusivities are assumed.

As a last remark, the Soret effect has been neglected in the mass transport equation. Similar to the energy equation, but with opposite effect, the Soret effect is the mass diffusion due to thermal gradients.

### Transport coefficients

The molecular fluxes for momentum  $\tau_{ij}$ , heat  $\dot{q}_j$  and mass  $j_{k,j}$  require the computation of mixture molecular transport coefficients, which in turn depend on the species molecular transport coefficients.

For the mixture averaged dynamic viscosity  $\mu$  the semi-empirical formula by Bird [11] has been used

$$\mu = \sum_{k=1}^N \frac{X_k \mu_k}{\sum_{\alpha=1}^N X_\alpha \Phi_{k\alpha}} \quad (1.28a)$$

$$\Phi_{k\alpha} = \frac{1}{\sqrt{8}} \left( 1 + \frac{W_k}{W_\alpha} \right)^{-1/2} \left( 1 + \left( \frac{\mu_k}{\mu_\alpha} \right)^{1/2} \left( \frac{W_\alpha}{W_k} \right)^{-1/4} \right)^2 \quad (1.28b)$$

where  $\mu_k$  are binary dynamic viscosities. Mixture and species thermal conductivities,  $\kappa$  and  $\kappa_k$  respectively, are evaluated using the same set of equations, using  $\kappa$  instead of  $\mu$  where appropriate. For cases where the viscosity is not required, a simpler expression can be used to estimate the thermal conductivity [12] with an error of a few percent [13]

$$\kappa = \frac{1}{2} \left( \sum_{k=1}^N X_k \kappa_k + \left( \sum_{k=1}^N \frac{X_k}{\kappa_k} \right)^{-1} \right) \quad (1.29)$$

The exact description of mass diffusion involves solving the Stefan-Maxwell equation with the evaluation of binary diffusivities. However, as stated this process is too

computationally demanding. Hence, when the Hirschfelder and Curtiss approximation is used with multicomponent diffusivities, a diffusivity of each species into the mixture is evaluated. The multicomponent mass diffusivity is estimated [2] through

$$D_{k,m} = D_k = \frac{1 - Y_k}{\sum_{\substack{\alpha=1 \\ \alpha \neq k}}^N \frac{X_\alpha}{D_{k\alpha}}} \quad (1.30)$$

where the subindex  $m$  indicating diffusion towards the mixture is dropped for the sake of readability, and  $D_{k,\alpha}$  is the binary diffusivity.

### Non-dimensional analysis

Evaluation of mixture properties can still involve a significant task, even with the simplifications just described. The non-dimensional analysis of the flame reveals several non-dimensional numbers relating the different transport properties. The Lewis number relates mass and heat transport

$$Le_k = \frac{\kappa/\rho c_p}{D_k}, \quad (1.31)$$

the Prandtl number relates momentum and heat transfer

$$Pr = \frac{\mu/\rho}{\kappa/\rho c_p} \quad (1.32)$$

and the Schmidt number compares momentum and mass diffusion

$$Sc_k = \frac{\mu/\rho}{D_k} \quad (1.33)$$

According to [2], the Lewis number variation for each species is small through the flame front. Hence, assuming a constant Lewis number for each species and defining a suitable expression for the thermal conductivity may be adequate for simplified analysis. Nonetheless, Giacomazzi et al. [14] reported that the assumption of constant Schmidt numbers was better suited due to the narrower distribution of Schmidt numbers against temperature compared to the Lewis numbers.

Two further non-dimensional numbers of interest are the Reynolds number and the Damköhler number. The former compares inertial forces to viscous forces and is defined as

$$Re = \frac{\rho v L}{\mu} \quad (1.34)$$

where  $v$  is a characteristic velocity of the case of study, and  $L$  is a characteristic length. In the present thesis, jet flames are studied and the reference values usually taken are the fuel jet bulk velocity and the fuel jet nozzle diameter.

The Damköhler number compares chemical time-scales  $\tau_{ch}$  with transport time-scales  $\tau_f$ , either through convection or diffusion,

$$Da = \frac{\tau_f}{\tau_{ch}} \quad (1.35)$$

### Thermal radiation

Heat transfer by radiation appears in the energy conservation equation Eq. (1.17) through the divergence of the radiant heat flux  $\dot{q}^R$ . Its evaluation involves solving for the Radiation Transfer Equation (RTE), which describes the transfer of radiant energy in a participating medium. The RTE is an integro-differential equation with seven independent variables: three spatial coordinates, two angular coordinates, which define the direction of propagation, one spectral variable, and time. However, since radiation beams travel at the speed of light in the medium, the time coordinate is usually negligible in most applications [15]. Still, solving the RTE is an expensive task. Furthermore, the complexity is increased by the need of evaluating the medium radiative properties.

Different models have been presented in the literature to solve the RTE. Among them, the Discrete Ordinates Method (DOM), the Finite Volume Method (FVM) or Monte Carlo methods [16–19] are well established. Simplified methods can be applied when the medium is considered optically thin. Hence, the flame has an unimpeded view of the surroundings. Furthermore, self-absorption is assumed negligible compared to emission in the Optically Thin Method (OTM) [20, 21]. Thus, the radiation flux is modelled as a heat loss at each control volume

$$\dot{q}^R = 4\sigma \left( T^4 \sum_{k=1}^N (p_k k_{P_k}) - T_s^4 \sum_{k=1}^N (p_k k_{I_k}) \right) \quad (1.36)$$

where  $\sigma$  is the Stefan-Boltzmann constant,  $p_k$  is the partial pressure of the  $k$ th species,  $k_{P_k}$  and  $k_{I_k}$  are the Planck-mean and incident-mean absorption coefficients, and  $T_s$  is the background temperature. Absorption coefficients obtained from RADCAL [22] were fitted to polynomials of the temperature. The radiant species considered are  $CO_2$ ,  $H_2O$ ,  $CH_4$  and  $CO$ .

This approach is significantly less expensive than the other cited methods and will be used in this thesis.

### 1.2.3 Burning mode

The mathematical framework described can be used to represent most flame configurations. For chemical reactions to take place, reactants have to be mixed at the molecular level with enough energy for chemical reactions to start. Hence, flame dynamics are controlled through two mechanisms, the mixing rate and chemical ki-

netics. Depending on which mechanism is the rate controlling, two different canonical burning modes are found.

On the one hand, in premixed flames reactants are mixed at the molecular level before arriving at the flame front. Hence, chemistry is the rate controlling mechanism. Premixed flames are more intense and pollute less because the burning conditions can be more accurately controlled through the inlet ratio of fuel and oxidant. However, their operation is dangerous since an increase of temperature at any point in the reactant stream can lead to uncontrolled ignition.

On the other hand, in diffusion flames reactants mix in the same region where the flame is located. Hence, depending on the Damköhler number, either the mixing rate or the reaction rate will be the limiting mechanism. Nevertheless, it is usually found that chemistry time-scales are much shorter than flow time-scales. Therefore, mixing is rate controlling. In this mode, fuel and oxidizer usually enter the combustion region through separated streams. This leads to lower reaction rates, but also to higher temperatures, since reactions take place at their most suitable conditions, namely at the stoichiometric mixture fraction. Flames in this regime are safer to operate since reactants are not mixed until they reach the reaction zone. The current thesis is focused on diffusion flames.

#### 1.2.4 Turbulence

In order to increase the thermal power output of diffusion flames, it is necessary to increase the mixing rate, since mixing is mainly the rate controlling mechanism. Hence, most applications of interest feature turbulent flows. However, turbulence adds another layer of complexity to the description of the flow. Turbulent flows are characterised by being transient, three-dimensional, random and involving a large number of temporal and spatial scales [23]. The characterisation of turbulent motions is performed through three different strategies.

The most detailed technique, and also the most computationally demanding, is the Direct Numerical Simulation (DNS) of the flow. With this technique, all flow scales of the Navier-Stokes equations are solved, without any model for turbulent motions<sup>1</sup>. This approach allows to fully characterise the flows of interest and obtain a detailed information of the physical phenomena. The large computational resources required made this approach unfeasible. However, with the advent of High Performance Computing (HPC), this technique is becoming more affordable. Still, nowadays is mostly restricted to academic cases.

Turbulence modelling is required for most practical situations. Two techniques are most commonly used, Reynolds-Averaged Navier Stokes (RANS) and Large Eddy Simulations (LES). In both cases the Navier-Stokes equations are filtered and tur-

---

<sup>1</sup>Note that models for other physical phenomena can still be introduced, for example for radiation, combustion, multiphase flows, etc.

bulence models are introduced. RANS techniques perform a temporal filtering, or averaging, whereas in LES the filtering operation is performed spatially. This filtering operation has different implications. In RANS all scales of the energy spectrum are modelled, whereas in LES a split between resolved and unresolved scales is introduced and only the latter require modelling.

Focusing on RANS techniques, it is based on a splitting where variables  $\phi$  are decomposed into an average  $\bar{\phi}$  and a fluctuating part  $\phi'$ , with  $\phi = \bar{\phi} + \phi'$ . The method solved for mean quantities of all variables. Models are required to close the Reynolds stress tensor and evaluate the chemical source term and heat of reaction. Although the models required are found to be case dependent and sensitive to the model parameters, the technique offers an affordable approach to many cases of academic and industrial relevance. It is still nowadays used in many fields as the standard approach. Nonetheless, since solution variables are temporally averaged quantities, the method struggles with transient phenomena. In combustion, ignition and extinction events or instabilities are an example of these shortcomings, among others.

Regarding LES, the method splits the different quantities of interest into a resolved and an unresolved part. The former are explicitly solved during CFD simulations, whereas the latter are modelled. The advantage of this approach, is that the behaviour of the flow small scales is found to be more universal [24, 25]. Hence, more general models can be proposed. Although less computationally demanding than DNS simulations, the increase with respect to RANS simulations is considerable. Nonetheless, this technique allows characterising transient events and similar phenomena. In the present thesis studies are carried out under an LES framework. Further details are given in the following.

### 1.2.5 LES

Large Eddy Simulation describes the motion of the large scales of the flow, whereas the small scales are modelled. Scale splitting is performed by means of a low-pass filter,

$$\overline{\rho\phi} = \int_{\Omega} \rho\phi G(\mathbf{x}, \xi) d\xi \quad (1.37)$$

In grid based, implicit filtering, the filter kernel  $G(\mathbf{x}, \xi)$  becomes a top-hat filter with size  $\Delta = (h_i)^{1/3}$ , where  $h_i$  is the mesh spacing in the  $i$ -direction. Additionally, for variable density flows, the filtered quantities are density weighted, or Favre filtered. Favre filtered quantities can be related to Reynolds filtered quantities through

$$\widetilde{\rho\phi} = \overline{\rho\phi} \quad (1.38)$$

Therefore, applying the filtering operation to the low-Mach Navier-Stokes equa-

tions, they become

$$\frac{\partial \bar{\rho}}{\partial t} + \frac{\partial \bar{\rho} \tilde{u}_j}{\partial x_j} = 0 \quad (1.39)$$

$$\frac{\partial \bar{\rho} \tilde{u}_i}{\partial t} + \frac{\partial \bar{\rho} \tilde{u}_j \tilde{u}_i}{\partial x_j} = -\frac{\partial \bar{p}}{\partial x_i} + \frac{\partial}{\partial x_j} (\tilde{\tau}_{ij} - \bar{\rho} \widetilde{u''_j u''_i}) + \bar{\rho} g_i \quad (1.40)$$

$$\frac{\partial \bar{\rho} \tilde{h}}{\partial t} + \frac{\partial \bar{\rho} \tilde{u}_j \tilde{h}}{\partial x_j} = \frac{dP_o}{dt} - \frac{1}{c_p} \tilde{q}^R - \frac{\partial}{\partial x_j} \left( \tilde{q}_j - \bar{\rho} \widetilde{u''_j h''} \right) \quad (1.41)$$

$$\frac{\partial \bar{\rho} \tilde{Y}_k}{\partial t} + \frac{\partial \bar{\rho} \tilde{u}_j \tilde{Y}_k}{\partial x_j} = -\frac{\partial}{\partial x_j} \left( \tilde{j}_{k,j} - \bar{\rho} \widetilde{u''_j Y''_k} \right) + \tilde{w}_k \quad (1.42)$$

where viscous dissipation and pressure dilation have been neglected, 2nd and 5th terms in Eq. (1.41), respectively. The filtered convective term has been split into a resolved part and an unresolved part

$$\widetilde{\bar{\rho} u_j \phi} = \bar{\rho} \tilde{u}_j \tilde{\phi} + \bar{\rho} \widetilde{u''_j \phi''} \quad (1.43)$$

where closure for the subgrid fluctuations is described in the next subsection.

Thermochemical properties, such as the density and molecular diffusivities, are provided by the combustion model and will be discussed in detail in Chapter 3. Similarly, closure for the radiation term is described in the same chapter.

### Turbulence models

Reynolds stresses are modelled through a subgrid viscosity concept proposed by Boussinesq [24]

$$\widetilde{\bar{\rho} u''_j u''_i} = -2 \frac{\partial}{\partial x_j} \left( \mu_t \left( \frac{\partial \tilde{u}_i}{\partial x_j} + \frac{\partial \tilde{u}_j}{\partial x_i} - \frac{2}{3} \delta_{ij} \frac{\partial \tilde{u}_k}{\partial x_k} \right) \right) \quad (1.44)$$

where  $\mu_t$  is a turbulent dynamic viscosity, which has to be modelled. Closures for it have been extensively studied [24, 26] and new models are still nowadays being postulated [27, 28]. Commonly used models include the Smagorinsky model [29], which is based on a strain invariant and uses a pre-specified constant, the Dynamic Eddy Viscosity (DEV) [26], which was developed to dynamically evaluate the constant in the Smagorinsky model, the Wall-Adapting Local Eddy-viscosity (WALE) [27], which is based on strain and rotational invariants, and the QR [28], based on two strain invariants.

Regarding the unresolved scalar fluxes, such as the temperature or the mixture

fraction, usually a gradient assumption is invoked

$$\widetilde{\rho u''_i h''} = -\frac{\partial}{\partial x_j} \left( \frac{\kappa_t}{c_{p,t}} \frac{\partial \tilde{T}}{\partial x_i} \right) \quad (1.45a)$$

$$\widetilde{\rho u''_i Y''_k} = -\frac{\partial}{\partial x_j} \left( D_{t,k} \frac{\partial \tilde{Y}_k}{\partial x_i} \right) \quad (1.45b)$$

where, analogously to the turbulent dynamic viscosity,  $\kappa_t$  and  $D_{t,k}$  are the turbulent thermal conductivity and species  $k$  diffusivity. Usually, turbulent Prandtl and, Schmidt or Lewis numbers, are assumed. These non-dimensional numbers are either constant or dynamically computed in a similar way as the Dynamic Eddy Viscosity model (DEV) [26, 30]. In Chapter 5 different combinations of models for the turbulent viscosity and turbulent scalar diffusivity are analysed.

### 1.2.6 Combustion closure

In the filtered transport equations of the species Eq. (1.42) there still remains an unclosed term, the filtered reaction rate  $\bar{w}_k$ . This filtered term cannot be easily modelled due to the presence of exponential terms, powers and products between them. Even for the simplest case of chemistry being described by a one step irreversible reaction, the filtered reaction rate is not correctly described through the mean density  $\rho$ , temperature  $\tilde{T}$  and mass fractions,  $\tilde{Y}_F$  and  $\tilde{Y}_O$

$$\bar{w}_k = \overline{A\rho^2 T^\beta Y_F Y_O \exp\left(-\frac{E_a}{RT}\right)} \neq A\bar{\rho}^2 \tilde{T}^\beta \tilde{Y}_F \tilde{Y}_O \exp\left(-\frac{E_a}{R\tilde{T}}\right) \quad (1.46)$$

Although Taylor series expansion could be used, the approach introduces new terms and correlations that also require modelling. Hence, the difficult closure of the filtered reaction rate, plus the high computational requirements to include large chemical mechanisms, led to the development of combustion models based on physical analysis. Several models and variants can be found in the literature. Furthermore, most of the models were developed in the context of one of the two burning modes previously described. Some of the most commonly used turbulent combustion models for diffusion flames are now described.

#### Eddy Dissipation Concept (EDC)

The Eddy Dissipation Concept by Magnussen and Mjertager [31] is an extension to diffusion flames of the Eddy-Break-Up model (EBU) proposed for premixed flames by Spalding [32, 33] (see also [2, 10]). The model was developed for flows at high Reynolds numbers ( $Re \gg 1$ ) and high Damköhler numbers  $Da \gg 1$ . Hence, chemistry was assumed infinitely fast and turbulent motions were assumed to be the rate

controlling mechanism. The model assumes that chemistry takes place through a one step irreversible reaction with the reaction rate controlled by the deficient species

$$\bar{w} = C_{mag} \frac{\bar{\rho}}{\tau_t} \min\left(\tilde{Y}_F, \frac{\tilde{Y}_O}{s}, \zeta \frac{\tilde{Y}_P}{1+s}\right) \quad (1.47)$$

where  $s = \nu_O W_O / \nu_F W_F$ ,  $\tau_t$  is a turbulent time-scale, and  $C_{mag}$  and  $\zeta$  are model constants.  $F, O, P$  sub-indexes denote fuel, oxidant and products, respectively.

### PDF methods

Stochastic methods aim at describing turbulent flow motions through their statistical distributions [23, 34]. The key element in these methods is the probability density function (*pdf*) of a quantity  $\phi$  which represents the probability  $P_\phi(\Phi)d\Phi$  of finding its value in the range  $\Phi < \phi < \Phi + d\Phi$ , where  $\Phi$  is the sample space. The dependence on several different variables is taken into account through joint probabilities  $P(\Phi_1, \dots, \Phi_N)$ . These statistical distributions are a function of space and time. Hence, transport equations are used to compute their spatial and temporal evolution. Usually joint probabilities are expressed for flow field variables, pressure and velocities [23, 35]. Similarly, this approach can be used to describe the different species and the temperature involved in complex chemistry.

The main interest of *pdf* methods is that one point statistics are naturally closed. For example, no model is required to close the filtered reaction rate. However, functions with spatial dependence, such as diffusion terms, must be modelled because the one-point *pdf* requires additional length scale information.

PDF methods represent a very general statistical description of turbulent reacting flows, since they do not require closure for the chemical source term. However, they are a computationally demanding, which limits their applicability [2]. *Pdf* balance equations are commonly solved using Monte Carlo methods [23, 36].

Based on the statistical description of flows, presumed *pdf* approaches have been applied in the context of other combustion modes, such as in the flamelet model described afterwards. Assuming the shape of a statistical distribution reduces the generality of the method. Nonetheless, several studies have shown their viability in the context of turbulent reacting flows [2, 34, 37].

### Conditional Moment Closure (CMC)

The Conditional Moment Closure (CMC) developed by Klimenko [38] and Bilger [39] is based on a description of diffusion flames in mixture fraction space. Hence, instead of directly solving for mass fractions and temperature, the method solves for conditional quantities  $\rho\phi|Z$ , where  $\phi$  represents either temperature or species mass fractions and  $Z$  represents a mixture fraction level. The method was also extended to premixed flames by Klimenko and Bilger [40], where variables were conditioned on

a progress-variable. Filtered quantities are then given by

$$\bar{\rho}\tilde{\phi} = \int_0^1 (\overline{\rho\phi|Z}) P(Z) dZ \quad (1.48)$$

where  $P(Z)$  is the probability density function. The method requires the solution of  $N+1$  transport equations corresponding to the number of species considered and the temperature, plus  $N_Z$  transport equations corresponding to each level of  $Z$  considered. In order to reduce the computational requirements, simplified versions of this model have been proposed where the statistical distribution is assumed. The latter approach is referred to as Presumed Conditional Approach (PCM) [41].

### Flamelet model

Flamelet models are based on a scale separation between flow and chemistry, where the latter is assumed to exist in locally laminar regions within a turbulent flow. Hence, reacting cases are decomposed into a flame structure problem and a transport problem. The former results in a set of reaction-diffusion equations in mixture fraction space. The latter describes the transport of the flame problem in physical space, which involves the momentum and the mixture fraction field transport. A further assumption is introduced which states that in this regime thermochemical changes occur mostly in the normal directions to the flame front. The resulting set of equations in mixture fraction space take the form [34, 42]

$$\rho \frac{\partial \phi_k}{\partial t} = \frac{\rho}{Le_{\phi_k}} \frac{\chi_Z}{2} \frac{\partial^2 \phi_k}{\partial Z^2} + \dot{w}_k + S_k \quad (1.49)$$

where  $\phi_k = \{Y_k, T\}$ ,  $Le_{\phi_k} = \{Le_k, 1\}$  and  $\dot{w}_k$  is the reaction rate for the species and the chemical energy release for the temperature equation.  $S_k$  represents any additional terms. The scalar dissipation rate  $\chi_Z = 2D_Z \left| \frac{\partial Z}{\partial x_i} \frac{\partial Z}{\partial x_i} \right|$  links the flame structure with the transport problem.

The reaction-diffusion set of equations can be solved in a pre-processing stage or together with the transport problem. The second approach is denoted as the interactive approach [43, 44]. It is possible to pre-process the flame structure, which in turn results in a reduction in computational costs. However, it requires a model for the influence of the transport problem on the flame structure, namely the scalar dissipation rate. If a model is set, flamelet databases may be built.

In laminar flows or in DNS, thermochemical data obtained from the flame structure can be directly used during the solution of the momentum equations. However, in LES and RANS filtered quantities are required. Therefore, the interaction between turbulence and chemistry has to be modelled. The common approach is to couple flamelet models with presumed *pdf*'s in order to reduce the computational load. Hence,

thermochemical variables are expressed as

$$\bar{\rho}\tilde{\phi} = \int_{\chi_Z} \int_0^1 \rho\phi\tilde{P}(Z, \chi_Z) dZ d\chi_Z \quad (1.50)$$

where a  $\beta - pdf$  is usually assumed for the mixture fraction  $pdf$  [2, 34, 37, 44, 45].

A last issue to consider for flamelet models with a pre-processing stage is the set of parameters used to represent the flamelet subspace. The classical model introduced by Peters [34] used the mixture fraction and the scalar dissipation rate as parameters. However, these two parameters could not fully describe the flamelet subspace. Pierce and Moin [37] proposed changing the parameters used to define the flamelet database in order to fully describe the flamelet subspace.

In this thesis the flamelet model with presumed  $pdfs$  is used. Specifically, the Flamelet/Progress-variable model is selected due to its capacity to represent the flamelet subspace. In Chapter 3 the model is discussed in detail.

### 1.3 Background at the CTTC

The present thesis belongs to the effort developed at the *Centre Tecnològic de Transferència de Calor* (CTTC) at the *Universitat Politècnica de Catalunya* (UPC) in the field of heat and mass transfer. The present thesis cannot be understood without the contributions, know-how and expertise of the Group, which over the years have developed and applied a variety of methods and techniques to solve different phenomena of interest, in the field of heat and mass transfer. The following description is by no means exhaustive. Nonetheless, it is representative of the effort of the CTTC Group.

Early steps in the combustion field were performed by A. Oliva in his thesis [46] where an experimental unit consisting of a combustion chamber was built and subsequently a chemical equilibrium code was developed.

In the context of turbulent modelling, the first studies in the Group were carried out in the thesis of C.D. Pérez-Segarra [47] which focused on the study of boundary layers. The next steps led to the use of RANS techniques applied to different flows of interest in both natural and turbulent convection.

As previously stated, CFD techniques are computationally demanding. Therefore, several techniques have been developed over the years in order to increase the simulation capabilities. One of the key aspect is parallelism, where the computational effort is split among several processing units, or CPU - and nowadays even including GPUs and other accelerators-. However, the opportunities that arise from parallelism come with several challenges. Work load split requires codes to be written specifically considering this aspect. Furthermore, it is of interest that the code easily scales when going from a few CPUs to a large number of them, being hundreds, thousands or tens

of thousands. To this end, the Message Passing Interface (MPI) standard is used, along with domain decomposition. With this strategy, the case of interest is decomposed into several smaller units, each solved by a different processing unit which must communicate with its neighbouring processes. Early works in the Group on domain decomposition, parallelism and parallel solvers were performed in the thesis of M. Soria [48], among others.

With this background, several thesis were carried out in the context of laminar diffusion flames using both finite rate chemistry and flamelet formulations. In the thesis of R. Cònsul [13] a framework for the computation of combustion processes was developed. K. Claramunt [49] extended the capabilities by developing a flamelet model for diffusion flames. Extension to turbulent diffusion flames in the context of RANS modelling was also performed. D. Carbonell [21] further evolved the flamelet model and performed studies of pollutant emissions.

During the doctoral thesis of O. Lehmkuhl [25] and R. Borrell [50] the TermoFluids code [51] was developed. The initial work carried out set the basis for the solution of turbulent incompressible flows around complex geometries using unstructured meshes with conservative discretisations and taking advantage of the computational capabilities of parallel computation. The work in F.X. Trias thesis [52] and the aforementioned thesis, showed that kinetic energy preserving discretisations are critical for the accurate simulation of turbulent flows in the incompressible regime. Hence, they are also applied throughout this thesis and shown to yield accurate results.

TermoFluids (TF) can be summarised as a general purpose multi-physics CFD software for HPC applications. It is an object oriented software programmed in C++ and designed to run in parallel computing systems. TF is composed of several libraries arranged in a hierarchical scheme from the most fundamental and general to the most specific ones (which deal for instance with only a particular physical phenomenon). General unstructured meshes are used for the geometric discretisations, and the basic equations are discretised by means of a Symmetry-Preserving energy-conserving approach. There are also a number of new generation LES and regularization turbulence models, and a library with general and application-specific linear solvers.

In the last years, through the work of several people of the CTTC Group, TF has been evolving into a multi-physics software incorporating, for example, radiation effects, reactive flows, multiphase flows, fluid-structure interactions, dynamic mesh methods and multi-scale systems. Besides the capability to properly simulate all these complex physical phenomena, one of the strengths of the code is its good parallel performance, demonstrated in several supercomputers, and explicitly tested with up to 16000 CPUs.

Concerning radiation modelling, which is not the main focus of the present thesis, but as future work can be coupled with the methods here developed, it can be highlighted the thesis of G. Colomer [53] and R. Capdevila [54]. As previously stated,

in combustion simulations, an OTM model is used. Nonetheless, the methods for computing radiation heat fluxes in the aforementioned thesis could be coupled with chemically reacting flows in situations where an OTM is clearly insufficient or inadequate to account for radiation heat transfer.

Summarising, the present thesis is developed based on the expertise and know-how of the CTTC-Group. Specifically, for the computation of thermochemical properties and thermochemistry computations, a software library has been developed based on the past work on combustion of the Group. The developed numerical methods for variable density flows and combustion cases have been implemented in the TermoFluids code, which provided an already existing high-level CFD library for handling unstructured meshes, parallel numerical solvers and turbulence models, among others. Part of the work concerning staggered grids in unstructured meshes described in *Chapter 2* was mainly developed in the thesis of Ll. Jofré [55].

## 1.4 Objectives

CFD techniques are an excellent approach for studying and understanding the physics of flow transport. They can be applied to both academic and industrial cases and to several different fields, such as aerodynamics, combustion, multiphase flows, etc. However, the capabilities come at the cost of requiring a large effort in solving the mathematical equations.

As previously stated, computation of chemically reactive flows involves accounting for a large set of participating species, which by themselves increase the computational load. Furthermore, the reaction rates are a non-linear function of the species concentrations and the temperature with a wide range of temporal and spatial scales. Hence, the system of equations is stiff due to this large span of scales, which in turn requires specific numerical methods to handle it, such as implicit methods like the Gear's method [56]. Nonetheless, in many applications of interest chemistry happens in shorter time- and spatial-scales than the flow ones [2, 34]. Those cases define the flamelet regime, which are characterised by having a large Damköhler number, or equivalently having chemical reactions with large activation energies. In this regime, a split can be introduced separating the flow problem, or transport, from the flame structure, which is defined through chemistry. Accordingly, the flame may be viewed as an interface characterised by thermochemistry. Then, chemistry may be precomputed and stored in a database, which is then accessed during CFD simulations.

Besides the complexity of describing chemically reacting flows, it also has to be taken into account that most cases of interest feature turbulent flows. If a DNS of the Navier-Stokes equations were to be performed, which would solve all temporal and spatial scales of the flow, once the flamelet database parameters had been computed in the CFD simulation, the flamelet database could be accessed. Although

this approach would be highly desirable due to the level of detail achieved, it is as of today limited to certain cases due to the computational requirements. The filtering operation performed in LES reduces the computational load while still retaining the capacity to describe the unsteadiness and three-dimensionality of the flow. Therefore, using LES more complex cases can be tackled. However, solution variables are Favre filtered quantities. Hence, in order to couple an LES simulation with the precomputed thermochemistry, the latter must be restated as a function of turbulent quantities, which in turn requires knowledge of the statistical distribution of the turbulence-chemistry interactions. As previously stated, the *pdf* may be either assumed or computed. Through these models, mixing at the subgrid level is introduced, which requires a level of modelling, since information at those scales is unavailable during LES simulations.

By and large, the increase in computational capacity is enabling researchers to tackle more and more complex problems with higher detail. Tools such as High Performance Computing (HPC), which enable researchers to use large numbers of processing units together to solve one case of interest, allow simulating even more complex cases. Concerning combustion processes, and mainly due to the complexity of chemical reactions, there is a need to reduce the dimensionality of the studied cases in order to make them computationally affordable. Since a significant amount of combustion designs of interest fall under the flamelet regime, there is a clear interest in developing accurate methods and models to describe them. Moreover, due to the large span of spatial scales involved in a combustion process it is of interest to be able to refine in certain regions of interest. Hence, techniques such as local refinements or unstructured meshing may lead to increased resolution. However, specific algorithms have to be developed and studied for these specific topologies.

Therefore, given the described challenges in the combustion field, the present thesis focuses on

- Developing algorithms to handle variable density flows on unstructured meshes. Furthermore, studying and understanding the effect of different spatial schemes applied on unstructured meshes when dealing with variable density cases. Additionally, due to the computational effort required, a focus on HPC is placed, so that the developed algorithms may be used in large computer clusters.
- Implementing and studying combustion models for flames in the flamelet regime, which can be readily used for the study of laminar and turbulent diffusion flames.
- Developing and using a code to create flamelet libraries for diffusion flames taking into account all phenomena of interest, such as differential diffusion and radiation effects. Furthermore, due to the interest in turbulent flows, the interaction between chemistry and turbulence is to be modelled and studied.

- Studying different numerical closures for the description of mixing at the subgrid level. Combustion models using chemistry databases assume a statistical distribution for the interaction between turbulence and chemistry at the subgrid level. Hence, the computation of the subgrid mixing becomes a critical aspect of the global model used to simulate turbulent diffusion flames.

## 1.5 Outline of the thesis

The present thesis is aimed at developing a computational framework to solve chemically reacting flows, specifically for turbulent diffusion flames. Therefore, the thesis encompasses the different aspects required to perform a numerical simulation of a turbulent diffusion flame.

In this chapter the basis for combustion modelling have been presented, including the description of thermochemistry, transport terms and their coefficients. Furthermore, an introduction to turbulent flows has been presented, which is one of the central topics of the present thesis. It has been argued that solving the combustion process directly using filtered quantities is not feasible due to the large fluctuations found in turbulent flames. Hence, combustion modelling is mostly achieved through phenomenological models.

In *Chapter 2*, a low Mach algorithm for variable density flows and specially adapted for unstructured grids is presented. The study focuses on using a suitable temporal integration scheme on unstructured meshes. Furthermore, different numerical schemes for evaluating convective fluxes at cell faces are assessed. Specifically, a Symmetry-Preserving scheme is studied for the momentum equations, and for the scalar transport equations central and upwinding schemes are studied. Both collocated and staggered formulations in the context of unstructured meshes are discussed. Test cases involve non-reacting and reacting cases.

Following, in *Chapter 3* the combustion model is described. As previously stated, including detailed chemical kinetics during CFD simulations results in an unwieldy task. Furthermore, in turbulent flows chemistry-turbulence interactions have to be taken into account, which increases even more the computational costs. Therefore, a flamelet model is described. The basis of the model in laminar flames is presented and then extended to turbulent flows. Moreover, a variant of the classical flamelet model is described, the Flamelet/Progress-Variable (FPV) model, which allows a unambiguous representation of the whole flamelet subspace. The FPV model relies on a progress-variable, which is not uniquely defined, and in fact, is case dependent: on the combustion mode, the chemical mechanism and fuel composition.

Then, in *Chapter 4* the definition of the progress-variable is studied when differential diffusion is considered. Besides the aforementioned dependencies for the definition of the progress-variable, in this chapter it is shown that including differential diffusion,

besides altering the species distribution in mixture fraction space, also influences the monotonicity of the progress-variables. In other words, a definition suitable when the flamelets are computed using Fickian diffusion may not be suitable when differential diffusion is accounted for. Two different jet diffusion flames are studied, the first being a turbulent diffusion flame using a mixture of methane and hydrogen as fuel and the second being a self-igniting methane flame in a vitiated coflow. The studied flames feature Reynolds numbers of  $\mathcal{O}(10^4)$ .

Afterwards, in *Chapter 5* the flamelet model is studied in the context of turbulent flames. In the flamelet model, turbulence-chemistry interactions are modelled through an assumed *pdf*, which commonly uses the first two moments, the mean and the variance. The former is directly computed during CFD simulations. However, the latter requires modelling. Therefore, *Chapter 5* studies different closures for the subgrid variance and shows their effect on the numerical effect on the flame stabilisation. The methane/hydrogen diffusion flame, from *Chapter 4*, is here used to assess the effect of different closures for the subgrid mixing on the flame stabilisation and scalars distribution.

Closing the document, conclusions and future work are presented.

## References

- [1] <http://www.claymath.org/millennium-problems>, 2015.
- [2] T. Poinsot and D. Veynante. *Theoretical and Numerical Combustion*. R.T. Edwards Inc., 2005.
- [3] K. Mahesh, G. Constantinescu, S. Apte, G. Iaccarino, F. Ham, and P. Moin. Large-eddy simulation of reacting turbulent flows in complex geometries. *Journal of Applied Mechanics*, 73(3):374–381, 2006.
- [4] M. Boileau, G. Staffelbach, B. Cuenot, T. Poinsot, and C. Bérat. Les of an ignition sequence in a gas turbine engine. *Combustion and Flame*, 73(3):374–381, 2008.
- [5] W.C. Gardiner. Thermochemical data for combustion calculations. In *Combustion Chemistry*. Springer-Verlag, New York, 1984.
- [6] A. Burcat and et al. [http://combustion.berkeley.edu/gri\\_mech/data/nasa\\_plnm.html](http://combustion.berkeley.edu/gri_mech/data/nasa_plnm.html), 2014.
- [7] C.T. Bowman, M. Frenklach, G. Smith, B. Gardiner, and et al. <http://www.me.berkeley.edu/gri-mech/releases.html>, 2012.
- [8] Jones and R.P. Lindstedt. Global reaction schemes for hydrocarbon combustion. *Combustion and Flame*, 73:233–249, 1988.

- [9] M. A. Mueller, T. J. Kim, R. A. Yetter, and F. L. Dryer. Flow reactor studies and kinetic modeling of the H<sub>2</sub>/O<sub>2</sub> reaction. *International Journal of Chemical Kinetics*, 31:113–125, 1999.
- [10] F.A. Williams. *Combustion Theory*. Perseus Books Publishing, L.L.C., 1985.
- [11] R.B. Bird, E.E. Stewart, and E.N. Lightfoot. *Transport phenomena*. John Wiley and Sons Inc., 1960.
- [12] J. Warnatz, U. Maas, and R.W. Dibble. *Combustion:Physical and Chemical Fundamentals Modeling and Simulation, Experiments Pollutant Formation*. Springer-Verlag, Berlin Heidelberg, 1996.
- [13] R. Cònsul. *Development of Numerical Codes for the Evaluation of Combustion Processes. Detailed Numerical Simulations of Laminar Flames*. PhD thesis, Polytechnic University of Catalonia, Terrassa, Spain, 2002.
- [14] E. Giacomazzi, F. R. Picchia, and N. Arcidiacono. A review of chemical diffusion: Criticism and limits of simplified methods for diffusion coefficient calculation. *Combustion Theory And Modelling*, 12(1):135–158, 2008.
- [15] P.J. Coelho. Numerical simulation of the interaction between turbulence and radiation in reactive flows. *Progress in Energy and Combustion Science*, 33(4):311–383, 2007.
- [16] P.J. Coelho. Advances in the discrete ordinates and finite volume methods for the solution of radiative heat transfer problems in participating media. *Journal of Quantitative Spectroscopy and Radiative Transfer*, 145:121–146, 2014.
- [17] W.A. Fiveland. Discrete-ordinates solutions of the radiative transport equation for rectangular enclosures. *Journal of Heat Transfer*, 106:699–706, 1984.
- [18] G.D. Raithby and E.H. Chui. A finite volume method for predicting radiant heat transfer in enclosures with participating media. *Journal of Heat Transfer*, 112:415–423, 1990.
- [19] M.F. Modest. *Radiative Heat Transfer*. Academic Press, Second edition, 2003.
- [20] R.S. Barlow, J.H. Karpetis A.N., Frank, and J.-Y. Chen. Scalar profiles and NO formation in laminar opposed-flow partially premixed methane/air flames. *Combustion and Flame*, 127(3):2102–2118, 2001.
- [21] D. Carbonell. *Numerical studies of diffusion flames. Special emphasis on flamelet concept and soot formation*. PhD thesis, Polytechnic University of Catalonia, Terrassa, Spain, 2010.

- [22] W.L. Grosshandler. RADCAL: A narrow-band model for radiation calculations in a combustion environment. Technical Note 1402, NIST, 1993.
- [23] S.B. Pope. *Turbulent Flows*. Cambridge University Press, 2000.
- [24] P. Sagaut. *Large Eddy Simulation for Incompressible Flows. An Introduction*. Springer-Verlag, 1980.
- [25] O. Lehmkuhl. *Numerical resolution of turbulent flows on complex geometries*. PhD thesis, Polytechnic University of Catalonia, Terrassa, Spain, 2012.
- [26] M. Germano, U. Piomelli, P. Moin, and W. Cabot. A dynamic subgrid-scale eddy viscosity model. *Physics of Fluids*, 3(7):1760–1765, 1991.
- [27] F. Nicoud and F. Ducros. Subgrid-scale stress modeling based on the square of the velocity gradient tensor. *Flow, Turbulence and combustion*, 62:183–200, 1999.
- [28] R. Verstappen. When does eddy viscosity damp subfilter scales sufficiently? In *Quality and Reliability of Large-Eddy Simulations II*, volume 16 of *Ercof tac Series*, volume 16, pages 421–430. M.V. Salvetti, B. Geurts, J. Meyers, and P. Sagaut, editors, 2010.
- [29] J. Smagorinsky. General circulation experiments with the primitive equations: 1. the basic experiment. *Monthly Weather Review*, 91:99–164, 1963.
- [30] P. Moin, W. Squires, W. Cabot, and S. Lee. A dynamic subgrid-scale model for compressible turbulence and scalar transport. *Physics of Fluids*, 3(11):2746–2757, 1991.
- [31] B.F. Magnussen and B.H. Mjertager. On mathematical modelling of turbulent combustion. In *Proceedings of the Sixteenth Symposium (International) on Combustion*, pages 719–727, 1976.
- [32] D.B. Spalding. Mixing and chemical reaction in steady confined turbulent flames. In *Proceedings of the Thirteenth Symposium (International) on Combustion*, pages 649–657, 1971.
- [33] D.B. Spalding. Development of the eddy-break-up model of turbulent combustion. In *Proceedings of the Sixteenth Symposium (International) on Combustion*, pages 1657–1663, 1976.
- [34] N. Peters. *Turbulent Combustion*. Cambridge University Press, 2000.
- [35] S.B. Pope. Pdf methods for turbulence reactive flows. *Progress in Energy and Combustion Science*, 11:119–192, 1985.

- [36] C. Dopazo. Recent developments in pdf methods. In *Turbulent Reacting flows*. Academic, London, 1994.
- [37] C.D Pierce and P. Moin. Progress-variable approach for large-eddy simulation of non-premixed turbulent combustion. *Journal of Fluid Mechanics*, 504:73–97, 2004.
- [38] A.Y. Klimenko. Multicomponent diffusion of various admixtures in turbulent flow. *Fluid Dynamics*, 25(3):327–334, 1990.
- [39] R.W. Bilger. Conditional moment closure for turbulent reacting flow. *Physics of Fluids A: Fluid Dynamics*, 5(22):436–444, 1993.
- [40] A.Y. Klimenko and R.W. Bilger. Conditional moment closure for turbulent combustion. *Progress in Energy and Combustion Science*, 25(6):595–687, 1999.
- [41] L. Vervisch, R. Hauguel, P. Domingo, and M. Rullaud. Three facets of turbulent combustion modelling: Dns of premixed v-flame, les of lifted nonpremixed flame and rans of jet-flame. *Journal of Turbulence*, 5(4):1–36, 2000.
- [42] H. Pitsch and N. Peters. A consistent flamelet formulation for non-premixed combustion considering differential diffusion effects. *Combustion and Flame*, 114:26–40, 1998.
- [43] H. Pitsch. Unsteady flamelet modelling of differential diffusion in turbulent jet diffusion flames. *Combustion and Flame*, 123:358–374, 2000.
- [44] H. Pitsch and H. Steiner. Large-eddy simulation of a turbulent piloted methane/air diffusion flame (Sandia flame D). *Physics of Fluids*, 12(10):2541–2554, 2000.
- [45] L. Liu, H. Guo, G.J. Smallwood, Ö.L. Gülder, and M.D. Matovic. A robust and accurate algorithm of the  $\beta$ -pdf integration and its application to turbulent methane-air diffusion combustion in a gas turbine combustor simulator. *International Journal Of Thermal Sciences*, 41:763–772, 2002.
- [46] A. Oliva. *Resolución sistemática por métodos numéricos de la transmisión de calor por conducción y convección en condiciones subsónicas y de estabilización*. PhD thesis, Polytechnic University of Catalonia, Terrassa, Spain, 1982.
- [47] C.D. Segarra-Pérez. *Criterios numéricos en la resolución de la transferencia de calor en fenómenos de convección*. PhD thesis, Polytechnic University of Catalonia, Terrassa, Spain, 1987.

- [48] M. Soria. *Parallel multigrid algorithms for computational fluid dynamics and heat transfer*. PhD thesis, Polytechnic University of Catalonia, Terrassa, Spain, 2000.
- [49] K. Claramunt. *Numerical Simulation of Non-premixed Laminar and Turbulent Flames by means of Flamelet Modelling Approaches*. PhD thesis, Polytechnic University of Catalonia, Terrassa, Spain, 2005.
- [50] R. Borrell. *Parallel algorithms for Computational Fluid Dynamics on unstructured meshes*. PhD thesis, Polytechnic University of Catalonia, Terrassa, Spain, 2012.
- [51] O. Lehmkuhl, C.D. Pérez Segarra, R. Borrell, M. Soria, and A. Oliva. Termofluids: A new parallel unstructured CFD code for the simulation of turbulent industrial problems on low cost PC cluster. *Proceedings of the Parallel CFD Conference*, pages 1–8, 2007.
- [52] F.X. Trias. *Direct Numerical simulation and regularization modelling of turbulent flows of on loosely coupled parallel computers using symmetry-preserving discretizations*. PhD thesis, Polytechnic University of Catalonia, Terrassa, Spain, 2006.
- [53] G. Colomer. *Numerical methods for radiative heat transfer*. PhD thesis, Polytechnic University of Catalonia, Terrassa, Spain, 2006.
- [54] R. Capdevila. *Numerical simulation of radiative heat transfer in turbulent flows*. PhD thesis, Polytechnic University of Catalonia, Terrassa, Spain, 2012.
- [55] Ll. Jofre. *Numerical simulation of multiphase immiscible flow on unstructured meshes*. PhD thesis, Polytechnic University of Catalonia, Terrassa, Spain, 2014.
- [56] E. Hairer and G. Wanner. *Solving Ordinary Differential Equations II. Stiff and Differential-Algebraic Problems*. Springer-Verlag Berlin-Heidelberg, 1996.

# Numerical assessment of conservative unstructured discretisations for Low-Mach flows

Main contents of this chapter have been presented at international conferences:

J.Ventosa, J. Chiva; O. Lehmkuhl, C.D. Pérez-Segarra. *Modelization of the Low-Mach Navier Stokes equations in unstructured meshes.* In Proceedings of the 7th International Conference on Computational Heat and Mass Transfer ICCHMT 2011, pp. 1-8., Istanbul, Turkey, July 2011.

J.Ventosa, J. Chiva; O. Lehmkuhl, C.D. Pérez-Segarra, A. Oliva. *Low Mach Navier-Stokes equations on unstructured meshes.* In Proceedings of the 15th Conference on Modelling Fluid Flow(CMFF'12): 15th event of International Conference Series on Fluid Flow Technologies, pp. 979-986, Budapest, September 2012.

**Abstract.** Unstructured meshes allow easily representing complex geometries and refining in regions of interest without increasing the number of control volumes in unnecessary regions. However, numerical schemes used in unstructured grids have to be properly defined in order to minimise numerical errors. An assessment of a low-Mach algorithm on unstructured meshes using collocated and staggered formulations is presented. For staggered formulations using cell centred velocity reconstructions, the standard first-order method is shown to be inaccurate in low Mach flows in unstructured grids. A recently proposed least squares procedure for incompressible flows is extended to the low Mach regime and shown to improve the behaviour of the algorithm. Regarding collocated discretisations, the odd-even pressure decoupling is handled through a kinetic energy conserving flux interpolation scheme. Besides, high and low order face interpolations for unstructured meshes are assessed using a numerical function reconstruction. A kinetic energy preserving scheme is applied to the momentum equations. Spatial schemes are assessed against a differentially heated cavity and a turbulent self-igniting diffusion flame.

## 2.1 Introduction

Numerical algorithms to simulate low Mach number flows have received increasing attention over the past decades since they apply to a wide range of applications, such as natural phenomena or in technological designs. Combustion processes, meteorological flows and solar energy are examples of their applicability.

The low Mach number approximation of the Navier-Stokes equations is characterized by being able to handle flows with a Mach number much lower than unity ( $Ma \ll 1$ ) but with strong density variations. Large temperature or concentration gradients may be the cause for them. These high variations in density do not correspond to high pressure variations within the flow, which in fact are low.

Despite having similar ranges of applicability, incompressible algorithms, which make use of the Boussinesq approximation, are not suitable when temperature variations are higher than 10% around the mean, as shown by Gray and Giorgini [1]. On the other side, compressible formulations of the Navier-Stokes equations are suited to study flows with strong density variations. However, at low Mach numbers the standard compressible algorithms present stability issues resulting in strong time step limitations. These limitations are imposed by numerical requirements, namely the Courant-Friedrich-Lowy (CFL) condition, for explicit methods, as the acoustic phenomena implicit in the compressible equations must be accounted for. At low Mach numbers, when acoustic phenomena is not of interest, a possible solution is to remove the high order dependencies of the Mach number of the Navier-Stokes equations. Consequently, Navier-Stokes equations could be expanded in power series of the Mach number, thus removing higher order dependencies. The time step of the resulting formulation is not restricted by the Mach number.

Several approaches have been developed in the past to solve flows with high density variations. Vierendeels et al.[2] used a finite-volume approach to solve the full compressible Navier-Stokes equations, applying a preconditioner to the temporal term in order to overcome the stiffness of compressible algorithms at low Mach numbers. Kloczko et al.[3] developed a matrix free method to solve the full compressible equations using also a low Mach preconditioner in order to overcome this stiffness. Becker and Braack [4] used the low Mach number approximation and solved the system of equations by means of a Galerkin finite element approach. Darbandi and Hosseiniyadeh [5] proposed a modification to the incompressible SIMPLE algorithm in finite-volume formulations to account for large density variations. Shunn et al. [6] studied a semi-implicit fractional step using structured and unstructured finite-volume meshes. Najm et al. [7] proposed a low Mach algorithm based on the classical fractional step of Kim and Moin [8] in a finite-volume approach. Similarly, Nicoud [9], Knikker [10] and Lessani and Papalexandris [11] proposed approaches in a finite difference context.

Regarding the spatial discretisation, most of the studies cited reported struc-

tured/cartesian meshes [2, 7, 9–14]. Use of structured meshes is suitable for simple geometries, but more complex ones used unstructured grids. Furthermore, this framework is of interest for industrial applications, where, due to the complex designs, use of unstructured meshes reduces the computational requirements or becomes a must if the geometry is very complex.

In the context of the finite-volume method, collocated or staggered discretisations are used to handle the pressure-velocity coupling. Collocated and staggered approaches differ in the location of the momentum’s primary variables, velocity and pressure. In the collocated formulation both pressure and velocity are placed at cell centres, while in the staggered formulation velocity is placed at cell faces and pressure at cell centres. This staggering of the velocity requires the construction of a displaced mesh around cells’ faces in order to perform the temporal integration. The collocated approach is preferred in complex grids as it is not required to construct these displaced meshes. However, the collocated formulation presents an *odd-even decoupling* between pressure and velocity, which the staggered formulation does not manifest. Felten and Lund [15] proposed a mass flux correction in order to avoid this pressure-velocity decoupling for incompressible flows. As for the staggered discretisation, the cost is then the construction of a suitably displaced mesh, which in cartesian meshes is easily performed. However, in body-fitted or unstructured meshes it is not as straightforward. Nonetheless, Perot [16] proposed an effortless method to construct a displaced grid on unstructured meshes. Still, this method relies on the computation of the cell centred velocities.

Aside from defining a framework to tackle the pressure-velocity coupling suitable to be used on unstructured meshes, attention must also be given to the numerical interpolations. As it can readily be seen in Segarra et al.[17], in the process of devising high order schemes for unstructured meshes, low order intermediate approximations must be made, thus affecting their theoretical high order properties. Non-orthogonal effects and the difficulties in defining high order stencils for a given interpolation hinder the possibility of constructing high order schemes. For this reason, the definition of the discrete convective and diffusive operators are mainly led by stability and kinetic energy preservation criteria, though accuracy is also taken into consideration. As described by Verstappen and Veldman [18], the discrete approximations of the differential convective and diffusive operators have to be performed so that the operators’ differential properties are preserved in their discrete counterparts. Felten and Lund [15] studied these discretisations in the context of collocated meshes, and showed the appropriateness of this discretisation procedure in order to reduce errors in the kinetic energy conservation. Trias et al. [19] and Jofre et al. [20] extended the formulation and studied their behaviour in unstructured meshes for incompressible flows. Additionally, since kinetic energy preservation does not play any role in the scalars transport equations, upwinding schemes are also considered.

The aim of the chapter is to study collocated and staggered discretisations in unstructured finite-volume grids for low Mach flows. The accuracy of face interpolation schemes in unstructured grids is also assessed. The cell centred flux correction proposed by Felten and Lund [15] for incompressible flows is applied to variable density flows and shown to correctly describe the fluid flow. Regarding the staggered discretisation, the first order cell centred velocity proposed by Perot [16] is analysed alongside a recently proposed second order velocity reconstruction proposed by Jofre et al. [20]. Additionally, based on a kinetic energy preservation criterion, a Symmetry-Preserving scheme [18] developed for incompressible flows, is applied to the velocities interpolations in the momentum equations.

In order to study the effect of unstructured discretisations on the different interpolation schemes several numerical tests are performed. First, a numerical test is conducted where an exact sinusoidal function is reconstructed. The global numerical algorithm is then validated against a non-reacting and a reacting test case. The non-reacting case of study is a differentially heated square cavity filled with air under a large temperature difference [12, 21, 22]. It serves to evaluate the accuracy of both collocated and staggered formulations together with the different discretisation schemes considered. The second case of study is a transient chemically reacting flow, consisting in the autoignition of a hydrogen jet flowing into a hot air coflow, based on the experiments of Markides and Mastorakos [23]. This case serves to ascertain the correct transient behaviour of the proposed algorithm.

The remainder of the chapter is organized as follows: in Sec. 2.2 the low Mach number approximation to the Navier-Stokes equations is presented, followed by the description of the unstructured spatial discretisations in Sec. 2.3. In Sec. 2.4 the temporal algorithm is described. In Sec. 2.5 the results for the test cases are presented and finally the conclusions.

## 2.2 Low-Mach number equations

In order to obtain the low-Mach Number approximation to the Navier-Stokes equations, these equations are taken in their compressible formulation and, as shown by Lessani and Papalexandris [11], the Mach dependant variables are expanded in power series of the ratio of the dynamic to the thermodynamic pressure ( $\gamma Ma^2$ ), which is a measure of the compressibility effects. For flows at low-Mach numbers here considered, this is a small parameter. Thus, keeping the lowest order terms of this

expansion, the low-Mach number equations are

$$\frac{\partial \rho}{\partial t} = -\frac{\partial \rho u_j}{\partial x_j} \quad (2.1)$$

$$\frac{\partial \rho u_i}{\partial t} = -\frac{\partial \rho u_j u_i}{\partial x_j} - \frac{\partial p}{\partial x_i} + \frac{\partial \tau_{ij}}{\partial x_j} + \rho g_i \quad (i = 1, 2, 3) \quad (2.2)$$

$$\rho \frac{\partial h}{\partial t} = -\rho u_j \frac{\partial h}{\partial x_j} + \frac{dP_o}{dt} - \frac{\partial \dot{q}_j}{\partial x_j} \quad (2.3)$$

where  $\tau_{ij} = \mu \left( \frac{\partial u_i}{\partial x_j} + \frac{\partial u_j}{\partial x_i} - \frac{2}{3} \delta_{ij} \frac{\partial u_k}{\partial x_k} \right)$  and  $\dot{q}_j = -\kappa \frac{\partial T}{\partial x_j}$ . In the momentum equation,  $p$  may be interpreted as the hydrodynamic pressure and in the energy equation  $P_o$  as the thermodynamic pressure, which is considered spatially uniform. Here, due to the low-Mach approximation, the viscous heating  $\tau_{ij} \frac{\partial u_i}{\partial x_j}$  and the pressure term  $u_i \frac{\partial p}{\partial x_i}$  are neglected. The enthalpy used for non-reacting flows is the sensible enthalpy

$$dh = c_p dT \quad (2.4)$$

The thermodynamic pressure, temperature and density are coupled through the equation of state

$$P_o = \rho R_g T \quad (2.5)$$

It should be noted that the scalars' transport equations are formulated in non-conservative form. The need for it will be clearly shown when the temporal integration algorithm is presented. Thermophysical properties of the fluid are a function of temperature and thermodynamic pressure, where it applies.

### 2.2.1 Chemically reacting flows

When a chemically reacting flow is considered, the distribution of the different species constituting the flow must also be tracked. Only  $N - 1$  additional equations are then introduced, since the sum of the  $N$  equations results in the continuity equation, Eq. (2.1). The transport equation of the  $k$ th specie mass fraction  $Y_k$  in non-conservative form, using Hirschfelder and Curtiss approximation [24] is

$$\rho \frac{\partial Y_k}{\partial t} = -\rho u_j \frac{\partial Y_k}{\partial x_j} + \frac{\partial}{\partial x_j} \left( \rho D_k \frac{\partial Y_k}{\partial x_j} \right) + \frac{\partial}{\partial x_j} \left( \rho Y_k \left( \frac{D_k}{M_w} \frac{\partial M_w}{\partial x_j} - V_j^c \right) \right) + \dot{w}_k \quad (2.6)$$

where  $V_j^c = \sum_k (D_k/M_w) (\partial(M_w Y_k)/\partial x_j)$  is a correction velocity to ensure global mass conservation. The term  $\dot{w}_k$  represents the chemical reaction rate,  $D_k$  is a species mass diffusivity and  $M_w$  is the mixture molar mass. The energy equation is solved in its enthalpy form, as shown in Eq. (2.3). For chemically reacting cases, the enthalpy

is equal to the sum of the enthalpy of formation plus the sensible enthalpy, resulting in

$$h = \sum_{k=1}^N Y_k h_k = \sum_{k=1}^N Y_k \left( \Delta h_{f,k}^o + \int_{T_0}^T c_{p_k} dT \right) \quad (2.7)$$

The heat transfer flux for reacting cases becomes

$$\dot{q}_j = -\kappa \frac{\partial T}{\partial x_j} - \sum_{k=1}^N \rho h_k \left( \frac{D_k}{M_w} \frac{\partial (M_w Y_k)}{\partial x_j} - Y_k V_j^c \right), \quad (2.8)$$

where the second term on the right hand side represents the transport of energy due to mass diffusion. For the present study, both Soret and Dufour effects are considered to be negligible, thus the energy equation remains unchanged as defined in Eq. (2.3).

### 2.2.2 Thermodynamic pressure

In low-Mach flows, the state equation Eq. (2.5) couples the temperature and the density through a spatially uniform thermodynamic pressure. Then, the energy equation acts as a constraint on the flow. Using the transport equations Eq. (2.1), Eq. (2.3), Eq. (2.6) and the state equation Eq. (2.5) the velocity divergence constraint for perfect gases becomes

$$\begin{aligned} \frac{\partial u_j}{\partial x_j} &= \frac{R_g}{c_p P_o} \left[ \frac{\partial}{\partial x_j} \left( \kappa \frac{\partial T}{\partial x_j} \right) - \left( \frac{c_p}{R_g} - 1 \right) \frac{dP_o}{dt} - \sum_{k=1}^N h_k \dot{w}_k \right. \\ &\quad \left. + \sum_{k=1}^N \rho c_{p,k} \left( \frac{D_k}{M_w} \frac{\partial (M_w Y_k)}{\partial x_j} - Y_k V_j^c \right) \frac{\partial T}{\partial x_j} \right] \end{aligned} \quad (2.9)$$

Integrating over the computational domain gives an equation for the thermodynamic pressure variation

$$\begin{aligned} \frac{dP_o}{dt} &= \frac{1}{\int_V \left( \frac{c_p}{R_g} - 1 \right) dV} \left[ \int_V \frac{\partial}{\partial x_j} \left( \kappa \frac{\partial T}{\partial x_j} \right) dV - \frac{P_o}{R_g} \int_V c_p \frac{\partial u_j}{\partial x_j} dV - \int_V \sum_{k=1}^N h_k \dot{w}_k dV \right. \\ &\quad \left. + \int_V \sum_{k=1}^N \rho c_{p,k} \left( \frac{D_k}{M_w} \frac{\partial (M_w Y_k)}{\partial x_j} - Y_k V_j^c \right) \frac{\partial T}{\partial x_j} dV \right] \end{aligned} \quad (2.10)$$

If the system is considered open, this thermodynamic pressure is deemed constant and set to ambient pressure or the reference pressure for the specific case. If the

system is closed, a mass conservation is invoked, and the pressure at a given time can be obtained through the total mass in the enclosure and the temperature field

$$M_o = \frac{P_o}{R_g} \int_V \frac{1}{T_{t=0}} dV \quad (2.11)$$

$$P_o(t) = \frac{M_o R_g}{\int_V \frac{1}{T(t)} dV} \quad (2.12)$$

### 2.2.3 Momentum projection scheme - Fractional Step method

In order to solve the pressure-velocity coupling that appears in the momentum equations, Eq. (2.2), a projection method is used, namely the Fractional Step method [8]. It begins by taking the momentum equation, approximating the temporal derivative and introducing a pseudo-velocity  $\hat{u}_i^l$ , thus splitting the original equation into two parts

$$\frac{\rho^l \hat{u}_i^l - \rho^n u_i^n}{\Delta t} = \alpha^n \left\{ -\frac{\partial \rho u_j u_i}{\partial x_j} + \frac{\partial \tau_{ij}}{\partial x_j} + \rho g_i \right\}^n \quad (2.13)$$

$$\frac{\rho^l u_i^l - \rho^l \hat{u}_i^l}{\Delta t} = -\frac{\partial p^l}{\partial x_i} \quad (2.14)$$

where  $l$  and  $n$  indicate the current substep and previous time step, respectively. The right hand side (r.h.s) of Eq. (2.13) is a function of the temporal integration scheme, denoted by  $\alpha^n$ . A dual step temporal algorithm is used, where the first substep is a second-order explicit Adams-Bashforth and the second substep is an implicit Crank-Nicholson. Prior to computing the momentum equations the scalars transport equations are solved and the density  $\rho^l$  is computed using Eq. (2.5), which is shown afterwards. The next step of this projection method is to take the divergence of Eq. (2.14). Two possibilities are considered

$$\frac{1}{\Delta t} \left( \frac{\partial}{\partial x_i} (\rho^l u_i^l) - \frac{\partial}{\partial x_i} (\rho^l \hat{u}_i^l) \right) = -\frac{\partial}{\partial x_i} \left( \frac{\partial p^l}{\partial x_i} \right) \quad (2.15a)$$

$$\frac{1}{\Delta t} \left( \frac{\partial u_i^l}{\partial x_i} - \frac{\partial \hat{u}_i^l}{\partial x_i} \right) = -\frac{\partial}{\partial x_i} \left( \frac{1}{\rho^l} \frac{\partial p^l}{\partial x_i} \right) \quad (2.15b)$$

Solving the Poisson equation in the form of Eq. (2.15b) requires at each substep the computation of the matrix's coefficients due to the presence of the density, whereas by using Eq. (2.15a) this is not required. On the one hand, solution of the variable coefficient Poisson equation Eq. (2.15b) requires the evaluation of the velocity divergence at the next time step, which is not known, but can be approximated using Eq. (2.9). Using the variable coefficient Poisson equation allows the divergence free constraint

to be recovered in the limit of inviscid flows. On the other hand, when the constant coefficient Poisson equation is considered, the mass divergence at the next time step is an unknown, but it can be approximated using mass conservation Eq. (2.1). The temporal derivative of the density is then introduced into Eq. (2.15a). Even though the advantages of the second formulation, Eq. (2.15b), the first one is preferred in this work because of its lower computational effort at each substep. In both predictor and corrector substeps the pressure Poisson equation is solved using a Direct Schur Decomposition [25, 26].

Use of a constant coefficient Poisson equation requires the computation of the mass divergence at the next substep  $\nabla \cdot (\rho u)^l$ , which is not known. The continuity equation is then used to approximate it. This term has been reported to introduce numerical instabilities [9–11] and no closed form to approximate this time derivative has been reported to be best suited.

In this work, the second-order backward approximation to the first derivative at the  $l$  substep proposed by Nicoud [9] is used

$$\frac{\partial \rho}{\partial t}^l = \frac{((\Delta t^n + \Delta t^{n-1})^2 - (\Delta t^n)^2)\rho^l - (\Delta t^n + \Delta t^{n-1})^2\rho^n + (\Delta t^n)^2\rho^{n-1}}{\Delta t^n \Delta t^{n-1} (\Delta t^n + \Delta t^{n-1})} \quad (2.16)$$

By using the continuity equation to approximate the mass divergence  $\nabla \cdot (\rho u)^l$ , mass conservation is enforced. The gas state law Eq. (2.5) is used in its form at each substep to compute the density. However, energy conservation is not satisfied as it can be seen by the use of the non-conservative form of the energy equation, Eq. (2.3). As reported by Knikker [10], both constraints can only be met when an iterative time scheme is used, at the cost of a higher computational effort per iteration.

### 2.3 Unstructured discretisation

The discrete set of equations is obtained employing the finite-volume technique, where the governing equations Eq. (2.1)-(2.3) and Eq. (2.6) in differential form are integrated giving a set of conservation equations to be solved at each control volume (CV).

The generic transport equation in integral form after applying Gauss theorem is

$$\begin{aligned} \int_V \frac{\partial \rho \phi}{\partial t} dV &= - \int_A \rho u_j n_j \phi dA + \int_A \Gamma \frac{\partial \phi}{\partial x_j} \Big|_f n_j dA + \int_V \mathbb{S} dV \\ &= -C_c + D_c + \mathbb{S} \cdot V \end{aligned} \quad (2.17)$$

where  $\phi$  represents any dependent variable ( $u_i, Y_k, T$ ) and  $C, D, \mathbb{S}$  represent the convective, diffusive and extra terms, respectively. Approximating the surface integrals

as summation over cell faces, the discrete cell centred convective and diffusive terms become

$$C_c = \sum_f \phi_f \rho_f u_{i,f} n_{i,f} A_f \quad (2.18a)$$

$$D_c = \sum_f \Gamma_f (\phi_{nbcv} - \phi_{cv}) \frac{A_f}{\delta_f} \quad (2.18b)$$

where  $\phi_f$  represents an interpolation of  $\phi$  at a cell face. In the diffusive term, the derivative of the variable at the face has been estimated using a centred approximation to the first derivative. The details of these interpolations will be discussed later. The distance  $\delta_f$  for unstructured meshes is the distance between two nodes projected in the normal direction to the face,  $\delta_f = (s_{i,f} n_{i,f})$ , where  $s_{i,f}$  is the vector from the centroid of the control volume to the centroid of the neighbour control volume, as it can be seen in Fig. 2.1.

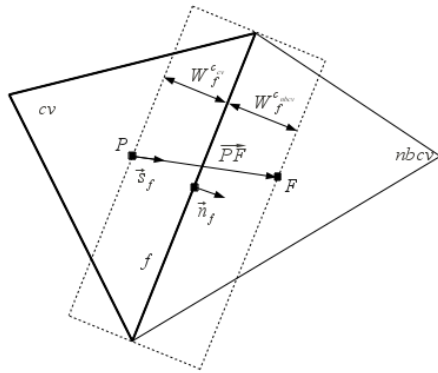


**Figure 2.1:** Geometrical parameters used to define both collocated and staggered formulations. Points **P** and **F** represent the cell centroids for collocated schemes and the cell circumcentres for staggered schemes.

Having defined the discrete form of the transport equations, in the following focus is placed on the spatial discretisation of the momentum equations in order to tackle the pressure-velocity coupling. Two formulations for unstructured meshes are here described, namely the collocated formulation detailed by Trias et al. [19] and Jofre et al. [20] and the staggered one of Perot [16].

The main difference between collocated and staggered formulations is the location of the primary solution variables. Both collocated and staggered schemes place scalar

variables  $(\rho, p, h, T, Y_k)$  at cell centres and the mass flow is placed at the cell faces. The velocity  $u_i$  is stored at the cell centres in the collocated scheme and the mass flux,  $\rho u$ , at the face centres in the staggered scheme.

Collocated formulations are known to suffer from an *odd-even decoupling* of the pressure field due to pressure and velocity being placed at the same points, as shown by Patankar [27]. Additionally, it has also been shown that collocated formulations do not fully preserve kinetic energy. Morinishi et al. [28] showed that the error was of  $\mathcal{O}(\Delta t^\alpha \Delta x_i^2)$ , with  $\alpha$  depending on the temporal integration scheme. However, when dealing with complex geometries or when non-cartesian grids are considered, the collocated mesh scheme is usually preferred due to its simplicity, as opposed to staggered formulations, which require defining displaced meshes. Construction of these displaced meshes is trivially performed for cartesian grids, but it is a more complex task for non-cartesian ones. Nonetheless, the method described by Perot [16] allows these displaced meshes to be built almost effortlessly. Staggered formulations present the advantage of not suffering from the pressure *odd-even decoupling*.

### 2.3.1 Collocated discretisation:

As described by Felten and Lund [15], collocated formulations suffer from two types of error. The first type is related to mass conservation, which also influences kinetic energy conservation. The rationale is that the pressure field obtained from the Poisson equation Eq. (2.15), ensures mass conserving fluxes at the faces, but not for the primary solution variables, which are located at the cell centres. This results in a pressure-velocity decoupling. In order to avoid it, a pressure correction to the cell centred velocities is applied. Therefore, once the pressure equation Eq. (2.15) has been solved, the cell centred velocities must be corrected using Eq. (2.14). Specifically, if the Poisson equation with constant coefficients is considered<sup>1</sup>, the cell centred velocity correction takes the form

$$u_{i,c}^l = \hat{u}_{i,c}^l - \frac{\Delta t}{\rho_c^l} \left. \frac{\partial p}{\partial x_i} \right|_c^l \quad (2.19)$$

where the cell centred pressure gradient is evaluated using the Gauss theorem.

The second type of error is related to the reconstruction of the mass flow at the

---

<sup>1</sup>An equivalent procedure is obtained in case the Poisson equation with variable coefficients is considered.

cells' faces. On the predictor stage of the Fractional Step method<sup>2</sup>, once the pseudo-velocities  $\hat{u}_i^l$  have been computed using Eq. (2.13), the pseudo-mass flow has to be evaluated

$$\hat{m}^l = (\rho \hat{u}_i)_f^l n_{if} A_f \quad (2.20)$$

where  $(\rho \hat{u}_i)_f^l$  must be approximated. As shown by Felten and Lund [15], the reconstruction of the variables at the faces is a critical issue. Therefore, in order to minimise errors in the conservation of the kinetic energy, the interpolation at the faces is performed by taking the average between neighbouring cells

$$\rho \hat{u}_i|_f^l = \frac{1}{2}(\rho \hat{u}_i|_{cv}^l + \rho \hat{u}_i|_{nbcv}^l) \quad (2.21)$$

Once the velocity at cell centres is known, the mass flow at the cell faces' is reconstructed accordingly

$$\dot{m}^l = (\rho \hat{u}_i)_f^l n_{if} A_f - \Delta t \left. \frac{\partial p}{\partial x_i} \right|_f^l \quad (2.22)$$

where the face pressure gradient is approximated by a centred finite difference  $\left. \frac{\partial p}{\partial x_i} \right|_f^l = \frac{(p_{nbcv}^l - p_{cv}^l)}{\delta_f} A_f$  and the pseudo-velocity at the cell faces is obtained through Eq. (2.19) and (2.21)

$$\rho \hat{u}_i|_f^l = \frac{1}{2} \left( \left( \rho u_i|_{cv}^l + \Delta t \left. \frac{\partial p}{\partial x_i} \right|_{cv}^l \right) + \left( \rho u_i|_{nbcv}^l + \Delta t \left. \frac{\partial p}{\partial x_i} \right|_{nbcv}^l \right) \right) \quad (2.23)$$

The above equation is derived imposing mass conservation to the velocity field at the faces. As shown by Jofre et al.[20], by taking the divergence of Eq. (2.14), approximating the volume integrals by summation over the faces and requiring mass conservation at an infinitesimal control volume at each face, Eq. (2.23) is obtained. The correction here presented reminds to the one presented by Rhie and Chow [29] based on a momentum-weighted interpolation strategy. Regarding the order of the error in kinetic energy conservation, this scheme gives an error of  $\mathcal{O}(\Delta t^2 \Delta x_i^m)$ , where  $m = \min(2, r)$  and  $r$  is the order of the interpolation of the velocities to the face.

### 2.3.2 Staggered discretisation:

As stated previously, staggered formulations place velocity and pressure at different grid locations. This methodology presents the advantage that inherently conserves momentum, kinetic energy and circulation. Additionally, it does not present the *odd-even decoupling* found in collocated schemes. Thus, provided that the discrete operators are conservative, this staggered scheme is fully conservative. These advantages

---

<sup>2</sup>Not to be confused with the predictor substep of the predictor-corrector time integration scheme.

come at the cost of requiring the construction of displaced meshes, which in structured meshes are easily built but on unstructured meshes it is not a straightforward task.

The method here employed follows the formulation by Perot [16], who proposes a technique to construct a displaced control volume at each face and shows that the overlapping of control volumes does not represent an issue. The construction of the staggered cells is sketched in Fig. 2.1. The width of the displaced control volume is defined as  $W_f = W_f^{cv} + W_f^{nbcv}$  where  $W_f^m$  is the distance from the face circumcentre to the “ $m$ ” neighbour cell circumcentre (remember that nodes are located at the cell centroid). The volume of the displaced control volume is then  $V_f = W_f A_f$ . Subindexes “ $cv$ ” and “ $nbcv$ ”, which refer to cells sharing the same face, are here maintained for consistency with the collocated formulation. The described method assumes that cells have a circumcentre, which is not required to be within a cell. However, highly distorted grids can impact the accuracy of the method.

The staggered formulation uses the displaced mesh to integrate the face normal mass fluxes,  $\rho u$ . Therefore, integrating<sup>3</sup> Eq. (2.13), taken in the form of Eq. (2.17), over each displaced cell and taking the dot product with the face normal vector, the staggered form of the fractional step is obtained, where the primary solution variable is the face normal mass flux

$$\frac{(\rho \hat{u})_f^l - (\rho u)_f^n}{\Delta t} V_f = \alpha^n \{-C_{i,f} n_{i,f} + D_{i,f} n_{i,f} + \rho_f g_i n_{i,f}\}^n \quad (2.24)$$

where convective and diffusive terms have to be calculated at the faces. Notice that the integrated variable is an scalar value located at the face and in the face normal direction. In the present formulation, convective and diffusive terms are interpolated to the faces from the cell centred values using a weighted sum

$$C_{i,f} = W_f^{cv} \frac{C_{i,cv}}{V_{cv}} + W_f^{nbcv} \frac{C_{i,nbcv}}{V_{nbcv}} \quad (2.25a)$$

$$D_{i,f} = W_f^{cv} \frac{D_{i,cv}}{V_{cv}} + W_f^{nbcv} \frac{D_{i,nbcv}}{V_{nbcv}} \quad (2.25b)$$

where  $C_{i,cv}$  and  $D_{i,cv}$  are calculated using Eq. (2.18). Analogously, for the pressure correction equation Eq. (2.14)

$$(\rho u)|_f^l = (\rho \hat{u})|_f^l - \Delta t (p_{nbcv}^l - p_{cv}^l) \frac{A_f}{V_f} \quad (2.26)$$

---

<sup>3</sup>The derivation here presented deals with the momentum projection scheme with a constant coefficient Poisson equation. Extension to the non-constant coefficient Poisson equation is straightforward.

where, due to the method of construction of the displaced cells around the cells' faces, the pressure gradient is computed as the pressure difference between the displaced control volume faces. Thereafter, the procedure is akin to the one presented for the collocated scheme. Taking the divergence of Eq. (2.26), a Poisson equation, Eq. (2.34), is obtained, where again the mass divergence at the next step is approximated through the continuity equation by the temporal derivative of the density Eq. (2.16). Once it has been solved, the face mass fluxes are corrected by means of Eq. (2.26) without any further modifications.

Lastly, one critical aspect remains to be considered for Perot's staggered formulation. The convective and diffusive operators have been approximated at the cell faces using their corresponding values at the cell centres. However, in order to compute these values at the cell centres, the velocity field at those locations must be computed. In this regard, two approaches are used in this work, the first order reconstruction (STAGG1) proposed by Perot [16], and a polynomial reconstruction method (STAGG2) proposed by Jofre et al.[20].

The first order reconstruction is based on Gauss' divergence theorem applied to the product of the mass flux  $\rho u_{i,c}$  and the position  $r_i$  at each cell

$$\int_{V_c} \rho_c u_{i,c}^l dV + \int_{V_c} r_i \frac{\partial \rho_c u_{j,c}^l}{\partial x_j} dV = \sum_f \int_{A_f} (r_j(\rho u_j^l)) \cdot n_i dA \quad (2.27)$$

where  $r_i = x_i - x_{0,i}$  represents the position with respect to the cell circumcentre. Then, assuming a constant mass field within the cell, thus making a first order approximation within the cell and rendering the second term on the left hand side equal to zero, the cell centred velocity is computed through

$$u_{i,c}^l = \frac{1}{\rho_c^l V_c} \sum_f \rho_f u_{i,f}^l r_{i,f}^c A_f \quad (2.28)$$

where  $r_{i,f}^c = x_{i,f}^{fg} - x_{i,c}^{cc}$  is the vector from the cell circumcentre  $x_{i,f}^{cc}$  to the face centroid  $x_{i,f}^{fg}$ .

The second reconstruction method (STAGG2) uses a least square procedure to obtain the cell centred velocities from the faces' mass fluxes. To that end, the cell centred velocity is approximated by a polynomial function around the cell centroid ( $u_c(r) = \mathbf{a} + \mathbf{b}x + \mathbf{c}y + \mathbf{d}z$ ) with the restriction that at the cell faces the computed mass fluxes have to be recovered

$$\rho_c u_{i,c}(r) n_{i,f} = (\rho u_i)|_f \quad (2.29)$$

Hence a linear system of equations is obtained where the coefficients  $(\mathbf{a}, \mathbf{b}, \mathbf{c}, \mathbf{d})$  of the polynomial are the unknowns. The resulting system is overdetermined, due to the

higher number of faces than unknowns. Therefore a least-squares method is used to solve the system. As it can readily be seen, this second approach is computationally more expensive than the STAGG1 method, mainly due to the need of solving a system of equations for each cell.

### 2.3.3 Face interpolation schemes

As previously stated, when the convective and diffusive operators were discretised, there remained to be detailed the interpolations of the face centred values for the convective term and the derivative at the faces for the diffusive term.

As shown by Verstappen and Veldman [18], in order to ensure good stability properties of the numerical algorithm, even at high Reynolds numbers with coarse meshes, it is necessary to preserve the properties of the differential operators in their discrete counterparts. Therefore, the discrete convective operator is required to be skew symmetric, the negative conjugate transpose of the discrete gradient operator to be exactly equal to the mass divergence operator and the diffusive terms to be strictly dissipative, being the diffusive operator symmetric and positive definite. These requirements are mainly placed for the momentum equations, from which kinetic energy conservation is derived. Therefore, in the momentum equations cell face values required by the convective operator are interpolated using a second order Symmetry Preserving (SP) interpolation, which produces a skew symmetric discretisation

$$\phi_f = \frac{1}{2}(\phi_{cv} + \phi_{nbcv}) \quad (2.30)$$

Regarding the diffusive operator, as it has already been shown in Eq. (2.18), it is discretised by means of a two point centred approximation to the first derivative (CDS), thus obtaining a symmetric and positive definite matrix.

Concerning the transport equations for scalars, such as enthalpy, temperature or mass fractions, the above requirements of kinetic energy preservation do not apply. However the guidelines just presented for the construction of the discrete counterparts of the differential operators are also applicable. Therefore, the discrete diffusive operator is approximated in the scalars' transport equations by means of the just detailed CDS scheme. With regard to the discretisation of the convective operator, additional considerations have to be taken into account. When the local Peclet is high, centred approximations to the derivatives were found to introduce oscillatory modes in the problem resolution [27]. Therefore, upwinding-like interpolations were proposed to address this stability issue. The classical Upwind Difference Scheme (UDS), where the face value is approximated by the upwinding cell value, is known to be dissipative and to introduce "false diffusion" effects, which are not desired in the current framework. Higher order upwinding interpolations such as the Quadratic Upstream Interpolation for Convective Kinematics (QUICK) [30] are able to deal with "false diffusion" effects, while reducing their dissipative effect. As opposed to cartesian

meshes, where the upwind and downwind nodes can readily be selected, when dealing with unstructured meshes several options are feasible as described by Segarra et al. [17]. In this work an extension to criterion C4 is used.

Criterion C4 generated new points on the face normal direction using only the nodal values and the gradient of the control volumes to which the face belonged, denoted in Fig. 2.2a as points  $C$  and  $D$ . In this work, instead of generating two points from the same nodal point, each point is the projection of a neighbouring control volume node on the face normal direction, as shown in Fig. 2.2b. Then, the projected variables' values are obtained using their nodal value and the gradient at their control volume. The advantage of the present method is that in case of using a cartesian mesh, since the nodal points would already be on the face normal direction, the projected points would be the control volume nodes, thus recovering the original QUICK scheme. On the other hand, using Criterion C4 two new points would still be generated from the same source point, therefore the final approximation would be of lower order.

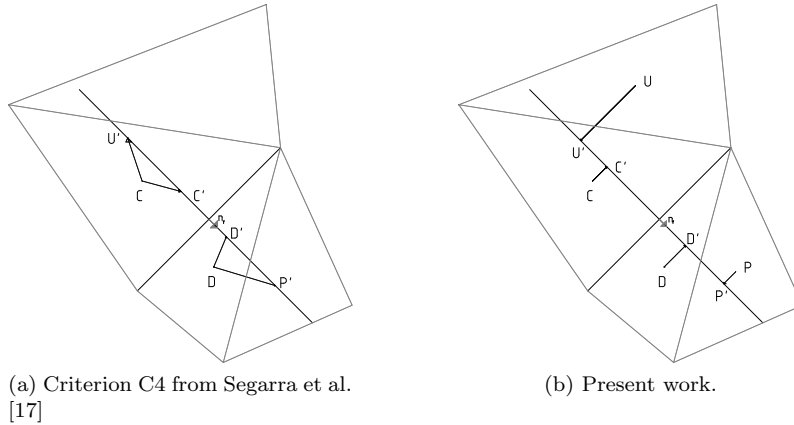


**Figure 2.2:** Points for the QUICK scheme interpolations.

Having defined the upwind and downwind nodes, face values using the QUICK scheme [30], with Fig. 2.2b notation and considering non-equidistant placement of the projected nodes, are computed

$$\bar{x} = \frac{x - x_{U'}}{x_{D'} - x_{U'}} \quad (2.31a)$$

$$\bar{\phi} = \frac{\phi - \phi_{U'}}{\phi_{D'} - \phi_{U'}} \quad (2.31b)$$

$$\bar{\phi}_f = \bar{x}_f + \frac{\bar{x}_f(\bar{x}_f - 1)}{\bar{x}_{C'}(\bar{x}_{C'} - 1)}(\bar{\phi}_{C'} - \bar{x}_{C'}) \quad (2.31c)$$

where the overbar denotes non-dimensional values and values in the normal face direction are obtained using the cell centred gradient

$$\phi_{C'} = \phi_C + \nabla\phi|_C \cdot \mathbf{CC}' \quad \phi_{D'} = \phi_D + \nabla\phi|_D \cdot \mathbf{DD}' \quad \phi_{U'} = \phi_U + \nabla\phi|_U \cdot \mathbf{UU}'$$

For the QUICK scheme on unstructured meshes, this first interpolation or projection diminishes its accuracy, and consequently its theoretical higher order properties can be lost. This aspect is discussed in Section 2.5.1. Nonetheless, false diffusion effects are greatly diminished.

With the statements developed so far, coupled with the requirement in turbulent flows to use conservative schemes, in order to preserve kinetic energy, and as described by Trias et al. [19] and Jofre et al. [20], showing the need for the convective operator to be skew-symmetric and the diffusive operator to be symmetric and positive-definite, the Symmetry Preserving is used in the momentum equations. In the scalar transport equations both centred (SP, CDS) and upwinding schemes (UDS, QUICK) are used. In cases where the Peclet number is high, upwinding schemes are used, where the QUICK has been favoured over the UDS scheme due to its higher order properties.

### 2.3.4 Boundaries

Regarding values at boundaries of the computational domain, both collocated and staggered formulations deal with them similarly. Dirichlet type conditions are imposed at face nodes. Neumann type conditions are applied analogously to the diffusive flux. Therefore, the flux at the face is computed using a one legged two point approximation to the first derivative. Concerning the displaced meshes in the staggered formulation, no displaced control volumes are created on the boundary faces. Similarly, in the evaluation of the convective operator, since values at the boundary faces are known, no interpolations such as Eq. (2.30) are needed.

## 2.4 Temporal Integration Algorithm

A variant of the predictor-corrector scheme shown by Najm et al.[7] is proposed here to solve the set of equations Eq. (2.1)-(2.3) and Eq. (2.5). When chemically reacting flows are considered, Eq. (2.6) is also taken into account. The pressure-velocity coupling is solved using a fractional step projection method as described by Nicoud [9], in which a constant coefficient Poisson results. This fractional stepping is discretised using both collocated [15] and staggered [16] formulations. In the predictor step, a second-order Adams-Bashforth time integration scheme is used to calculate the intermediate scalar and velocity fields. A pressure correction step ensures that the continuity equation, Eq. (2.1), is satisfied. The corrector step uses a Crank-Nicolson

time integration scheme to advance the scalar fields. The velocity is reintegrated using again an Adams-Bashforth scheme, with the density at the next time step ( $n + 1$ ). This corrector step also involves the resolution of a Poisson equation.

In explicit temporal algorithms, as shown by Knikker [10], the scalar transport equations must be expressed in non-conservative form because the density is computed afterwards, being itself a function of the previously computed scalars. Unless an implicit approach is taken, both energy conservation Eq. (2.3) and gas state-law Eq. (2.5) cannot be simultaneously satisfied.

#### 2.4.1 Temporal integration algorithm

In this subsection the explicit two-step temporal integration algorithm is described. Predictor-corrector schemes were proposed for low-Mach number flows due to the numerical instabilities observed when a fully one step explicit time integration scheme was used [7].

##### Predictor

1. Scalars are advanced using an Adams-Bashforth scheme

$$\rho^n \frac{\phi^l - \phi^n}{\Delta t} = \frac{3}{2} \left( \rho^n \frac{\partial \phi}{\partial t} \Big|_n \right) - \frac{1}{2} \left( \rho^{n-1} \frac{\partial \phi}{\partial t} \Big|^{n-1} \right) \quad (2.32)$$

where  $\phi = Y_k$  for the species equation and  $\phi = h$  for the energy equation. In Eq. (2.32), the first and second terms on the r.h.s are evaluated using Eq. (2.6) for the species and Eq. (2.3) for the energy transport, at time steps  $n$  and  $n - 1$ . In these scalar transport equations no distinction is made between collocated and staggered schemes as in both formulations scalar variables are stored at cell centres.

2. Evaluate the thermodynamic pressure  $P_o$  from Eq. (2.12), if it is not constant.
3. Evaluate the density  $\rho^l$  from the state equation Eq. (2.5), using the predictor temperature  $T^l$ .
4. Pressure corrector step.
  - (a) Calculate the pseudo velocities using Eq. (2.13)

$$\frac{\rho^l \hat{u}_i^l - \rho^n u_i^n}{\Delta t} = \frac{3}{2} \left( \frac{\partial \rho u_i}{\partial t} \Big|_n \right) - \frac{1}{2} \left( \frac{\partial \rho u_i}{\partial t} \Big|^{n-1} \right) \quad (2.33)$$

When using the collocated formulation, the temporal derivatives of the cell centred velocity in the above equation are computed using the discrete

version of Eq. (2.13) as detailed in Eq. (2.17). When dealing with the staggered formulation, mass fluxes at the cell faces are integrated in time and computed through Eq. (2.24).

- (b) Solve the Poisson equation.

$$\frac{\partial}{\partial x_i} \left( \frac{\partial p^l}{\partial x_i} \right) = \frac{1}{\Delta t} \left[ \frac{\partial}{\partial x_i} (\rho^l \hat{u}_i^l) - \frac{\partial}{\partial x_i} (\rho^l u_i^l) \right] \quad (2.34)$$

where the pseudo-mass flow, first term on the r.h.s, is obtained from Eq. (2.20) in the collocated scheme. This pseudo-mass flow is directly obtained from the time integration, Eq. (2.24) and (2.33) in staggered meshes. The mass divergence at the next substep is approximated using the continuity equation Eq. (2.1)

$$\frac{\partial}{\partial x_i} (\rho^l u_i^l) = - \frac{\partial \rho}{\partial t} \Big| ^l$$

- (c) Calculate the predictor velocities

$$\frac{\rho^l u_i^l - \rho^l \hat{u}_i^l}{\Delta t} = - \frac{\partial p^l}{\partial x_i} \quad (2.35)$$

This correction is applied to cell centred velocities in collocated schemes, while it is applied to face centred mass fluxes in staggered schemes.

- (d) Final computations have to be performed for both formulations, as described in the previous section. In short, in the collocated scheme the faces mass flow have to be computed using Eq. (2.22). Analogously, in the staggered scheme the cell centred velocities have to be reconstructed from the face centred ones using either STAGG1 or STAGG2 reconstruction method.

### Corrector

For the sake of brevity, comments regarding staggered and collocated differences have been omitted in this subsection. The reader is referred to the *Predictor* subsection for differences between both spatial formulations within the temporal algorithm.

1. With the values computed at the Predictor step, the r.h.s. of Eq. (2.3) is used to evaluate the time derivative of the predictor enthalpy ( $\rho^{l-1} \frac{\partial h}{\partial t} |^{l-1}$ ) and the r.h.s. of Eq. (2.6) to evaluate the time derivative of the predictor mass fraction ( $\rho^{l-1} \frac{\partial Y_k}{\partial t} |^{l-1}$ ). Then, the time derivative at the next time is evaluated using a Crank-Nicholson scheme

$$\rho^{l-1} \frac{\phi^{n+1} - \phi^n}{\Delta t} = \frac{1}{2} \left( \rho^n \frac{\partial \phi}{\partial t} \Big|_{}^n + \rho^{l-1} \frac{\partial \phi}{\partial t} \Big|_{}^{l-1} \right) \quad (2.36)$$

where  $\phi = Y_k$  for the species equation and  $\phi = h$  for the energy equation.

2. Evaluate the thermodynamic pressure  $P_o$  from Eq. (2.12), if it is not constant.
3. Using the ideal gas law Eq. (2.5), the density field at the next time step is computed.
4. Finally, the pressure corrector step to compute the velocity field.
  - (a) Calculate the pseudo velocities using Eq. (2.13)

$$\frac{\rho^{n+1} \hat{u}_i^l - \rho^n u_i^n}{\Delta t} = r.h.s. \{ \text{Eq. (2.33)} \} \quad (2.37)$$

- (b) Solve the Poisson equation.

$$\frac{\partial}{\partial x_i} \left( \frac{\partial p^{n+1}}{\partial x_i} \right) = \frac{1}{\Delta t} \left[ \frac{\partial}{\partial x_i} (\rho^{n+1} \hat{u}_i^l) - \frac{\partial}{\partial x_i} (\rho^{n+1} u_i^{n+1}) \right] \quad (2.38)$$

where, as in the predictor stage the momentum divergence  $\nabla \cdot (\rho^{n+1} u^{n+1})$  is replaced, using the continuity equation Eq. (2.1), by the density time derivative Eq. (2.16).

- (c) Calculate the velocities at the next time step

$$\frac{\rho^{n+1} u_i^{n+1} - \rho^{n+1} \hat{u}_i^l}{\Delta t} = - \frac{\partial p^{n+1}}{\partial x_i} \quad (2.39)$$

- (d) In collocated schemes, the face mass flow  $\dot{m}_f^{n+1}$  has to be computed using Eq. (2.22). Analogously, in staggered schemes the cell centred velocities  $u_{i,c}^{n+1}$  have to be reconstructed from the face centred mass fluxes using either STAGG1 or STAGG2 reconstruction method.

## 2.5 Numerical Tests

In the following the numerical schemes presented are tested in order to study the effect of non-structured meshes. The general purpose unstructured and parallel object-oriented CFD code TermoFluids [31] is used in this work. Three test cases are discussed. *Test Case 1* consists in a numerical reconstruction of a solenoidal field,

which is used to assess the accuracy of the interpolation schemes. *Test Case 2* is a differentially heated cavity under a large temperature difference, through which the spatial discretisation of the low Mach equations is analysed. *Test Case 3* is a self-igniting turbulent jet flame, whereby the effect of the spatial discretisations on the transient algorithm is evaluated.

### 2.5.1 Test Case 1 - Interpolation schemes accuracy

The accuracy of the presented interpolation schemes is studied by means of an exact sinusoidal function, *Test Case 1*. The reduction of the interpolations numerical error with respect to the exact analytical value provides the order of accuracy. The target function to be interpolated is a sinusoidal function

$$\psi = \frac{1}{2\pi L} \sin(2\pi Lx) \cos(2\pi Ly) \quad (2.40)$$

This function is used twofold, as the function to be interpolated at the faces and as a stream function from which the velocity field is derived by taking the rotational of the function  $\vec{u} = \nabla \times \psi$

$$\begin{aligned} u_x &= -\sin(2\pi Lx) \sin(2\pi Ly) \\ u_y &= -\cos(2\pi Lx) \cos(2\pi Ly) \\ u_z &= 0 \end{aligned} \quad (2.41)$$

This velocity field is used by the upwinding schemes to determine the upwind and downwind nodes. The numerical domain is a cube of length unit ( $L=1$ ) in each dimension. To carry out the grid refinement study, instead of creating several meshes, the length scale, or wavelength, of the sinusoidal function is modified. With this strategy, a single mesh of  $n_{CV}$  volumes is generated and then the mesh is coarsened by increasing the length scales of the function with respect to the mesh average spacing. Therefore, in order to quantify the amount of scales actually being captured by the mesh two quantities have to be defined. In the first place, the average mesh spacing is defined as  $V_{avg} = \frac{1}{n_{CV}} \sum_c V_c$ , which allows defining an average mesh spacing as  $\Delta x_{avg} = \sqrt[3]{V_{avg}}$ . Secondly, the effective length of the domain is defined as  $L_{eff} = 1/L$ , where  $L$  is an integer value, which controls the sinusoidal wavelength. In consequence, the relative mesh size is  $\Delta x_{avg}/L_{eff} = \Delta x_{avg}L$ .

In order to assess the influence of the unstructured meshing on the face interpolations, two meshes were generated: a structured one and an unstructured one. Both meshes have similar average mesh spacings and the relative mesh spacings ranged from 0 to 0.4. For each relative mesh size the values of the function Eq. (2.40) were interpolated at the faces using the analytical values at the cell centres. The error  $\varepsilon$  is

then computed as the root mean square (rms) between the numerical approximations and the analytical values computed at the faces

$$\varepsilon = \sqrt{\frac{1}{n_F} \sum_f \varepsilon_f^2} \quad (2.42)$$

where  $\varepsilon_f$  is the error in each face value and  $n_F$  is the number of faces. The errors of the interpolations along with their accuracy are plotted in Fig. 2.3. Four interpolation methods are here presented: the Symmetry Preserving (SP) scheme, which is equivalent to an average, the UDS, the QUICK and, for completion, a Central Difference Scheme using Criterion I1a of Segarra et al.[17] (CDS2), which makes a linear interpolation between neighbouring nodes and takes into account non-equal distances between the face and the neighbouring nodes.

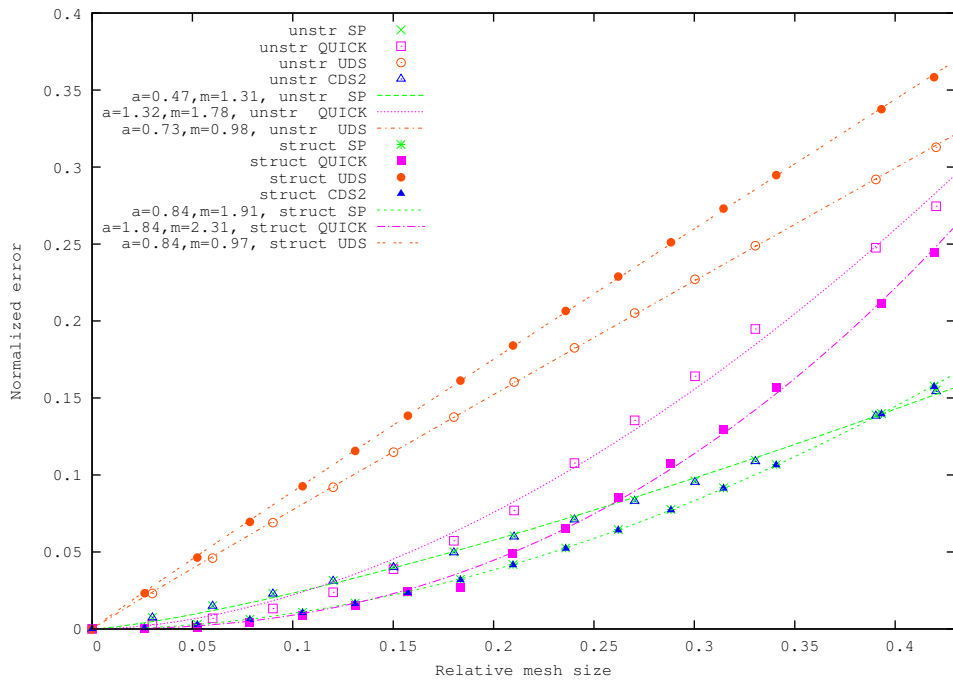


**Figure 2.3:** Test Case 1 - Accuracy of the numerical interpolations in structured ('struct') and unstructured ('unstr') meshes. Dots represent the computed errors and lines show the accuracy of each interpolation in the form  $\varepsilon = ah^m$ , where  $h$  denotes the mesh spacing and  $m$  indicates the order of accuracy.

A first aspect to be highlighted is that the order of accuracy of the different methods is the expected on structured meshes. On unstructured meshes, the order decreases for both the SP and the QUICK schemes. The UDS' order of accuracy remains almost unchanged. However, the cause for the deterioration is different for each scheme. On the one hand, in the QUICK scheme, as described previously, the gradients of the cell values are used to approximate the value on the normal direction to the face. This intermediate interpolation is a first order approximation, which is responsible for the reduction of the interpolation order. On the other hand, central difference schemes, both SP and CDS2, mainly deteriorate due to non-orthogonal effects. Additionally, comparing the SP with the CDS2 scheme, both schemes behave almost identically on both structured and unstructured meshes, indicating that the non-equal weights in the CDS are of minor importance in contrast to non-orthogonal effects.

It should be noted that the UDS scheme on unstructured meshes presents lower errors than on structured meshes. This may be attributable to the likely alignment of the unstructured mesh with the solution. Nonetheless, in both cases the accuracy of the scheme is first order as expected.

Considering these results, it can be seen that the slight errors introduced using SP discretisations in the momentum equations, compared to CDS scheme, are compensated by the reported gain in numerical stability [15, 18] when using kinetic energy preserving formulations in turbulent flows. From these results, it can also be inferred that low order approximations present in the construction of high order schemes on unstructured meshes causes a deterioration of the properties of those high order schemes. Nonetheless, the accuracy order of the QUICK schemes is higher than the UDS and even SP scheme.

Finally, it should be noted that though the QUICK scheme presents a higher order of accuracy, on coarse meshes, the SP produces a lower level of error. Nonetheless, as the mesh is refined the errors of the QUICK scheme become lower and at a faster rate than the SP. Therefore, in scalar transport equations the QUICK scheme is a good alternative in cases where due to stability issues, centred approximations are not viable.

### 2.5.2 Test Case 2 - Analysis of the spatial discretisations

The differentially heated square cavity, *Test Case 2*, benchmark case [21, 32] of side L=1 under a large temperature difference ( $\Delta T = 720K$ ) is used. The cavity left wall is at a high temperature ( $T_h$ ) and the right wall is at a low temperature ( $T_c$ ). These temperatures are related to the temperature difference by  $\epsilon = \frac{T_h - T_c}{2T_0}$ . Here a value of  $\epsilon = 0.6$  has been taken, in order to match the benchmark case. The temperature ratio defined between the highest temperature  $T_h$  and the lowest  $T_c$  is 4. As reported by Najm [7], for ratios higher than 2 at least a predictor-corrector scheme, as the one here proposed, is necessary.

The top and bottom walls are considered adiabatic. The fluid filling the cavity is air with a constant Prandtl number ( $Pr = 0.71$ ) and a constant specific heat capacity ( $c_p = \gamma R_g / (\gamma - 1)$  where  $R_g = 287 \text{ J/(kg K)}$  and  $\gamma = 1.4$ ). Its dynamic viscosity and thermal diffusivity follow Sutherland's law

$$\frac{\mu(T)}{\mu_{ref}} = \left( \frac{T}{T_{ref}} \right)^{3/2} \frac{T_{ref} + 110.5}{T + 110.5} \quad (2.43a)$$

$$\kappa(T) = \frac{\mu(T)c_p}{Pr} \quad (2.43b)$$

where the reference temperature for this expression has been taken as  $T_{ref} = 273\text{K}$  and the reference viscosity is  $\mu_{ref} = 1.68 \cdot 10^{-5}\text{kg/(m s)}$ . The ideal gas law Eq. (2.5) is used to calculate the density. The Rayleigh number ( $Ra = Pr \frac{g \rho_0^2 \Delta T L^3}{T_0 \mu_0^2}$ ) considered here corresponds to the laminar regime ( $Ra = 10^6$ ). With these parameters and the reference conditions ( $Po_0 = 101325\text{Pa}$ ,  $T_0 = 600\text{K}$ , and  $\rho_0 = Po_0 / (R_g T_0)$ ) the problem is defined.

To study the accuracy of the described predictor-corrector scheme on unstructured meshes several uniform unstructured meshes were created, whose mesh spacings were  $L/N_p$ , where  $N_p$  is the number of points at the boundaries. With this definition of the mesh spacing, equivalent structured uniform meshes are easily defined<sup>4</sup>. Uniform meshes were chosen in order to minimise variations in mesh properties such as cells' aspect ratio, measuring the ratio between the smallest cell's face area and its biggest, and orthogonality factor, measuring the angle between a face normal and the vector joining the neighbours cells centroids.

Fig. 2.4 shows the numerical errors of the thermodynamic pressure  $Po$ , where the error is defined with respect to the reference case [32], shown in Table 2.1. It can be seen that the convergence rate of the global algorithm is between first and second order.

The collocated scheme, using either SP or QUICK in the energy equation, and the staggered scheme using STAGG2 reconstruction method with the QUICK show similar results, being their convergence rate close to second order. The STAGG2 method with the SP shows first order accuracy, which indicates that interpolation errors in the energy equation due to the SP affect the cell centred velocities reconstruction. The staggered scheme using the STAGG1 reconstruction method shows a lower convergence rate, which is of first order. This lower order of convergence for the STAGG1 will be discussed in the following, along with convergence rate of the Nusselt number at the wall. Comparing the curves for the SP and the QUICK schemes, it can be seen

---

<sup>4</sup>For example, if a uniform structured mesh were to be used to discretise the horizontal direction of the square cavity with  $N_p = 64$ , the mesh spacing would be  $1/64 = 0.0156$

Discretisation	Collocated		Staggered (Stagg2)		Ref. [32]
	Case	Unstruct.	Struct.	Unstruct.	
Scheme	SP	QUICK	SP	QUICK	-
$P_o/P_{o,0}$	0.9249	0.9237	0.9262	0.9250	0.9245
$Nu_h$	8.6864	8.7013	8.6742	8.6742	8.6866
$Nu_c$	8.6859	8.6461	8.6739	8.6358	8.6866
$\frac{Nu_p - Nu_c}{0.5(Nu_h + Nu_c)}$	0.0058%	0.6358%	0.0030%	0.5948%	0%

**Table 2.1:** Results for the Differentially Heated Cavity with  $Ra = 10^6$  using a mesh spacing of 1/320.

that the errors on the coarse meshes are noticeably higher for the QUICK scheme. However, when finer meshes were used, the QUICK scheme delivered errors similar to the SP scheme. As was mentioned in Sec. 2.3, momentum equations are solved using SP, while different schemes are used for the scalar transport equations.

Fig. 2.5 shows the error for the Nusselt number at the hot wall with respect to the reference case [32]. The evaluation of the heat fluxes is performed analogously to the evaluation of the diffusive flux in the discrete transport equations, Eq. (2.18b).

As described for Fig. 2.4, similar trends are observed regarding the order of accuracy for both collocated and structured staggered schemes. The global behaviour of the algorithm is between first and second order, with the exception the staggered scheme using STAGG1 reconstruction method

First-order accuracy for the local Nusselt number is expected due to the approximation to the first derivative, where a two point one legged stencil is used. However, globally the Nusselt number is seen to behave between first and second order. The influence of the different schemes, which were used for the convective term, is of minor importance, causing small variations on the actual error.

Considering the first-order accuracy for a local value, such as the Nusselt number at the wall, and the almost second-order accuracy for a global value, such as the thermodynamic pressure and the average Nusselt number at the walls, serves to illustrate the increase in accuracy from local approximations of the operators to the global scheme, due to error cancelling within the mesh [33].

Additionally, it must be highlighted that the results obtained with the staggered formulation using the STAGG1 reconstruction method on unstructured meshes show an accuracy of order zero, regardless of the convective discretisation scheme. However, if structured meshes are considered, the computed accuracy is between first and second order. The justification of this phenomenon may be attributed to the cell centred velocities reconstruction. Comparing the results obtained with the STAGG1 staggered formulation, unstructured against structured, it can be inferred that the or-

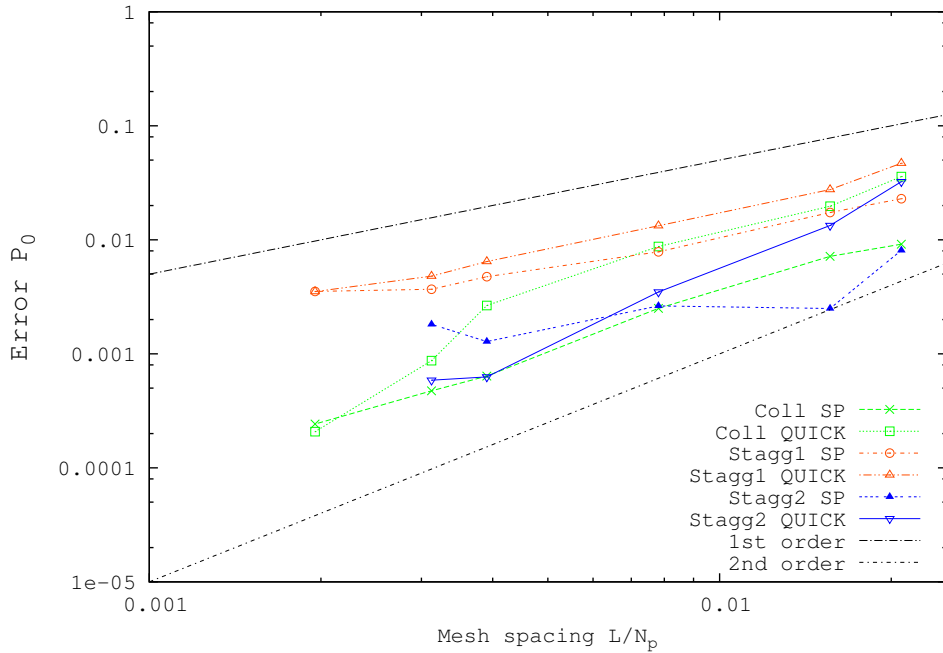


**Figure 2.4:** *Test Case 2 - Numerical error for the thermodynamic pressure using unstructured meshes. For comparison, short-dashed-dotted and long-dashed-dotted lines are plotted, showing first and second order convergence rates. Mesh spacing is expressed in terms of equivalent uniform structured mesh number of points,  $N_p$ .*

der of accuracy of the cell centred velocities reconstruction in the unstructured meshes becomes null, whereas on the structured ones it is of first order. Thus, the errors in reconstructing the cell centred velocities affect the evaluation of the convective term, which in turn affect the magnitude of the diffusive term. Structured meshes do not suffer from this deterioration of the solution due to their inherent geometric properties. Still, it can be seen in Fig. 2.5 that results obtained using the STAGG1 method converge to a solution, indicating that the computed velocity fields on each mesh are intrinsically coherent, although incorrect. Additional simulations were conducted where the second term on the right hand side of Eq. (2.27) was not assumed to be zero, to test the influence of this assumption. However, steady state results did not vary because at the stationary state mass divergence is zero, since transient density variations are null. Therefore, higher order approximations are required for the cell centred

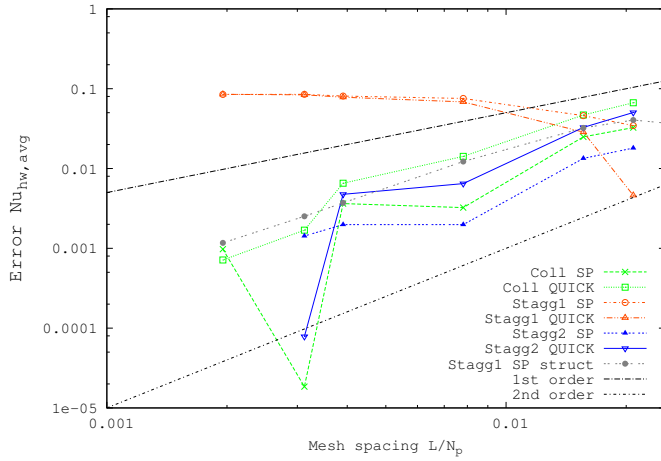


**Figure 2.5:** *Test Case 2* - Numerical error of the averaged Nusselt number at the hot wall. For comparison, short-dashed-dotted and long-dashed-dotted lines are plotted, showing first and second order convergence rates, respectively. Mesh spacing is expressed in terms of equivalent uniform structured mesh number of points,  $N_p$ .

velocities reconstruction, such as the STAGG2 reconstruction method, which is shown to provide accurate results. However, as previously stated, the STAGG2 method is computationally more demanding, which hinders its viability. Results for the finer mesh are not reported for the STAGG2 method due to computational limitations. However it can be seen that the staggered method using the STAGG2 reconstruction shows a similar trend as the collocated method.

With respect to the cold wall, trends are similar as at the hot wall although minor discrepancies are noticeable. The reason is that the boundary layer is thinner at the cold wall than at the hot wall, therefore smaller grid spacings are required to correctly characterise the thermal boundary layer at the cold wall. However, in this work successive uniform meshes have been used.

Concerning the noticeable lower error for the mesh with equivalent spacing 1/320, it should be remarked that these small errors are caused by supraconvergence effects, which lower the errors globally, as described by Trias et al. [33]. It should be borne in mind that although uniformly spaced meshes were used, in unstructured meshes there can be variations in the cells properties, such as aspect ratio, orthogonality, among others, which can cause deviations in the theoretical trends.

Due to the use of the non-conservative form of the energy equation, it was stated

that the algorithm would produce an error in the energy error. Its reduction as the mesh is refined is shown in Fig. 2.6. On the one hand, it can be seen that the Symmetry-Preserving scheme is not capable of reducing this error. On the other hand, the QUICK scheme is capable of reducing it. However, on coarser meshes, the SP scheme results in a lower error than the QUICK scheme, which is similar to the previously shown results.

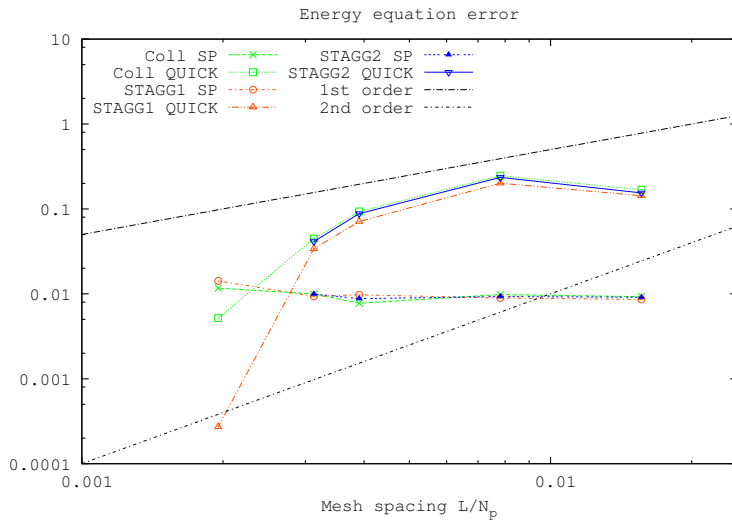


**Figure 2.6:** Test Case 2 - Error in the energy equation. For comparison, short-dashed-dotted and long-dashed-dotted lines are plotted, showing first and second order convergence rates.

Finally, detailed results comparing the SP and QUICK schemes using a mesh spacing of 1/320 are shown in Table 2.1 along with the reference results. For the staggered formulation, only results using the STAGG2 reconstruction method are reported, because the computed values with STAGG1 reconstruction method were not in accordance. It can be seen that the QUICK suffers a deterioration due to the lower order intermediate interpolations. Furthermore, the QUICK scheme deviates further from the mean in the cold wall. This behaviour is attributable to the fact that the boundary layer is thinner in the cold wall.

### 2.5.3 Test Case 3 - Analysis of the transient behaviour

The experimental configuration by Markides and Mastorakos [23] is used to test the transient behaviour of the proposed numerical algorithm. It consists of a fuel

jet with a preheated co-flowing air stream, as shown in Fig. 2.7. The co-flowing air is forced to pass through a perforated plate to promote turbulence. The perforated plate (3.0mm holes and 44% *blockage*) is located 63mm upstream of the fuel nozzle to allow turbulence to develop. The fuel nozzle has a diameter of 2.25mm and is thin walled (0.32mm). The main test section consists of a 500mm long and 25mm inner diameter vacuum insulated quartz tube. The reference experiments were performed over a wide range of operating conditions and four regimes, namely 'No ignition', 'Random spots', 'Flashback', and 'Lifted flame' were identified.

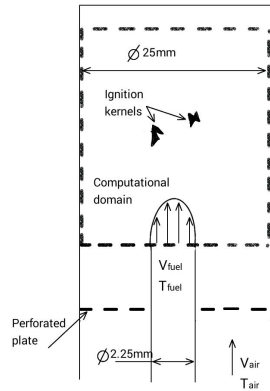


**Figure 2.7:** Autoignition experimental configuration (*Test Case 3*).

In the present work the 'Random spots' regime is simulated, *Test Case 3*, where autoignition kernels appear but are quenched and convected out of the domain before they can act as a flame anchoring point or cause flashback. The fuel is a mixture of  $H_2$  and  $N_2$  ( $Y_{H_2} = 0.13$ ,  $Y_{N_2} = 0.87$ ) at  $750K$  and the co-flow oxidizer is air ( $Y_{O_2} = 0.233$ ,  $Y_{N_2} = 0.767$ ). For the 'Random spots' regime, the oxidiser temperature is  $950K$ . Both fuel and air inlet velocities are  $26m/s$ . The fuel jet Reynolds number is 330 and the coflow Reynolds number is 5800. The simulation domain spanned from the fuel jet nozzle up to  $135mm$  in the downstream direction. In order to reproduce the turbulence generated by the perforated plate, an auxiliary non-reactive simulation was performed in an annular mesh, recreating the physical domain upstream to the injector lips. In this non-reacting simulation, the plate was placed inside the domain using the immersed boundary technique. The solution of this non-reactive simulation was then stored and afterwards loaded during the reactive CFD simulation. This method allows a significant saving of computational resources during the numerical simulation, and

develops a realistic divergence-free velocity field, as opposed to synthetic turbulence generators based on digital filters. For the fuel jet, a laminar parabolic velocity profile is assumed.

Since the test case here considered is of turbulent nature, the set of transport equations Eq. (2.1)-(2.3), (2.5) and (2.6) previously presented have to be formulated in the context of Large Eddy Simulations (LES) models using Favre-filtered quantities and closures for the subgrid turbulent fluxes have to be introduced. For the sake of brevity, the equations are not here rewritten, but it is just stated that the variables are Favre-filtered quantities and that in the right hand side of the equations, there appears an extra term representing the subgrid turbulent transport. Closure for the momentum turbulent stresses is preformed by means of the Wall-Adapting Local Eddy-viscosity (WALE) model [34]. The scalar subgrid turbulent fluxes are modelled using a constant turbulent Schmidt number with value 0.4. The chemical source term is treated explicitly, thus the filtered reaction terms are assumed to be equal to the reaction rate computed using the filtered quantities  $\tilde{w}_k(Y_k, T) = \dot{w}_k(\tilde{Y}_k, \tilde{T})$ . The detailed chemical mechanism of Mueller et al. [35] is used, which involved 9 species and 21 reactions.

Numerical simulations were performed using a collocated discretisation on a  $4 \cdot 10^5$  CV unstructured mesh. Mesh refinement was performed near the air-fuel shear layer. Since the temporal scheme is independent from the spatial discretisation, the present case is analysed using only the collocated formulation. The decision is justified by the better behaviour of the collocated scheme compared with the staggered scheme using the first order velocity reconstruction method (see Sec. 2.5.2). Additionally, as shown by Jofre et al. [20] in LES simulations of turbulent flows, the required meshes are fine enough to make the kinetic error of the collocated formulation imperceptible to the physics of the problem. Furthermore, no significant differences are expected between staggered formulation with the STAGG2 method and the collocated one, based on the results of a turbulent flow by Jofre et al. [20]. Additionally, no mesh refinement was performed since changes in the mesh would modify the effect of the LES model.

In the random spots case, the ignition length oscillates around a mean distance from the fuel inlet. This is caused by the appearance of random autoignition kernels, which are quenched and convected out of the domain. Several snapshots of the process are shown in Fig. 2.8, where it can be seen that the mixture ignites at different axial locations.

Fig. 2.9 shows the evolution of autoignition lengths in time for the random spots regime for different numerical schemes used in the scalar equations. The ignition length is determined using as criterion a rise of 1% in the initial co-flow temperature [36]. Upwinding schemes, namely the UDS and QUICK schemes, show good agreement with the experimental data. Furthermore, the QUICK is seen to reproduce accurately the experimental data. Explicit treatment of chemical reactions is

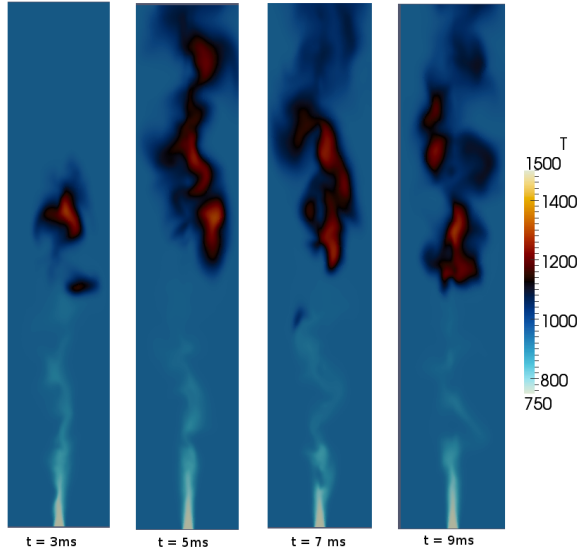


**Figure 2.8:** *Test Case 3 - Instantaneous snapshots of the temperature. Time scale is adjusted to the beginning of fuel injection ( $t = 0$ ). The axial length of the computational domain is 135mm. Results computed using the UDS scheme.*

shown to perform adequately for the current Reynolds numbers. Regarding the CDS2 scheme, it features ignition spots at two different heights. One close to the fuel nozzle exit and another at a higher axial location, which is also shorter than the distance predicted when using the UDS scheme. These upstream ignition kernels are a product of numerical diffusion caused by the numerical scheme and they do not achieve a temperature high enough to ignite a meaningful quantity of the mixture and stabilise the autoignition process at this short distance. The higher axial autoignition distances captured by the CDS2, which are similar to those of the upwinding schemes, show where the mixture is actually being completely burned. Comparing the QUICK and UDS schemes, the influence of the numerical diffusivity introduced by the UDS can be seen by the shorter autoignition distances predicted by it.

## 2.6 Conclusions

In this chapter, both collocated and staggered spatial discretisations for unstructured grids have been analysed in the context of low Mach flows. A new approach to define the upwind and downwind nodes of the QUICK interpolation scheme has been

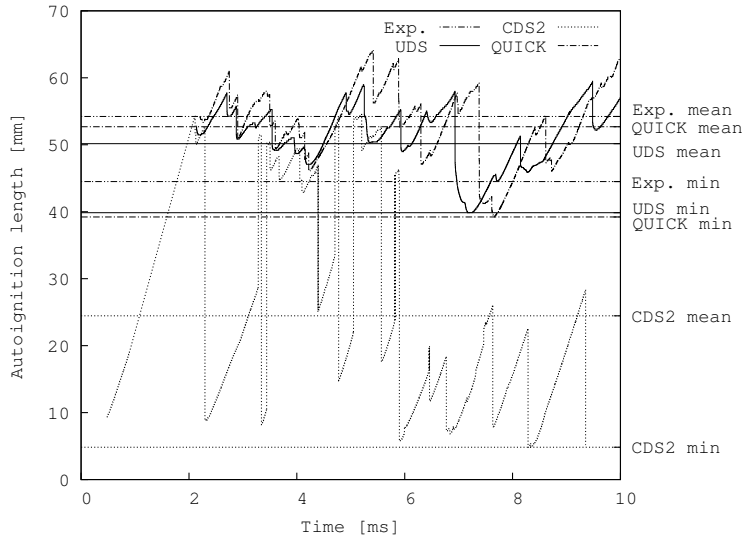


**Figure 2.9:** Test case 3 - Autoignition distances for the random spots regime. Horizontal lines represent mean and minimum autoignition distances for each numerical scheme and the experimental data. For the latter only mean and minimum values are plotted.

presented. SP, UDS and QUICK discretisation schemes have been assessed in both structured and unstructured meshes. It has been shown that the QUICK scheme did not provide the expected order of accuracy on unstructured meshes due to intermediate interpolation errors. Therefore, concerning the interpolations in the scalar's equations, low order schemes are best suited in coarse meshes. When finer meshes are used, it is worth switching to higher order schemes.

Regarding the spatial discretisations, collocated and staggered schemes have been described to be used on unstructured meshes. Following Felten and Lund [15], in the collocated scheme the cell faces mass fluxes are computed using an average, even in unstructured grids. The aim is to minimise errors in the conservation of kinetic energy. Despite the use of constant coefficients for the computation of the cell faces mass fluxes, the numerical results showed good agreement with the reference data. Concerning the staggered discretisation, it has been shown that the cell centred velocity reconstruction plays a central role in its correct behaviour. The original first-order reconstruction method has been shown to perform correctly on structured meshes. However, when unstructured meshes were considered, a convergence of the results could be observed, albeit to a different solution than the reference one. The new

approach proposed by Jofre et al. [20], which has been extended to variable-density flows, improved the behaviour of the scheme. However, the computational resources increased considerably.

Both reacting and non-reacting test cases were carried out using a Symmetry-Preserving scheme for the cell face velocities interpolations. Overall, good agreement between the reference data and the presented results has been shown, despite using constant weights for the cell faces velocity interpolations, even in non-uniform grids. Nonetheless, the purpose of this schemes is to preserve kinetic energy.

A benchmark differentially heated cavity, *Test Case 2*, has been numerically studied. In general, the numerical algorithm applied to solve this case showed almost second-order behaviour. However, as initially discussed, the algorithm presents an intrinsic error in the energy conservation due to the temporal scheme. Since an explicit time integration is used, mass conservation and the ideal gas state law can be met at the cost of using the energy equation in its non-conservative form.

In *Test Case 3*, the self-igniting turbulent case, it has been shown the effect of numerical diffusion on the auto-ignition location of a flame. The CDS2 scheme exhibited numerically caused ignition spots. Similarly, comparing the mean ignition distances between the UDS and QUICK schemes, the diffusive nature of the UDS scheme resulted in shorter distances than the QUICK. Nonetheless, good agreement using both UDS and QUICK schemes was found with the experimental data.

## References

- [1] D.D. Gray and A. Giorgini. The validity of boussinesq approximation for liquids and gases. *International Journal Of Heat And Mass Transfer*, 19:545–551, 1976.
- [2] J. Vierendeels, J. Merci, and E. Dick. Numerical study of natural convective heat transfer with large temperature difference. *International Journal of Numerical Methods for Heat and Fluid Flow*, 11(4):329–341, 2001.
- [3] T. Kloczko, C. Corre, and A. Beccantini. A matrix-free implicit method for flows at all speeds. In *Proc. ICCFD3 Conference, Toronto, Canada*, 11–15 July, 2004.
- [4] E. Becker and M. Braack. Solution of a stationary benchmark problem for natural convection with large temperature difference. *International Journal Of Thermal Sciences*, 41:428–439, 2002.
- [5] M. Darbandi and S.F. Hosseiniزاده. General pressure-correction strategy to include density variation in incompressible algorithms. *Journal of Thermophysics and Heat Transfer*, 17(3):372–380, 2003.
- [6] L. Shunn, F. Ham, and P. Moin. Verification of variable-density flow solvers using manufactured solutions. *Journal of Computational Physics*, 231:3801–3827, 2012.

- [7] Habib N. Najm, Peter S. Wyckoff, and Omar M. Knio. A semi-implicit numerical scheme for reacting flow. *Journal of Computational Physics*, 143:381–402, 1998.
- [8] J. Kim and P. Moin. Application of a fractional-step method to incompressible Navier–Stokes equations. *Journal of Computational Physics*, 59(2):308–323, 1985.
- [9] F. Nicoud. Conservative high-order finite difference schemes for low-mach number flows. *Journal of Computational Physics*, 158:71–97, 2000.
- [10] R. Knikker. A comparative study of high-order variable -property segregated algorithms for unsteady low mach number flows. *International Journal for Numerical Methods in Fluids*, 66:403–427, 2011.
- [11] B. Lessani and M.V. Papalexandris. Time-accurate calculation of variable density flows with strong temperature gradients and combustion. *Journal of Computational Physics*, 212:218–246, 2006.
- [12] M. Darbandi and S.F. HosseiniZadeh. Numerical simulation of thermobuoyant flow with large temperature variation. *Journal of Thermophysics and Heat Transfer*, 20(2):285–296, 2006.
- [13] C.-D. Munz, S. Roller, R. Klein, and K.J. Geratz. The extension of incompressible flow solvers to the weakly compressible regime. *Computers and Fluids*, 32:173–196, 2003.
- [14] H. Reza Ebrahimi-Kebria1, M. Darbandi, and S.F. HosseiniZadeh. Numerical simulation of low-mach-number laminar mixing and reacting flows using a dual-purpose pressure-based algorithm. *Numerical Heat Transfer, Part B: Fundamentals*, 59:495–514, 2011.
- [15] F.N. Felten and T.S. Lund. Kinetic energy conservation issues associated with the collocated mesh scheme for incompressible. *Journal of Computational Physics*, 215:465–484, 2006.
- [16] B. Perot. Conservation properties of unstructured staggered mesh schemes. *Journal of Computational Physics*, 159:58–89, 2000.
- [17] C.D. Pérez-Segarra, C. Farre, J. Cadafalch, and A. Oliva. Analysis of different numerical schemes for the resolution of convection-diffusion equations using finite-volume methods on three-dimensional unstructured grids. Part I: discretization schemes. *Numerical Heat Transfer, Part B: Fundamentals*, 49:4:351–375, 2006.
- [18] R.W.C.P. Verstappen and A.E.P. Veldman. Symmetry-preserving discretization of turbulent flow. *Journal of Computational Physics*, 187:343–368, 2003.

- [19] F.X. Trias, O. Lehmkuhl, A. Oliva, C.D. Pérez-Segarra, and R.W.C.P. Verstappen. Symmetry-preserving discretization of Navier-Stokes equations on collocated unstructured grids. *Journal of Computational Physics*, 258(1):246–267, 2014.
- [20] Ll. Jofre, O. Lehmkuhl, J. Ventosa, F. Xavier Trias, and A. Oliva. Conservation properties of unstructured finite-volume mesh schemes for the Navier-Stokes equations. *Numerical Heat Transfer, Part B: Fundamentals*, 65(1):53–79, 2013.
- [21] P. Le Quéré, C. Weisman, H. Paillère, J. Vierendeels, E. Dick, E. Becker, M. Braack, and J. Locke. Modelling of natural convection flows with large temperature differences: a benchmark problem for low mach number solvers. part 1. reference solutions. *ESAIM: Mathematical Modelling and Numerical Analysis*, 39(3):609–616, 2005.
- [22] J. Vierendeels, B. Merci, and E. Dick. Benchmark solutions for the natural convective heat transfer problem in a square cavity with large horizontal temperature differences. *International Journal of Numerical Methods for Heat and Fluid Flow*, 13(8):1057–1078, 2003.
- [23] C. Markides and E. Mastorakos. An experimental study of hydrogen autoignition in a turbulent co-flow of heated air. *Proceedings of the Combustion Institute*, 30:883–891, 2005.
- [24] T. Poinsot and D. Veynante. *Theoretical and Numerical Combustion*. R.T. Edwards Inc., 2005.
- [25] F.X. Trias, M. Soria, C.D. Pérez Segarra, and A. Oliva. A direct schur-fourier decomposition for the efficient solution of high-order poisson equations on loosely coupled parallel computers. *Numerical Linear Algebra with Applications*, 13(4):303–326, 2006.
- [26] R. Borrell, O. Lehmkuhl, M. Soria, and A. Oliva. Schur complement methods for the solution of poisson equation with unstructured meshes. *Proceedings of the Parallel CFD Conference*, pages 1–8, 2007.
- [27] S. V. Patankar. *Numerical heat transfer and fluid flow*. Hemisphere Publishing Corporation, 1980.
- [28] Y. Morinishi and T.S. Lund. Fully conservative higher order finite difference schemes for incompressible flow. *Journal of Computational Physics*, 143:90–124, 1998.
- [29] C.M. Rhie and W.L. Chow. A numerical study of the turbulent flow past an isolated airfoil with trailing edge separation. *AIAA Journal*, 21:1525, 1983.

- [30] B.P. Leonard. A stable and accurate convective modelling procedure based on quadratic upstream interpolation. *Computer Methods in Applied Mechanics and Engineering*, 19:59–98, 1979.
- [31] O. Lehmkuhl, C.D. Pérez Segarra, R. Borrell, M. Soria, and A. Oliva. Termofluids: A new parallel unstructured CFD code for the simulation of turbulent industrial problems on low cost PC cluster. *Proceedings of the Parallel CFD Conference*, pages 1–8, 2007.
- [32] H. Paillère, P. Le Quéré, C. Weisman, J. Vierendeels, E. Dick, M. Braack, F. Dabbene, A. Beccantini, E. Studer, T. Kloczko, C. Corre, M. Heuveline, V. Darbandi, and S.F. Hosseini-zadeh. Modelling of natural convection flows with large temperature differences: a benchmark problem for low mach number solvers. part 2. contributions to the june 2004 conference. *ESAIM: Mathematical Modelling and Numerical Analysis*, 39(3):617–621, 2005.
- [33] F.X. Trias, A. Gorobets, and A. Oliva. A simple approach to discretize the viscous term with spatially varying (eddy-)viscosity. *Journal of Computational Physics*, 253:405–417, 2013.
- [34] F. Nicoud and F. Ducros. Subgrid-scale stress modeling based on the square of the velocity gradient tensor. *Flow, Turbulence and combustion*, 62:183–200, 1999.
- [35] M. A. Mueller, T. J. Kim, R. A. Yetter, and F. L. Dryer. Flow reactor studies and kinetic modeling of the H<sub>2</sub>/O<sub>2</sub> reaction. *International Journal of Chemical Kinetics*, 31:113–125, 1999.
- [36] I. Stanković and B. Merci. Analysis of auto-ignition of heated hydrogen-air mixtures with different detailed reaction mechanisms. *Combustion Theory And Modelling*, 15(3):409–436, 2011.



# Flamelet modelling of nonpremixed combustion phenomena

**Abstract.** In the present chapter the theoretical background of the flamelet model for diffusion flames is presented. First, the flamelet equations are deduced by applying a coordinate transformation, from physical space to a mixture fraction space, to the species and energy transport equations. The transformation splits the combustion process into two different steps: a flame structure problem and a transport problem. The former is characterised by a set of reaction-diffusion equations which are transported and wrinkled by the latter. The transport problem mainly involves the continuity and momentum equations in physical space. The applied transformation allows preserving in the formulation differential diffusion effects. The flamelet model is described in its classical form and with a recently proposed approach which allows a more general description of the flamelet subspace, the Flamelet/Progress-Variable (FPV) model. Algorithms for the solution of the set of reaction-diffusion equations are presented. Both Gauss-Seidel and Newton-Raphson methods are used to compute steady state solutions. An Implicit-Explicit Runge-Kutta-Chebyshev (IMEX RKC) method is used to compute transient flamelets. In addition, the generation of databases and its usage for Computational Fluid Dynamics (CFD) applications are also described. Moreover, the method of presumed probability density functions (*pdf*) is detailed to account for turbulence-chemistry interactions. Alongside, the inclusion of radiation is also discussed.

### 3.1 Introduction

In turbulent combustion, as stated in the introduction of this thesis, closure for the chemical reaction source terms is achieved by means of combustion models. Therefore, the present chapter aims at presenting the flamelet model and its variants. The flamelet model offers a suitable approach to include detailed chemistry into Computational Fluid Dynamics (CFD) simulations. The model here presented will be used in the following chapters to model turbulent diffusion flames.

Numerical solution of combustion phenomena is computationally expensive because its resolution requires solving for the transport of tens or hundreds of species while taking into account hundreds or thousands of chemical reactions [1]. Furthermore, these reactions are exothermic and induce large density variations in the flow. These chemical reactions usually take place in thin layers which in many cases are smaller than the smallest flow scales, the Kolmogorov scale [2]. Moreover, the range of time-scales of these reactions spans from nanoseconds up to flow times. This large span in (time-)scales introduces what in mathematical terms is denoted as stiffness of a system of equations [3].

If chemical reactions are assumed to happen in thin layers within a flow, which the flow only strains and wrinkles, a scale separation may be introduced. Peters [2] proposed applying a coordinate transformation to the species and energy equation from physical space to a coordinate frame located at the flame front, with one direction in the flame normal and the other two in the flame plane. With Peter's transformation, computation of a flame is split into solving the flame structure, defined by a reaction-diffusion process, and a transport process, which transports, strains and wrinkles the flame. A further assumption is required to define the flamelet regime: flow structures do not penetrate the inner flame region, where chemical reactions are taking place. Thus, the flame may be viewed as an ensemble of laminar flames embedded in locally laminar regions within a turbulent flow. Alternatively, the split can be derived from a two-scale asymptotic expansion based on the described scale separation.

Hence, the split enables solving separately the flame structure and its transport. Furthermore, flamelet modelling allows computing the flame structure, denoted as flamelets, in a preprocessing stage and afterwards solving its transport within either laminar or turbulent flows [2, 4, 5]. In order to link both problems, a proper set of parameters is required to represent the flamelets. The classical model uses the mixture fraction and the scalar dissipation rate. However, the whole flamelet subspace, represented by an S-shaped curve, cannot be represented with only these two parameters. Hence, Pierce and Moin [6] proposed changing the scalar dissipation rate for a progress-variable as a parameter to fully represent the flamelet subspace.

Thanks to the scale separation, solution of the flame structure problem allows flamelet databases to be created a priori. To this end, the flamelet equations in mixture fraction space are solved, in either their steady or unsteady form. Due to the

stiffness of the reaction rate term, specific algorithms are applied to the solution of the flamelet equations, mostly being of the implicit form. Specifically, for the steady case, iterative Gauss-Seidel and Newton-Raphson methods are presented. The latter shows good convergence speed if a good initial solution is available. Otherwise, the method easily diverges. On the contrary, the former method shows slow convergence, since it requires small relaxation coefficients due to the stiffness of the chemical source term. Nonetheless, it is not as sensible to initial solutions. For unsteady cases, an Implicit-Explicit Runge-Kutta-Chebyshev (IMEX RKC) method is presented [7]. The method combines an explicit treatment of diffusion terms and an implicit evaluation of the chemical reaction term. The advantage of a hybrid explicit-implicit scheme is that it only requires solving locally implicit systems of equations, as the diffusive term, which couples all the domain, is treated explicitly.

Regarding radiation modelling, since the flamelet equations are solved in mixture fraction space, radiation heat losses can only be described by models without space dependence. Besides, it must also be taken into consideration the computational cost of describing radiation heat transfer. Therefore, an Optically Thin Model (OTM) is used, which evaluates radiation heat as a fraction of the black body emissivity.

Since the flows of interest are mainly turbulent, which are described by turbulent or stochastic quantities, the flamelet databases have to be restated in terms of stochastic quantities. Specifically, in Large Eddy Simulations (LES) solution quantities are space filtered variables. The filtering operation introduces a scale separation between resolved quantities and sub-grid quantities, which require modelling. The method used here is the presumed probability density function (*pdf*) approach [1, 5, 6, 8, 9]. Therefore, turbulence-chemistry interactions are assumed *a priori* and described through statistical distributions.

The chapter is organised as follows. First, the flamelet regime in the context of diffusion flames is detailed, followed by the description of the flamelet model. The classical flamelet model is first introduced and its limitations detailed. Afterwards, a change in parameters capable of solving these shortcomings is introduced. In both cases, the regime and model are presented for laminar variables. Subsequently, numerical algorithms are presented to solve the flamelet equations in mixture fraction space. Finally, in order to use the model for turbulent flames, where turbulent, or statistically distributed, quantities are used, the model has to be restated as a function of stochastic quantities.

## 3.2 Flamelet model

Combustion processes are described by the motion of a flame front within a gas mixture flow. The latter process is described by the Navier-Stokes equations, while the former encompasses both chemical reactions and heat and mass transport within

the flow. The set of equations describing this process is

$$\frac{\partial \rho}{\partial t} + \frac{\partial \rho u_j}{\partial x_j} = 0 \quad (3.1)$$

$$\frac{\partial \rho u_i}{\partial t} + \frac{\partial \rho u_j u_i}{\partial x_j} = -\frac{\partial p}{\partial x_i} + \frac{\partial \tau_{ij}}{\partial x_j} + \rho g_i \quad (i = 1, 2, 3) \quad (3.2)$$

$$\rho \frac{\partial Y_k}{\partial t} + \rho u_j \frac{\partial Y_k}{\partial x_j} = \frac{\partial}{\partial x_j} \left( \rho D_k \frac{\partial Y_k}{\partial x_j} \right) + \frac{\partial}{\partial x_j} \left( \rho Y_k \left( \frac{D_k}{M_w} \frac{\partial M_w}{\partial x_j} - V_j^c \right) \right) + \dot{w}_k \quad (3.3)$$

$$\rho \frac{\partial h}{\partial t} + \rho u_j \frac{\partial h}{\partial x_j} = \frac{dP_o}{dt} - \dot{q}^R - \frac{\partial}{\partial x_j} \left( -\kappa \frac{\partial T}{\partial x_j} - \sum_{k=1}^N \rho h_k \left( \frac{D_k}{M_w} \frac{\partial (M_w Y_k)}{\partial x_j} - Y_k V_j^c \right) \right) \quad (3.4)$$

where the Hirschfelder and Curtiss model for mass diffusion is used.

The focus of the present analysis are diffusion flames, which are characterised by placing fuel and oxidiser in different separated streams. Therefore, chemical reactions cannot take place until reactants are mixed in proper proportions. The reactants distribution can be described using a mixing tracker, namely the mixture fraction  $Z$ . Its classical definition is based on the work of Burke and Schumann [10], derived from a one-step description of the chemical reaction process.



where  $\nu_F$ ,  $\nu_O$  and  $\nu_P$  are the molar stoichiometric coefficients of fuel, oxidant and products, respectively. Then, the reaction rate  $\dot{w}_k$  for each specie is

$$\dot{w}_F = -\nu_F M_{w,F} \mathcal{R} \quad (3.6)$$

$$\dot{w}_O = -\nu_O M_{w,O} \mathcal{R} \quad (3.7)$$

$$\dot{w}_P = \nu_P M_{w,P} \mathcal{R} \quad (3.8)$$

where  $\mathcal{R}$  is the reaction progress-rate defined in *Chapter 1*. For this case, under the assumption of equal diffusivities, the transport equations of the three species reduce to,

$$\begin{aligned} \rho \frac{\partial Y_F}{\partial t} + \rho u_j \frac{\partial Y_F}{\partial x_j} &= \frac{\partial}{\partial x_j} \left( \rho D \frac{\partial Y_F}{\partial x_j} \right) + \dot{w}_F \\ \rho \frac{\partial Y_O}{\partial t} + \rho u_j \frac{\partial Y_O}{\partial x_j} &= \frac{\partial}{\partial x_j} \left( \rho D \frac{\partial Y_O}{\partial x_j} \right) + \dot{w}_O \\ \rho \frac{\partial Y_P}{\partial t} + \rho u_j \frac{\partial Y_P}{\partial x_j} &= \frac{\partial}{\partial x_j} \left( \rho D \frac{\partial Y_P}{\partial x_j} \right) + \dot{w}_P \end{aligned} \quad (3.9)$$

Linear combination of the fuel and oxidiser species transport equations leads to the following coupling function

$$\zeta = \frac{Y_F}{\nu_F M_{w,F}} - \frac{Y_O}{\nu_O M_{w,O}} \quad (3.10)$$

Normalising the coupling function yields the mixture fraction definition

$$Z = \frac{\nu Y_F - Y_O + Y_{O,2}}{\nu Y_{F,1} + Y_{O,2}} \quad (3.11a)$$

$$\nu = \frac{\nu_O M_{w,O}}{\nu_F M_{w,F}} \quad (3.11b)$$

where  $Y_{F,1}$  is the fuel mass fraction at the fuel boundary and  $Y_{O,2}$  is the oxidiser mass fraction at the oxidiser boundary. In addition, the stoichiometric mixture fraction is defined as the location where both fuel and oxidant are completely consumed, leading to

$$Z_{st} = \frac{Y_{O,2}}{\nu Y_{F,1} + Y_{O,2}} = \frac{1}{1 + \nu \frac{Y_{F,1}}{Y_{O,2}}} \quad (3.12)$$

If more complex chemistry is to be considered, alternative definitions have to be used. For example, if all chemical elements are considered, the mixture fraction may be computed using a local element balance [11, 12]

$$Z = \frac{\frac{2Y_C - Y_{C,2}}{M_{w,C}} + \frac{Y_H - Y_{H,2}}{2M_{w,H}} - \frac{Z_O - Z_{O,2}}{M_{w,O}}}{\frac{2Y_{C,1} - Y_{C,2}}{M_{w,C}} + \frac{Y_{H,1} - Y_{H,2}}{2M_{w,H}} - \frac{Y_{O,1} - Y_{O,2}}{M_{w,O}}} \quad (3.13)$$

Although comprehensive, calculation of the mixture fraction with this equation from experimental data is difficult since all participating species have to be accounted for. The approach presented here relies on an assumption of equal diffusivities for all species. For light or heavy species the model does not correctly describe the mixing process. Hence, flame predictions deviate from experimental data.

In order to include differential diffusion, a different approach was proposed by Pitsch and Peters [4], where the mixture fraction is directly defined as a conserved scalar in a two feed system

$$\rho \frac{\partial Z}{\partial t} + \rho u_j \frac{\partial Z}{\partial x_j} = \frac{\partial}{\partial x_j} \left( \rho D_Z \frac{\partial Z}{\partial x_j} \right) \quad (3.14)$$

where  $D_Z$  is the mixture fraction diffusivity, which can be arbitrarily chosen. For example, a unity Lewis number may be taken,  $Le_Z = \kappa / (\rho D_Z c_p) = 1$ . With the mixture fraction defined through a transport equation, it no longer represents the

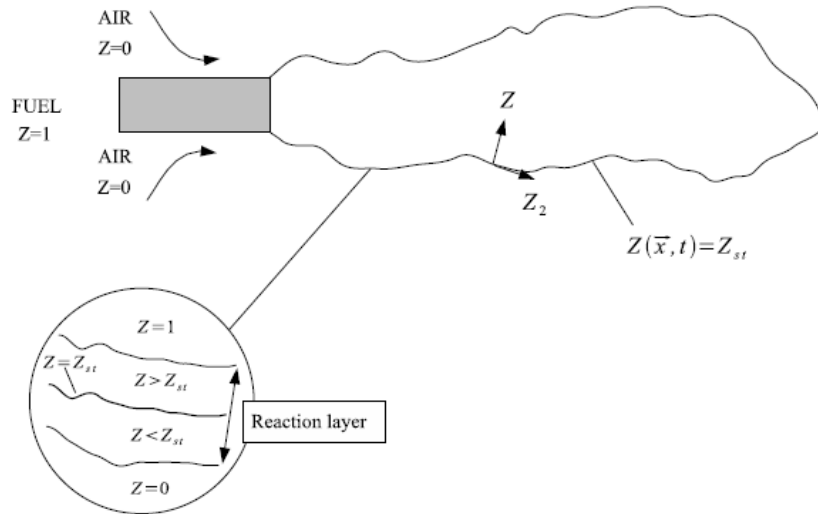


**Figure 3.1:** Flamelet local coordinates. Extracted from D. Carbonell's thesis [5].

local composition. Furthermore, the computed stoichiometric mixture fraction value  $Z_{st}$  is not equivalent to the one obtained from Eq. (3.11) or (3.13). However, since the resulting flamelet model is not dependent on the stoichiometric mixture fraction this is not a critical aspect.

Thereafter, a coordinate system attached to the flame front, depicted in Fig. 3.1, described by the mixture fraction is defined, where variations are assumed to be mainly in the flame normal direction. Thus, variations in the flame-tangential plane are neglected [4, 5].

Applying the formal coordinate transformation rules, for the time coordinate  $\frac{\partial}{\partial t} = \frac{\partial}{\partial \tau} + \frac{\partial Z}{\partial t} \frac{\partial}{\partial Z}$  and flame normal space coordinate  $\frac{\partial}{\partial x} = \frac{\partial Z}{\partial x} \frac{\partial}{\partial Z}$ , to the species and energy transport equations (Eq. (3.3) and (3.4)) results in

$$\begin{aligned}
\rho \frac{\partial Y_k}{\partial \tau} = & \dot{w}_k + \frac{\rho \chi_Z}{2} \frac{Le_Z}{Le_k} \frac{\partial^2 Y_k}{\partial Z^2} + \frac{\rho \chi_Z}{2} \frac{Le_Z}{Le_k} \frac{Y_k}{M_w} \frac{\partial^2 M_w}{\partial Z^2} \\
& - \frac{\rho \chi_Z}{2} \sum_{\alpha=1}^N \left( \frac{Le_Z}{Le_\alpha} Y_k \frac{\partial^2 Y_\alpha}{\partial Z^2} + \frac{Y_k}{M_w} Y_\alpha \frac{Le_Z}{Le_\alpha} \frac{\partial^2 M_w}{\partial Z^2} \right) \\
& + \frac{1}{4} \left[ 2\rho \chi_Z \frac{\partial}{\partial Z} \left( \frac{Le_Z}{Le_k} \right) + \left( \frac{Le_Z}{Le_k} - 1 \right) \left( \frac{\partial \rho \chi_Z}{\partial Z} + \rho \chi_Z Le_Z \frac{c_p}{\kappa} \frac{\partial}{\partial Z} \left( \frac{\kappa}{c_p Le_Z} \right) \right) \right] \frac{\partial Y_k}{\partial Z} \\
& + \frac{1}{4} \left[ 2\rho \chi_Z \frac{Y_k}{M_w} \frac{\partial}{\partial Z} \left( \frac{Le_Z}{Le_k} \right) + \left( \frac{Le_Z}{Le_k} \right) \left( \frac{\partial}{\partial Z} \left( \rho \chi_Z \frac{Y_k}{M_w} \right) + \rho \chi_Z Le_Z \frac{c_p}{\kappa} \frac{\partial}{\partial Z} \left( \frac{\kappa}{c_p Le_Z} \frac{Y_k}{M_w} \right) \right) \right] \frac{\partial M_w}{\partial Z} \\
& - \frac{1}{4} \sum_{\alpha=1}^N \left[ 2\rho \chi_Z Y_k \frac{\partial}{\partial Z} \left( \frac{Le_Z}{Le_\alpha} \right) + \left( \frac{Le_Z}{Le_\alpha} \right) \left( \frac{\partial \rho \chi_Z Y_k}{\partial Z} + \rho \chi_Z Le_Z \frac{c_p}{\kappa} \frac{\partial}{\partial Z} \left( \frac{\kappa}{c_p Le_Z} Y_k \right) \right) \right] \frac{\partial Y_\alpha}{\partial Z} \\
& - \frac{1}{4} \sum_{\alpha=1}^N \left[ 2\rho \chi_Z \frac{Y_k Y_\alpha}{M_w} \frac{\partial}{\partial Z} \left( \frac{Le_Z}{Le_\alpha} \right) \right. \\
& \quad \left. + \left( \frac{Le_Z}{Le_\alpha} \right) \left( \frac{\partial}{\partial Z} \left( \rho \chi_Z \frac{Y_k}{M_w} Y_\alpha \right) + \rho \chi_Z Le_Z \frac{c_p}{\kappa} \frac{\partial}{\partial Z} \left( \frac{\kappa}{c_p Le_Z} \frac{Y_k Y_\alpha}{M_w} \right) \right) \right] \frac{\partial M_w}{\partial Z}
\end{aligned} \tag{3.15a}$$

$$\begin{aligned}
\rho \frac{\partial T}{\partial \tau} = & \frac{\rho \chi_Z}{2} Le_Z \frac{\partial^2 T}{\partial Z^2} - \frac{1}{c_p} \dot{q}^R - \frac{1}{c_p} \sum_{k=1}^N \dot{w}_k h_k + \frac{\rho \chi_Z}{2} \frac{Le_Z}{c_p} \frac{\partial c_p}{\partial Z} \frac{\partial T}{\partial Z} \\
& + \frac{1}{4} \left[ 2\rho \chi_Z \frac{\partial Le_Z}{\partial Z} + (Le_Z - 1) \left( \frac{\partial \rho \chi_Z}{\partial Z} + \rho \chi_Z Le_Z \frac{c_p}{\kappa} \frac{\partial}{\partial Z} \left( \frac{\kappa}{c_p Le_Z} \right) \right) \right] \frac{\partial T}{\partial Z} \\
& - \sum_{k=1}^N \frac{\rho \chi_Z}{2} \frac{Le_Z}{Le_k} \left( \frac{\partial Y_k}{\partial Z} + \frac{Y_k}{M_w} \frac{\partial M_w}{\partial Z} \right) \left( 1 - \frac{c_{p,k}}{c_p} \right) \frac{\partial T}{\partial Z}
\end{aligned} \tag{3.15b}$$

where  $\chi_Z$  is the scalar dissipation rate, which introduces flow effects into flamelet space, and is defined as

$$\chi_Z = 2D_Z \left( \frac{\partial Z}{\partial x_i} \frac{\partial Z}{\partial x_i} \right) \tag{3.16}$$

If Fickian diffusion is assumed, and all diffusion coefficients are assumed equal, or equivalently all Lewis numbers equal to  $Le_Z = Le_k$ , the flamelet equations can be reduced

$$\rho \frac{\partial Y_k}{\partial t} = \dot{w}_k + \frac{\rho \chi_Z}{2} \frac{\partial^2 Y_k}{\partial Z^2} \quad (3.17a)$$

$$\rho \frac{\partial T}{\partial t} = \frac{\rho \chi_Z}{2} \frac{\partial^2 T}{\partial Z^2} - \frac{1}{c_p} \dot{q}^R + \frac{1}{c_p} \sum_{k=1}^N \dot{w}_k h_k - \frac{\rho \chi_Z}{2} \left( \frac{1}{c_p} \frac{\partial c_p}{\partial Z} \frac{\partial T}{\partial Z} + \sum_{k=1}^N \frac{\partial Y_k}{\partial Z} \left( 1 - \frac{c_{p,k}}{c_p} \right) \frac{\partial T}{\partial Z} \right) \quad (3.17b)$$

where gradients of the molar mass are neglected due to the Fickian approximation. Furthermore, if heat capacities are assumed constant, the flamelet equations based on the Shvab-Zeldovich formulation are obtained

$$\rho \frac{\partial Y_k}{\partial t} = \frac{\rho \chi_Z}{2} \frac{\partial^2 Y_k}{\partial Z^2} + \dot{w}_k \quad (3.18a)$$

$$\rho \frac{\partial T}{\partial t} = \frac{\rho \chi_Z}{2} \frac{\partial^2 T}{\partial Z^2} - \frac{1}{c_p} \dot{q}^R - \frac{1}{c_p} \sum_{k=1}^N \dot{w}_k h_k \quad (3.18b)$$

The flamelet equations defined in Eq. (3.15) can be solved once the scalar dissipation rate is set. Therefore, two possibilities arise. Either the flamelet equations are solved alongside a CFD simulation, where the mixture fraction is obtained in physical space, usually denoted as the interactive strategy, or a functional form is assumed. The former approach involves computing the mixture fraction field through Eq. (3.14) and afterwards evaluating the scalar dissipation rate through Eq. (3.16). The latter approach requires setting the conditional dependence of the scalar dissipation on the mixture fraction.

The interactive strategy requires solving the flamelet equations Eq. (3.15), or their Fickian counterparts Eq. (3.17), during numerical simulations. If large chemical mechanisms were to be used, this procedure requires large computational resources, since the flamelet equations would have to be solved at each control volume. Therefore, computational resources limited the applicability of the model. Nonetheless, by assuming Fickian diffusion the complexity of the system of equations is reduced allowing the inclusion of larger chemical mechanisms.

If flamelets are to be solved in a preprocessing stage and stored in flamelet libraries, an alternative approach is required. Therefore, a functional form for the scalar dissipation rate has to be assumed. Based on an analogy between counter-flow flames and flames in the flamelet regime, Peters [2] modelled the scalar dissipation rate as

$$\chi_Z(Z) = \frac{a_\infty}{\pi} \Phi \exp(-2[erfc^{-1}(2Z)]^2) \quad (3.19)$$

where  $a_\infty$  is the nominal strain rate in a counter-flow configuration and  $\Phi$  is a coefficient later introduced to account for variable density effects [4, 13]. The function

$\text{erfc}^{-1}$  is the inverse, not the reciprocal, of the complementary error function. Interestingly, Peters [2] also derived the same functional dependence of the scalar dissipation rate on the mixture fraction from the analysis of unsteady mixing layers. As it will be shown later, it is of interest to restate the functional form of the scalar with respect to a characteristic scalar dissipation rate,

$$\chi_Z(Z) = \chi_{st} \frac{\Phi}{\Phi_{st}} \frac{f(Z)}{f_{st}(Z)} \quad (3.20)$$

where  $f(Z)$  represents the exponential term in Eq. (3.19). With this approach, the shape of the curve is defined by  $f(Z)$  and its height is controlled by the scalar dissipation rate at the stoichiometric mixture fraction,  $\chi_{st} = \chi_Z|_{Z=Z_{st}}$ , which becomes a measure of the strain rate  $a_\infty$ .

Alternative functional forms for the assumed scalar dissipation rate have been proposed [14, 15] based on a semi-infinite mixing layer, modelled by homogeneous boundary conditions on the fuel side

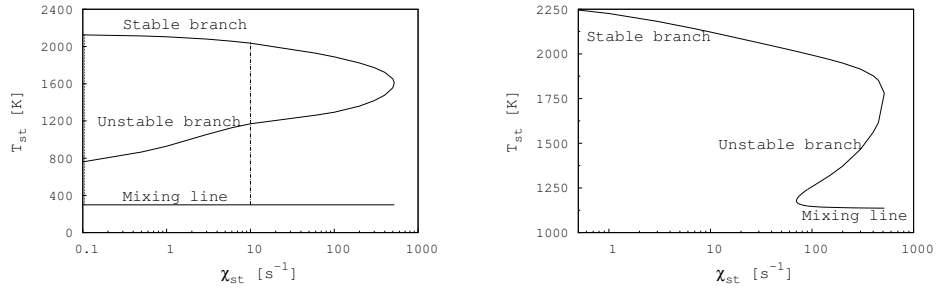
$$\chi_Z(Z) = \chi_{st} \frac{Z^2 \ln(Z)}{Z_{st}^2 \ln(Z_{st})} \quad (3.21)$$

Once the scalar dissipation rate is defined, the flamelet equations may be solved. In the following, the discussion is centred around the approach using an assumed distribution for the scalar dissipation rate as it allows solving the flamelet equations in a preprocessing stage. The flamelet subspace can be represented through the solution of the flamelet equations, Eq. (3.15) or Eq. (3.18). The set of flamelet equations are solved in their steady state form for a range of stoichiometric scalar dissipation rates  $\chi_{st}$ . Each one of the solutions consists of temperature and species profiles as a function of the mixture fraction  $Z$ . With these solutions, a representation of the flamelet subspace is obtained by plotting the temperature at stoichiometric mixture fraction  $T_{st}$  as a function of  $\chi_{st}$ .

In Fig. 3.2 the range of solutions for two diffusion flames are shown. As it can be seen, the curve representing steady state solutions takes the form of an inverted 'S'. Hence, the curve is usually referred to as the S-shaped curve. Fig. 3.2a shows the S-shaped curve for a  $\text{CH}_4/\text{H}_2$  diffusion flame [16] and Fig. 3.2b is for a  $\text{CH}_4$  self-igniting flame [17].

Flamelet solutions range from  $\chi_{st} \rightarrow 0$  to  $\chi_q$ , the latter representing the scalar dissipation rate at which the flame is quenched. The limit of zero scalar dissipation rate represents an unstrained diffusion flame. However, the flamelet equations cannot reproduce this limit, because unstrained one dimensional diffusion flames become choked by their combustion products.

The upper branch, up to the quenching scalar dissipation rate  $\chi_q$ , is denoted as the stable burning branch. The middle or unstable branch corresponds to transition states



(a) Methane-hydrogen/air diffusion flame [16] computed using the GRI3.0 mechanism [18]. Discontinuous lines indicate the  $\chi_{st}$  for Fig. 3.3

(b) Self-igniting methane/air flame [17] computed using the GRI2.11 mechanism [18].

**Figure 3.2:** S-shaped curves for two different diffusion flames.

between igniting and quenching flamelets. The bottom branch corresponds to the pure mixing line. These branches represent steady state solutions. Regions in between are transient states described by the unsteady solution of the flamelet equations. The region enclosed between the stable and unstable branches and for  $\chi_{st} < \chi_q$  represents an igniting regime. On the contrary, extinguishing processes fall below the unstable branch and for scalar dissipation rates higher than the extinction one. Nonetheless, Pitsch and Fedotov [19] showed that scalar dissipation rate fluctuations may cause transient flamelets to cross the middle branch. Therefore, the middle branch does not uniquely separate igniting and extinguishing flamelets.

As can be observed in Fig. 3.2b, the unstable branch extends down to a given stoichiometric scalar dissipation rate which is denoted as the ignition scalar dissipation rate  $\chi_I$ , taking a value of approximately of  $70 s^{-1}$ . This is characteristic of self-igniting flames where the flame ignites without external contributions. In the region  $\chi_{st} < \chi_I$  heat and mass diffusion are not able to counter the chemical reaction progress. Hence, after an initial delay time the mixture ignites. Flames with a preheated oxidant stream are an example of this case.

In Fig. 3.3 are shown temperature profiles at two  $\chi_{st}$  corresponding to the vertical lines in Fig. 3.2a.

### 3.2.1 Classical Flamelet

In order to use the flamelet model in CFD simulations, flamelet solutions have to be compiled into a database. Furthermore, to retrieve data from this database, a set of parameters has to be defined. Since flamelet equations are solved in mixture fraction

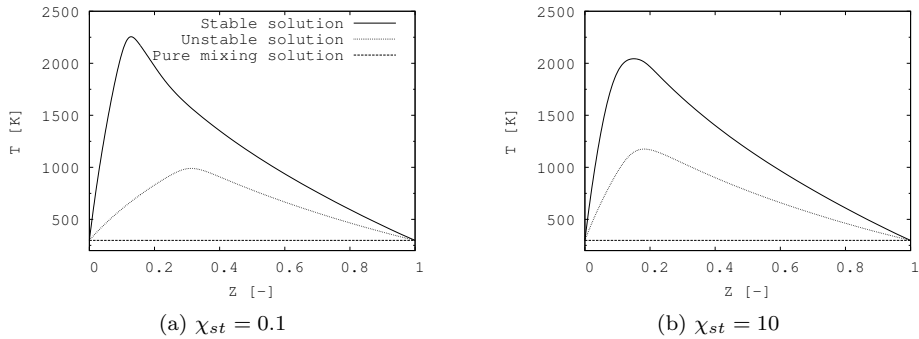


**Figure 3.3:** Temperature distribution in mixture fraction space for a methane-hydrogen/air diffusion flame [16], corresponding to the vertical lines in Fig. 3.2a ( $\chi_Z = 0.1$  and 10).

space at several stoichiometric scalar dissipation rates, the natural representation of the flamelet library is using the mixture fraction  $Z$  and the stoichiometric scalar dissipation rate  $\chi_{st}$ , and, for unsteady cases, the flamelet time  $\tau$ .

Beginning with steady cases, solution of the flamelet equations can be represented as an equation of state (EoS) of the form

$$\phi = \xi(Z, \chi_{st}) \quad (3.22)$$

However, a database using only  $Z$  and  $\chi_{st}$  can only uniquely represent one branch of the S-shaped curve. Therefore, to include burning solutions, the flamelet database only includes the stable burning branch solutions and the extinguished mixing solutions for scalar dissipation rates past  $\chi_q$ , as shown afterwards in Fig. 3.4b. Therefore, the steady model only includes a limited subset of the steady flamelet solutions, which limits the applicability of the model. In terms of flame physics, the steady model projects vertically all solutions in the flamelet space. For  $\chi_{st} < \chi_q$  the flamelet model always predicts an ignited flame and for higher  $\chi_{st}$  the flame is always extinguished.

Contrarily to the steady model, the unsteady model can represent the different states in the flamelet subspace. However, in the unsteady form of the flamelet equations a flamelet time-scale,  $\tau$ , has to be considered. The time coordinate is a Lagrangian time coordinate because the coordinate transformation applied to the species and energy transport equations, Eq. (3.3) and Eq. (3.4) respectively, is defined to be attached to the flame front at the stoichiometric surface. Therefore, this implies that the time derivative in Eq. (3.15) is to be evaluated at constant mixture fraction  $Z$ . Hence, the unsteady flamelet model requires the flamelet equations to be evaluated with the interactive strategy in order to compute the flamelet time. In jet-like flames,

flamelets are assumed to be introduced through the fuel nozzle and travel downstream [14, 15]. Hence, the flamelet time can be computed as follows

$$\tau = \int_0^x \frac{1}{u(x')|Z = Z_{st})} dx' \quad (3.23)$$

where  $x$  represents the axial distance and  $u(x)|\{Z = Z_{st}\}$  is the axial velocity conditioned on the stoichiometric mixture fraction. The numerical viability of the model is restricted by the computation of the flamelet time, which is only feasible for certain geometries, and the need of solving the flamelet equations coupled with the CFD simulations.

### Radiation heat transfer

The models discussed so far do not include radiation heat losses, represented by  $\dot{q}^R$  in the flamelet equations. On the one hand, if the unsteady flamelet model is used, since an interactive approach is required, any radiation model can be used to model the radiative heat transfer. Anyway, it must be borne in mind that the interactive approach is computationally demanding and a complex radiation calculation may increase these requirements even further. On the other hand, if the steady flamelet approach is considered, a limitation on the functional form of the radiation model is placed. Due to the coordinate change, the flame structure is solved in a flame based coordinate system. Therefore, radiation heat losses have to be either computed without spatial dependencies or a generic enthalpy loss introduced. In the latter approach, once radiation heat losses are computed in physical space, they are related to this enthalpy loss. In the former approach, the medium is assumed optically thin, meaning that the flame has an unimpeded view of the surroundings. In the Optically Thin Model (OTM) it is assumed that self-absorption is negligible compared to emission [5, 20]. Thus, the radiation flux is modelled as a heat loss at each control volume, and evaluated as

$$\dot{q}^R = 4\sigma \left( T^4 \sum_{k=1}^N (p_k k_{P_k}) - T_s^4 \sum_{k=1}^N (p_k k_{I_k}) \right) \quad (3.24)$$

where  $\sigma$  is the Stefan-Boltzmann constant,  $p_k$  is the partial pressure of the  $k$ th species,  $k_{P_k}$  and  $k_{I_k}$  are the Planck-mean and incident-mean absorption coefficients and  $T_s$  is the background temperature. Absorption coefficients obtained from RADCAL [21] are fitted to polynomials of the temperature. The radiant species considered in this work are  $CO_2$ ,  $H_2O$ ,  $CH_4$  and  $CO$ .

The steady flamelet model assumes that the chemical state relaxes infinitely fast to the steady state. This translates into mixtures reaching the chemical and thermal steady state rapidly. However, radiation and NOx formation are slow processes which are then inaccurately captured [5, 22, 23]. If a flamelet is identified with a fluid

particle travelling throughout the flow domain, then it can be seen that if chemistry relaxes rapidly to the steady state, slow processes such as radiation and NOx will be overestimated. The rationale is that these fluid particles will remain in regions of high temperatures during longer periods of time compared to the case where the flamelet was not assumed to be in its steady state.

Nonetheless, modifications to the steady model have been proposed to overcome these limitations. Two methods, among others, have been most widely used. On the one hand, an enthalpy defect parameter has been proposed to be used as an additional parameter [24–27]. Thus, a further dimension is introduced in the flamelet database. With this method successive steady flamelets are computed by setting different levels of arbitrary heat losses. If the heat loss is defined independent of the mixture fraction, the temperature at the boundaries can decrease to unrealistic low temperatures. Hence, with this approach either the mixture fraction domain is limited or the chemical composition of the boundaries changed [5, 23]. Alternatively, this limitation may be avoided if a variable heat loss in mixture fraction space is used. To this end, a radiation parameter [5, 22] is introduced, which relates the enthalpy of a mixture at adiabatic conditions  $T^{ad}, Y_k^{ad}$  to a mixture with the same composition but cooled down to standard conditions  $T^u, Y_k^{ad}$ .

On the other hand, if the enthalpy is computed during CFD simulations, with an appropriate radiation model, the temperature field can be reconstructed using the ideal gas law and the species mass fractions retrieved from a steady flamelet database [22, 28]. Since the enthalpy is a nonlinear function of the temperature and species, this approach requires an iterative process, which evidently implies a higher computational cost.

In both cases a further transport equation is to be solved during CFD simulations in order to account for the enthalpy transport. Studies using either model have been reported and shown to improve results compared to the base steady flamelet model [5, 22].

### 3.2.2 Flamelet/Progress-variable (FPV) model

In order to overcome the limitations of the classical flamelet model, Pierce and Moin [6] proposed changing the parameters used to define the flamelet library. Particularly, changing  $\chi_{st}$  as a parameter in favour of a progress-variable parameter  $\Lambda = c|Z_{st}|$  to represent steady flamelets, where  $c$  is the progress-variable. In this way, it is possible to fully characterise the S-shaped curve and consequently being able to describe partially-extinguished or partially-ignited states. Therefore, this progress-variable parameter must be defined so it uniquely identifies each flamelet within the database. The progress-variable is usually defined in terms of a linear, or weighted

linear, combination of species mass fractions

$$c = \sum_k \omega_k Y_k \quad (3.25)$$

In the literature several definitions have been proposed for the progress-variable, either using different sets of species and/or weights or using the temperature. The range of proposed definitions indicates the dependence of this parameter on the studied case: chemical mechanism, fuel composition and combustion mode [29]. Furthermore, in *Chapter 4* the influence of the diffusion model is studied.

Beginning again with the steady state solutions, with the newly introduced progress-variable parameter, the full S-shaped curve can be expressed as an EoS function

$$\phi = \zeta(Z, \Lambda) \quad (3.26)$$

where  $\Lambda = c|Z = Z_{st}\}$  is the progress-variable parameter. Although it is possible to construct a transport equation for the progress-variable parameter, when applied to turbulent flows it contains several difficult to model terms. Therefore, it is more suitable to use the progress-variable itself as parameter. Since the progress-variable can be retrieved from the database, Eq. (3.26), assuming that the relation between the progress-variable parameter and the progress-variable is bijective

$$\Lambda = \zeta^{-1}(Z, c) \quad (3.27)$$

the EoS for the steady Flamelet/Progress-Variable model (SFPV) can be expressed as

$$\phi = \{\rho, \dot{w}_c, D_Z, Y_k, T, \dots\} = F^{SFPV}(Z, c) \quad (3.28)$$

With this approach all points on the S-shaped curve are uniquely defined, allowing igniting or extinguishing flamelets to be represented.

Slow processes, such as nitric oxides formation or radiation, or self-ignition phenomena do not relax to the steady solution in fast time-scales as assumed by the steady flamelet model. Therefore, it is important to retain the transient terms in the flamelet equations. However, as previously stated, the computation of the flamelet time introduced several restrictions to the flamelet model. Nonetheless, introducing the progress-variable as a tracking quantity, the evolution of the mixture composition at a given stoichiometric scalar dissipation rate can be traced, provided that the progress-variable uniquely defines the transient process. Therefore, the unsteady Flamelet/Progress-Variable (UFPV) model can be viewed from two equivalent points of view. On the one hand, as an extension of the SFPV model where the scalar dissipation rate allows including transient states [30, 31]. On the other hand, as a variable change with respect to the classical flamelet model, where the flamelet time is

replaced by a progress-variable. The second point of view emphasises the requirement for the progress-variable to be a monotonically varying magnitude.

Hence, the set of solutions of the unsteady model becomes a function of the mixture fraction  $Z$ , the progress-variable  $c$  and the stoichiometric scalar dissipation rate  $\chi_{st}$ . Hence, the database for the unsteady flamelet can be computed in a preprocessing stage. The EoS for the unsteady Flamelet/Progress-Variate (UFPV) adds the stoichiometric scalar dissipation rate to the steady one

$$\phi = \{\rho, \dot{w}_c, D_Z, Y_k, T, \dots\} = F_\phi^{UFPV}(Z, c, \chi_{st}) \quad (3.29)$$

#### Accessible flamelet subspace

The change in parameters between the classical flamelet and the Flamelet/Progress-Variate model results in significantly different flamelet subspaces being accessed. Using the mixture fraction and the progress-variable it is possible to represent the whole S-shaped curve. However, as opposed to the classical flamelet, the FPV model cannot account for solutions past the quenching scalar dissipation rate. Furthermore, there is a change in how the flamelet subspace is accessed. The SFPV model projects horizontally flamelets transitioning from burning to extinction, or vice versa, shown in Fig. 3.4a. Oppositely, the classical flamelet performs a vertical projection, shown in Fig. 3.4b.

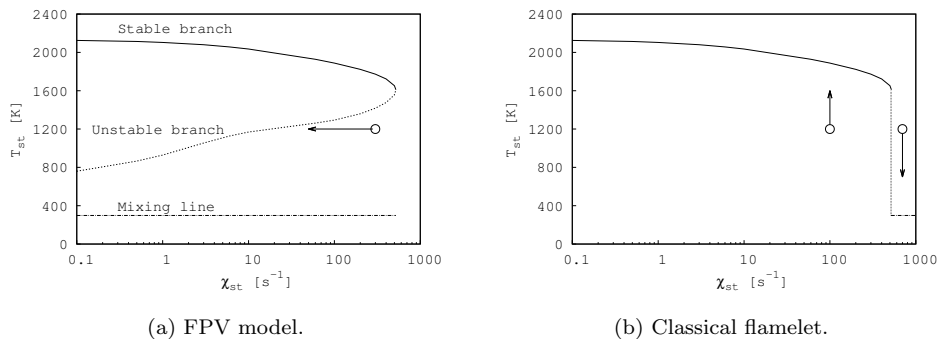


**Figure 3.4:** Flamelet accessible subspace. S-shaped curves for a methane/air flame [16]. Flamelet solutions were computed using the GRI3 mechanism.

#### Progress-variable definition

As stated, the progress-variable has to be defined unambiguously in order to uniquely characterise the flamelet thermochemical state. The progress-variable is a magnitude also found in several models for premixed combustion. Therefore, in the

literature, several definitions can be found for different flames and configurations. In general, a linear summation of species is used, as indicated in Eq. (3.25). Additionally, a reduced temperature has also been used. This is indicative of the difficulty in finding a general definition for this parameter. Most definitions of the progress-variable involve the major combustion products mass fractions  $CO_2$ ,  $H_2O$ ,  $CO$  and  $H_2$ . Pierce and Moin [6] defined it as a linear combination of  $CO_2$  and  $H_2O$ , Vreman et al. [32] and Oijen and de Goey [33], in the context of premixed flames, included  $H_2$  into the definition and used as weights the inverse of the molar mass. Domingo et al. [34] also for premixed flames used a combination of only  $CO$  and  $CO_2$ . Ihme et al. [23, 31] used the four major species, as well as analysing the effect of the definition on its monotonicity and proposing an optimisation method for finding the coefficients of each species, so that the bijective relation in Eq. (3.27) was met [29]. The method showed improvements over existing definitions. However, results still showed non-bijective regions. A dependence on the combustion mode, premixed or non-premixed, the chemical mechanism and considered fuel was also shown. In non-premixed flames, diffusion, or mixing, is the rate controlling mechanism of the flame. Usually a Fickian approximation is made, which simplifies the computations. However, accounting for differential diffusion modifies the species distribution. *Chapter 4* is partially focused on this topic.

In this thesis, the progress-variable is defined as a linear summation of different species mass fractions. Therefore, the transport equation to be computed during CFD simulations is a linear summation of the transport equation of the different species

$$\rho \frac{\partial c}{\partial t} + \rho u_j \frac{\partial c}{\partial x_j} = \frac{\partial}{\partial x_j} \left( \rho D_c \frac{\partial c}{\partial x_j} \right) + \dot{w}_c \quad (3.30)$$

where  $D_c$  is the progress-variable diffusivity, which is taken equal to the mixture fraction diffusivity, and  $\dot{w}_c$  is the progress-variable reaction rate defined similarly to the progress-variable as a linear summation of species reaction rates. The transport equation for the progress-variable is used in its Fickian form also when flamelet databases accounting for differential diffusion are used. This choice is justified in Chapter 4.

### Radiation FPV

If radiation heat losses are accounted for during the computation of the flamelet equations, these solutions define a subspace within the S-shaped curve. In Fig. 3.5 the radiation subspace is depicted by the dotted region, which represents the region where radiation effects are significant. The computation of the solutions is described in Sec. 3.3.1. In short, an OTM model is used to model radiation heat losses and transient extinguishing flamelets are computed beginning from the steady adiabatic branch. The radiation subspace spans between the adiabatic upper stable solution and the “radiation” stable solution, which is the steady state solution with radiation accounted for.

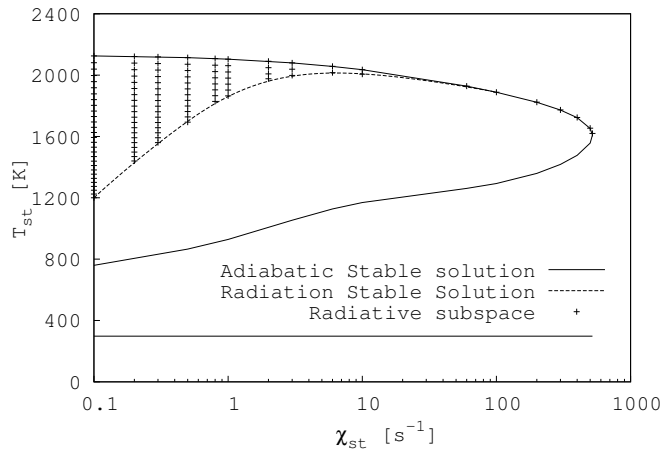


**Figure 3.5:** Flamelet accessible subspace with radiation heat losses denoted by the region with crosses. S-shaped curves for a methane/air flame [16]. Flamelet solutions were computed using the GRI3 mechanism.

Analysing the radiation subspace, two significant aspects can be highlighted. On the one hand, the radiation subspace overlaps with the adiabatic transient solution, located between the stable upper branch and the unstable middle branch. On the other hand, radiation is known to be mainly significant at low scalar dissipation rates. Analysing the flamelet equations, using the Fickian transport equation for the temperature Eq. (3.18b), it can be observed that this effect can be explained by the diffusion term having a more preponderant role at high  $\chi_{st}$ .

This overlap between radiation and unsteady flamelet subspaces does not translate into an equivalency between solutions, but it reflects a limitation of the model. Unsteady effects and radiation heat losses cannot be taken into account simultaneously with the current tabulated flamelet approach. If the interactive unsteady flamelets are used, as previously described, both effects could be included. However, this would lead to the aforementioned increase in computational load.

Concerning radiation heat losses, the steady FPV model does not present any difference with respect to the classical steady model, since it deals only with the adiabatic solutions. Similar strategies to those used for the classical flamelet can be employed in the FPV model. However, Ihme and Pitsch [23] proposed a new approach to include radiation effects into flamelet models based on the FPV model. The approach introduced an additional parameter to measure the effect of radiation losses, either the enthalpy itself or a heat loss parameter. Then, the radiation subspace

can be uniquely defined using the progress-variable  $c$  and the enthalpy  $h$  for each mixture fraction  $Z$ . Hence, the dotted region in Fig. 3.5 is represented by the progress-variable and the enthalpy at  $Z_{st}$ . The EoS for the radiation Flamelet/Progress-variable (RFPV) is

$$\phi = \{\rho, \dot{w}_c, D_Z, Y_k, T, \dots\} = F_\phi^{RFPV}(Z, c, h) \quad (3.31)$$

The new parameter, the enthalpy, has to be computed during CFD simulations. Therefore, a transport equation for the enthalpy is computed

$$\rho \frac{\partial h}{\partial t} + \rho u_j \frac{\partial h}{\partial x_j} = \frac{\partial}{\partial x_j} \left( \rho D_h \frac{\partial h}{\partial x_j} \right) - \dot{q}^R \quad (3.32)$$

where  $D_h$  is the thermal diffusivity, which is taken to be equal to the mixture fraction diffusivity  $D_Z$ .

This latter approach is applied in this thesis because it overcomes the limitations of the enthalpy defect model and it does not suffer from time-scales differences between fast chemistry and slow radiation. Therefore, the progress-variable together with the enthalpy become a tracer of the energy loss process.

### Modelling Nitric Oxide ( $NO_x$ ) emissions

Similar to radiation heat losses, nitric oxides ( $NO_x$ ) generation occurs in long timescales which are not correctly captured when steady flamelet models are used. Therefore, Ihme and Pitsch [23] proposed a submodel specifically for  $NO_x$ . It consists of computing a transport equation for  $NO$  during CFD simulations and adjusting its reaction rate to compensate for the timescale difference between flamelet models and  $NO$  formation. The transport equation is like the transport of any other species mass fraction

$$\rho \frac{\partial Y_{NO}}{\partial t} + \rho u_j \frac{\partial Y_{NO}}{\partial x_j} = \frac{\partial}{\partial x_j} \left( \rho D_{NO} \frac{\partial Y_{NO}}{\partial x_j} \right) + \dot{w}_{NO}^* \quad (3.33)$$

where  $Y_{NO}$ ,  $D_{NO}$ ,  $\dot{w}_{NO}^*$  are  $NO$  mass fraction, diffusivity and corrected reaction rate, respectively. The latter is derived as follows. Assuming simple one-step reactions for the production of  $NO$ ,  $R_1 + R_2 \xrightleftharpoons[k_b]{k_f} NO + P$ , the reaction rate stored in the flamelet database is

$$\dot{w}_{NO} = \dot{w}_{NO}^+ + \dot{w}_{NO}^- \quad (3.34)$$

where production and destruction are given by

$$\dot{w}_{NO}^+ = \frac{M_{w,NO}}{\rho^{RFPV}} k_f \left( \frac{\rho^{RFPV} Y_{R_1}}{M_{w,R_1}} \right) \left( \frac{\rho^{RFPV} Y_{R_2}}{M_{w,R_2}} \right) \quad (3.35a)$$

$$\dot{w}_{NO}^- = -Y_{NO}^{RFPV} k_b \left( \frac{\rho^{RFPV} Y_P}{M_{w,P}} \right) \quad (3.35b)$$

which shows a dependence of the destruction rate on the  $NO$  mass fraction. To remove this dependence, the computed  $NO$  mass fraction is used to correct the reaction rate through

$$\dot{w}_{NO}^* = \dot{w}_{NO}^+ + \frac{Y_{NO}}{Y_{NO}^{RPFV}} \dot{w}_{NO}^- \quad (3.36)$$

where  $Y_{NO}$  is calculated using Eq. (3.33) and  $Y_{NO}^{RPFV}$  is retrieved from the radiation flamelet database.

### 3.3 Flamelet database

Having defined the flamelet model, in the following the procedure to compute the flamelet database is discussed. The numerical discretisation of the flamelet equations, the resolution method to obtain steady state solutions and the temporal integration method for the transient ones are described. Flamelets with radiation are described afterwards, being computed as transient flamelets under radiation heat losses. It will then be clear the incompatibility of transient and radiation flamelets because their subspaces overlaps.

#### 3.3.1 Solution of the flamelet equations

A dedicated one dimensional finite differences code has been developed to solve the set of equations Eq. (3.15), or alternatively their Fickian counterparts Eq. (3.17) or Eq. (3.18). Besides the chemical source term, which is computed using finite rate kinetics, the numerical discretisation of the differential equations requires specifying the numerical counterparts of first and second derivatives. Additionally, the chemical composition is described by species present in large amounts, of the order of  $10^{-1}$ , and species in small concentrations  $O(10^{-6} - 10^{-9})$ . Furthermore, steep gradients for both species and temperature gradients are present. Therefore, good numerical accuracy is required. Hence, 4th order numerical approximations to the first and second derivatives are used. Moreover, the resulting profile is not evenly distributed and is usually located near the stoichiometric mixture fraction. Thus, using non-uniform meshes is essential to reduce the computational load. To this end, 4th order numerical approximations to the derivatives with variable coefficients are used, taking into account non-equidistant distances between nodes.

The finite differences approximation to the  $d$ -th order derivative is constructed using a linear summation of neighbour node values

$$\frac{h^d}{d!} \frac{\partial^d F(Z)}{\partial Z^d} + O(h^{d+p}) = \sum_{i=i_{min}}^{i=i_{max}} C_i F(x + ih) \quad (3.37)$$

where  $i$  indicates the range of points required to define the  $C_i$  coefficients in order to achieve the desired error order  $(d + p)$  and  $h$  is the step between nodes. The set of

coefficients is not dependent on the actual function to be represented and they can be computed in a pre-processing stage.

In order to construct the numerical approximations Taylor series expansion around each mesh point are performed. The expansion is performed up to the desired order of accuracy

$$\begin{aligned} F(Z \pm h_1) &= F(Z) \pm h_1 \frac{\partial F(Z)}{\partial Z} + \frac{h_1^2}{2!} \frac{\partial^2 F(Z)}{\partial Z^2} \pm \frac{h_1^3}{3!} \frac{\partial^3 F}{\partial Z^3} + \frac{h_1^4}{4!} \frac{\partial^4 F(Z)}{\partial Z^4} + O(h^5) \\ F(Z \pm (h_1 + h_2)) &= F(Z) \pm (h_1 + h_2) \frac{\partial F(Z)}{\partial Z} + \frac{(h_1 + h_2)^2}{2!} \frac{\partial^2 F(Z)}{\partial Z^2} \pm \frac{(h_1 + h_2)^3}{3!} \frac{\partial^3 F}{\partial Z^3} \\ &\quad + \frac{(h_1 + h_2)^4}{4!} \frac{\partial^4 F(Z)}{\partial Z^4} + O(h^5) \end{aligned} \quad (3.38)$$

where  $h_1$  is the distance to the neighbour point and  $h_2$  is the distance between the neighbour point and a further located point. The only requirement placed on the distances is that they be positive definite.

The discrete derivatives are expressed using a local formulation (see Fig. 3.6) at each control point

$$\left. \frac{\partial^d F(Z)}{\partial Z^d} \right|_i = a_{ww} F(Z_{i=ww}) + a_w F(Z_{i=w}) + a_p F(Z_{i=p}) + a_e F(Z_{i=e}) + a_{ee} F(Z_{i=ee}) \quad (3.39)$$

where  $p$  corresponds to the current point and  $ww, w, e, ee$  are west and east points, respectively.

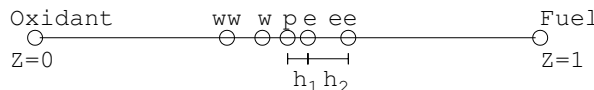


**Figure 3.6:** Mixture fraction space discretisation. The points used to create the discrete derivatives are also shown.

Expressing Eq. (3.38) in the form of Eq. (3.37) with a different coefficient for each considered point results in a system of equations which can be solved using a LU algorithm. 5-point stencils are used to represent the derivatives. For a uniform mesh

with  $h_1 = h_2$ , the 4th order centred approximation to first and second derivatives are

$$\begin{aligned}\frac{\partial F(Z)}{\partial Z} &= \frac{-F(Z+2h) + 8F(Z+h) - 8F(Z-h) + F(Z-2h)}{12h} + O(h^4) \\ \frac{\partial^2 F(Z)}{\partial Z^2} &= \frac{-F(Z+2h) + 16F(Z+h) - 30F(Z) + 16F(Z-h) - F(Z-2h)}{12h} + O(h^4)\end{aligned}\quad (3.40)$$

Boundary conditions are imposed as Dirichlet boundary conditions. At  $Z = 0$  and  $Z = 1$  oxidiser and fuel species and temperatures are set, respectively. Derivatives at points near the boundaries are computed using lower order approximations to the derivatives. Specifically, the first and last inner nodes are computed with second order centred approximations due to the reduced number of available points.

A numerical test comparing the numerical approximation against the analytical evaluation of a function derivatives has been performed to ascertain the order of accuracy of the method. The target function was  $f(Z) = Z^2 \cdot \exp(Z)$ . Fig. 3.7 shows the order of accuracy of the described numerical approximations to the derivative. Two sets of results for each derivative are shown, one with a constant step and a second one with different steps between all 5 points of the stencil. When a constant step is used, the accuracy is clearly 4th order for both first and 2nd derivatives. When variable stepping is introduced, first derivatives are also approximated with 4th order accuracy, although the points are more sparsely located. However, the second derivative approximation shows a diminution in the order of accuracy, lying between 3rd and 4th order. Nonetheless, it is expected that in usual applications, the method will usually be of 4th order for the 2nd derivative because when meshes are created, it is common practice to produce as smooth as possible transitions between nodes. It is even highly possible that meshes used are uniform in zones of interest with small transitions between them. Therefore, it is expected that this decrease in accuracy will have a small impact.

The resulting discrete set of reaction-diffusion equations are tightly coupled through the chemical reaction term and the summation terms involving the N species. Furthermore, the reaction term causes the resulting set of equations to be stiff due to the large range of characteristic scales involved. The analysis of the reaction matrix reveals eigenvalues with dissimilar values, requiring specific numerical methods to ensure stability of the method. If explicit methods were to be used, small time-steps would be required in order to ensure that the process falls within the region of stability of the numerical method. Therefore, implicit methods are usually preferred.

### Steady flamelet

The computation of the steady state solutions, which define the S-shaped curve previously described, requires evaluating a coupled system of equations defined by the N species equations plus the energy equation. The curve is composed by the solutions

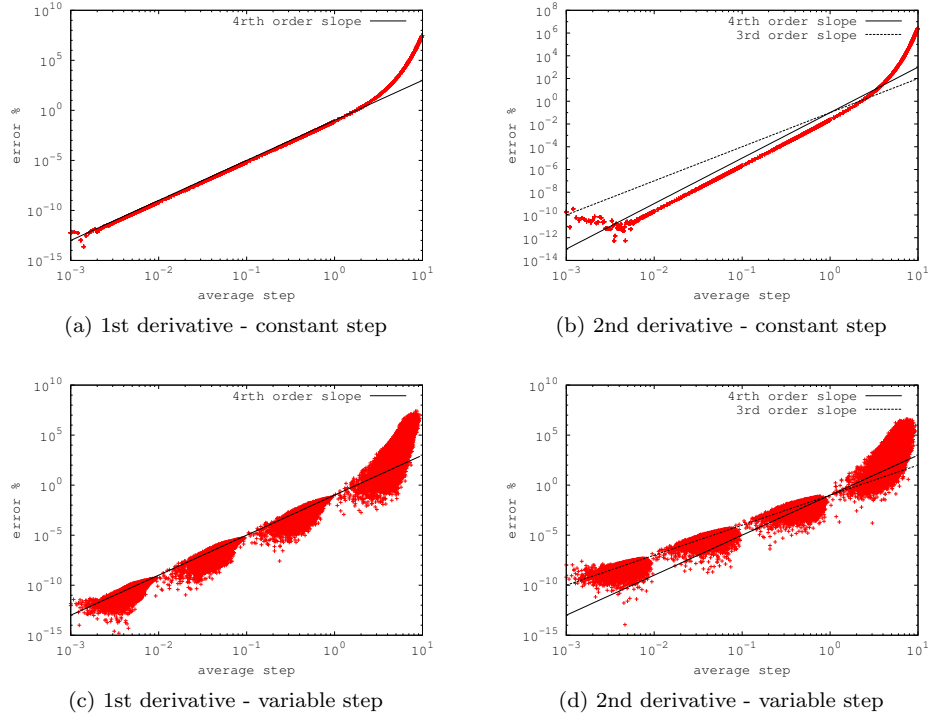


**Figure 3.7:** Comparison of numerical and analytical computation of first and second derivative of  $f(Z) = Z^2 \cdot \exp(Z)$ . Vertical axis shows the relative error and lines depict the order of accuracy. Results shown are evaluated at  $Z = 8.5$ .

of the flamelet equations at different stoichiometric scalar dissipation rates. Two solution procedures are applied to solve the set of equations. A Gauss-Seidel method, or more generally a Successive Over-Relaxation (SOR) method, and a Newton-Rapshon method.

The former is an iterative method which computes new values from known ones in an orderly fashion and updating the variables as they are computed. The method shows a slow convergence. However, it offers a simple approach to solve complex sets of equations. For the sake of simplicity, the flamelet equations in their Fickian form, Eq. (3.18), are taken. The equations are used in their steady state form and written in discrete form using Eq. (3.39)

$$-\frac{\rho\chi_Z}{2} \left( a_{ww}\phi_{ww} + a_w\phi_w + a_p\phi_p + a_e\phi_e + a_{ee}\phi_{ee} \right) = S \quad (3.41)$$

where  $\phi$  represents either mass fractions  $Y_k$  or temperature  $T$  and  $S$  represents the equation's source terms and additional terms. The Gauss-Seidel algorithm is depicted in Alg. 1.

```

repeat
    Compute transport coefficients  $D_Z, \lambda, c_p, \dots$ 
    Evaluate the chemical reaction terms  $\dot{w}_k$  and the heat release rate  $\dot{w}_k h_k$ 
    for  $k=0; k < N$  do
        for  $i=0; i < N_p$  do
            | Using Eq. (3.15a) (or Eq. (3.18a)) in their discrete form Eq. (3.41),
            | compute  $a_i$  and  $S$  using  $Y_k^n$  and  $T^n$ 
        end
        Solve a matrix equation for  $Y_k^*$ . A band diagonal solver is used.
    end
    for  $i=0; i < N_p$  do
        | Using Eq. (3.15b) (or Eq. (3.18b)) in their discrete form Eq. (3.41),
        | compute  $a_i$  and  $S$  using  $Y_k^n$  and  $T^n$ 
    end
    Solve a matrix equation for  $T^*$ . A band diagonal solver is used.
     $\phi^{new} = \phi^{old} + f_r(\phi^* - \phi^{old})$ 
    until  $|\frac{\phi^{new} - \phi^{old}}{\phi^{old}}| < \epsilon$  ;

```

**Algorithm 1:** Gauss Seidel - Successive Over-Relaxation (SOR) algorithms

The relaxation coefficient  $f_r$  appearing in the algorithm can be adjusted during the solution process to speed-up convergence or to ensure stability. For the present case due to the highly nonlinear reaction rate term, the relaxation coefficient usually takes small values, causing the convergence of the process to be slow. Currently, its value is constant and set at the beginning of the computations. The iterative process is carried out until a convergence criteria is met, usually specifying a relative variation  $\epsilon$  of the solution variables.

The second method, the Newton-Raphson method, requires also linearizing the equations. Furthermore, the calculation of the function derivative with respect to the solution variables, the Jacobi matrix, is required. Ideally, this would be performed analytically. However, in this case, as in many others, the derivatives have to be numerically evaluated, which introduces an additional layer of numerical errors to the method. Although it shows quadratic convergence, the method is not guaranteed to converge. Usually, a good first approximation to the solution is required by the method to converge fast or even to converge at all. The method applied to a univariate

function is expressed as

$$\phi^{n+1} = \phi^n - \frac{g^n(Z)}{\left(\frac{\partial g^n(Z)}{\partial Z}\right)} \quad (3.42)$$

where  $g(Z)$  stands for the function whose root is to be found.

Applying the Newton-Raphson to a set of  $N + 1$  equations with “spatial” dependence, discretised with  $N_p$  points, results in a matrix equation

$$\begin{bmatrix} Y_0 \\ \vdots \\ Y_k \\ \vdots \\ Y_{N-1} \\ T \end{bmatrix}_i^* = \begin{bmatrix} Y_0 \\ \vdots \\ Y_k \\ \vdots \\ Y_{N-1} \\ T \end{bmatrix}_i^n - J^{-1} \begin{bmatrix} EqY_0 \\ \vdots \\ EqY_k \\ \vdots \\ EqY_{N-1} \\ EqT \end{bmatrix}_i^n \quad (3.43)$$

where  $EqY_k$  and  $EqT$  have been used to represent the species and energy flamelet equations, Eq. (3.15) or Eq. (3.18) and  $i$  represents the control point. The Jacobian of the  $N_p$  points discrete set of equations is a matrix of  $N_p \times ((N + 1) \times (N + 1))$  entries. The matrix contains the derivatives of each equation with respect to all solution variables,  $Y_k$  and  $T$ . The matrix is numerically evaluated due to the presence of derivatives in Z-space and the presence of the reaction rate, for which it is difficult to compute a general analytic derivative. A sub-entry of the global matrix is as follows

$$J_{ij} = \begin{vmatrix} \frac{\partial EqY_0|_i}{\partial Y_0|_j} & \dots & \frac{\partial EqY_k|_i}{\partial Y_0|_j} & \dots & \frac{\partial EqY_{N-1}|_i}{\partial Y_0|_j} & \frac{\partial EqT|_i}{\partial Y_0|_j} \\ \vdots & \ddots & & & \vdots & \vdots \\ \frac{\partial EqY_0|_i}{\partial Y_\alpha|_j} & & \frac{\partial EqY_k|_i}{\partial Y_\alpha|_j} & & \frac{\partial EqT|_i}{\partial Y_\alpha|_j} & \vdots \\ \vdots & & \ddots & & \vdots & \vdots \\ \frac{\partial EqY_0|_i}{\partial T|_j} & \dots & \frac{\partial EqY_k|_i}{\partial T|_j} & \dots & \frac{\partial EqY_{N-1}|_i}{\partial T|_j} & \frac{\partial EqT|_i}{\partial T|_j} \end{vmatrix} \quad (3.44)$$

where  $J_{i,j}$  represents the Jacobian at point  $i$  with respect to variables at point  $j$ .  $\frac{\partial EqY_k|_i}{\partial Y_\alpha|_j}$  represents the variation of species  $Y_k$  equation evaluated at point  $i$  with respect to a perturbation in species  $Y_\alpha$  at point  $j$ . The global algorithm is detailed in Alg. 2.

```

repeat
    Compute transport coefficients  $D_Z, \lambda, c_p, \dots$ 
    Evaluate the chemical reaction terms  $\dot{w}_k$  and the heat release rate  $\dot{w}_k h_k$ 
    for  $i=0; i < N_p$  do
        for  $j=j_{min}; j < j_{max}$  do
            Compute the matrix entry  $J_{ij}$  as shown in Eq. (3.44) using  $Y_k^n$  and
             $T^n$ .
        end
    end
    Solve the global matrix equation Eq. (3.43)
     $\phi^{new} = \phi^{old} + f_r(\phi^* - \phi^{old})$ 
    until  $|\frac{\phi^{new} - \phi^{old}}{\phi^{old}}| < \epsilon$  ;

```

**Algorithm 2:** Newton-Raphson Algorithm

The matrix is mostly populated around the diagonal and up to a limited number of neighbouring points, mostly set by the numerical discretisation of the derivatives. Therefore, the matrix is stored in sparse form and the solution of the matrix equation is performed by a sparse LU. Similar to the iterative algorithm, the relaxation coefficient is set at the beginning of the computation and kept constant. Nonetheless, if the initial guess is adequate, the relaxation coefficient for the Newton-Raphson method can be set to higher values than in the Gauss-Seidel algorithm.

### Unsteady flamelet

Unsteady flamelets are evaluated at constant  $\chi_{st}$  beginning from solutions on the unstable steady branch of the S-shaped curve. Thus, to compute igniting solutions, a steady solution of the unstable branch is initially perturbed by slightly decreasing the stoichiometric scalar dissipation rate. With the perturbation, the flamelet enters the ignition region, which is located between the upper stable branch and the unstable steady branch. Hence, the flamelet transitions between both states. On the contrary, to compute extinguishing flamelets, the stoichiometric scalar dissipation rate is slightly increased, which in turn increases heat diffusion, and the flamelet transitions decreasing the thermal state down to the pure mixing line.

A special case is found for self-igniting mixtures which do not feature unstable steady solutions at low  $\chi_{st}$ . The transient process begins from the pure mixing line after an initial time delay, which is characteristic of the mixture.

Solution of the transient flamelet equations is performed using an Implicit/Explicit Runge-Kutta Scheme (IMEX RKC) [7, 35]. This method combines explicit evaluation of non-stiff methods with implicit solution of stiff terms. Specifically, diffusion terms are evaluated explicitly and the chemical reaction term is solved implicitly. The algorithm implements a family of second-order Runge-Kutta-Chebyshev methods.

Additionally, the scheme is self-starting and features a variable number of substeps. Furthermore, it selects a method that is both stable and efficient by dynamically adjusting the time-step and the number of stages per time-step. The  $s \geq 2$  substeps method with variable time-step  $\tau_n$  and  $n$  denoting the current time-step is

$$\begin{aligned}\Phi_0 &= \phi^n \\ \Phi_1 &= \Phi_0 + \tilde{\sigma}_1 \tau_n F_{E,0} + \tilde{\sigma}_1 \tau_n F_{I,1} \\ \Phi_r &= (1 - \sigma_r - v_r) \Phi_0 + \sigma_r \Phi_{r-1} + v_r \Phi_{r-2} + \tilde{\sigma}_r \tau_n F_{E,r-1} + \tilde{\gamma}_r \tau_n F_{E,0} \\ &\quad + [\tilde{\gamma}_r - (1 - \sigma_r - v_r) \tilde{\sigma}_1] \tau_n F_{I,0} - v_r \tilde{\sigma}_1 \tau_n F_{I,r-2} + \tilde{\sigma}_1 \tau_n F_{I,r} \\ \phi^{n+1} &= \Phi_s\end{aligned}\quad (3.45)$$

for  $r = [2, s]$ , where subindexs  $E$  and  $I$  denote the explicit and implicit evaluated terms, respectively. The coefficients can all be analytically evaluated

$$\begin{aligned}\tilde{\sigma}_1 &= b_1 \omega_1 \\ \sigma_r &= \frac{2b_r \omega_0}{b_{r-1}}, \quad v_r = \frac{-b_r}{b_{r-2}}, \quad \tilde{\sigma}_r = \frac{2b_r \omega_1}{b_{r-1}}, \quad \tilde{\gamma}_r = -\left(1 - b_{r-1} T_{r-1}(\omega_0)\right) \tilde{\sigma}_r\end{aligned}\quad (3.46a)$$

$$\begin{aligned}b_0 &= \frac{1}{4\omega_0^2}, \quad b_1 = \frac{1}{\omega_0}, \quad b_r = \frac{T_r''(\omega_0)}{(T_r'(\omega_0))^2}, \quad r = 2..s \\ \omega_0 &= 1 + \frac{\varepsilon}{s^2} \quad \omega_1 = \frac{T_s'(\omega_0)}{T_s''(\omega_0)}\end{aligned}\quad (3.46b)$$

where  $\varepsilon = 2/13$  is a coefficient to introduce some damping in the explicit part of the temporal algorithm. The  $T_r$  terms are the Chebyshev polynomials of the first kind and degree  $r$  and  $T_r'$  and  $T_r''$  its derivatives. For arguments  $\omega_0 > 1$  they take the form

$$T_r(\omega_0) = \cosh\left(r \operatorname{arccosh}(\omega_0)\right) = \cosh\left(r \ln\left(\omega_0 + \sqrt{\omega_0^2 - 1}\right)\right) \quad (3.47)$$

Alternatively, these coefficients, and their derivatives, can be computed through Chebyshev recursion

$$\begin{aligned}T_0(x) &= 1, & T_1(x) &= x, & T_r(x) &= 2xT_{r-1}(x) - T_{r-2}(x), & 2 \geq r \geq s \\ T'_0(x) &= 0, & T'_1(x) &= 1, & (1 - x^2)T'_r(x) &= -rxT_r(x) + rT_{r-1}(x) \\ T''_0(x) &= 0, & T''_1(x) &= 0, & T''_r(x) &= 2xT''_{r-1}(x) + 4T'_{r-1}(x) - T''_{r-2}(x)\end{aligned}\quad (3.48)$$

At each substep an implicit equation has to be solved at each mesh point. Rearranging the terms of each substep, the equation to be solved has the same functional form as in Backward Differentiation Schemes

$$\Phi_r - \tilde{\sigma}_1 \tau_n F_{I,r}(\Phi_r) = V_r \quad (3.49)$$

where  $V_r$  represents all explicit terms, and the implicit terms evaluated at previous substeps in Eq. (3.45). This equation is solved at each mesh point, uncoupled from its neighbours. A Newton method is here used, which is akin to the one presented for the steady case. The difference is that in the present case the matrix does not involve the whole set of points but it is used at each control point independently.

The method offers a procedure to evaluate the time-step based on an analysis of the local truncation error. The time-step is set to meet the user-specified absolute and relative tolerances. For the present case the absolute one is set to  $atol = 10^{-10}$  and the relative one to  $rtol = 10^{-5}$ . The local error is computed at each control point  $i$  out of  $N_p$  control points as the Euclidean norm of the  $N+1$  equations ( $N$  species and the temperature)

$$err_i = \sum_{k=1}^{N+1} \left( \frac{Est_{n+1,i}^k}{atol + rtol \cdot \max(\phi_{n,i}^k, \phi_{n+1,i}^k)} \right) \quad (3.50)$$

where the error estimate for each equation is computed through

$$(I - \tau_n F'_{I,n}) Est_{n+1} = \frac{1}{2} \tau_n (F_{n+1} - F_n) + \tau_n \tilde{\sigma}_1 (F_{I,n+1} - F_{I,n}) \quad (3.51)$$

The global error is then computed by taking the rms norm

$$\|Est_{n+1}\| = \sqrt{\frac{1}{N_p} \sum_{i=0}^{N_p-1} err_i} \quad (3.52)$$

Then, if  $\|Est_{n+1}\| \leq 1$  the current step is accepted and the next time step is computed through

$$\begin{aligned} \tau_{new} &= \min(10, \max(0.1, fac)) \tau_n \\ fac &= 0.8 \left( \frac{\|Est_n\|^{1/2}}{\|Est_{n+1}\|^{1/2}} \frac{\tau_n}{\tau_{n-1}} \right) \frac{1}{\|Est_{n+1}\|^{1/2}} \end{aligned} \quad (3.53)$$

### Radiation flamelet

The radiation flamelet subspace is computed using the transient algorithm presented previously. The main difference lays on the procedure. If transient igniting and extinguishing flamelets were previously computed, now only extinguishing flamelets are evaluated. Furthermore, the transient process starts from the upper stable burning branch of the S-shaped curve. Then, extinguishing flamelets are computed due to radiation heat losses. Radiation is modelled using the Optically Thin Method (OTM).

### 3.3.2 Flamelet solutions

#### Steady Flamelets

Different sets of solutions are obtained from the three procedures described in the previous subsection. Solutions of the steady state flamelet equations define the S-shaped curve, such as the ones shown in Fig. 3.2 or Fig. 3.4. These curves represent a collection of solutions computed at different  $\chi_{st}$ . Results for a methane/hydrogen flamelet at two stoichiometric scalar dissipation rates are shown in Fig. 3.3.

#### Unsteady Flamelets

Focusing on unsteady flamelets, the transient algorithm previously described allows computing the ignition or extinction process of a flamelet, also at a constant scalar dissipation rate. Hence, as described, transient flamelet computations start with a slightly perturbed solution of the unstable branch. Fig. 3.8 shows the evolution at one  $\chi_{st}$ , depicting the change in shape of the temperature of a flamelet during an ignition and extinction process. All these intermediate flamelets, between the unstable and stable branches, are represented in the S-shaped curve as points, parametrised by their stoichiometric temperature  $T_{st}$  and scalar dissipation rate  $\chi_{st}$ .

#### Radiation Flamelets

Similar to the unsteady flamelets, radiation flamelets are computed through unsteady simulations at constant  $\chi_{st}$ . However, the initial solution for these cases is a flamelet solution located at the stable branch. Then, the process involves the decrease in the thermal state due to radiation heat losses. The radiation flamelet subspace is shown in Fig. 3.5 by the region with crosses. Fig. 3.9 shows the transient temperature and enthalpy decrease due to radiation heat losses at a constant  $\chi_{st}$ .

## 3.4 Flamelets in turbulent flows

The flamelet model presented can readily be applied to laminar flames and to turbulent flames when performing Direct Numerical Simulations (DNS). However, due to the large computational requirements of DNS, Large Eddy Simulations (LES) or Reynolds-Averaged Navier Stokes (RANS) are typically used to model turbulent flames. Nevertheless, in LES or RANS models solution variables are spatially or temporally filtered quantities, respectively. Therefore, the state relations detailed previously have to be restated in terms of statistical quantities. In stochastic methods turbulent fluctuating quantities are described through their statistical distribution [2, 8], which can be defined as the probability  $p$  of finding a value  $\phi < \Phi$

$$F_\phi = p(\phi < \Phi) \quad (3.54)$$

where  $\Phi$  is the sample space associated with the random variable  $\phi$ . The former consists of all possible realisations of  $\phi$ . The probability density function (*pdf*), being

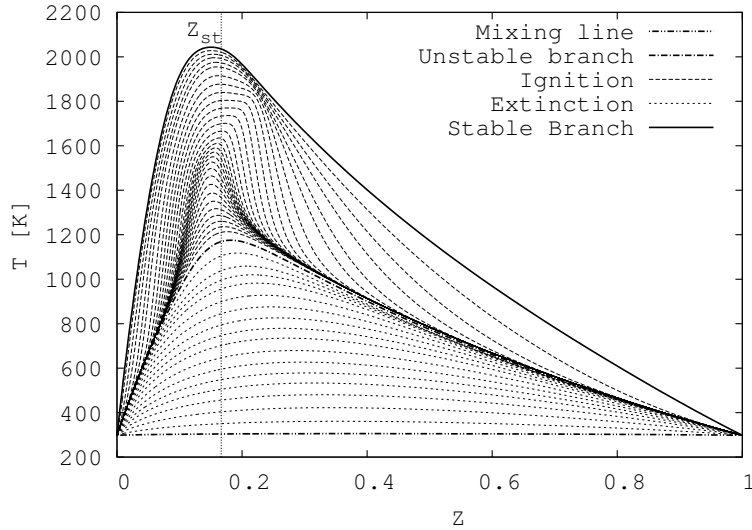


**Figure 3.8:** Transient flamelet in mixture fraction space for a methane/air diffusion flame [16], corresponding to the vertical lines in Fig. 3.2a at  $\chi_{st} = 10$ . Differential diffusion was included during the computations. The transient process begins at the unstable branch for both igniting and extinguishing processes. The vertical line depicts the stoichiometric mixture fraction  $Z_{st}$  for this flame.

the probability of finding  $\phi$  between a certain interval  $\Phi_- < \phi < \Phi_+$ , is defined as

$$P_\phi(\Phi) = \frac{dF_\phi(\Phi)}{d\Phi} \quad (3.55)$$

Integration of the latter expression over all possible realisations, or equivalently stating the certainty of an event, is

$$\int_{-\infty}^{+\infty} P_\phi(\Phi) d\Phi = 1 \quad (3.56)$$

which also serves as a normalising criteria for the *pdf*. The method just described applied to CFD cases results in a *pdf* with temporal and spatial dependence,  $P_\phi(\Phi) \rightarrow P_\phi(\Phi; x_i, t)$ , indicating that the *pdf* is a function in  $\Phi$  space at each location in space and time. In the following, for the sake of simplicity, no distinction is made between  $\phi$  and  $\Phi$ . Therefore,  $P_\phi(\Phi; x_i, t) \rightarrow P_\phi(\phi; x_i, t)$ . With the statistical description of fluctuating quantities, different moments can be defined. Of main interest are the

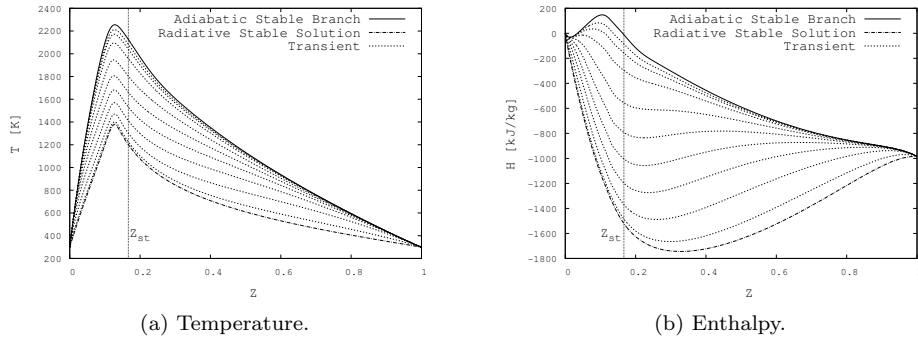


**Figure 3.9:** Radiation flamelet in mixture fraction space for a methane/air diffusion flame [16], corresponding to crosses in Fig. 3.5 at  $\chi_{st} = 0.1$ . Flamelets computed with differential diffusion included. The transient process begins at the stable branch. The vertical line indicates the location of the stoichiometric mixture fraction  $Z_{st}$  for this flame.

first moment or mean, and the second central moment or variance,

$$\bar{\phi}(x_i, t) = \int_{-\infty}^{+\infty} \phi P_\phi(\phi; x_i, t) d\phi \quad (3.57)$$

$$\overline{(\phi(x_i, t) - \bar{\phi}(x_i, t))^2} = \overline{\phi'^2} = \phi_v = \int_{-\infty}^{+\infty} (\phi - \bar{\phi})^2 P_\phi(\phi; x_i, t) d\phi \quad (3.58)$$

The variance of a statistical distribution is related to the first  $\bar{\phi}$  and second  $\overline{\phi^2}$  moments [36]

$$\phi_v = \overline{\phi^2} - \bar{\phi}^2 \quad (3.59)$$

Focusing on the Navier-Stokes equations, its description involves a coupled solution of pressure and velocities. Hence, there is a correlation among them, which can be described through a probability distribution. Specifically, the probability distribution is described through a joint probability density function,  $P(\phi, \psi; x_i, t)$ . Hence, the *pdf* of  $\phi$ , denoted as the marginal *pdf* of  $\phi$ , is the probability of  $\phi$  over all possible realisations of  $\psi$

$$P_\phi(\Phi) = \int_{-\infty}^{+\infty} P(\phi, \psi; x_i, t) d\psi \quad (3.60)$$

Additionally, Baye's theorem states that any joint *pdf* of two independent variables can be written as the product of a conditional *pdf* of one variable and a marginal *pdf*

of the other

$$P(\phi, \psi; x_i, t) = P(\phi|\psi; x_i, t)P(\psi; x_i, t) \quad (3.61)$$

Furthermore, if the variables are not correlated and can be considered statistically independent, their joint *pdf* becomes the product of the marginal *pdfs*

$$P(\phi, \psi; x_i, t) = P(\phi; x_i, t)P(\psi; x_i, t) \quad (3.62)$$

Hence, the interest in previous sections in finding independent parameters for the flamelet database.

A special case of interest are flows with large density changes, where the density appears in most of the terms of the transport equations. Thus, a further variable is introduced in the correlations. In order to reduce the complexity of the filtered transport equations, a density weighted average is introduced, denoted as Favre average, and defined as

$$\overline{\rho\phi} = \overline{\rho}\widetilde{\phi} \quad (3.63)$$

which leads to

$$\overline{\rho\phi\psi} = \overline{\rho}\overline{\phi}\overline{\psi} = \overline{\rho}\widetilde{\phi}\widetilde{\psi} + \overline{\rho}\widetilde{\phi'}\widetilde{\psi'} \quad (3.64)$$

where  $\phi'$  and  $\psi'$  are fluctuations. With this approach density fluctuations do not appear and the expression has the same structure as in incompressible flows  $\overline{\phi\psi} = \overline{\phi}\overline{\psi} + \overline{\phi'}\overline{\psi'}$ . However, it must be remembered that Favre filtered quantities are mass averaged quantities. Returning to the statistical representation of fluctuating quantities, the joint Favre *pdf* becomes

$$\widetilde{\phi} = \int_{-\infty}^{+\infty} \phi \widetilde{P}(\phi) d\phi \quad (3.65)$$

where the statistical distribution  $\widetilde{P}(\phi)$  is now Favre weighted. The density weighted *pdf* can be related to the unweighted one [2]

$$\overline{\rho P}(\phi) = \overline{\rho}\widetilde{P}(\phi) \quad (3.66)$$

At this point, two paths can be taken. Either the *pdf* is computed at every point through a balance equation or the shape of the *pdf* is presumed. The former approach is the focus of *pdf* transport models [8, 37]. The latter approach is usually used in moments methods. Although the first represents a very general statistical description of turbulent reacting flows, since it does not require closure for the chemical source term, it is a computationally demanding model, which limits its applicability. The reader is referred to [1, 8] and references therein for more details. In the following the discussion is centred around the presumed *pdf* approach.

The EoS defined in the previous section for the different variants of the flamelet model, Eq. (3.28), (3.29) and (3.31), can be expressed in terms of their *pdf*. Any thermochemical quantity, excepting the density, can be represented as

$$\tilde{\phi} = \int_Z \int_{\Lambda} \int_{\Xi} \zeta_{\phi}(Z, \Lambda, \Xi) \tilde{P}(Z, \Lambda, \Xi) dZ d\Lambda d\Xi \quad (3.67)$$

where  $\Xi$  has been used to represent either  $\chi_{st}$  or  $H$  in the UFPV and RFPV models, respectively. In the SFPV model this dependence is dropped. Regarding the density, since density weighting is being considered, the Favre average of  $\rho^{-1}$  has to be computed

$$\bar{\rho}^{-1} = \int_Z \int_{\Lambda} \int_{\Xi} \frac{1}{\zeta_{\rho}(Z, \Lambda, \Xi)} \tilde{P}(Z, \Lambda, \Xi) dZ d\Lambda d\Xi \quad (3.68)$$

There is no general *pdf* function to describe the statistical distribution  $\tilde{P}(Z, \Lambda, \Xi)$  in the latter equation. However, applying Baye's theorem, the *pdf* could be split into a product of the marginal *pdf* of  $Z$  and a conditional *pdf*

$$\tilde{P}(Z, \Lambda, \Xi) = \tilde{P}(Z) P(\{\Lambda, \Xi\}|Z) \quad (3.69)$$

Furthermore, under the assumption of statistical independence between the different variables conforming the *pdf*, certain presumed functions have been successfully used. Hence, the joint *pdf* becomes the product of the marginal *pdf*s

$$\tilde{\phi} = \int_Z \int_{\Lambda} \int_{\Xi} \zeta_{\phi}(Z, \Lambda, \Xi) \tilde{P}(Z) P(\Lambda) P(\Xi) dZ d\Lambda d\Xi \quad (3.70)$$

The discussion in preceding sections concerning the need of defining the different parameters independently from each other is now evident. In the following, different *pdf* used for the mixture fraction, the progress-variable, the stoichiometric scalar dissipation rate and enthalpy are presented. Although the *pdf* has been stated using the progress-variable parameter, after the integration, a variable change is performed to restate the database as a function of the progress-variable. Similarly, since the scalar dissipation rate is defined using a functional form which depends on the mixture fraction, the use of the stoichiometric scalar dissipation rate removes this dependence.

Several authors have shown that the residual *pdf* of a conserved scalar can reasonably be approximated by a beta distribution [1, 2, 38]. The weighted *pdf* for the mixture fraction is then the  $\beta$ -*pdf*

$$\tilde{P}(Z; x_i, t) = \tilde{\beta}(Z; x_i, t) = \frac{1}{B(a, b)} Z^{a-1} (1-Z)^{b-1} = \frac{\Gamma(a+b)}{\Gamma(a) + \Gamma(b)} Z^{a-1} (1-Z)^{b-1} \quad (3.71)$$

where  $B(a, b)$  is a normalising factor and  $\Gamma(x)$  is the gamma function, defined as,

$$\begin{aligned} B(a, b) &= \int_0^1 Z^{a-1}(1-Z)^{b-1} dZ \\ \Gamma(x) &= \int_0^\infty e^{-t} t^{x-1} dt \end{aligned} \quad (3.72)$$

Using the definition of the Favre mean mixture fraction  $\tilde{Z}$  and Favre mixture fraction variance  $Z_v$ ,

$$\begin{aligned} \tilde{Z} &= \int_0^1 Z \tilde{\beta}(Z) dZ \\ Z_v &= \int_0^1 (Z - \tilde{Z})^2 \tilde{\beta}(Z) dZ \end{aligned} \quad (3.73)$$

the two parameters  $a$  and  $b$  of the  $\beta$ -pdf are determined

$$\begin{aligned} a &= \tilde{Z}\gamma \quad ; \quad b = (1 - \tilde{Z})\gamma \\ \gamma &= \frac{\tilde{Z}(1 - \tilde{Z})}{Z_v} - 1 \geq 0 \end{aligned} \quad (3.74)$$

where the latter explicitly states the range of values that the variance can take  $Z_v = [0, 0.25]$ .

The main advantage of the  $\beta$ -pdf is its capacity on changing continuously from one or two peak shapes to Gaussian shapes, as shown in Fig. 3.10. The  $\beta$ -pdf takes four characteristic shapes depending on the level of fluctuations and the mean value. Region I represents strong fluctuations occurring at any point of the domain. This region has two singularities at the boundaries. Oppositely, Region III represents situations of low fluctuations at any mixture fraction. Regions II and IV represent situations of strong fluctuations near  $Z=0$  and  $Z=1$ , respectively. They present singularities at their respective the boundaries.

In order to overcome the singularities near  $Z = 0$  (pure oxidiser) or  $Z = 1$  (pure fuel) boundaries, Liu et al [38] proposed a numerical integration method to remove the function singularities at  $Z$  extremes

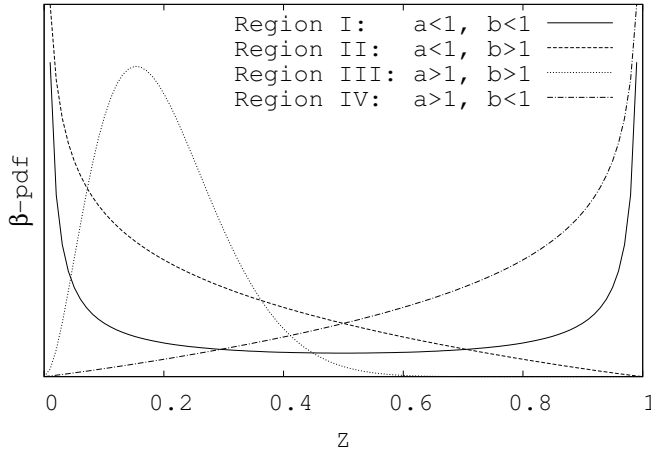


**Figure 3.10:** Representative shapes of the  $\beta$ -pdf as a function of  $a$  and  $b$ .

$$\begin{aligned}
 & \int_0^1 \phi(Z) Z^{a-1} (1-Z)^{b-1} dZ = \\
 & \int_0^\varepsilon \phi(Z) Z^{a-1} (1-Z)^{b-1} dZ + \int_\varepsilon^{1-\varepsilon} \phi(Z) Z^{a-1} (1-Z)^{b-1} dZ + \int_{1-\varepsilon}^1 \phi(Z) Z^{a-1} (1-Z)^{b-1} dZ \\
 & \approx \phi_{ox} \frac{\varepsilon^a}{a} + \int_\varepsilon^{1-\varepsilon} \phi(Z) Z^{a-1} (1-Z)^{b-1} dZ + \phi_{fu} \frac{\varepsilon^b}{b}
 \end{aligned} \tag{3.75}$$

where  $\varepsilon$  is a small parameter. Furthermore, in that study it was investigated the effect of applying the  $\beta$ -pdf to the unweighted pdf instead of the weighted pdf. It was found that applying the  $\beta$ -pdf to the mass-weighted pdf resulted in lower densities, which were in better agreement with a semi-analytical method. Furthermore, the study simulated a turbulent jet flame and the lower predicted densities resulted in a jet with a longer penetration into the flow compared to results when the  $\beta$ -pdf was applied to the unweighted pdf.

Regarding the other quantities, progress-variable, scalar dissipation rate and enthalpy, usually a  $\delta$ -pdf is employed, which implies that the flamelet state can be

uniquely characterised by the filtered, or mean, value

$$P(\Xi; x_i, t) = \delta(\Xi = \Xi_0) \quad (3.76)$$

Thus, fluctuations at the subfilter level are neglected. Nonetheless, in the literature different presumed *pdf* have been proposed for the progress-variable and the scalar dissipation rate. For the enthalpy, or alternatively the enthalpy loss, it has been mainly modelled using a  $\delta - \text{pdf}$ .

Regarding the progress-variable, it has been usually argued that a presumed *pdf* cannot be easily specified for several reasons [9]: i) its actual shape is multi-modal, ii) turbulence-chemistry interactions influence the shape of the *pdf* and iii) higher moment information is usually required. Therefore, the  $\delta - \text{pdf}$  has been usually chosen. Alternatives are (clipped) Gaussian functions, the beta distribution or the Statistically Most-Likely Distribution (SLMD) proposed by Ihme et al. [9]. These have been applied to different flames with different degrees of success. Specifically, the SLMD has been reported to offer a more accurate representation of the complex *pdf* shape of the progress-variable once higher moments were accounted for. From analysis of DNS data, it was reported that the SLMD improved marginally the results compared to the  $\beta - \text{pdf}$ . Thus, reinforcing the previous arguments. However, the *pdf* computed by the SLMD was in better agreement than the  $\beta - \text{pdf}$ . Furthermore, when higher moments were included the SLMD was in better agreement with the reference data.

Concerning the scalar dissipation rate, besides the  $\delta - \text{pdf}$  [6], in the context of the classical flamelet a log normal distribution was also proposed [1, 39]. Nonetheless, in the present thesis the former approach is taken.

The scalar dissipation rate is computed during CFD simulations. However, the database parameter is the stoichiometric scalar dissipation rate. Therefore, to relate both quantities the application of the  $\beta - \text{pdf}$  to the conditional scalar dissipation rate Eq. (3.20) which results in

$$\widetilde{\chi}_Z = \widetilde{\chi}_{st} \int_0^1 \frac{f(Z)}{f(Z_{st})} \widetilde{\beta}(Z) dZ \quad (3.77)$$

Summarising, using the defined *pdf*, turbulent fluctuating quantities are obtained through

$$\widetilde{\phi} = \int_Z \int_\Lambda \int_\Xi \zeta_\phi(Z, \Lambda, \Xi) \widetilde{\beta}(Z; \widetilde{Z}, Z_v) \delta(\Lambda = \Lambda^*) \delta(\Xi = \Xi^*) dZ d\Lambda d\Xi \quad (3.78)$$

where a  $\beta - \text{pdf}$  is used for the mixture fraction and  $\delta - \text{pdf}$ s are presumed for the other variables, either progress-variable, stoichiometric scalar dissipation rate or enthalpy.

Hence, the EoS of the different variants of the FPV model read, once the appropriate variable changes have been applied,

$$\tilde{\phi} = \{\tilde{\rho}, \tilde{w}_c, \tilde{D}_Z, \dots\} = \tilde{F}_\phi^{SF PV}(\tilde{Z}, Z_v, \tilde{c}) \quad (3.79a)$$

$$\tilde{\phi} = \{\tilde{\rho}, \tilde{w}_c, \tilde{D}_Z, \dots\} = \tilde{F}_\phi^{UF PV}(\tilde{Z}, Z_v, \tilde{c}, \chi_{st}) \quad (3.79b)$$

$$\tilde{\phi} = \{\tilde{\rho}, \tilde{w}_c, \tilde{D}_Z, \dots\} = \tilde{F}_\phi^{RF PV}(\tilde{Z}, Z_v, \tilde{c}, \tilde{h}) \quad (3.79c)$$

Therefore, in order to retrieve thermochemical quantities from the database the different parameters have to be computed during CFD simulations. Both filtered mixture fraction  $\tilde{Z}$  and filtered progress-variable  $\tilde{c}$  are directly obtained from their transport equations. Similarly, the enthalpy is computed from the energy transport equation. Two derived quantities remain, the mixture fraction variance and the (stoichiometric) scalar dissipation rate. *Chapter 5* focuses on modelling these two quantities, which characterise the mixing state at the subfilter level. Several models are presented and their effect in the prediction of turbulent diffusion flames analysed. Particularly, four models are studied. First, a local equilibrium assumption model (LEA) [40, 41], where production and destruction of variance at the subgrid level is assumed to cancel out. Second, a variance transport equation (VTE) [36, 42] and, third, a transport equation for the second moment transport  $\tilde{Z}^2$  (STE) [43]. The last two models require closure for the subfilter scalar dissipation rate, which is performed either using a turbulent time-scale [36, 42, 44] or modelling the filtered squared mixture fraction gradient  $\widetilde{|\nabla Z|^2}$  [43].

### 3.4.1 Radiation and NOx in turbulent flows

A further issue to consider when using the radiation database and the NOx model is the closure of the radiation-turbulence interactions and the filtering of the NO reaction rate, respectively. Regarding radiation, despite the theoretical and experimental evidence of Turbulence-Radiation Interactions (TRI) found in many publications [28, 45–47], the common approach is to neglect this influence. The main reason is the computational cost required to account for the interactions. Therefore, in the current thesis the filtered radiation heat losses are computed through the OTM model using the filtered temperature

$$\widetilde{\dot{q}^R} \approx 4\sigma \left( \widetilde{T}^4 \sum_{k=1}^N (\widetilde{p}_k k_{P_k}) - T_s^4 \sum_{k=1}^N (\widetilde{p}_k k_{I_k}) \right) \quad (3.80)$$

which neglects cross-correlations between temperature, species partial pressures and radiative properties. The background temperature  $T_s$  has no spatial dependence.

Analogously, the NOx reaction rate is filtered and only leading terms are kept

$$\overline{\dot{w}_{NO}} = \overline{\dot{w}_{NO}^+} + \overline{\frac{Y_{NO}}{Y_{NO}^{RPFV}} \dot{w}_{NO}^-} \approx \overline{\dot{w}_{NO}^+} + \overline{\frac{\tilde{Y}_{NO}}{\tilde{Y}_{NO}^{RPFV}} \dot{w}_{NO}^-} \quad (3.81)$$

where  $\overline{\dot{w}_{NO}^+}$  and  $\overline{\dot{w}_{NO}^-}$  are integrated using Eq. (3.78).

### 3.5 Database for CFD

The previous sections were focused on the theoretical background of the flamelet model and the generation of a database containing the solutions of the flamelet equations in mixture fraction space. The set of parameters to be used has been shown to be dependent on the target subspace to be represented. Additionally, the database and its parameters have been extended to describe stochastic processes, namely turbulent flows. With this framework, the flamelet model is readily applicable in CFD cases.

The model is used in two stages, a preprocessing one and during the actual CFD simulations. In the former, the flamelet equations are previously solved. The process is outlined in Fig. 3.11. First, steady solutions are computed using either Gauss-Seidel or Newton-Raphson methods, Sec. 3.3.1. If the unsteady flamelet is considered, once the solutions defining the S-shaped curve are calculated, transient flamelets are computed using the IMEX RKC algorithm, as described in Sec. 3.3.1. Alternatively, if radiation heat losses are to be accounted for, transient flamelets beginning from steady stable burning flamelet solutions are computed, as described in Sec. 3.3.1. Then, if the case of interest is laminar, a database using deterministic, or laminar, parameters is generated. Either steady Eq. (3.28), unsteady Eq. (3.29) and radiation Eq. (3.31) databases are created and loaded at the beginning of CFD simulations. Should the target problem be of turbulent nature, the previous databases have to be set as a function of stochastic parameters, as described in Sec. 3.4. A  $\beta - pdf$  is used to describe the mixture fraction and  $\delta - pdfs$  are applied to the other parameters. After the integration, Eq. (3.78), databases are stored for either steady Eq. (3.79a), unsteady Eq. (3.79b) or radiation Eq. (3.79c) flamelet calculations.

In order to build the databases, the different parameters must be discretised taking into account its later use. During CFD simulations, in order to reduce the operations and their complexity, linear interpolations are used. Therefore, it is important to refine in the regions of high gradients, which are mainly located near the stoichiometric mixture fraction. Analogously, the mixture fraction variance is refined close to its null boundary, since high values of the variance result in lower gradients. Both progress-variable and enthalpy are mostly uniformly distributed since their profiles at different mixture fractions varies greatly. Nonetheless, refinements can be made if common

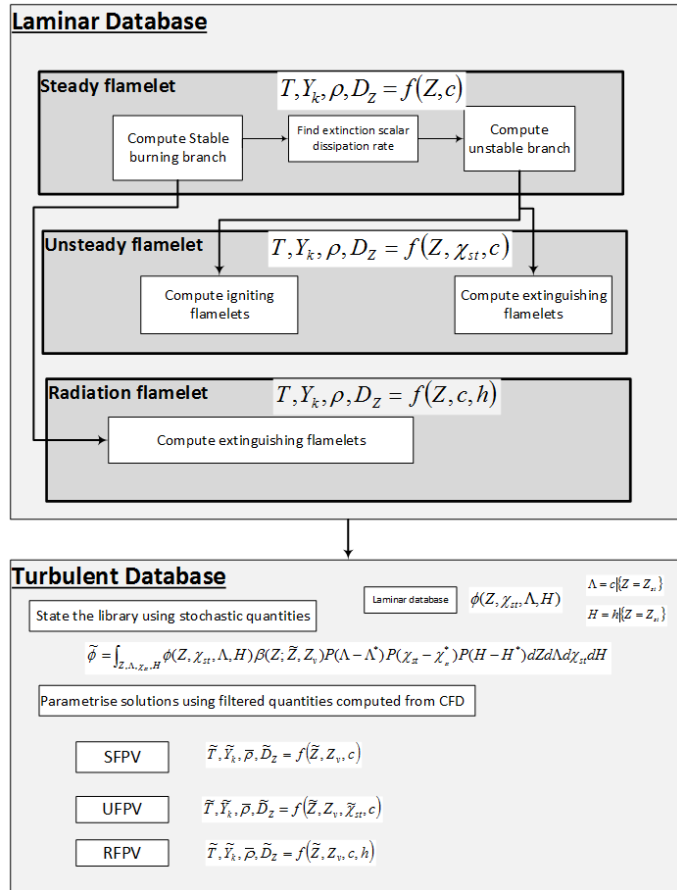


Figure 3.11: Flamelet database creation.

trends are detected, such as solutions being concentrated around specific values of the progress-variable.

Another issue to consider is the limits of the discretisation. The mixture fraction is by definition bounded, ranging between 0 and 1. The mixture fraction variance is also bounded. However, its upper value is variable,  $Z_v^{max}(Z) = Z(1 - Z)$ . Therefore, the unmixedness, or normalized variance,  $Z_v(Z)/(Z_v^{max}(Z))$  is used instead of the variance. The progress variable is only partially bounded. The lower bound corresponds to the pure mixing line solution. However, the upper value depends on the stable burning solution. Hence, a similar approach as for the mixture fraction variance is

adopted, where instead of using a dimensional progress-variable, a non-dimensional one is used. Similarly, the enthalpy discretisation is also expressed in non-dimensional terms. The last parameter to consider is the scalar dissipation rate. Since flamelets are computed at constant  $\chi_{st}$ , the straightforward discretisation is to use values equal to the computed flamelets. Hence, if five different transient flamelets are computed, those five  $\chi_{st}$  are used as discretisation.

The chosen form for the database parameters is motivated by the need of minimising the computational cost of data retrieval. Different decisions were taken during the definition of the database computational infrastructure. First, taking into account that the number of parameters  $N_p$  grows with the complexity of the considered model, the first choice was to impose that each parameter would be uniquely discretised. This restriction implies that only  $N_p$  searches would be required. Otherwise, interpreting the data search as a binary tree, as depicted in Fig. 3.12, the number of searches, or data interpolations, grows as  $2^{N_p} - 1$ . Hence, a one dimensional (1D) array requires one search, a 2D table results in 3 searches, a 3D table involves 7 searches, etc.

The cost increase with the number of parameters easily becomes computationally expensive. Thus, the unique discretisation per parameter was chosen. However, as stated, each variable has difference ranges. For example, the mixture fraction variance maximum value is a function of the mixture fraction. Therefore, two possibilities were considered; either set the range for each variable to its maximum possible range or use non-dimensional ranges.

The former approach required that some entries of the database to be empty. Furthermore, during the interpolations the actual range for each parameter would have to be checked in order to perform the interpolations between valid points. For example, the mixture fraction variance at  $Z = 0.1$  would span up to  $Z_v^{max} = 0.25$ , although its maximum value is  $Z_v^{max}(Z = 0.1) = 0.09$ . Nonetheless, this range limitation could be easily enforced through computational code, where “non-physical” entries could be made to point to the last “physical” entry. However, addition of subsequent parameters into the database and further interpolations become more complex. Furthermore, it implies that for a given number of points, not all of them would be used. For example, for small values of the mixture fraction, with corresponding small ranges of the mixture fraction variance, the number of used points would also be small.

Alternatively, use of non-dimensional parameters results in a database with well defined parameter extremes and without any useless points. In addition, it avoids the issue of variable ranges for subsequent parameters. However, this approach does not fully overcome the problem of different ranges because for each secondary parameter, prior to performing any interpolation, the input parameter has to be made non-dimensional. This, in turn, introduces a further operation prior to the actual search.

The second approach has been preferred because it results in a higher database accuracy compared to the first one, although it requires a small increase in operations.

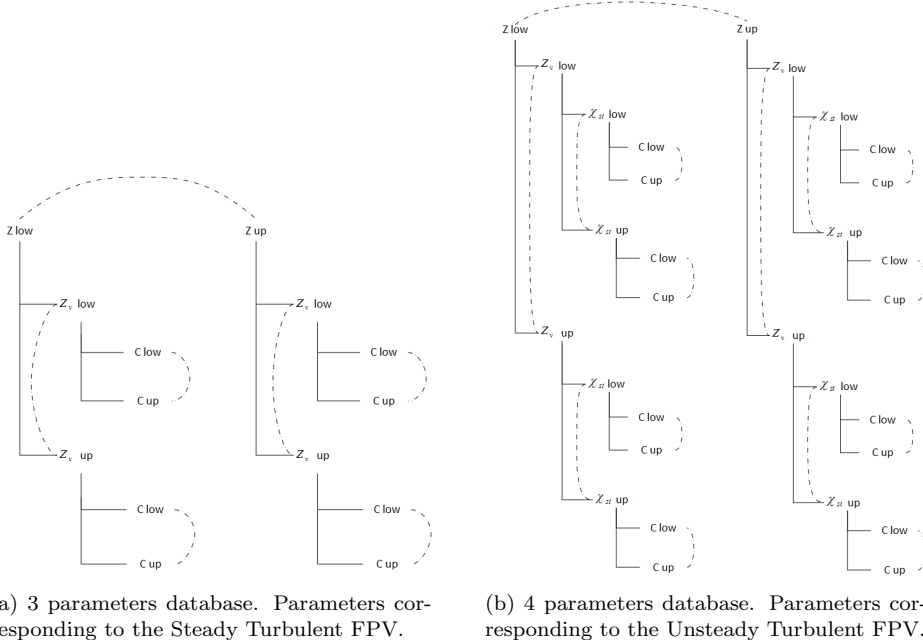


**Figure 3.12:** Binary search tree for databases with two different number of parameters. Solid lines indicate dimension dependence and dot-dashed lines indicate interpolation operations. If the discretisation of each parameter is not unique, then prior to the interpolation operation a search has to be performed, which increases the computational cost.

Alternative database set ups could also be considered. For example, since the database is made up of several flamelet solutions, interpolation methods for scattered data could be considered, such as radial basis functions [48, 49]. However, these methods require a matrix vector multiplication for each variable to be interpolated, involving a large number of points. Per contra, with the current approach, once the database entry for a set of parameters has been found, the cost increase for retrieving an additional quantity is marginal.

Concerning the discretisation, and specifically in turbulent cases, the FPV variant with the lowest dimensionality is the steady FPV model, which uses three parameters, the mixture fraction, its variance and the progress-variable. They are usually discretised using  $100 \times 25 \times 100$  points, respectively, leading to a database with  $2,5 \cdot 10^5$  entries. This figure is to be multiplied by the number of variables to be stored. Regarding the unsteady FPV variant, the database contains an additional parameter,

the stoichiometric scalar dissipation rate. Assuming that between 10 and 20 different transient flamelets are included, the number of entries increases to 2–5 millions per stored variable. Concerning the radiation FPV, instead of using  $\chi_{st}$ , the enthalpy is used. The number of points that would be required is similar to those of the progress-variable, resulting in a table of 100x25x100x100 entries. Hence, the number of entries rises to about 25 million entries per stored variable, which easily exceeds the number of control volumes of a LES mesh.

It can readily be seen that the tabulated approach reaches a computational limit in terms of available memory. The number of entries to be stored are the density, transport coefficients, such as viscosity, diffusivity, and the progress-variable reaction. Simplified transport coefficients can be computed during CFD simulations as a function of the temperature in order to reduce the number of stored quantities. When models for NO<sub>x</sub> are included, both its mass fraction and the reaction rate need to be stored. In the studies presented in the following chapters both steady and unsteady FPV variants are discretised using the stated number of points. However, when the radiation variant is used, the number of points is reduced to 75x25x75x65 points in  $\tilde{Z}, Z_v, \tilde{c}$  and  $\tilde{h}$  directions.

The second stage of the flamelet model involves its usage during CFD simulations. Fig. 3.13 depicts the interaction between the CFD simulation and the flamelet database. Mixture fraction and progress-variable are computed through their respective transport equations, Eq. (3.14) and Eq. (3.30). The mixture fraction variance is computed through specific models for it, as previously described. In LES, the scalar dissipation rate is split into resolved and unresolved parts. Its resolved part requires the calculation of the square of the mixture fraction gradients, and its subgrid part requires modelling. Once the scalar dissipation rate has been calculated, the stoichiometric scalar dissipation rate is computed by inverting Eq. (3.77). Lastly, the enthalpy is computed through its transport equation Eq. (3.32).

Once all parameters of the database are computed, it is accessed. Variables of interest are retrieved performing linear interpolations in each direction. The use of non-dimensional parameters is aimed at reducing the number of searches within the database.

### 3.6 Concluding remarks

In this chapter a combustion model for diffusion flames in the flamelet regime has been presented. First, it has been shown that the flamelet model introduces a split in the combustion process. As a result, two independent but interconnected process result. On the one hand, a reaction-diffusion problem which defines the flame structure. On the other hand, a transport problem which describes the motion of the flame. The split is performed through a coordinate transformation from physical space to a mix-

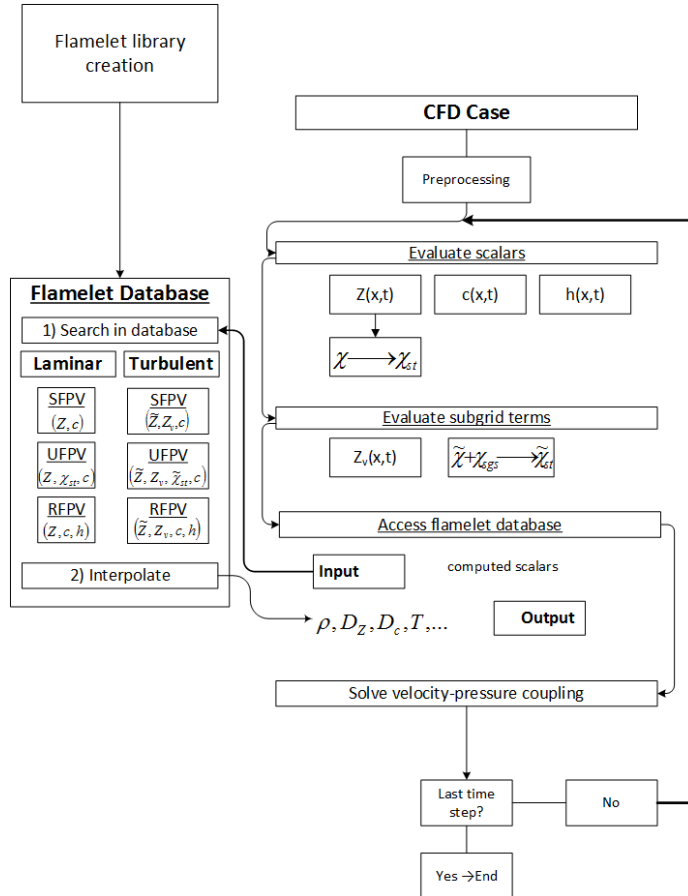


**Figure 3.13:** Interaction between a CFD simulation and the flamelet database.

ture fraction space. In the transformation, the scalar dissipation rate appeared and introduced flow effects from the transport problem into the flame structure problem.

Once the foundations of the flamelet model were detailed, focus was placed on the representation of the flame structure or flamelet subspace. To this end, the S-shaped curve was used. First, the classical flamelet model has been presented. This model uses three parameters to represent the flamelet subspace: the mixture fraction  $Z$ , the stoichiometric scalar dissipation rate  $\chi_{st}$  and a time coordinate  $\tau$ . The latter, since it is a Lagrangian coordinate, requires the flamelet equations to be solved interactively during CFD simulations. Per contra, if a database is to be created, the flamelet

equations can be solved in their steady form and stored in a preprocessing stage. However, only using  $Z$  and  $\chi_{st}$  as parameters results in representing a limited subset of the S-shaped curve, the upper steady burning branch and the extinguished flamelets parts. Hence, the viability of the model is limited. Nonetheless, the unsteady variant can represent the whole subspace, although it requires solving the flamelet equations during CFD simulations.

In order to overcome the limitations of the classical model, a variant of the classical flamelet model has been discussed. The Flamelet/Progress-Variable (FPV) model is capable of representing the whole flamelet subspace by using a different set of parameters. The main change is the use of a progress-variable instead of the scalar dissipation rate as a parameter. For steady cases, the S-shaped curve can be represented through the mixture fraction and the progress-variable. Extension to unsteady flamelets reintroduces the scalar dissipation rate as parameter. However, in this case unsteady flamelets can be computed in a preprocessing stage and stored in a flamelet database, as opposed to the classical flamelet. Additionally, the definition of the progress-variable for this model has been stated as a critical aspect. A specific study is conducted in *Chapter 4*.

In the discussion of both classical and FPV flamelet models, radiation heat losses have also been considered. It has been discussed that radiation occurs in larger time-scales than chemistry. Therefore, specific modelling is required. Additionally, it has been shown that including radiation during the flamelet computations introduces certain limitations in the shape of the radiation model used. Different approaches have been discussed, namely the enthalpy defect approach, the use of interactive flamelets and the computation of radiation flamelets through extinguishing unsteady flamelets. The latter approach is taken in this thesis. Similar to radiation heat losses, certain pollutant emissions occur in larger time-scales. Specifically, a model for  $NO_x$  emissions has been presented.

Next, algorithms for the solution of the flamelet equations have been detailed. The numerical discretisation of the derivatives in the flamelet equations in mixture fraction space has been presented. A finite-differences approach is described which uses 4th order approximations to first and second derivatives. Algorithms for either steady, unsteady and radiation flamelets are presented. An iterative Gauss-Seidel and a Newton-Raphson algorithms have been used to compute steady state flamelet solutions. Due to the presence of highly nonlinear terms in the flamelet equations and the stiffness of the reaction rate, convergence of the flamelet equations is slow. It has been stated that the iterative approach shows slower convergence rate compared to the Newton-Raphson. However, the latter requires a good initial guess in order to properly converge to a solution. Concerning transient flamelets, an Implicit-Explicit Runge-Kutta-Chebyshev (IMEX RKC) method has been used. The method combines explicit evaluation of non-stiff terms with implicit evaluation of stiff terms, namely the

reaction rate. The procedure for computing igniting and extinguishing flamelets has been described. Similarly, flamelets under radiation heat losses have been computed using the transient method described for unsteady flamelets.

As a last step of the creation of flamelet databases, the extension of the model to turbulent cases has been considered. Many cases of academic and industrial interest feature turbulent flows, which are then described using stochastic or random quantities. Hence, the flamelet database has to be restated in terms of stochastic quantities. Furthermore, since the flows of interest feature noticeable density variations, Favre averaging is introduced. The description of stochastic quantities is performed through probability density functions. Two procedures are considered, either computing the *pdf* and performing the integration interactively or presuming the shape of the statistical distribution. Although the former approach offers a general model, it is computationally expensive since it precludes the preprocessing of the database. Hence, the latter approach is preferred. Several *pdf* shapes are discussed and the choice for each variable argued. The mixture fraction statistical distribution is assumed to follow a  $\beta - \text{pdf}$ , which is described by the mean and the variance. For the other quantities, progress-variable, stoichiometric scalar dissipation rate and enthalpy, a  $\delta - \text{pdf}$  is taken, which is described only by the mean value.

Finally, the use of the model coupled with CFD simulations is described. A summary of the process to create the laminar flamelet database is made, followed by the extension to turbulent cases. It is commented that several parameters are restated in non-dimensional form in order to simplify the creation of the database. Furthermore, issues concerning the database size and storage in computer memory are discussed. It is shown that the increase in dimensionality easily leads to excessively large flamelet database, which require reducing the number of points per parameter. As a last step, the interaction between the flamelet database and a CFD simulation is detailed.

## References

- [1] T. Poinsot and D. Veynante. *Theoretical and Numerical Combustion*. R.T. Edwards Inc., 2005.
- [2] N. Peters. *Turbulent Combustion*. Cambridge University Press, 2000.
- [3] E. Hairer and G. Wanner. *Solving Ordinary Differential Equations II. Stiff and Differential-Algebraic Problems*. Springer-Verlag Berlin-Heidelberg, 1996.
- [4] H. Pitsch and N. Peters. A consistent flamelet formulation for non-premixed combustion considering differential diffusion effects. *Combustion and Flame*, 114:26–40, 1998.

- [5] D. Carbonell. *Numerical studies of diffusion flames. Special emphasis on flamelet concept and soot formation.* PhD thesis, Polytechnic University of Catalonia, Terrassa, Spain, 2010.
- [6] C.D Pierce and P. Moin. Progress-variable approach for large-eddy simulation of non-premixed turbulent combustion. *Journal of Fluid Mechanics*, 504:73–97, 2004.
- [7] L.F. Shampine, B.P. Sommeijer, and J.G. Verwer. IRKC: An IMEX solver for stiff diffusion-reaction PDE's. *Journal of Computational and Applied Mathematics*, 196:485–497, 2006.
- [8] S.B. Pope. *Turbulent Flows.* Cambridge University Press, 2000.
- [9] M. Ihme and H. Pitsch. Prediction of extinction and reignition in nonpremixed turbulent flames using a flamelet/progress variable model 1. A priori study and presumed PDF closure. *Combustion and Flame*, 155(1-2):70–89, 2008.
- [10] S.P. Burke and E.W. Schumann. Diffusion flames. *Industrial and Engineering Chemistry*, 20(10):998–1004, 1928.
- [11] R.W. Bilger, S.H. Starner, and R.J. Kee. On reduced mechanisms for methane-air combustion in nonpremixed flames. *Combustion and Flame*, 80:135–149, 1990.
- [12] R.S. Barlow and J.H. Franck. Effects of turbulence on species mass fractions in methane/air flames. *Proceedings of the Combustion Institute*, 27:1087–1095, 2000.
- [13] J.S. Kim and F.A. Williams. Structures of flow and mixture-fraction fields for counterflow diffusion flames with small stoichiometric mixture fractions. *SIAM Journal On Applied Mathematics*, 53:1551–1566, 1993.
- [14] H. Pitsch, M. Chen, and N. Peters. Unsteady flamelet modeling of turbulent hydrogen-air diffusion flames. *Twenty-Seventh Symposium (International) on Combustion*, pages 1057–1064, 1998.
- [15] H. Pitsch. Unsteady flamelet modelling of differential diffusion in turbulent jet diffusion flames. *Combustion and Flame*, 123:358–374, 2000.
- [16] W. Meier, R.S. Barlow, Y.-L. Chen, and J.-Y. Chen. Raman/Rayleigh/LIF measurements in a turbulent CH<sub>4</sub>/H<sub>2</sub>/N<sub>2</sub> jet diffusion flame: Experimental techniques and turbulence-chemistry interaction. *Combustion and Flame*, 123:326–343, 2000.

- [17] R. Cabra, J. Chen, R. Dibble, A. Karpetis, and R Barlow. Lifted methane-air jet flames in a vitiated coflow. *Combustion and Flame*, 143(4):491–506, 2005.
- [18] C.T. Bowman, M. Frenklach, G. Smith, B. Gardiner, and et al. <http://www.me.berkeley.edu/gri-mech/releases.html>, 2012.
- [19] H. Pitsch and S. Fedotov. Investigation of scalar dissipation rate fluctuations in non-premixed turbulent combustion using a stochastic approach. *Combustion Theory And Modelling*, 5(1):41–57, 2001.
- [20] R.S. Barlow, J.H. Karpetis A.N., Frank, and J.-Y. Chen. Scalar profiles and NO formation in laminar opposed-flow partially premixed methane/air flames. *Combustion and Flame*, 127(3):2102–2118, 2001.
- [21] W.L. Grosshandler. RADCAL: A narrow-band model for radiation calculations in a combustion environment. Technical Note 1402, NIST, 1993.
- [22] P.J. Coelho and N. Peters. Unsteady modelling of a piloted methane/air jet flame based on the eulerian particle flamelet model. *Combustion and Flame*, 124(3):444–465, 2001.
- [23] H. Pitsch. Modeling of radiation and nitric oxide formation in turbulent non-premixed flames using a flamelet/progress variable formulation. *Physics of Fluids*, 20(5):055110, 2008.
- [24] M Hossain, JC Jones, and W. Malalasekera. Modelling of a bluff-body non-premixed flame using a coupled radiation/flamelet combustion model. *Flow, Turbulence and combustion*, 67:217–234, 2001.
- [25] K. W. Lee and D. H. Choi. Numerical study on high-temperature diluted air combustion for the turbulent jet flame in crossflow using an unsteady flamelet model. *International Journal Of Heat And Mass Transfer*, 52(25-26):5740–5750, 2009.
- [26] D. Carbonell, C D Pérez-Segarra, P J Coelho, and A. Oliva. Flamelet mathematical models for non-premixed laminar combustion. *Combustion and Flame*, 156:334–347, 2009.
- [27] D. Carbonell, A. Oliva, and C.D. Pérez-Segarra. Implementation of two-equation soot flamelet models for laminar diffusion flames. *Combustion and Flame*, 156(3):621–632, 2009.
- [28] P. S. Cumber. Validation study of a turbulence radiation interaction model : Weak, intermediate and strong tri in jet flames. *International Journal Of Heat And Mass Transfer*, 79:1034–1047, 2014.

- [29] M. Ihme, L. Shunn, and J. Zhang. Regularization of reaction progress variable for application to flamelet-based combustion models. *Journal of Computational Physics*, 231(23):7715–7721, 2012.
- [30] H. Pitsch and M. Ihme. An unsteady flamelet/progress variable method for les of nonpremixed turbulent combustion. In *Proceedings of the 43rd Aerospace Sciences Meeting and Exhibit*, 2005.
- [31] M. Ihme and Y.C. See. Prediction of autoignition in a lifted methane/air flame using an unsteady flamelet/progress variable model. *Combustion and Flame*, 157(10):1850–1862, 2010.
- [32] a. W. Vreman, J. a. Oijen, L. P. H. Goey, and R. J. M. Bastiaans. Subgrid scale modeling in large-eddy simulation of turbulent combustion using premixed flamelet chemistry. *Flow, Turbulence and combustion*, 82(4):511–535, 2008.
- [33] J. a. van Oijen and L. P. H. de Goey. Modelling of premixed counterflow flames using the flamelet-generated manifold method. *Combustion Theory And Modelling*, 6(3):463–478, 2002.
- [34] P. Domingo, L. Vervisch, and D. Veynante. Large-eddy simulation of a lifted methane jet flame in a vitiated coflow. *Combustion and Flame*, 152(3):415–432, 2008.
- [35] J.G. Verwer and B.P. Sommeijer. An implicit-explicit runge–kutta–chebyshev scheme for diffusion-reaction equations. *SIAM Journal on Scientific Computing*, 25(5):1824–1835, 2004.
- [36] C. Jiménez, F. Ducros, B. Cuenot, and B. Bédat. Subgrid scale variance and dissipation of a scalar field in large eddy simulations. *Physics of Fluids*, 13(6):1748, 2001.
- [37] C. Dopazo. A probabilistic approach to turbulent flame theory. *Acta Astronautica*, 3:853–878, 1976.
- [38] L. Liu, H. Guo, G.J. Smallwood, Ö.L. Gülder, and M.D. Matovic. A robust and accurate algorithm of the  $\beta$ -pdf integration and its application to turbulent methane-air diffusion combustion in a gas turbine combustor simulator. *International Journal Of Thermal Sciences*, 41:763–772, 2002.
- [39] E. Effelsberg and N. Peters. Scalar dissipation rates in turbulent jets and jet diffusion flames. *Proceedings of the Combustion Institute*, 22(1):693–700, 1989.
- [40] C.D. Pierce and P. Moin. A dynamic model for subgrid-scale variance and dissipation rate of a conserved scalar. *Physics of Fluids*, 10:3041, 1998.

- [41] G. Balarac, H. Pitsch, and V. Raman. Development of a dynamic model for the subfilter scalar variance using the concept of optimal estimators. *Physics of Fluids*, 20:035114, 2008.
- [42] M. Ihme and H. Pitsch. Prediction of extinction and reignition in nonpremixed turbulent flames using a flamelet/progress variable model 2. Application in LES of Sandia flames D and E. *Combustion and Flame*, 155(1-2):90–107, 2008.
- [43] E. Knudsen, E.S. Richardson, E.M. Doran, N. Pitsch, and J.H. Chen. Modeling scalar dissipation and scalar variance in large eddy simulation: Algebraic and transport equation closures. *Physics of Fluids*, 24:055103, 2012.
- [44] C.M. Kaul, V. Raman, E. Knudsen, E.S. Richardson, and J.H. Chen. Large eddy simulation of a lifted ethylene flame using a dynamic nonequilibrium model for subfilter scalar variance and dissipation rate. *Proceedings of the Combustion Institute*, 34(1):1289–1297, 2013.
- [45] P.J. Coelho, O.J. Teerling, and D. Roekaerts. Spectral radiative effects and turbulence/radiation interaction in a non-luminous turbulent jet diffusion flame. *Combustion and Flame*, 133:2075–2088, 2000.
- [46] P.J. Coelho. Numerical simulation of the interaction between turbulence and radiation in reactive flows. *Progress in Energy and Combustion Science*, 33(4):311–383, 2007.
- [47] R. S. Mehta, M. F. Modest, and D. C. Haworth. Radiation characteristics and turbulence–radiation interactions in sooting turbulent jet flames. *Combustion Theory And Modelling*, 14:105–124, 2010.
- [48] D. Shepard. A two-dimensional interpolation function for irregularly-spaced data. In *23rd ACM national conference*, pages 517–524, 1968.
- [49] O. Estruch, O. Lehmkuhl, R. Borrell, C. D Pérez Segarra, and A. Oliva. A parallel radial basis function interpolation method for unstructured dynamic meshes. *Combustion and Flame*, 80:44–54, 2013.

# Differential diffusion effects in the progress-variable definition for Flamelet/Progress-variable models for non-premixed flames

Parts of this chapter have been submitted to international conferences:

J. Ventosa-Molina, O. Lehmkuhl, C.D. Pérez-Segarra and A. Oliva. *Towards a Direct Numerical Simulation of a lifted CH<sub>4</sub>-air diffusion flame*. In Proceedings of the 8th International Symposium on Turbulence, Heat and Mass Transfer, Sarajevo, Bosnia and Herzegovina, September 2015.

**Abstract.** The Flamelet/Progress-variable (FPV) model enables representing unambiguously the whole flame structure in composition space. However, one of its parameters, the progress-variable, does not have a unique definition. Dependencies on combustion mode, fuel composition and chemical mechanism have been reported.

The effects of accounting for differential diffusion in the generation of the flamelet databases are studied in the context of a FPV model. The influence of the diffusion model in the accessible solution space and the extinction scalar dissipation rate is shown. The S-shaped curve is used to represent the differences between diffusion models. FPV models require the progress-variable to uniquely identify each flamelet included in the chemical database. Commonly used definitions for the progress-variable are considered and assessed against this criterion. It is shown that the use of the main combustion products *CO*, *CO*<sub>2</sub>, *H*<sub>2</sub> and *H*<sub>2</sub>*O* is usually adequate. However, small regions remain where the progress-variable requires a more complex definition, either by adding additional species or using weighted combinations.

Two study cases are considered. A methane/hydrogen diffusion flame is first assessed, since hydrogen presents a markedly different Lewis number than 1. Differential diffusion is shown to have a significant effect on the maximum strain that the flame can withstand. An auto-igniting methane flame is then used to assess differential diffusion effects on the

progress-variable and auto-ignition delay times. Alongside, two detailed and commonly used chemical mechanism are considered, the GRI2.11 and the GRI3.0.

## 4.1 Introduction

Numerical resolution of combustion processes by means of Computational Fluid Dynamics (CFD) involve solving for momentum, energy, and species mass fractions transport equations, alongside with the computation of chemical reactions that characterise the combustion process. Detailed evaluation of chemical reactions require taking into account tens or hundreds of species and similar number of chemical reactions. It can easily be seen that the computational requirements become prohibitive with ease [1]. The literature is rich in models devised to reduce the computational effort, most of them limited to a particular combustion regime of interest. In this sense, in the context of diffusion flames, the flamelet regime is found in many industrial applications, and therefore the interest to develop accurate models to describe it.

In the flamelet regime, chemical reactions are assumed to take place in shorter length scales than the characteristic flow scales. Furthermore, the flame is viewed as one dimensional, where changes to the flow mixture only take place in the flame normal direction. Therefore, energy and mass transport may be rewritten in a flame normal coordinate system, resulting in a reaction-diffusion set of equations [2, 3]. These reaction-diffusion processes, or flamelets, are then convected by the flow, thus characterising the flamelet regime. The coordinate transformation introduces two parameters to describe the flame, the mixture fraction  $Z$  and the stoichiometric scalar dissipation rate  $\chi_{st}$ . The former is a measure of the mixing process and the latter introduces flow effects into the reaction-diffusion problem.

The full range of solutions of the flamelet equations describe the full flame subspace: the stable burning solutions, the unstable equilibrium solutions and the pure mixing between reactants, as well as transient states, ignition and extinction from the unstable solutions. However, using only  $Z$  and  $\chi_{st}$  to characterise the flame is found to be limiting, only the stable burning solution can be represented [4, 5]. Thus, transient effects such as ignition or extinction effects cannot be included. A change in the parameters used to describe the flame was proposed by Pierce and Moin [4], the Flamelet/Progress-variable (FPV) model, where the scalar dissipation rate is substituted by a progress-variable. This change enables the full characterisation of the S-shaped curve, thus accounting for the stable burning branch, the unstable one and the non-burning mixing one.

As opposed to the mixture fraction, which is uniquely defined by the coordinate transformation, the progress-variable is an open parameter and must be properly defined. Two main constraints are placed: it has to be independent of the mixture fraction and it has to uniquely represent the flame state for each mixture fraction. Several definitions have been proposed, such as using a reduced temperature [6] or a combination of several major species [7–9]. The range of proposed definitions indicates the dependency of this parameter on the studied case, chemical mechanism, fuel

composition and combustion mode [10].

A common practice when computing flamelet solutions is to assume Fickian diffusion, mainly due to the main species having similar Lewis numbers or because molecular diffusion was considered negligible compared to the turbulent transport. Regarding the latter, Hilber et al. [11] discussed the importance of retaining molecular diffusion terms even in turbulent flows. They also concluded that the diffusion model choice could have a similar impact as the choice of the chemical mechanism. In the following, it is shown that the diffusion model may introduce another case dependency to the progress-variable dependence. Additionally, when diffusion flames are considered, the mixture is composed of different species at the inflow streams. Then, the mixture may present significantly different diffusion velocities at each end. Differential diffusion effects are mainly noticeable when the mixture of gases contains species which are markedly lighter or heavier than the average of the mixture. It is then found that these substance are capable of moving along the domain faster or slower than the mean [1, 3]. Therefore, the diffusion model used will influence the distribution of species and the available pool of reactants at each position in the domain. Furthermore, depending on their energetic capacity, heat distribution may as well be affected. In the following it is shown that the consideration of differential diffusion affects the shape of S-shaped curve and the implications it entails to CFD simulations.

Returning to the combustion model, another limitation encountered with the classical flamelet model was of a computational nature. When using unsteady flamelets during CFD simulations, the flamelet equations were required to be solved alongside. Inclusion of differential diffusion led to an increase in computational costs due to the extra terms compared to Fickian diffusion [3]. When the FPV model is used this argument does not apply, since the flame database is compiled prior to numerical simulations.

Two detailed chemical mechanisms are considered for the computations, the GRI2.11 and GRI3.0. Both versions of the mechanism are taken into account due to their common use when considering methane flames. Additionally, their predictions regarding NOx have been shown to differ considerably [12]. Therefore, it is of interest to assess whether different definitions of the progress-variable are required.

Two turbulent diffusion flames are here studied. The first one is a simple jet with a Reynolds number of 15200, which uses a mixture of  $CH_4/H_2/N_2$  as fuel [13, 14]. The significant quantity of  $H_2$ , which has a Lewis number markedly different than 1, is the main cause for differential diffusion effects. The second case is a self-igniting  $CH_4/O_2/N_2$  flame with a jet Reynolds number of about 24760, which was experimentally studied by Cabra et al. [15]. In this flame, the oxidant boundary is composed of the products of a premixed hydrogen-air combustion. It was reported that differential diffusion effects are negligible in the present flame [15]. In the following it will be

shown that, they are low in most part of the domain. However, the species evolution in the induction region is greatly affected by the diffusion model. Nonetheless, once the mixture is ignited, no further significant effects are found.

The chapter is organised as follows. First, the flamelet mathematical model is presented. Thereafter is presented the discussion about the two studied flames. In both cases, first are discussed the aspects regarding the generation of the database using Fickian and differential diffusion models. Alongside are discussed the effect of two chemical mechanisms. The FPV model is discussed in all its variants: steady, unsteady and radiation. Afterwards, results in physical space are presented.

## 4.2 Mathematical model

Combustion phenomena in the low Mach regime are described by the Navier-Stokes equations in their low Mach limit

$$\frac{\partial \rho}{\partial t} + \frac{\partial \rho u_j}{\partial x_j} = 0 \quad (4.1)$$

$$\frac{\partial \rho u_i}{\partial t} + \frac{\partial \rho u_j u_i}{\partial x_j} = -\frac{\partial p}{\partial x_i} + \frac{\partial \tau_{ij}}{\partial x_j} + \rho g_i \quad (i = 1, 2, 3) \quad (4.2)$$

where  $\rho$  is density of mixture,  $u_i$  is a velocity component,  $p$  is the hydrodynamic pressure and  $g_i$  is a gravity component. The viscous stress tensor reads  $\tau_{ij} = \mu \left( \frac{\partial u_i}{\partial x_j} + \frac{\partial u_j}{\partial x_i} - \frac{2}{3} \delta_{ij} \frac{\partial u_k}{\partial x_k} \right)$ , where  $\mu$  is the dynamic viscosity. Scalars transport equations, namely species mass fractions  $Y_k$  and energy in its enthalpy form  $h$ , read

$$\rho \frac{\partial Y_k}{\partial t} + \rho u_j \frac{\partial Y_k}{\partial x_j} = \frac{\partial}{\partial x_j} \left( \rho D_k \frac{\partial Y_k}{\partial x_j} \right) + \frac{\partial}{\partial x_j} \left( \rho Y_k \left( \frac{D_k}{M_w} \frac{\partial M_w}{\partial x_j} - V_j^c \right) \right) + \dot{w}_k \quad (4.3a)$$

$$\rho \frac{\partial h}{\partial t} + \rho u_j \frac{\partial h}{\partial x_j} = \frac{dP_o}{dt} - \frac{1}{c_p} \dot{q}^R - \frac{\partial}{\partial x_j} \left( -\kappa \frac{\partial T}{\partial x_j} - \sum_{k=1}^N \rho h_k \left( \frac{D_k}{M_w} \frac{\partial (M_w Y_k)}{\partial x_j} - Y_k V_j^c \right) \right) \quad (4.3b)$$

where  $D_k$  is the species mass diffusivity,  $\kappa$  is the thermal conductivity,  $M_w$  is the molar mass,  $P_o$  is the thermodynamic pressure and  $\dot{q}^R$  is the radiant heat flux. Furthermore, the Hirschfelder and Curtiss approximation [1] with a correction velocity  $V_j^c$  to ensure mass conservation has been used

$$V_j^c = \sum_{k=1}^N \left( D_k \frac{\partial Y_k}{\partial x_j} + \frac{Y_k D_k}{W} \frac{\partial W}{\partial x_j} \right) \quad (4.4)$$

When Fickian diffusion is used, the second term on the right hand side of Eq. (4.3a) is dropped. Similarly, the second term within the summation in Eq. (4.3b) is also dropped, along with the mixture fraction dependency of the first. Mass conservation is enforced then by having all mass fractions add to 1.

The flamelet model splits the combustion phenomenon into two independent problems: a flame structure problem and a transport problem by performing a coordinate transformation. The former describes the thermochemistry part of the combustion process and the latter deals with transport phenomena. This splitting is based on a scale separation, where it is assumed that the flow does not penetrate the inner structure of the flame. Then, in physical space the flame is convected, strained and wrinkled by the flow. The flame-based coordinate system, is attached to the flame front [3, 16]. Furthermore, variations along tangential coordinates are deemed negligible. This flame coordinate system is based on the mixture fraction  $Z$  defined as a conserved scalar satisfying the transport equation of a passive scalar

$$\rho \frac{\partial Z}{\partial t} + \rho u_j \frac{\partial Z}{\partial x_j} = \frac{\partial}{\partial x_j} \left( \rho D_z \frac{\partial Z}{\partial x_j} \right) \quad (4.5)$$

where  $D_z$  is the diffusivity of the mixture, here defined through a unity Lewis number assumption  $Le_Z = \kappa/(\rho D_z c_p) = 1$ . In addition, the scalars transport equations Eq. (4.3) in the flame-based coordinate system are

$$\begin{aligned} \rho \frac{\partial Y_k}{\partial \tau} &= \dot{w}_k + \frac{\rho \chi_Z}{2} \frac{Le_Z}{Le_k} \frac{\partial^2 Y_k}{\partial Z^2} + \frac{\rho \chi_Z}{2} \frac{Le_Z}{Le_k} \frac{Y_k}{M_w} \frac{\partial^2 M_w}{\partial Z^2} \\ &- \frac{\rho \chi_Z}{2} \sum_{\alpha=1}^N \left( \frac{Le_Z}{Le_\alpha} Y_k \frac{\partial^2 Y_\alpha}{\partial Z^2} + \frac{Y_k}{M_w} Y_\alpha \frac{Le_Z}{Le_\alpha} \frac{\partial^2 M_w}{\partial Z^2} \right) \\ &+ \frac{1}{4} \left[ 2\rho \chi_Z \frac{\partial}{\partial Z} \left( \frac{Le_Z}{Le_k} \right) + \left( \frac{Le_Z}{Le_k} - 1 \right) \left( \frac{\partial \rho \chi_Z}{\partial Z} + \rho \chi_Z Le_Z \frac{c_p}{\kappa} \frac{\partial}{\partial Z} \left( \frac{\kappa}{c_p Le_Z} \right) \right) \right] \frac{\partial Y_k}{\partial Z} \\ &+ \frac{1}{4} \left[ 2\rho \chi_Z \frac{Y_k}{M_w} \frac{\partial}{\partial Z} \left( \frac{Le_Z}{Le_k} \right) + \left( \frac{Le_Z}{Le_k} \right) \left( \frac{\partial}{\partial Z} \left( \rho \chi_Z \frac{Y_k}{M_w} \right) + \rho \chi_Z Le_Z \frac{c_p}{\kappa} \frac{\partial}{\partial Z} \left( \frac{\kappa}{c_p Le_Z} \frac{Y_k}{M_w} \right) \right) \right] \frac{\partial M_w}{\partial Z} \\ &- \frac{1}{4} \sum_{\alpha=1}^N \left[ 2\rho \chi_Z Y_k \frac{\partial}{\partial Z} \left( \frac{Le_Z}{Le_\alpha} \right) + \left( \frac{Le_Z}{Le_\alpha} \right) \left( \frac{\partial \rho \chi_Z Y_k}{\partial Z} + \rho \chi_Z Le_Z \frac{c_p}{\kappa} \frac{\partial}{\partial Z} \left( \frac{\kappa}{c_p Le_Z} Y_k \right) \right) \right] \frac{\partial Y_\alpha}{\partial Z} \\ &- \frac{1}{4} \sum_{\alpha=1}^N \left[ 2\rho \chi_Z \frac{Y_k Y_\alpha}{M_w} \frac{\partial}{\partial Z} \left( \frac{Le_Z}{Le_\alpha} \right) \right. \\ &\quad \left. + \left( \frac{Le_Z}{Le_\alpha} \right) \left( \frac{\partial}{\partial Z} \left( \rho \chi_Z \frac{Y_k}{M_w} Y_\alpha \right) + \rho \chi_Z Le_Z \frac{c_p}{\kappa} \frac{\partial}{\partial Z} \left( \frac{\kappa}{c_p Le_Z} \frac{Y_k Y_\alpha}{M_w} \right) \right) \right] \frac{\partial M_w}{\partial Z} \end{aligned} \quad (4.6a)$$

$$\begin{aligned} \rho \frac{\partial T}{\partial \tau} = & \frac{\rho \chi_Z}{2} Le_Z \frac{\partial^2 T}{\partial Z^2} - \frac{1}{c_p} \dot{q}^R - \frac{1}{c_p} \sum_{k=1}^N \dot{w}_k h_k + \frac{\rho \chi_Z}{2} \frac{Le_Z}{c_p} \frac{\partial c_p}{\partial Z} \frac{\partial T}{\partial Z} \\ & + \frac{1}{4} \left[ 2\rho \chi_Z \frac{\partial Le_z}{\partial Z} + (Le_z - 1) \left( \frac{\partial \rho \chi_Z}{\partial Z} + \rho \chi_Z Le_z \frac{c_p}{\kappa} \frac{\partial}{\partial Z} \left( \frac{\kappa}{c_p Le_z} \right) \right) \right] \frac{\partial T}{\partial Z} \quad (4.6b) \\ & - \sum_{k=1}^N \frac{\rho \chi_Z}{2} \frac{Le_z}{Le_k} \left( \frac{\partial Y_k}{\partial Z} + \frac{Y_k}{M_w} \frac{\partial M_w}{\partial Z} \right) \left( 1 - \frac{c_{p,k}}{c_p} \right) \frac{\partial T}{\partial Z} \end{aligned}$$

where  $\chi$  is the scalar dissipation rate, which introduces flow effects into the flamelet space, and is defined afterwards. When Fickian diffusion is considered and equal diffusivities are taken for all species  $Le_i = Le_Z$ , the flamelet equations reduce to

$$\rho \frac{\partial Y_k}{\partial t} = \dot{w}_k + \frac{\rho \chi_Z}{2} \frac{\partial^2 Y_k}{\partial Z^2} \quad (4.7a)$$

$$\rho \frac{\partial T}{\partial t} = \frac{\rho \chi_Z}{2} \frac{\partial^2 T}{\partial Z^2} - \frac{1}{c_p} \dot{q}^R + \frac{1}{c_p} \sum_{k=1}^N \dot{w}_k h_k - \frac{\rho \chi_Z}{2} \left( \frac{1}{c_p} \frac{\partial c_p}{\partial Z} \frac{\partial T}{\partial Z} + \sum_{k=1}^N \frac{\partial Y_k}{\partial Z} \left( 1 - \frac{c_{p,k}}{c_p} \right) \frac{\partial T}{\partial Z} \right) \quad (4.7b)$$

In contrast, the flamelet equations based on the Shvab-Zeldovich formulation, with equal diffusivities and using a coupling function based on, the fuel and oxidiser mass fraction or a local element balance, results in

$$\rho \frac{\partial Y_k}{\partial t} = \frac{\rho \chi_Z}{2} \frac{\partial^2 Y_k}{\partial Z^2} + \dot{w}_k \quad (4.8a)$$

$$\rho \frac{\partial T}{\partial t} = \frac{\rho \chi_Z}{2} \frac{\partial^2 T}{\partial Z^2} - \frac{1}{c_p} \dot{q}^R - \frac{1}{c_p} \sum_{k=1}^N \dot{w}_k h_k \quad (4.8b)$$

which is equivalent to Eq. (4.7) if all species heat capacities are equal and constant.

In order to study the influence of differential diffusion, results from Eq. (4.6), the differential diffusion model, and Eq. (4.8), the Fickian model, are compared. Moreover, the “extended” Fickian model, Eq. (4.7), is used to characterise changes caused by variable heat capacities.

The sets of equations Eq. (4.6), (4.7) or (4.8) are function of the mixture fraction and the scalar dissipation rate, which is a central element in the coordinate transformation as it represents flow effects in the flame structure problem. It is defined as

$$\chi_Z = 2D_Z \left( \frac{\partial Z}{\partial x_i} \frac{\partial Z}{\partial x_i} \right) \quad (4.9)$$

and has dimension of the inverse of time [1/s], usually regarded as a characteristic diffusion time.

As the scalar dissipation rate is defined as a function of the mixture fraction, once the mixture fraction field in physical space is known, it can be computed. This approach requires a coupled strategy to solve the flamelet equations, which in turn means that the flamelet equations have to be solved during CFD computations.

Alternatively, Peters [2] showed that diffusion flames in the flamelet regime may be viewed as counter-flow flames or unsteady mixing layers. From the analytic solution and asymptotic analysis of those one-dimensional diffusion flames, an expression was obtained [2, 16],

$$\chi_Z(Z) = \frac{a_\infty}{\pi} \Phi \exp\left(-2[\operatorname{erfc}^{-1}(2Z)]^2\right) = \chi_{st} \frac{\Phi}{\Phi_{st}} \frac{f(Z)}{f_{st}(Z)} \quad (4.10)$$

where  $a_\infty$  is the nominal strain rate in a counter-flow configuration or an inverse of the decaying time of an unsteady mixing layer.  $\chi_{st}$  is the scalar dissipation rate at the stoichiometric mixture fraction  $\chi_{st} = \chi_Z|_{\{Z = Z_{st}\}}$ . The function  $\operatorname{erfc}^{-1}$  is the inverse of the complementary error function.

In the right hand side (r.h.s.) of Eq. (4.10),  $f(Z)$  represents the exponential term, and  $\Phi$  is a coefficient which accounts for variable density effects [3, 17] and takes the form

$$\Phi = \frac{3}{4} \frac{(\sqrt{\rho_\infty/\rho(Z)} + 1)^2}{2\sqrt{\rho_\infty/\rho(Z)} + 1} \quad (4.11)$$

where  $\rho_\infty$  represents the density at the oxidiser side.

The last form of Eq. (4.10) is motivated by the interest to express  $\chi_Z$  as a function of a parameter independent of the mixture fraction. Therefore, the scalar dissipation rate is related to its stoichiometric value, which ranges from  $\chi_{st} \rightarrow 0$  to  $\chi_q$ , the latter representing the scalar dissipation rate at which the flame is quenched. The limit of zero scalar dissipation rate represents an unstrained diffusion flame. However, the flamelet equations cannot reproduce this limit, because unstrained one dimensional diffusion flames become choked by their combustion products. Hence, solutions are usually obtained down to a numerical zero.

Taking advantage of this analogy, a functional form for the scalar dissipation rate is prescribed, which allows solving the flamelet equations in a preprocessing stage.

#### 4.2.1 Flamelet/Progress-variable (FPV) model

The classical flamelet model requires solving the flamelet equations during CFD simulations due to the presence of the temporal term. Furthermore, since the coordinate transformation is attached to the flame front, the temporal timescale  $\tau$  is a Lagrangian-like coordinate [18, 19], which requires the computation of a flamelet Lagrangian time and consequently limited the model applicability to simple geometries. Additionally, use of large chemical mechanisms is limited by computational resources. Dropping the temporal dependency, thus considering the flamelet equations in their

steady state, allows a database to be created in a preprocessing stage and accessing it during CFD simulations. In turn, this introduced an additional scale separation, a temporal one. Chemistry is then assumed to be faster than the characteristic flow time, relaxing to its steady state in a sufficiently fast time-scale.

Solutions of the flamelet set of equations in their adiabatic steady form can be parametrised by means of the mixture fraction  $Z$  and the scalar dissipation rate at stoichiometric mixture fraction  $\chi_{st}$ . Therefore, a two parameter representation of the flamelet space is obtained. Plotting the temperatures at stoichiometric mixture fraction  $T_{st}$  as a function of the stoichiometric scalar dissipation rate  $\chi_{st}$  results in the representative S-shaped curve for diffusion flames. The reader is referred to Fig. 4.2 in Sec. 4.3 and Fig. 4.14 in Sec. 4.4 for the curves of the two cases here studied.

A database of steady flamelets using solely  $Z$  and  $\chi_{st}$  can only represent the upper branch of the S-shaped curve, which limits the applicability of the model. The steady model projects vertically all solutions under the stable burning branch to it. Therefore, mixing at  $\chi_{st} < \chi_q$  always led to an ignited mixture. The unsteady model, which is capable of representing all states, required solving the flamelet equations interactively during CFD simulations.

Pierce and Moin [4] proposed changing  $\chi_{st}$  as a parameter in favour of a progress-variable  $c$  to represent steady flamelets. Hence, it would be possible to fully characterise the S-shaped curve and consequently being able to describe partially-extinguished or partially-ignited states. Therefore, this progress-variable must uniquely identify each flamelet within the database. Its actual definition will be discussed once the model and, requirements on the parameter, have been presented. As stated, its definition is found to be case dependent [6–10].

As similarly done for the scalar dissipation rate, the parameter substituting the stoichiometric scalar dissipation rate is the progress-variable at the stoichiometric mixture fraction  $\Lambda = c|Z_{st}$ . This definition is based on the same arguments for using  $\chi_{st}$  instead of  $\chi_Z$ . With it, the three branches of the S-shaped curve can be uniquely characterised. However, use of  $\Lambda$  during CFD simulations has been shown to be complex, as its transport equation for turbulent flows requires modelling complex unclosed terms. Hence, it is more convenient to use the progress-variable itself as a parameter. Therefore a bijective relation between  $\Lambda$  and  $c$  is required in order to properly define the flamelet space

$$\Lambda = \zeta^{-1}(Z, c) \quad (4.12)$$

In the steady Flamelet/Progress-variable (SFPV) model, all the precomputed thermochemical variables, including thermophysical quantities and reaction rates, are stored into a database, which is accessed during CFD simulations. The database is then treated as an equation of state (EoS)

$$\phi = \{\rho, \dot{w}_c, D_Z, \dots\} = F_\phi^{SFPV}(Z, c) \quad (4.13)$$

If transient terms are retained, in the classical flamelet model, the flamelet equations would have to be solved during CFD simulations in order to account for the time scale  $\tau$  in the flamelet equations. With the parameter change, the transient evolution at each  $\chi_{st}$  can be tracked using the progress-variable [5, 20]. Hence, the progress-variable must be a monotonically varying magnitude. The set of solutions of the unsteady model becomes a function of the mixture fraction  $Z$ , the progress-variable  $c$  and the stoichiometric scalar dissipation rate  $\chi_{st}$ . Thus, the database for the unsteady flamelet can be computed in a preprocessing stage. The EoS for the unsteady Flamelet/Progress-variable (UFPV) adds the stoichiometric scalar dissipation rate to the steady one

$$\phi = \{\rho, \dot{w}_c, D_Z, \dots\} = F_\phi^{UFPV}(Z, c, \chi_{st}) \quad (4.14)$$

Both steady and unsteady FPV databases are generated under the assumption of adiabatic heat transfer, i.e. without radiative heat loses. Thermal radiation effects are relevant at high temperatures, which translates into radiation playing a significant role near the stable burning branch of the S-shaped curve. However, radiation effects, and similarly NO formation, are slow processes which are not well represented by steady flamelet models. It is assumed that flamelets relax to steady form in sufficiently short timescales. As proposed by Ihme and Pitsch [21], starting from the adiabatic steady state solution at the burning branch, transient flamelets at constant  $\chi_{st}$  are computed, where the temperature of the mixture is decreased due to thermal radiation, modelled through an Optically Thin model (OTM) [16, 22]. The enthalpy at stoichiometric mixture fraction  $H = h|Z_{st}$  is introduced as parameter, where  $h$  is the total enthalpy, defined as the sum of chemical and sensible enthalpies. As done for  $\Lambda$ , the enthalpy itself is used rather than the enthalpy parameter. Therefore, a bijective relation between  $h$  and  $H$  is required. Solutions at different stoichiometric scalar dissipation rates define the radiation subspace of the flamelet, which are parametrised as a function of the mixture fraction  $Z$ , the progress-variable  $c$  and the total enthalpy  $h$ . An example of the radiation flamelet space may be seen in Fig. 4.9 of Sec. 4.3.4. Based on the EoS of the steady FPV plus the enthalpy, the EoS for the radiation Flamelet/Progress-variable (RFPV) is

$$\phi = \{\rho, \dot{w}_c, D_Z, \dots\} = F_\phi^{RFPV}(Z, c, h) \quad (4.15)$$

### Progress-variable definition

The FPV model relies on a progress-variable which uniquely identifies each solution included into the database. Several restrictions are to be taken into account in its definition. Above all, the progress-variable should uniquely characterise the thermochemical state and its reaction rate should be non-negative, so that, the progress-variable evolves from an initial state to a final state. Additionally, the species used

should evolve on comparable timescales and their mass fractions have comparable magnitudes, in order to avoid the use of large weights.

The progress-variable has been usually defined as a summation of different species mass fractions,  $c = \sum_k Y_k$ . Several definitions may be found in the literature with regard to the actual species considered in this definition. Usually a combination of  $CO_2$ ,  $H_2O$ ,  $CO$  and  $H_2$  mass fractions is used. Likewise, the progress-variable may be defined as a weighted summation  $c = \sum_k \omega_k Y_k$ . Pierce and Moin [4] defined it as a linear combination of  $CO_2$  and  $H_2O$ , Vreman et al. [8] and Oijen and de Goey [23], in the context of premixed flames, included  $H_2$  into the definition and used as weights the inverse of the molar mass. Domingo et al. [9], also for premixed flames, used a combination of only  $CO$  and  $CO_2$ . Ihme et al. [20, 21] used the four major species, as well as analysing the effect of the definition on its monotonicity and proposing an optimisation method for finding the coefficients of each specie, so that the bijective relation in Eq. (4.12) was met [10]. The method showed improvements over existing definitions. However, results still showed non-bijective regions. In addition, a dependency on the combustion mode, premixed or non-premixed, the chemical mechanism and considered fuel was shown. In non-premixed flames, diffusion, or mixing, is the rate controlling mechanism of the flame. Usually, a Fickian approximation is made, which simplifies the computations. However, accounting for differential diffusion modifies the species distribution. Therefore, definitions suitable for the Fickian model may not be extrapolated to the differential diffusion model.

In this work, the definition of the progress-variable is restricted to two definitions, one considering only  $CO_2$  and  $H_2O$ , denoted as  $CD1$ ,  $c_{CD1} = Y_{CO_2} + Y_{H_2O}$ , and a second one considering  $CO_2$ ,  $H_2O$ ,  $CO$  and  $H_2$ , denoted  $CD2$ ,  $c_{CD2} = Y_{CO} + Y_{CO_2} + Y_{H_2} + Y_{H_2O}$ . It will be shown that in some cases it may be interesting to expand this definition by introducing other species or using different weights. However, establishing the optimal values for the coefficients would require an optimisation procedure which exceeds the aim of the present work.

Since the progress-variable is taken as a summation of species mass fractions, the transport equation to be computed in physical space is a linear summation of the transport equation of the different species

$$\rho \frac{\partial c}{\partial t} + \rho u_j \frac{\partial c}{\partial x_j} = \frac{\partial}{\partial x_j} \left( \rho D_c \frac{\partial c}{\partial x_j} \right) \quad (4.16)$$

where  $D_c$  is the progress-variable diffusivity, which is taken equal to the mixture fraction diffusivity. The transport equation of the progress-variable is used in its Fickian form for two reasons.

First, and foremost, differential diffusion effects are important when different species diffuse at different speeds [3, 24]. Since the progress-variable is defined as a combination of species, and most of them present low sensitivity to differential

diffusion, these effects become negligible compared to Fickian diffusion. That is, diffusion due to species gradients is the dominant term for the progress-variable. Fig. 4.1 shows the different terms of Eq. (4.6a) in mixture fraction space for the  $CH_4/H_2/N_2$  diffusion flame. As it can be seen in Fig. 4.1a, differential diffusion terms, 5th and 6th terms on r.h.s of Eq. (4.6a), play a significant role for  $H_2$ . However, for species with Lewis number close to 1 the effect is much more limited, as shown for  $H_2O$  in Fig. 4.1b. Therefore, diffusion due to species mass fractions gradients, 2nd term, and the reaction rate are the leading terms for the progress-variable, as shown in Fig. 4.1c and 4.1d.

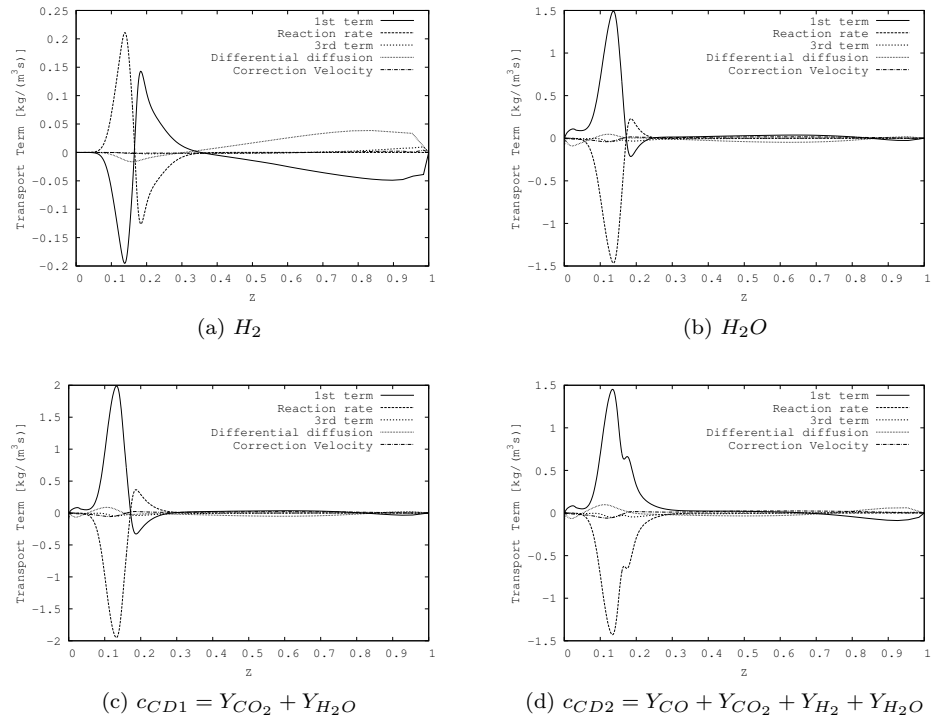


**Figure 4.1:** Transport terms in the r.h.s of Eq. (4.6a). Results correspond to the stable branch at  $\chi_{st} = 1$ . The fuel is a mixture of  $H_2$  and  $CH_4$ , corresponding to the DLR flame [13, 14]. Diffusion due to mass fraction gradients are denoted as "1st term", and due to molar mass gradients as "3rd term". Differential diffusion accounts for the 5th and 6th terms. Correction Velocity includes the 4th, 7th and 8th terms. Results were obtained using the GRI3.0 chemical mechanism.

Second, the correction terms involve all species. Hence, the computational requirements would considerably increase if the correction terms were included, because it would entail retrieving all species from the flamelet database during CFD simulations.

#### 4.2.2 Numerical method

Two numerical codes are used in this work. For the flamelet database generation a high order one dimensional code is used. CFD simulations are performed using the general purpose unstructured and parallel object-oriented CFD code TermoFluids [25].

##### Flamelet database

In order to build the flamelet database, the set of equations Eq. (4.6), or alternatively their Fickian counterparts Eq. (4.7) or Eq. (4.8), are solved using a one dimensional finite differences code. First and second order derivatives are evaluated using 4th order centred approximations. Meshes are refined near the stoichiometric mixture fraction in order to correctly capture the reaction zone. Boundary conditions are imposed as Dirichlet boundary conditions. At  $Z = 0$  and  $Z = 1$  oxidiser and fuel species and temperatures are set, respectively.

Solution of the flamelet equations in their steady form is performed by means of a Newton Method. The resulting matrix system is solved by means of a sparse LU solver. The resulting solutions define the S-shaped curve.

Transient solution of the flamelet equations, for both unsteady and radiation models, are performed by means of an Implicit/Explicit Runge-Kutta Scheme (IMEX RKC) [26]. The stiff chemical reaction term is treated implicitly, whereas all diffusive terms are treated explicitly. The scheme allows for a variable time-step, which becomes a function of the allowed local truncation error at each step and the number of iterations per step. The advantage of an hybrid explicit-implicit scheme is that it only requires solving locally implicit systems of equations, as the diffusive term is treated explicitly. The implicit set of equations for the stiff chemical reaction term is solved using an sparse LU solver.

Due to the coordinate change, the flame structure is solved in a flame based coordinate system. Therefore, radiation heat losses have to be computed without spatial dependencies. Furthermore, the medium is assumed optically thin. The Optically Thin model (OTM) assumes that self-absorption is negligible compared to emission [16, 22]. Therefore, each control volume has an unimpeded view of the surrounding, viewed as a black body. Thus, the radiation flux is modelled as control volume heat loss, and is evaluated as

$$\dot{q}^R = 4\sigma \left( T^4 \sum_{k=1}^N (p_k k_{P_k}) - T_s^4 \sum_{k=1}^N (p_k k_{I_k}) \right) \quad (4.17)$$

where  $\sigma$  is the Stefan-Boltzmann constant,  $p_k$  is the partial pressure of the  $k$ th species,

$k_{P_k}$  and  $k_{I_k}$  are the Planck-mean and incident-mean absorption coefficients and  $T_s$  is the background temperature. Absorption coefficients obtained from RADCAL [27] have been fitted to polynomials of the temperature. The radiant species considered are  $CO_2$ ,  $H_2O$ ,  $CH_4$  and  $CO$ .

### CFD simulations

The set of equations Eq. (4.1), (4.2), (4.5) and (4.16) are solved using a finite volume approach. Particularly, general 3D collocated meshes, either structured or unstructured are used. In order to preserve kinetic energy, a Symmetry-Preserving scheme [28] is used in the construction of the discrete convective term of the momentum equation. For the scalar convective terms, a SMART scheme is used [29]. A second order centred difference scheme is used to construct the discrete diffusive term for all transported quantities. Temporal integration is performed using a linear multi-step method, as described in *Chapter 2*, with a second order Adams-Bashforth in the predictor step and a Crank-Nicholson scheme in the corrector step. The pressure-velocity coupling is solved by means of a Fractional Step method.

Regarding boundary conditions, scalars are fixed at the inlet boundaries through Dirichlet conditions. In addition, the experimental fuel inflow, in both analysed flames, was reported to behave as a fully developed turbulent pipe flow. Therefore, a fully developed pipe flow is assumed for the turbulent fuel jet in the present simulations. Hence, a loosely coupled strategy has been carried out in order to reproduce the experimental inlet conditions. First, in a preprocessing stage a turbulent pipe flow, at the fuel inlet conditions, is simulated and stored. After, during CFD simulations, at each time-step, velocities are retrieved. Neumann conditions are set for the velocity at the exit plane.

### 4.3 Turbulent diffusion $CH_4/H_2/N_2$ flame - DLR A flame

The first case of study is the  $CH_4/H_2/N_2$  jet flame referred as DLR Flame A [13, 14]. It consists of a  $D_j = 8mm$  wide jet with a thinned rim at the exit. The inner jet is composed of 33.2%  $H_2$ , 22.1%  $CH_4$ , and 44.7%  $N_2$  by volume and the outer jet is regular air with 20.1%  $O_2$ . The cold jet exit bulk velocity is fixed to  $42.15m/s$  resulting in a Reynolds number of 15,200. The jet was mounted concentrically to the coflow nozzle, which had a diameter of 140mm and provided air at  $0.3m/s$ . Both fuel and coflow air were at 300K. The stoichiometric mixture fraction is  $Z_{st} = 0.167$ . The present flame is stabilised by shear between fuel and oxidiser streams. Thus, proper modelling of the mixing process is critical. As there is a significant amount of hydrogen in the fuel stream, it has been shown experimentally [13, 14] and numerically [30] that differential diffusion plays a significant role. Due to the presence of  $H_2$  in significant proportions, this case will serve to assess how the progress-variable definition is affected when differential diffusion is included. First, the flamelet database

is analysed to assess the effect of the diffusion model and the chemical mechanism. Then, results of CFD simulations are presented.

#### 4.3.1 Flamelet burning region - Fickian vs Differential

First the flamelet accessible subspace is analysed using the S-shaped curve. When differential diffusion is accounted for, a twofold effect on the flamelet burning region is shown in Fig. 4.2: it produces an increase in the temperatures of the stable branch of the curve and it increases the scalar dissipation rate at extinction  $\chi_q$ . This temperature increase also translates into higher heat fluxes between burned and unburned mixtures. Part of this increase is also attributable to gradients of the heat capacity. The reason for this influence is explained by the significant difference in heat capacities between fuel and oxidant species. Nonetheless, differential diffusion enables the flame to sustain higher scalar dissipation rates without extinguishing. In the unstable branch it can be seen a convergence between both models between  $\chi_{st} = 1$  and 10. Afterwards, the curves diverge again. In any case, accounting for differential diffusion results in the ignition region of the S-shaped beginning at lower temperatures. Thus, igniting flamelets are found at slightly lower temperatures. In this region, the effect of the heat capacity is limited when compared to its effect on the upper branch.

Comparing the two chemical mechanisms, GRI2.11 against GRI3.0, there is a small effect in the accessible regions of the flame. For the GRI2.11, the extinction scalar dissipation rate is marginally increased and temperatures at the stoichiometric mixture fraction are slightly decreased. Therefore, no significant differences between both mechanisms with regard to the ignition and extinction of the flame for this configuration is expected. Nonetheless, it is interesting to note that at the smallest  $\chi_{st}$  of the stable branch, the effect of the chemical mechanisms is almost negligible, whereas close to  $\chi_q$  the effect is small but noticeable. Along the unstable branch, a similar effect is observed.

#### 4.3.2 Progress-variable definition - steady

The FPV model assumes a bijective relation between the progress-variable at the stoichiometric mixture fraction,  $\Lambda$ , and the progress-variable,  $c$ , at each mixture fraction. Consequently, the progress-variable must be a monotonic function, ranging between the extinguished state and the steady stable burning solution.

In Fig. 4.3 are shown the progress-variable values obtained from the steady flamelet equations with differential diffusion at different stoichiometric scalar dissipation rates as a function of the mixture fraction for the two definitions considered. It can be seen that the progress-variable parameter  $\Lambda$  is monotonic in all cases. Regarding the considered definitions, it can be seen that neither *CD1* nor *CD2* result in a bijective relation. Furthermore, *CD1* shows overlapping regions around the stable and unstable regions. In the former, near  $Z_{st}$  at low  $\chi_{st}$  and for the latter at high mixture fraction regions *CD2* improves the definition in both branches. At the stable

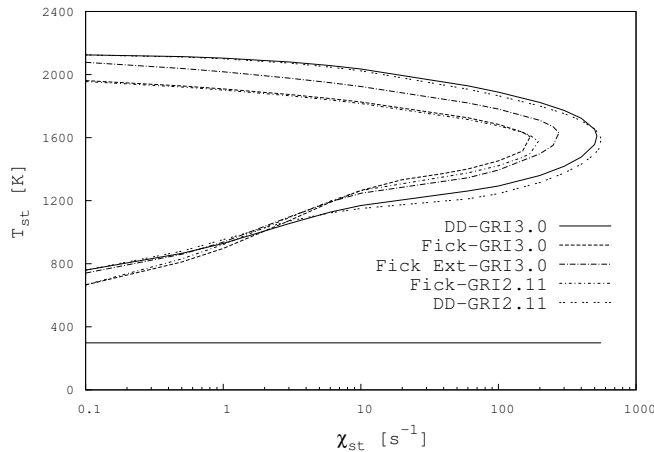


**Figure 4.2:** S-shaped curve for a  $CH_4/H_2/N_2$  diffusion jet flame. Curves with differential diffusion effects are denoted by *DD*.

branch is monotonic except at low  $\chi_{st}$ . The smallest included  $\chi_{st}$  is 0.1, and it has been seen that up to  $\chi_{st} = 0.2$ , *CD2* definition is bijective, see the inset in Fig. 4.3b.

Concerning the chemical mechanism, there is a slight difference at the unstable branch, where the GRI2.11 manifests a smaller overlapping than the GRI3.0. However, at the stable branches when the GRI2.11 is used there is a slight overlapping at intermediate scalar dissipation rates  $\chi_{st} = [1, 10]$ . On the contrary, the GRI3.0 does not manifest this behaviour.

If Fickian diffusion is used, shown in Fig. 4.4, and considering *CD2* definition, Eq. (4.12) is bijective at the stable branch for both mechanisms. However, the unstable branch is poorly represented, as there is a large overlapping of solutions at high mixture fraction values. *CD1* definition results in a better description of the unstable branch. Nonetheless, it is not monotonic. Furthermore, a marked non-monotonic region is observed around the stable branch at the rich side of the flame. Considering the chemical mechanism, similar trends are observed in both cases.

The overlap at the unstable branch is found at small  $\chi_{st}$  as the peak of the progress-variable is displaced from values close to  $Z_{st}$  to values closer to  $Z = 0.5$ , which is the point where the scalar dissipation peaks. Both diffusion models feature similar effects regarding the flamelets profiles.

Considering the extended Fickian flamelet equations, Eq. (4.7), for the species distributions around the stable branch no significant differences with respect to the baseline results are observed. Differences are found in the temperature profiles at

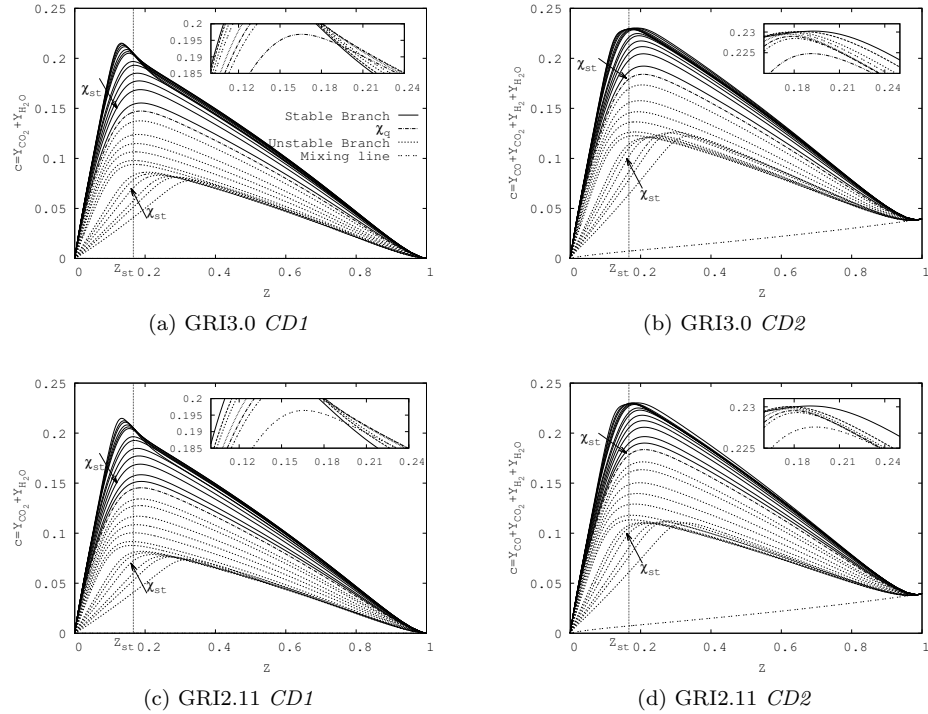


**Figure 4.3:** Progress-variable definition for a steady laminar flamelet using differential diffusion. Arrows indicate increasing  $\chi_{st}$ . Note that the legend applies only to the big plot, the inset line-styles are set to distinguish between different curves of the stable branch.

the unstable branch. For the base Fickian diffusion model, past the stoichiometric mixture fraction, the temperature profile is curved instead of a straight line due to the presence of the heat capacity gradients. Regarding the “extended” one, it can be seen in Fig. 4.5 that the overlapping regions are greatly reduced. However, including  $CO$  and  $H_2$ ,  $CD2$  definition, causes overlapping regions to reappear. Therefore, the overlap reduction seen in the differential diffusion model is basically due to heat capacity gradients term in the flamelet equations.

Overall, there is a competing effect in the progress-variable definition when including  $H_2$  and  $CO$ . On the one hand, including them improves the mapping of the flamelet solutions around the upper branch. On the other hand, these species cause the opposite effect around the unstable branch. However, when differential diffusion

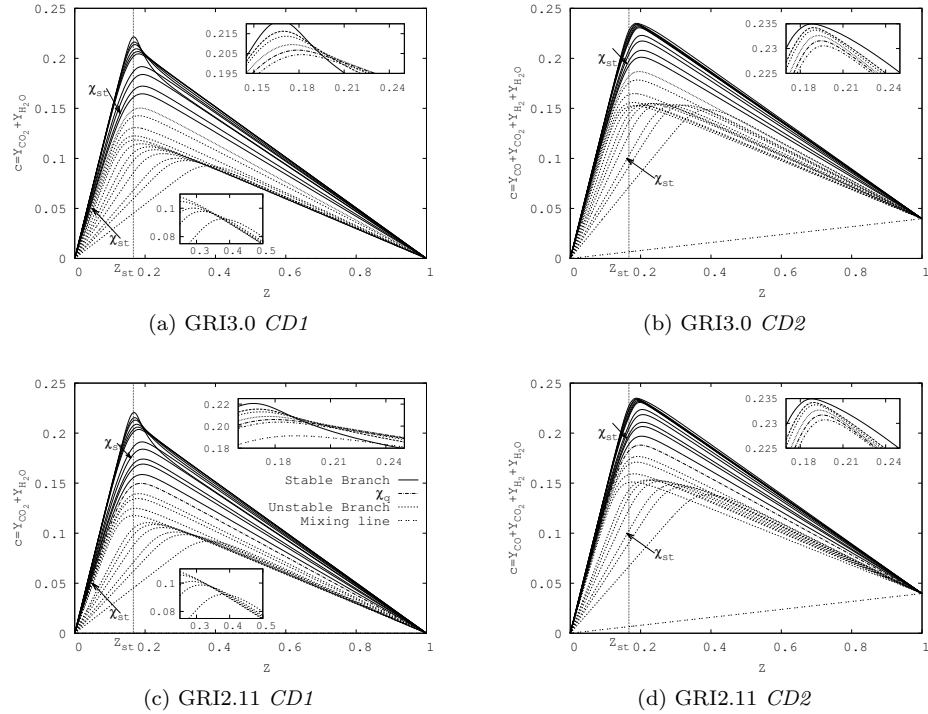


**Figure 4.4:** Progress-variable definition for a steady laminar flamelet using Fickian diffusion. See comments of Fig. 4.3 for further details.

is considered, the overlapping is less pronounced. With *CD2*, a smoother evolution of the progress-variable in the upper curve region is observed using Fickian diffusion. On the contrary, the differential diffusion model results into a more cramped flamelet solution, see insets in Fig. 4.3b, 4.3d, 4.4b and 4.4d. If each specie is analysed separately, it is observed that  $CO_2$  curves overlap near the stable branch, whereas the  $H_2O$  ones overlap near the unstable branch.  $H_2$  and  $CO$  feature complex evolution. It is then difficult to manually find an optimal definition for the progress-variable. A coefficient optimisation, which could include other minor species, such as the one proposed by Ihme et al. [10] or similar, would be required to obtain a fully bijective relation. Nevertheless, CFD results to be presented in the following sections show that *CD2* with minor modifications is adequate for the current case. Alternative definitions using mainly major species, such as  $c = Y_{CO} + Y_{CO_2}$ , result also, for the present case, in Eq. (4.12) being non-monotonic.

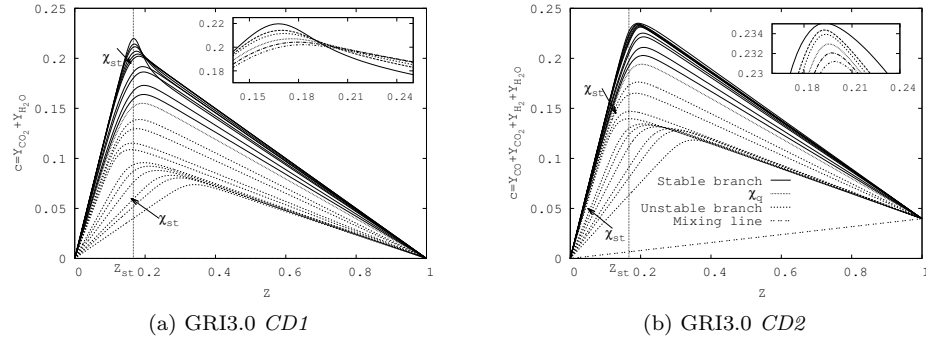


**Figure 4.5:** Progress-variable definition for a steady laminar flamelet using the extended Fickian diffusion. See comments of Fig. 4.3 for further details.

Fig. 4.3 and 4.4 also depict the difference in ignited regions seen in Fig. 4.2. The differential diffusion model features a larger region of ignited solutions and consequently, larger ignited reaction rates. This will be shown to have direct consequences during CFD simulations. Additionally, at the unstable branch as  $\chi_{st}$  is reduced, a subtle effect of the diffusion model can be seen in the figures. For both models, a  $\chi_{st}$  reduction results in a lower value of the flamelet maximum progress-variable and a displacement of this maximum towards  $Z = 0.5$ , where the maxima of the  $\chi$  distribution is located. *CD1* shows a similar trend for both diffusion models, where  $CO_2$  and  $H_2O$  mass fractions are reduced. However, *CD2* shows interesting differences. It can be seen that there is a local minimum for all cases. On the one hand, for flamelets with the GRI3.0 mechanism, the flamelet maximum does not change. On the other hand, the GRI2.11 shows a continuous decrease after going through a local maximum. Thus, highlighting differences in  $H_2$  and  $CO$  predictions between chemical mechanisms at intermediate temperatures. The just described phenomenon is not fully captured by the S-shaped curve.

### 4.3.3 Progress-variable definition - unsteady

When the unsteady FPV model is considered, the scalar dissipation rate at stoichiometric mixture fraction is used as an additional parameter. Therefore, the progress-variable follows the ignition/extinction process of the mixture at a constant  $\chi_{st}$ . Hence, the monotonic evolution of the progress-variable is evaluated at each  $\chi_{st}$  independently.

For the unsteady flamelets with differential diffusion, no significant differences, regarding the monotonic growth of the progress-variable are observed between *CD1* or *CD2*. In both cases the progress-variable is non-monotonic as the ignition process

approaches the stable solution, as shown in Fig. 4.6 for *CD2*. However, if the mass fraction of  $C_2H_2$  is added to the summation, with a coefficient of 5, the resulting definition is monotonic, excepting for the lowest  $\chi_{st} = 0.1$ . However, at  $\chi_{st} = 0.5$ , the definition is bijective. It should be noted, that the resulting reaction rate of the progress-variable is not always positive. Near the stable solution, the reaction rate becomes slightly negative. The use of minor species with a large coefficient is required since major product species account for most of the mass fraction near the stable branch. Alternatively, a combination of the major product species,  $CO$ ,  $CO_2$ ,  $H_2$  and  $H_2O$  using a non-trivial set of coefficients could probably result in a uniquely mapping of the flamelet evolution at each  $\chi_{st}$ . Nonetheless, the proposed approach, which is to add  $C_2H_2$ , is viable if the range of flamelets is limited to  $\chi_{st} \geq 0.5$ .

Concerning the chemical mechanisms, no noticeable differences regarding the monotonic growth of the progress-variable are observed between them. Therefore, only results with the GRI3.0 are shown. As the stoichiometric scalar dissipation rate is increased, lower overlapping is found.

Unsteady flamelets with Fickian diffusion are correctly described using *CD1* definition for the progress-variable at all  $\chi_{st}$ , as shown in Fig. 4.7. Addition of  $H_2$  and  $CO$  results in a non-monotonic evolution for  $\chi_{st} \leq 10$ , as it can be seen in Fig. 4.7a and Fig. 4.7b for *CD2* definition. Addition of  $C_2H_2$  has the same effect in correcting *CD2* as in the differential diffusion case.

Comparing results from cases with differential and Fickian diffusion, it is found that the higher/lower mobility of light/heavy species results in a modified pool of reactants during the transient ignition. This leads to a larger local production of  $CO_2$  and  $H_2O$ , which afterwards diffuses, causing the non-monotonic evolution as the peak is reduced. On the other hand, with the Fickian diffusion model, created species diffuse at enough speed so as not to build-up a large pool of products. Focusing on the cases at low  $\chi_{st}$ , when Fickian diffusion is considered, ignition is seen to start around the peak of the unstable branch and as the mixture reacts it diffuses heat and reactants simultaneously up to the equilibrium values. However, when differential diffusion is accounted for, a narrow reaction zone can be identified, which evolves the progress-variable locally. Then, after the reaction has been completed, it diffuses heat and products until the steady state solution is reached, namely the stable branch solution. Comparing the flamelet evolution at high scalar dissipation rates, Fig. 4.6d and 4.7d, it can be seen that they feature similar transitions. This indicates that diffusion due to species gradients is dominant, thus concealing differential diffusion effects. Comparison of the ignited solutions at  $\chi_{st} = 100$ , Fig. 4.6d and 4.7d, shows that for the Fickian case the region of ignited solutions is narrower than in the differential diffusion case. The reason is that for this  $\chi_{st}$  the Fickian flamelet is closer to the extinction scalar dissipation rate  $\chi_q$  than the one with differential diffusion, depicted as the turning point in Fig. 4.2.

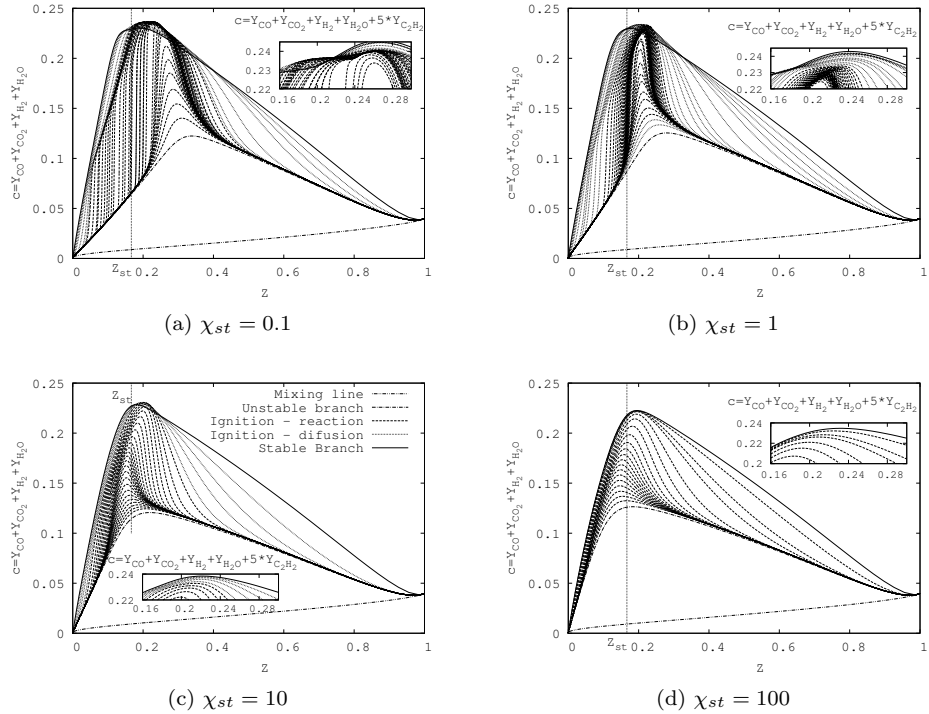


**Figure 4.6:** Progress-variable for unsteady laminar flamelets using differential diffusion. The extinction process is not shown as no overlapping of solutions is found. The inset plot shows the non-bijective region using a modified *CD2* definition, where the mass fraction of  $C_2H_2$  is taken into account.

Similarly, in the extinction process, between the unstable branch and the mixing line, which is not shown in the figures, a monotonic evolution of the progress-variable is obtained in all cases, Fickian or differential diffusion, using either *CD1* or *CD2*.

Regarding the progress-variable evolution, a limited influence of the heat capacity gradients is observed. Fig. 4.8 shows the ignition at  $\chi_{st} = 0.1$  and 1, and it can readily be seen that they show similar evolutions compared to Fig. 4.7. Therefore, differences between Fickian and differential diffusion models are not attributable to heat capacity gradients.

Compared to the steady FPV model, adding  $H_2$  and  $CO$  to the progress-variable in the unsteady FPV model results in non-monotonic evolution near the stable branch at each  $\chi_{st}$  due to an overproduction of intermediate species. After reaching their peak

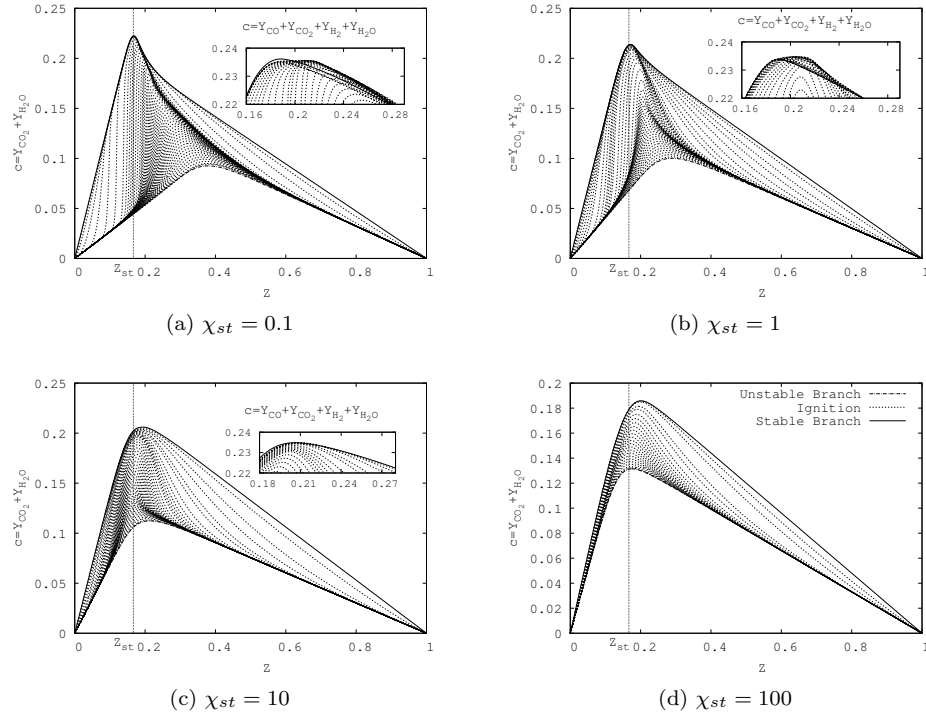


**Figure 4.7:** Progress-variable for unsteady laminar flamelets using Fickian diffusion. Vertical axis corresponds to  $CD1$ , whereas the inset shows the progress-variable around the curve peak using  $CD2$ .

value, they recombine into more stable molecules and/or diffuse away. Furthermore, when differential diffusion is taken into account, this peak is more pronounced, which can be related to the narrower ignition process observed.

#### 4.3.4 Progress-variable definition - radiation

In order to consider radiation effects, a subset of the flamelet space is considered. The parameters of the database are the mixture fraction, the progress-variable and the mixture enthalpy. However, in the following analysis, the definition of the progress-variable is studied independently from the enthalpy because the generation of the flamelet database is performed by means of unsteady flamelets with radiation at constant  $\chi_{st}$ . Besides, the enthalpy as a function of the mixture fraction is not shown since it is unambiguously defined and its evolution is monotonic. The enthalpy

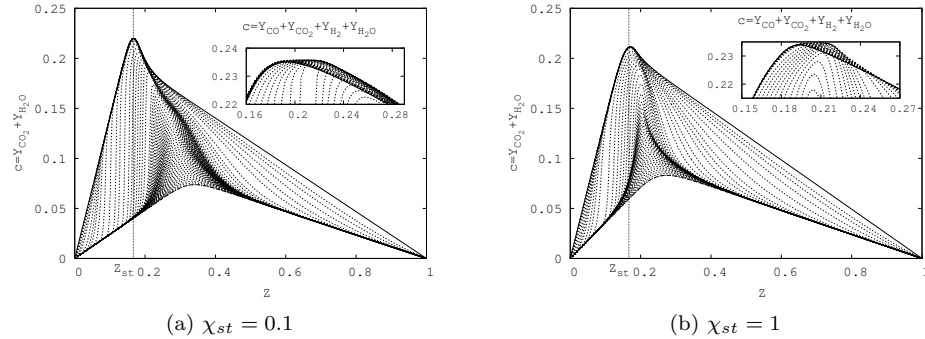


**Figure 4.8:** Progress-variable for unsteady laminar flamelets with extended Fickian diffusion model. See Fig. 4.7 for further explanation.

decreases as radiation heat losses increase.

Beginning with the accessible burning region, Fig. 4.9 shows that at low  $\chi_{st}$ , the stable solutions considering radiation tend to similar temperatures at stoichiometric mixture fraction, regardless of the diffusion model. This suggests that when radiation plays a significant role, differences between Fickian and differential diffusion become less pronounced, even though the adiabatic temperatures are significantly different. The extended Fickian model also follows this trend. Furthermore, as shown in Fig. 4.2, the main difference between the two variants of the Fickian diffusion model is found at the stable burning branch. Therefore, as in the steady FPV model, part of the differences between diffusion models are accountable to gradients of the heat capacity. Regarding the chemical mechanism, the trends are similar for both chemical mechanisms. Fig. 4.9 is obtained for the GRI3.0, but no significant differences are found when the GRI2.11 is used. This is consistent with the similar behaviour between the two mechanism at the stable burning branch for this flame.

In Fig. 4.10 and 4.11 are shown the progress-variable profiles using differential and Fickian diffusion, respectively. Results are shown for  $\chi_{st} = 0.1$ . Similar trends are observed at higher scalar dissipation rates. It should be noted that temperature decreases from the adiabatic solution to the “radiation” stable solution, which is the flamelet stable solution at a given  $\chi_{st}$  with radiation considered.

First of all, a similar trend, regarding  $CD1$  and  $CD2$ , is observed in both differential and Fickian diffusion models. On the one hand, when  $CD1$  is used, the progress-variable evolves increasing its value from the steady adiabatic solution to the steady “radiation” solution, as it can be seen in Fig. 4.10a, 4.10c, 4.11a and 4.11c. On the other hand, using  $CD2$ , that is including  $CO$  and  $H_2$ , causes the opposite behaviour, the progress-variable evolves decreasing its value from the steady adia-

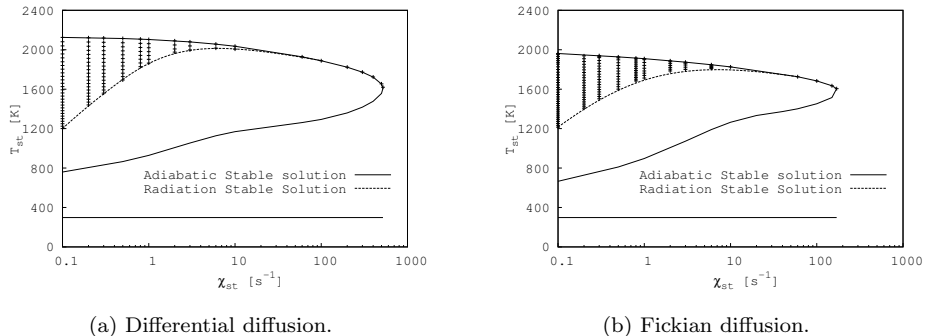


**Figure 4.9:** S-shaped curve depicting the radiation flamelet subspace as the area between the adiabatic and "radiation" curves. Results obtained using the GRI3.0 mechanism.

batic solution to the steady "radiation" solution, shown in Fig. 4.10b, 4.10d, 4.11b and 4.11d. Albeit this clear trends, no general conclusions can be drawn from it, because the four species feature complex evolutions, changing from increase to decrease around the stoichiometric mixture fraction, and at some regions close to the oxidiser boundary, which can be inferred from the insets in Fig. 4.10 and 4.11. Furthermore, the change of each specie's mass fraction is different. For example,  $H_2O$  is the dominant specie. However, its variation is small compared to  $CO_2$ , which features a larger change ( $\Delta Y_{CO_2} > \Delta Y_{H_2O}$ ), but its absolute mass fraction is lower than  $H_2O$  ( $Y_{H_2O} > Y_{CO_2}$ ). Therefore,  $CD1$  mostly tracks  $H_2O$  mass fraction with the variations of  $CO_2$ .

Considering  $CD1$  definition with the differential diffusion model, it can be seen in Fig. 4.10 that it behaves monotonically at almost all mixture fractions. However, there is a small region where Eq. (4.12) is not bijective. Furthermore, addition of  $H_2$  and  $CO$ ,  $CD2$  variant, results in two non-bijective regions. Taking into account the previous discussion regarding the behaviour of the different species composing  $CD2$ , a variant of this definition using different weights for each species has been found to result in a monotonic evolution of the progress-variable. The new definition is  $c = 0.5Y_{CO} - Y_{CO_2} + Y_{H_2} + Y_{H_2O}$  and is shown in the inset at the top right corner of Fig. 4.10b. A minor drawback is that the resulting reaction rate of the progress-variable is slightly negative around the uppermost curve for a small range of mixture fractions.

When Fickian diffusion is considered, use of  $CD1$  results in a large non-bijective region close to  $Z_{st}$ . Opposite to the differential diffusion case,  $CD2$  is almost bijective. However, there remains a small non-monotonic region at  $Z < Z_{st}$ . The variant used

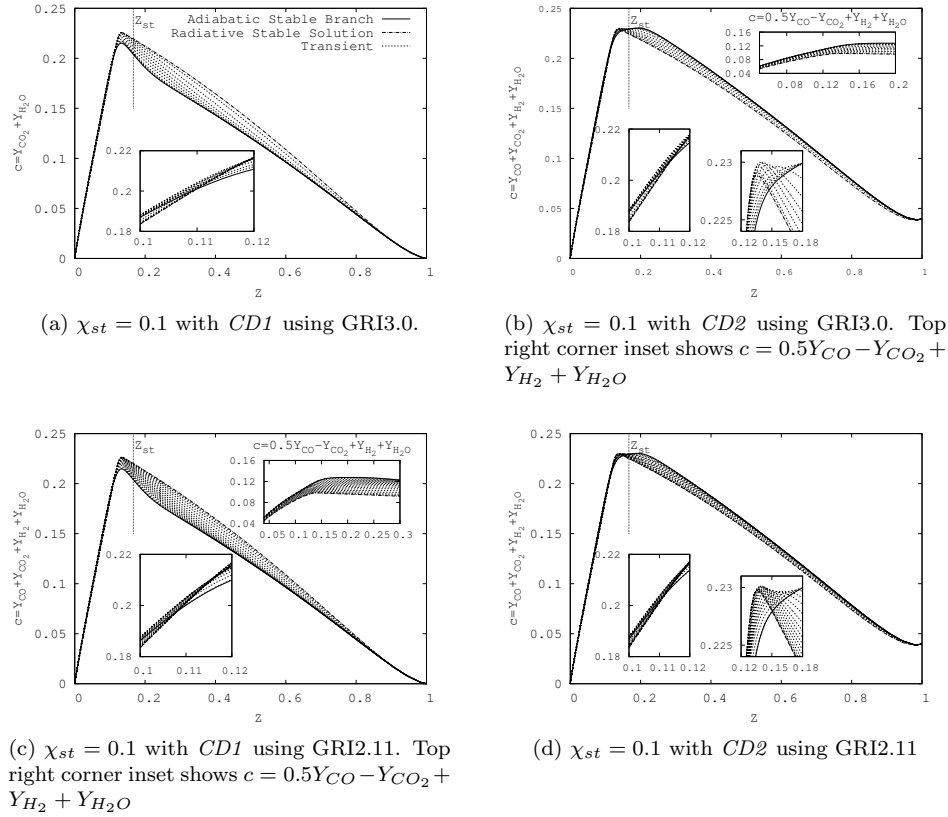


**Figure 4.10:** Progress-variable for radiation flamelets with differential diffusion.

for the differential diffusion model, in which  $CO_2$  had a negative coefficient, does not correct the problem in flamelets using the Fickian diffusion model. The reason is again related to the evolution of  $CO_2$  and  $H_2O$ , which present different trends when the Fickian diffusion model is used. Addition of  $OH$  and  $C_2H_2$  with adequate coefficients to  $CD2$ ,  $c = Y_{CO} + Y_{CO_2} + Y_{H_2} + Y_{H_2O} + 5Y_{OH} - 0.1Y_{C_2H_2}$ , corrects the overlapping. However, similarly to the differential diffusion model, slightly negative reaction rates at the uppermost curves are obtained.

Regarding the extended Fickian model no significant differences with respect to the base Fickian model are observed concerning the progress-variable.  $CD1$  shows the overlapping region around  $Z_{st}$ , which  $CD2$  reduces, but does not fully resolve. The variant using  $OH$  and  $C_2H_2$  fixes the overlapping, with the same issues about

the reaction rate.

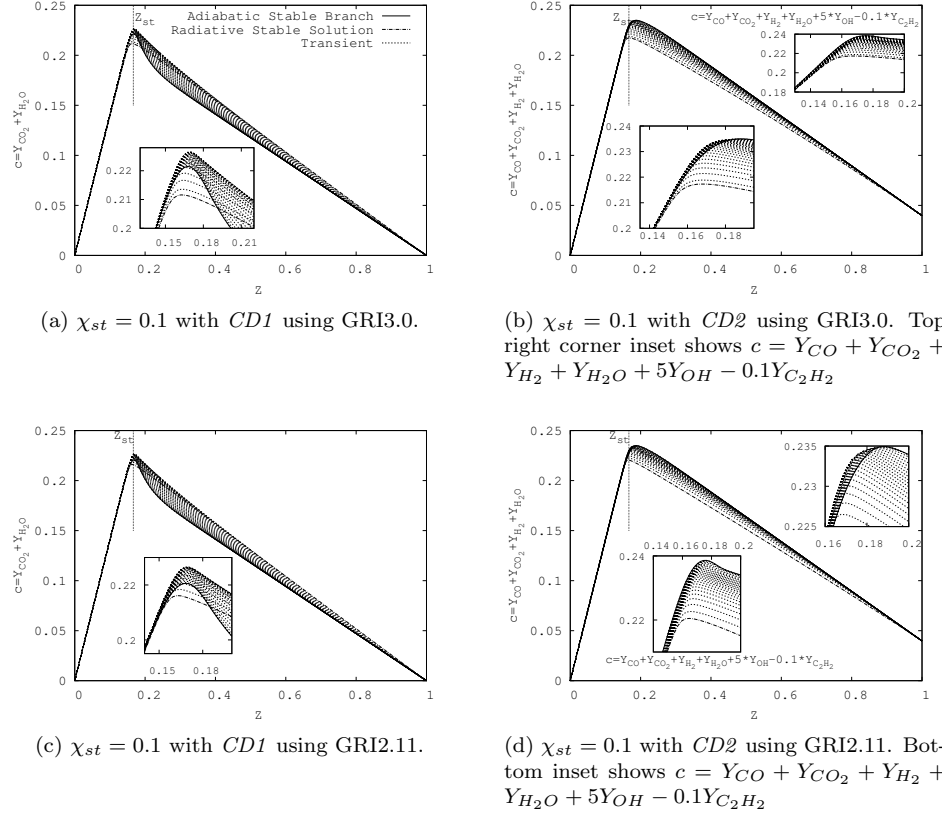


**Figure 4.11:** Progress-variable for radiation flamelets with Fickian diffusion.

In addition, no significant differences between chemical mechanisms have been observed concerning the monotonic growth of the progress-variable. Still, in Fig. 4.10 and 4.11, when the GRI2.11 is used, both definitions of the progress-variable show a larger overlap compared to the GRI3.0. Nonetheless, both mechanisms show similar sensitivity to the diffusion model and progress-variable definition.

As a side note, the flamelet model with heat losses is usually used when slow processes, such as radiation or *NO* formation are of interest. Additionally, it has been reported that the GRI3.0 NO predictions are higher than with the GRI2.11 [12]. Comparing *NO* profiles from flamelets using either mechanism shows 20% difference in peak *NO* at low  $\chi_{st}$ . However, as stated, no significant differences are observed for

major species, which are used to define the progress-variable.

#### 4.3.5 CFD analysis

Large Eddy Simulation (LES) have been performed in order to test the differences between the databases created using Fickian and differential diffusion. The computational domain is  $75D_j$  in the axial direction, with a circular base of  $11.5D_j$  and an upstream base of  $31.5D_j$ . A structured mesh of around 1.9MCV has been used, consisting of  $645x95x32$  nodes in the axial, radial and azimuthal directions, respectively. The mesh has been stretched close to the central jet, where cell size is around 15-20 times the Kolmogorov scale. Thus, ensuring that the subgrid scales ( $sgs$ ) model was working in the inertial range. Turbulent fluxes have been modelled using an eddy diffusivity model with the turbulent viscosity evaluated using the WALE  $sgs$  model [31].

Up so far, the discussion was centred around the laminar database. However, in LES Favre filtered quantities are obtained from the CFD simulations. Therefore, it is necessary to restate the database as a function of turbulent Favre-filtered variables. The statistical distributions of the variables used to create the flamelet database are presumed, allowing to retain the preprocessing advantage of the method. Hence, the mixture fraction statistical distribution is modelled using a  $\beta$ -pdf and a  $\delta$ -pdf for the progress-variable [4]. The resulting state relation for the SFPV model is then

$$\tilde{\phi} = \iint \zeta_\phi(Z, \Lambda) \tilde{P}(Z, \Lambda) dZ dc = \iint \zeta_\phi(Z, \Lambda) \tilde{\beta}(Z; \tilde{Z}, Z_v) \tilde{P}(\Lambda - \tilde{\Lambda}) dZ d\Lambda = \tilde{F}(\tilde{Z}, Z_v, \tilde{c}) \quad (4.18)$$

where  $Z_v$  is the subfilter variance of the mixture fraction and a bijective relation between  $\tilde{\Lambda}$  and the progress-variable is assumed, as in Eq. (4.12). Evaluation of subgrid mixture fraction variance and subfilter scalar dissipation rate is performed through a scale similarity model [32], which assumes a local equilibrium between production and dissipation of the variance at the small scales. When the unsteady or radiation databases are used, in Eq. (4.18),  $\delta$ -pdfs are assumed for  $\chi_{st}$  [5, 7] and for the enthalpy at stoichiometric mixture fraction  $H = h|Z_{st}$  [33]. For the latter, as with the progress-variable, a bijective relation between  $H = h|Z_{st}$  and  $h$  is assumed. Therefore, the database is parametrised as a function of the latter. For the simulations including radiation heat losses, an OTM is used, computed using Eq. (4.17), as done in the flamelet calculations.

A database with  $100x25x100$  points in the  $\tilde{Z}, Z_v, \tilde{c}$  directions was created. For the unsteady variant 13 different transient flamelets were considered. The radiation variant, due to computational limitations, used  $75x25x75x65$  points in  $\tilde{Z}, Z_v, \tilde{c}$  and  $\tilde{h}$  directions.

Following the discussion in the previous section, the progress-variable is defined using the most suitable definition for each flamelet model. The current flame has

been reported to be attached to the fuel nozzle and to feature low levels of extinction and re-ignition. Furthermore, experimental conditional profiles [13] are seen to match mostly the flamelet profiles of the burning branch. Therefore, for the SFPV, *CD2* definition is used, since it results in a better description of the stable burning branch. Besides, chemical reactions are mostly taking place at lean mixture fractions. Hence, the overlapping at high mixture fraction values and around the unstable branch should have limited consequences. In order to create the database, in this particular region, the flamelet variables are replaced by a monotonic evolution between the adjacent bijective regions. Computations using the UFPV model use the modified variant of *CD2* with  $\chi_{st} > 0.5$ . Similarly, simulations with the RFPV including differential diffusion use *CD2* variant with a negative coefficient for  $CO_2$ .

Instantaneous snapshots of the progress-variable are shown in Fig. 4.12 using the different variants of the FPV model. The SFPV using either Fickian or extended Fickian diffusion models resulted in a flame lift-off and the flame stabilising at around  $30D_j$ , where jet velocities are low, as shown in Fig. 4.12a and Fig. 4.12b respectively. Since the Fickian case showed a large non-bijective region at the unstable branch, a simulation was run using *CD1* to rule out the progress-variable definition as cause for the flame lift-off. Nonetheless, the flame did also lift-off. When the database considering differential diffusion was used, flame stabilisation was found closer to the fuel jet nozzle, Fig. 4.12c, and with a shape similar to those of the experiments. The difference in stabilisation distance, for the steady FPV model, between Fickian and differential diffusion models may be related to the differences in the S-shaped curve, Fig. 4.2. For the latter model, the ignition region begins at lower temperatures, thus the flame reaches sooner the ignition region, where the reaction rate starts to grow non-linearly. Furthermore, when differential diffusion is considered, the stable branch is located at higher temperatures, which results in higher heat and mass fluxes once the mixture has reached the stable burning conditions. Nonetheless, using the SPFV model, in all cases the flame lifts-off, which is not in accordance with the experimental results. However, differential diffusion shows a significant effect in the stabilisation of the flame. Similarly, Chan et al. [34] also found that differential diffusion played a significant role in the stability of the flame when studying a flame in a jet-in-cross-flow.

Current results using the UFPV model do not show a significant improvement regarding the stabilisation distance. The reason is that the region under the unstable branch, and focusing on the reaction rate profiles, is similar between the unsteady and steady FPV variants. Hence, it is not until the progress-variable has increased enough, up to the unstable branch, that differences between both variants are perceptible. This can be observed in Fig. 4.13, where differences between reaction rates profiles at different mixture fractions are shown. Furthermore, experimentally the flame is seen to be immediately ignited, thus it reaches the stable burning branch rapidly. Therefore, transient effects should be of secondary importance and thus, no significant

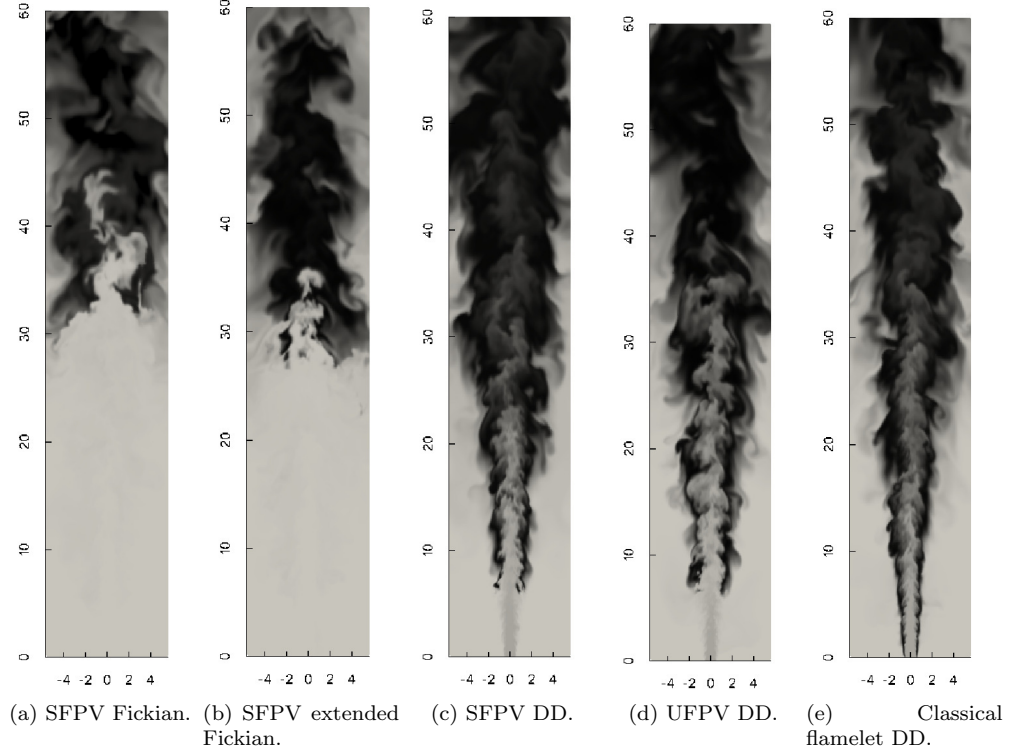


**Figure 4.12:** Instantaneous snapshots of CFD results using different flamelet and diffusion models. *DD* indicates differential diffusion. Black indicates the maximum progress-variable and light-grey indicates a zero progress-variable. The domain shown has been clipped for plotting purposes. Dimensions have been made non-dimensional using the fuel nozzle diameter  $D_j$ .

differences would be expected between steady and unsteady models.

An important aspect to consider is that the assumed *pdf* for the progress-variable can limit the effectiveness of the model. A  $\delta$ -pdf assumption implies that a particular control volume can be characterised by a single flamelet. Plotting the progress-variable reaction rate against the progress-variable it can be seen that at lean mixture fraction values the SFPV database contains higher values of the reaction rate than the unsteady one. However, as the stoichiometric mixture fraction is approached, the unsteady database, at intermediate  $\chi_{st}$ , contains higher reaction rates. In Fig. 4.13 it is shown the reaction rate as a function of the progress-variable for three mixture frac-

tions, between the oxidiser boundary and the stoichiometric mixture fraction. Close to the fuel jet nozzle, little diffusion between fuel and oxidiser has taken place. Thus the lean and rich side of the database are accessed, being the former region more chemically active. As it can be seen, at  $Z = 0.05$ , the database with the SPFV model includes higher reaction rates at smaller values of the progress-variable.

Nonetheless, for both steady and unsteady models, the  $\delta$ -pdf implies that the progress-variable fluctuations do not influence the retrieved reaction rate from the database. It has been reported that the progress-variable features a complex bimodal probability distribution [6, 35]. Pdfs such as the  $\beta$ -pdf [6] or the Statistically Most Likely Distributions (SLMD) [36] have been proposed to be used with different degrees of success. As the reaction rate is a highly non-linear function, we presume that accounting for the progress-variable fluctuations would lead to a correct characterisation of the flame stabilisation. The reason is that with a  $\delta - \text{pdf}$  the flame state is represented by the flamelet at the computed mean progress-variable value. If subgrid fluctuations are taken into account and focusing on the reaction rate, this results in flamelets at higher and lower mean progress-variable values to influence the current state. Therefore, at low progress-variable values, accounting for the subgrid variance causes flamelets with higher reaction rates to increase the “laminar” value. Similarly, flamelets at high values of the progress-variable experience a decrease in their reaction rate, since flamelets with lower reaction rates are also included. Since the observed phenomenon is that the flame lifts-off, we presume that not accounting for this interactions at the subgrid level is the main reason for the difference between the numerical computations and the experimental results.

From Fig. 4.13 it can also clearly be seen why with the Fickian database the flame stabilises at higher axial distances. The reaction rate at very lean mixture fractions, Fig. 4.13a, is almost non-existent, and it is not until the mixture reaches stoichiometric conditions and the progress-variable has increased sufficiently that the reaction rate takes high enough values to sustain the combustion.

When the classical flamelet model is used, which only includes solutions at the upper stable branch and extinguished solutions for scalar dissipation rates higher than  $\chi_q$ , an attached flame to the fuel nozzle rim results. The rationale is that the classical flamelet projects the solution to the stable burning branch for  $\chi_{st} < \chi_q$ , because it only considers the stable burning subset of solutions of the flamelet database. Hence, the mixture becomes ignited once the scalar dissipation rate is lower than the extinction one, without transient evolution. Besides, regarding the stabilisation no differences are observed between Fickian and differential diffusion because  $\chi_{st}$  is higher than  $\chi_q$  only in a small region close to the fuel nozzle rim. Then, as soon as  $\chi_{st}(y) < \chi_q$  the flame becomes ignited instantly, where  $y$  indicates axial location.

Similarly, when the radiation FPV model was used an attached flame to the fuel

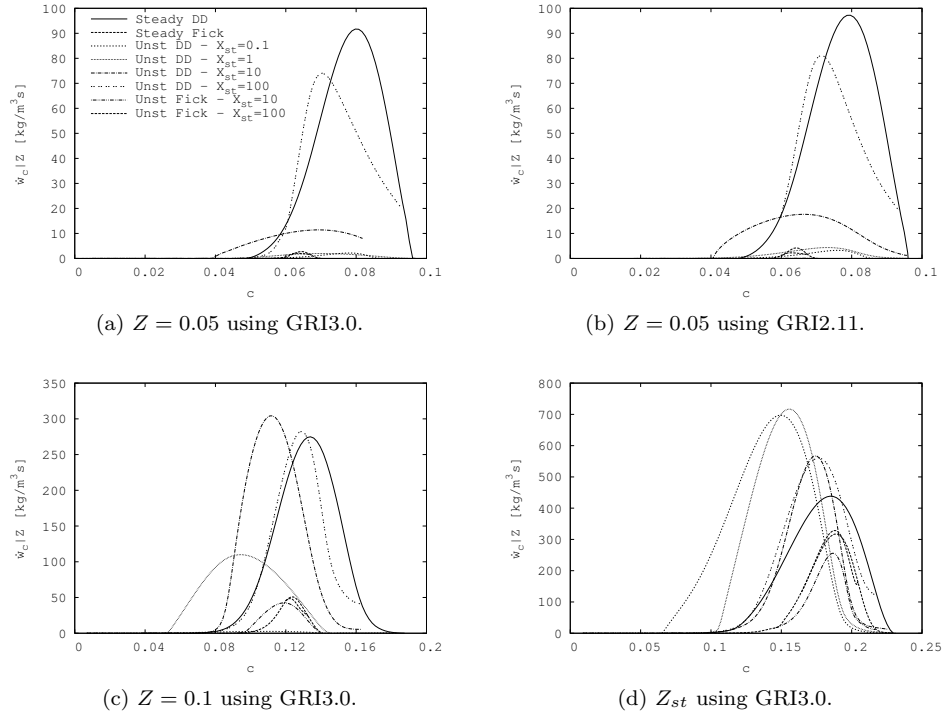


**Figure 4.13:** Progress-variable reaction rate as function of the progress-variable at different mixture fraction. *DD* stands for differential diffusion.

nozzle rim resulted. The rationale is that the RFPV model behaves similarly to the classical steady flamelet model in this regard, because it also only considers the stable burning subset of solutions of the flamelet database. Evidently, since the the RFPV model includes more flamelet solutions for  $\chi_{st} < \chi_q$ , predicted temperatures and species concentrations will differ from the ones predicted by the classical flamelet. However, concerning flame stabilisation location both models are equivalent.

A further issue to consider for improving the stabilisation of the flame would be the assumptions made regarding the closure of the subgrid terms, which exceeds the purpose of the present chapter, but is studied in *Chapter 5*. Briefly, the current approach assumes an equilibrium between production and destruction of the mixture fraction variance at the subgrid level. Models not relying on this assumption can be found in the literature, where the mixture fraction variance is either computed through its transport equation [7] or through its statistical definition [37]. The latter

approach requires a transport equation for the filtered squared mixture fraction  $\widetilde{Z}^2$ . In both cases, closure for the subgrid scalar dissipation rate is also required. About the progress-variable, it has already been discussed the limitations of the present approach.

Nonetheless, it can be clearly seen that including differential diffusion in the flamelet database not only does it affect the actual definition of one of the model parameters, the progress-variable, but also plays an important role in the stabilisation of the flame.

#### 4.4 Turbulent auto-igniting diffusion $CH_4$ flame - Cabra flame

The second case of study is a self-igniting flame, which uses methane as fuel, and was experimentally studied by Cabra et al. [15] and Gordon [38]. It consists of a  $D_j = 4.57\text{mm}$  wide jet, through which a mixture of methane and air at  $320K$  issues with a bulk velocity of  $100\text{m/s}$ , resulting in a Reynolds number of 24760. The experiment was devised to provide a definite composition of the hot products. Particularly, the coflow composition is the result of a premixed hydrogen-air combustion. Table 4.1 shows the detailed composition of both streams.

Recirculation of hot combustion products into either fuel or oxidizer streams is a technique that has been shown to reduce flame temperatures, and consequently reduce NOx formation, together with increased flame stability. Technical applications are found in Flameless and MILD combustion modes, and exhaust gas recirculation (EGR) in internal combustion engines. Similarly, in gas turbines, the oxidizer is preheated due to the flow compression prior to reaching the combustion chamber. Due to the increased temperature, autoignition becomes a key characteristic, which must be properly described by the combustion model.

	D[mm]	V[m/s]	T[K]	$X_{CH_4}$	$X_{O_2}$	$X_{N_2}$	$X_{H_2O}$	$X_{OH}$	$X_{H_2}$
Jet	4.57	100	320	0.3275	0.1452	0.5243	0.0029	-	0.0001
Coflow	210	5.4	1350	0.0003	0.1193	0.728	0.1516	0.0002	0.0002

**Table 4.1:**  $CH_4$  lifted jet flame parameters.

Although both fuel and oxidiser streams are dominated by species with similar Lewis numbers, it is shown that accounting for differential diffusion affects the pool of reactants during the induction period prior to the flame ignition. Usually, Fickian diffusion would be assumed, since the major species Lewis numbers are similar. However, in order to fully characterise the flame, differential diffusion is accounted for.

As done in the previous flame, first the flamelet database is analysed and then

CFD simulation results are presented.

#### 4.4.1 S-shaped curve

Representation of the transient behaviour of the flame is critical in characterising auto-igniting flames. Therefore, the steady FPV model is not adequate and is not considered for this case. Similarly, the radiation variant is also not suitable, as it only accounts for the stable burning solution. Therefore, only the unsteady FPV model is considered. Nonetheless, it is of interest to first analyse the accessible region of burning solutions through the analysis of the S-shaped curve.

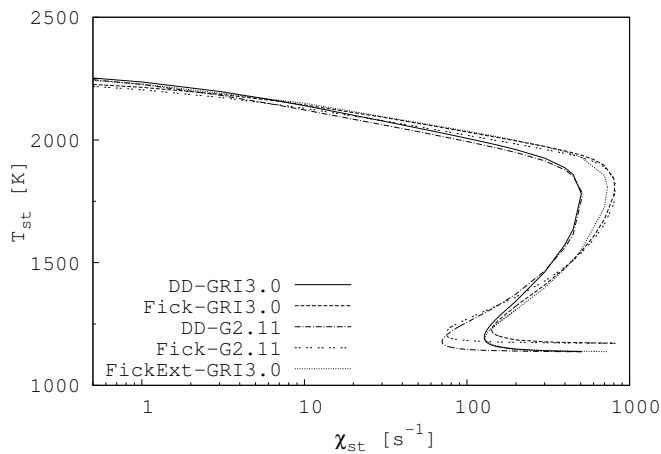


**Figure 4.14:**  $CH_4$  self-igniting flame S-shaped curve. *DD* stands for differential diffusion.

Even though there are not species with Lewis number much different than 1 at the boundaries of the current case, Fig. 4.14 shows a clear difference between Fickian and differential diffusion models regarding the extinction scalar dissipation rate  $\chi_q$ . When Fickian diffusion is considered, the mixture remains ignited at higher  $\chi_{st}$ . Including the gradients of the heat capacity only accounts for a small fraction of the difference. Then, inspecting the ignition scalar dissipation rate at stoichiometric mixture fraction  $\chi_{ig}$ , it can be seen that no significant differences are found regarding the diffusion model. On the contrary, the chemical mechanism has a substantial effect. The GRI3.0 predicts auto-ignition at higher values of the scalar dissipation rate, when compared to the GRI2.11. Additionally, taking a closer look at the mixing line, at scalar dissipation rates between  $\chi_{ig}$  and  $\chi_q$ , it can be observed that the stoichiometric temperatures are slightly different between both mixing models. However, taking into

account the extended Fickian diffusion, it can be concluded that the difference in the temperature at the mixing line is caused by the gradients of the heat capacity. This is in contrast with the previous case, the DLR A flame, where no differences at the pure mixing line were found. The probable cause for this effect is the large temperature difference between fuel and oxidiser streams.

The region where  $\chi_{st}$  is lower than  $\chi_{ig}$  is the auto-ignition region, where the mixture will self-ignite after a characteristic time delay, or auto-ignition time  $\tau_{ig}$ . Here it is taken as the time required for the mixture at  $Z_{st}$  to reach a temperature halfway between the pure mixing temperature  $T_{st}^u$  and the stable burning temperature  $T_{st}^b$

$$\tau_{ig} = t | \{ T_{st} = (T_{st}^u + T_{st}^b)/2 \} \quad (4.19)$$

Fig. 4.15 shows the autoignition delay times at different  $\chi_{st}$  for each pair of diffusion model, Fickian or differential, and chemical mechanism, GRI3.0 or GRI2.11. Since the chemical mechanism has a significant effect in the value of  $\chi_{ig}$ , the ignition

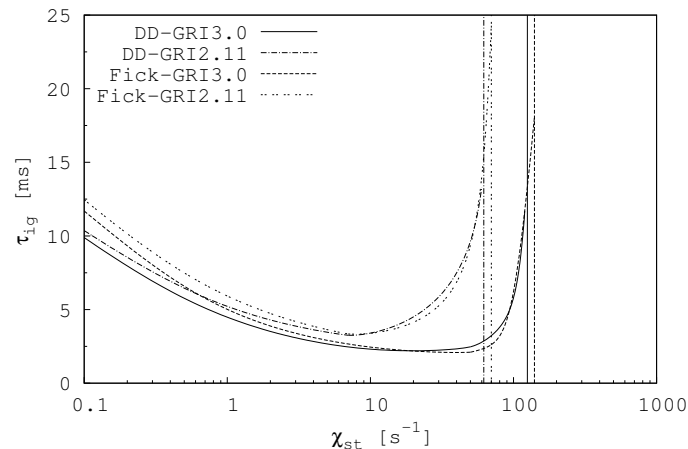


**Figure 4.15:** Autoignition delay times. Vertical lines represent the last self-igniting flamelet  $\chi_{st} = \chi_i$  for each chemical mechanism and diffusion model. *DD* stands for differential diffusion.

delays close to it also show this dependency. Still, the diffusion model plays a minor role. Overall, not only does the GRI3.0 predict auto-ignition up to higher scalar dissipation rates, but also the ignition delay is shorter. This may have important consequences regarding the prediction of auto-ignition lengths during computations in physical space. If the database with the GRI3.0 is used, once the stoichiometric scalar dissipation rate diminishes to values equal or smaller than  $\chi_{ig}$ , the mixture will

be ignited in a shorter time, compared to a database using the GRI2.11. The opposite interpretation is also valid, being that a database using the GRI2.11 will require a further  $\chi_{st}$  diminution and then a longer time to reach an ignited mixture.

Concerning the diffusion model, as  $\chi_{st}$  nears to  $\chi_{ig}$ , past the minimum auto-ignition delay time, the differential diffusion model is seen to slightly increase  $\tau_{ig}$ . However, as  $\chi_{st}$  is decreased the inverse effect can be seen. Furthermore, it can be seen that as the scalar dissipation is reduced the effect of the chemical mechanism is reduced and the diffusion model effect is more significant. Heat capacities gradients, included in the extended Fickian model, do not introduce significant variations with respect to the base Fickian model, and therefore have been omitted from the figure. At  $\chi_{st} = 10$  and using the GRI3.0 mechanism, using the Fickian diffusion model results in  $\tau_{ig} = 2.28ms$ , whereas with the extended one  $\tau_{ig} = 2.297ms$ . For completeness, the differential diffusion model resulted in  $\tau_{ig} = 2.111ms$ .

It is interesting to notice in Fig. 4.14 that near the ignition scalar dissipation rate, the chemical mechanism has a dominant effect, whereas close to the extinction scalar dissipation rate and at small stoichiometric scalar dissipation rates, the diffusion model is more significant. This last point could be thought to be in contradiction with results from Perfectly Stirred Reactors (PSR), where chemical mechanisms play a central role in predicting the combustion process, as there are no diffusion effects. The reason for this behaviour in the flamelet model can be related to the transition of the reaction between the most reactive mixture fraction, being in this case around  $Z_{MR} \approx 0.004$  [15], and the stoichiometric mixture fraction. At any  $\chi_{st} < \chi_{ig}$  the mixture starts to react at  $Z_{MR}$  and then it displaces towards  $Z_{st}$ , around which the maximum burning temperature is found. This transition is controlled by the diffusion model.

If instead of plotting  $\tau_{ig}$  a new time definition is taken, such as an increase in a 2% of the temperature at  $Z_{MR}$ , a monotonic increase for it with increasing  $\chi_{st}$  is observed, as depicted in Fig. 4.16. The rationale is that an increase in  $\chi_{st}$  results in an increase in diffusion which hinders the local reaction in favour of heat transfer. At the most reactive mixture fraction, where the onset of the chemical reaction is located, the role of the diffusion model is almost negligible and the chemical mechanism is determinant, as in PSRs. Therefore, at low mixture fraction values, where the onset of the chemical reaction takes place, chemistry has a predominant effect. However, the reaction is mostly active around  $Z_{st}$ . The transition between both states is controlled by diffusion. Hence, the prevalent role of the diffusion model at low  $\chi_{st}$  depicted in Fig. 4.15.

The just described process, the scalar dissipation rate prevalence over the chemical mechanism at low  $\chi_{st}$ , is similar to the one seen for the previous case, the DLR flame A. In the ignition process at low  $\chi_{st}$  two phases could be identified, a local ignition with little diffusion effects and a diffusion controlled phase. The difference between both

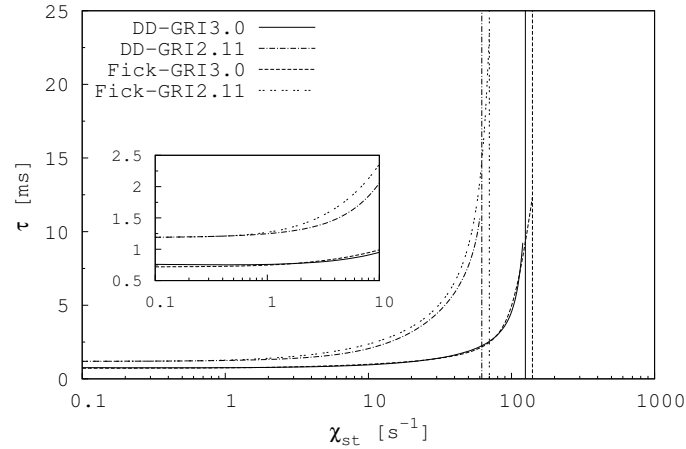


**Figure 4.16:** Time for a 2% temperature increase at  $Z = 0.004$ . Below  $\chi_{st} = 1$ , although the time looks constant, the curve is monotonically growing. See Fig. 4.15 for further details.

flames lies in the initial state. In the DLR A flame, ignition starts from the unstable branch, whereas in the present self-igniting case, ignition starts from a “mixing” state.

#### 4.4.2 Progress-variable definition

As stated previously, species with significantly different Lewis number at the boundaries are not present in this flame. Therefore, the main part of the progress-variable transient evolution is similar between Fickian and differential diffusion. Focus is placed at  $\chi_{st} < \chi_{ig}$ , due to the importance of self-ignition in the present case. Then, two narrow regions require special attention i) the initial region ( $\tau \rightarrow 0$ ) and ii) the transient evolution close to the steady solution. Fig. 4.17 and 4.18 show the transient evolution of the progress-variable and the main combustion products. In each figure insets depict the evolution of several species and progress-variable during the induction region and close to the stable burning solution. The presented evolution is at  $\chi_{st} = 10$  and shows the temporal evolution of the flamelet at a constant mixture fraction,  $Z = Z_{st}$ . No remarkable differences are observed between variants of the Fickian model. Hence, as for the ignition delays, plots for the extended Fickian model are omitted. Notice that  $H_2$  mass fraction is significantly lower than the other major species when the reaction is close to completion. However, in the induction region,  $H_2$  mass fraction is present in higher amounts. Although,  $H_2O$  is the dominant reactive species,  $H_2$  diffusion, and of other species, alter the reactants pool, as the chemistry

in this stage is slow.

In Fig. 4.17 and 4.18 it can also be seen the difference in auto-ignition delays between chemical mechanisms. For the present scalar dissipation rate,  $\chi_{st} = 10$ , the GRI3.0 predicts a 50% shorter ignition delay.

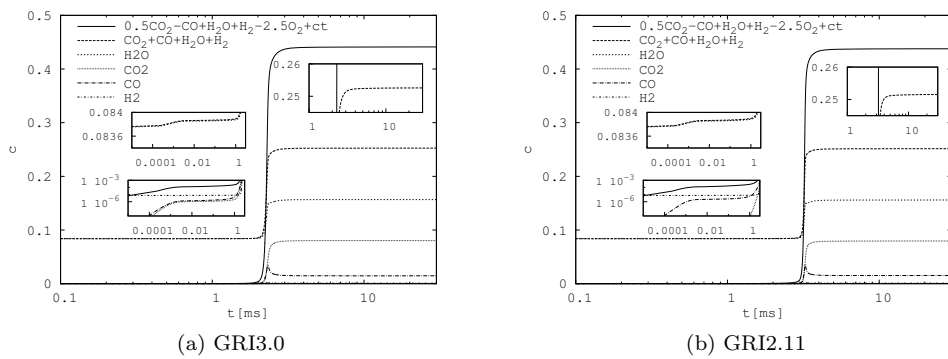


**Figure 4.17:** Auto-ignition evolution at  $Z = Z_{st}$  with  $\chi_{st} = 10$ , with Fickian diffusion. Notice the different vertical scale for the bottom left inset.

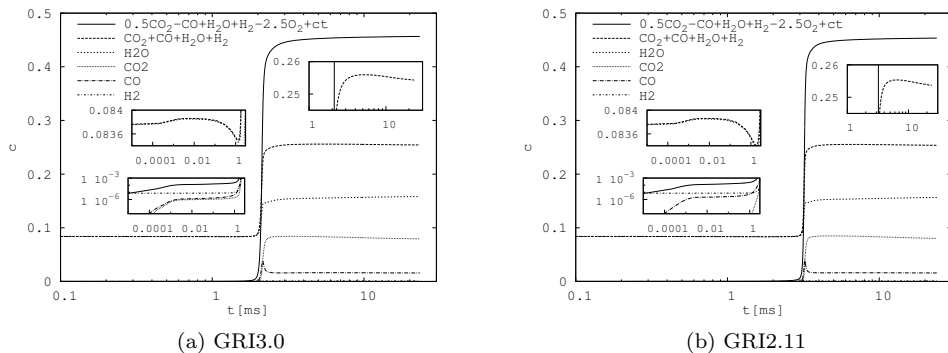


**Figure 4.18:** Auto-ignition evolution at  $Z = Z_{st}$  with  $\chi_{st} = 10$ , with differential diffusion. Notice the different vertical scale for the bottom left inset.

During the induction period,  $H_2O$ , which has the largest mass fraction of the species included in the progress-variable definition, experiences a distinct behaviour depending on the diffusion model. On the one hand, for Fickian diffusion the mass fraction increases monotonically. On the other hand, with the differential diffusion

model, initially its mass fraction slightly increases. Prior to ignition, a marked decrease in  $H_2O$  mass fraction is observed. The same phenomenon is observed for both chemical mechanisms. Turning the attention to carbon compounds, there is a clear difference in the initial production of  $CO_2$ . The GRI3.0 mechanism predicts a similar rate of production for  $CO$  and  $CO_2$ , whereas the GRI2.11 initially predicts  $CO$  production, followed subsequently by  $CO_2$ . These differences at this stage do not show any further consequences close to the stable branch.

Regarding the diffusion model and the progress-variable definition, using the Fickian diffusion model, both  $CD1$  and  $CD2$ , result in a monotonically increasing progress-variable at the induction region. However, close to the stable burning branch for small  $\chi_{st}$ , both definitions show small overlapping regions at mixture fractions slightly richer than the stoichiometric one. When differential diffusion is considered, the  $H_2O$  mass fraction, which is dominant since it originates from the oxidant boundary, experiences a non-monotonic evolution, as shown in Fig. 4.18. Since it is dominant and the other major species, such as  $H_2$ ,  $CO$  or  $CO_2$  have considerably lower mass fractions, it is required either not to include the  $H_2O$  mass fraction in the progress-variable definition or to include additional species, which at least initially present a monotonic growth ( $\tau \rightarrow 0$ ).

Another issue to consider when adding species to the progress-variable definition is the reaction rate of the progress-variable. When chemical databases are built using PSRs, the reaction rate must be strictly positive ( $\dot{\omega}_c > 0$ ) at  $\tau = 0$ . Otherwise, the reaction would not initially progress. For diffusion flamelets, such a requirement is not usually stated, because diffusion can “transport” the ignition from one mixture fraction towards another. Nonetheless, in diffusion flamelets the reaction rate should not be negative, since a requirement of monotonic evolution is enforced to the progress-variable.

Two regions require modifications of the proposed definitions: the induction region when differential diffusion is accounted for and close to the burning branch for both diffusion models. For both cases, if minor species were to be used to correct the non-bijective regions, usually large coefficients would be required in order to correct the progress-variable. The issue that arises is that minor species are present in small quantities, but their reaction rate may not be proportionally small. Hence, if large coefficients are used, then the reaction rate of the progress-variable is greatly modified, with the possibility of becoming negative when a minor specie is destroyed.

Alternatively, and focusing on the induction region,  $O_2$  is seen to vary monotonically at the beginning of the reaction. Consequently,  $O_2$  mass fraction, with a suitable coefficient, results in a monotonic growth of the progress-variable, without affecting the stable solution, since it is already mostly depleted. Therefore, a variant of  $CD2$  is used, in which the progress-variable is a linear combination of species with different

coefficients, with  $O_2$  as an additional specie

$$c = \eta_{CO} \cdot Y_{CO} + \eta_{CO_2} \cdot Y_{CO_2} + \eta_{H_2} \cdot Y_{H_2} + \eta_{H_2O} \cdot Y_{H_2O} + \eta_{O_2} \cdot Y_{O_2} + \text{constant} \quad (4.20)$$

Analysing several flamelets at different stoichiometric scalar dissipation rates, a coefficient of  $\eta_{O_2} = -2.5 \cdot \eta_{H_2O}$  has been found to be adequate to correct the non-bijective induction region. As stated, when Fickian diffusion is considered  $\eta_{O_2} = 0$ , as *CD1* and *CD2* are found to properly describe the initial transient process.  $\eta_{H_2O}$  and  $\eta_{H_2}$  are set to one.

Regarding the region close to the stable burning branch, for the differential diffusion model, *CD1* and *CD2* definitions resulted in a non-bijective function in lean regions. By setting the coefficient of  $CO$  and  $CO_2$  in Eq. (4.20) to  $\eta_{CO_2} = 0.5$  and  $\eta_{CO} = -1$ , a monotonic evolution results. However, at  $\chi_{st} < 5$ , this combination does not result in a monotonic function and a small non-bijective region close to the burning branch ensues. As for the Fickian diffusion model, using *CD1* definition results in a non-monotonic evolution around the stoichiometric mixture fraction. *CD2* improves the definition in general, showing fewer overlapping regions. However, at lower  $\chi_{st}$  and around  $Z \approx 0.25$ , small regions of non-monotonic evolution are still present. Use of Eq. (4.20) with the proposed coefficients for differential diffusion, does not improve the behaviour of the progress-variable when Fickian diffusion is considered. In general, a systematic approach to determine the coefficients would be required, as previously discussed.

Concerning the constant in Eq. (4.20), it has been added due to the negative coefficient of the  $O_2$  mass fraction, which results in a negative progress-variable at the boundaries. Either a constant value, and equal to the progress-variable at the boundary, or the  $O_2$  mass fraction distribution at  $\tau = 0$  may be used. Consequently, the progress-variable becomes a non-negative value.

A last remark regarding the temporal evolution of the flamelet, following the discussion in the previous section, that can be observed in Fig. 4.19 is that the mixture ignites in very lean conditions and then it propagates to richer mixture fractions. The behaviour is similar for both Fickian and differential diffusion models. In both cases the reaction starts at  $Z_{MR}$  and transitions towards the stoichiometric mixture fraction, where it reaches the stable burning solution. Thereafter, a diffusion process occurs where the rich part of the mixture reaches the stable solution.

Regarding other progress-variable definitions, a common definition for the progress-variable used when hydrocarbon fuels are considered is  $c = Y_{CO} + Y_{CO_2}$ . In the present case, although the fuel is basically methane, a high concentration of  $H_2O$  at the oxidiser boundary, makes it more suitable to include it in the definition in order to represent more accurately the induction region. In most cases, this definition does not represent an improvement over the other two definitions. In other cases, as detailed,  $CO$  and  $CO_2$  exhibit non-monotonic evolution in some regions, which

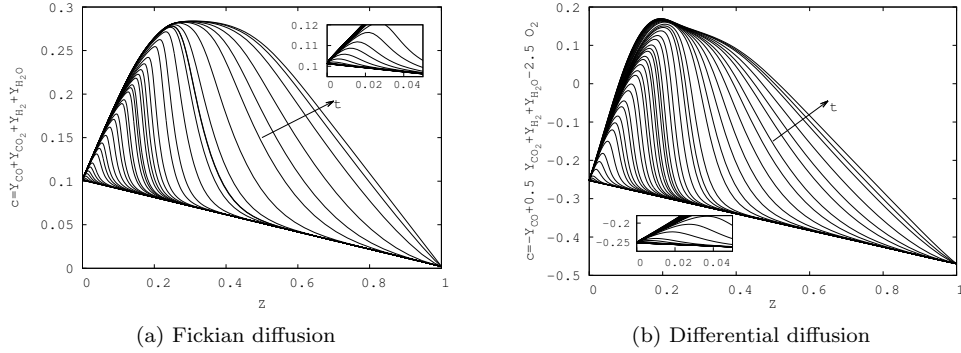


**Figure 4.19:** Autoignition evolution at  $\chi_{st} = 10$ . Different definition of the progress-variable are used to ensure a monotonic evolution.

decreased the suitability of the function. Furthermore, in general the reaction rate for this combination is null at  $\tau = 0$ , making it unsuitable to represent auto-ignition.

As shown, at low  $\chi_{st}$  with the presented definitions the function Eq. (4.18) is not bijective in some regions around the stable burning branch. Nonetheless, the definition has been found suitable to be used during CFD simulations. As detailed for the DLR flame, the small non-bijective regions are replaced by linear interpolations between adjacent regions.

#### 4.4.3 CFD analysis

Direct Numerical Simulation (DNS) of a combustion process taking into account detailed finite rate chemistry is from a computational point of view extremely expensive. However, under the assumption of the flamelet regime the simulation is affordable due to the scale splitting. Hence, the DNS approach applies to the description of the transport phenomena. Presumed conditional moments are a common approach to simulate turbulent combustion phenomena in Large Eddy Simulation (LES) and Reynolds Averaged Navier-Stokes (RANS) models. Usually, chemical databases are built in a preprocessing stage as a function of a limited set of variables, such as the mixture fraction and a progress-variable. Specifically, for the current case flamelet modelling has been applied in the context of diffusion flamelets [20] and the flame prolongation of intrinsic low-dimensional manifolds (FPI-ILDM), coupled with a PSR, [9]. In both cases, closure for both subgrid mixture fraction and progress-variable variances as well as subgrid scalar dissipation rates were required. DNS simulations can provide detailed data to improve those models.

The simulation algorithms and boundary conditions are similar to those described

for the numerical simulations of the previous case. Hence, they are omitted here. Concerning the flamelet database, only databases including differential diffusion are used in the present analysis since no significant differences are observed in the induction region.

A near jet simulation spanning up to 20 jet diameters ( $D_j$ ) has been carried out. In order to establish the DNS mesh, successive refined unstructured meshes were generated and simulations were run. Meshes were refined near the jet shear layer. For each mesh, statistics were collected and the Kolmogorov scale was computed based on the ratio between viscosity and dissipation. The finer mesh retained, denoted as the DNS mesh, showed characteristic cell sizes 6 times higher than the Kolmogorov scale. The final mesh consisted of 64 planes in the azimuthal direction, each one using roughly 390k control volumes, resulting in a mesh of around 25MCV. Regarding the diffusive thickness and the Obukhov/Corrsin scales, since the characteristic Schmidt number is lower than one, once the Kolmogorov length is resolved, the diffusive part of the problem is properly described [39]. Results shown in the following correspond to this mesh. Concerning the reaction thickness, since combustion is assumed to take place in the flamelet regime, its thickness is smaller than the Kolmogorov size. Hence, the use of the FPV model.

In Fig. 4.20 are shown snapshots of the velocity and temperature fields using the two chemical mechanisms. Temperature snapshots show that the flame using the flamelet database computed with the GRI3.0 mechanisms ignites at around  $10D_j$  from the fuel jet nozzle. In contrast, when the GRI2.11 was used, ignition was found close to the  $20D_j$  mark. Even though this ignition could be related to an influence of the boundary condition, results presented afterwards indicate that the ignition position for the GRI2.11 is indeed at around the  $20D_j$  mark. Reported experimental results by Cabra et al. [15] show that the stabilisation distance should be around  $30 - 40D_j$ . Hence, the ignition distances are not correctly captured. Nonetheless, the differences in ignition delays detailed previously have a direct impact in the computed ignition distance.

As a next step, the domain size was increased in order to analyse the early ignition. A mesh up to  $60D_j$  was created, retaining the same cell size to Kolmogorov scale ratio. In the following, results were obtained using the flamelet database computed with the GRI2.11 mechanism. Fig. 4.21 shows the computed axial evolution of the temperature and mixture fraction fields. Alongside are plotted the experimental results and two of the LES results from Ihme and See [20], where LES simulations assuming a  $\delta$ -pdf and a  $\beta$ -pdf for the statistical distribution of the progress-variable were performed.

In the figure it can be seen that, for the present computations, the flame ignites at around  $20D_j$ . Up to this distance, the temperature increase is driven by heat diffusion from the hot coflow, depicted through the profile " $T_O + (T_F - T_O)Z$ ", where "O" refers to the coflow temperature and "F" to the fuel stream temperature. The numerical

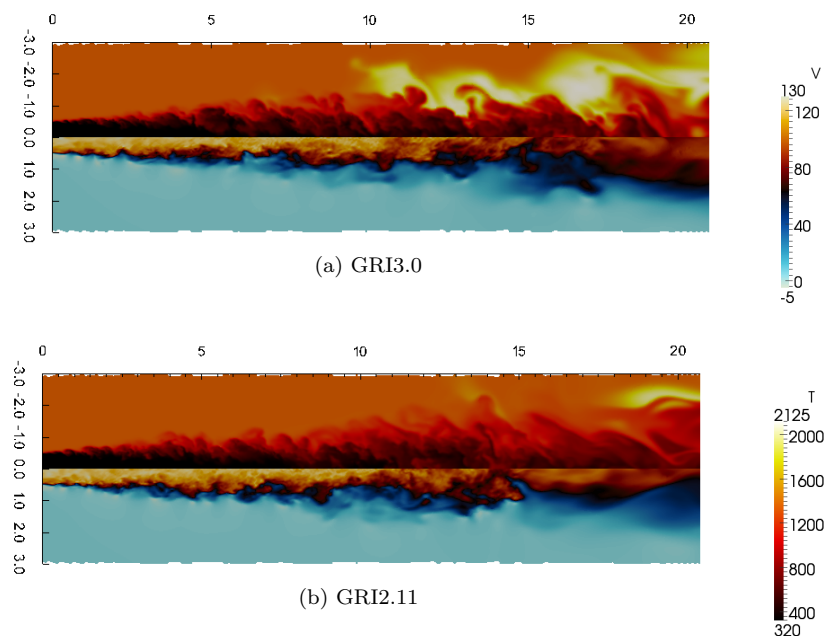


**Figure 4.20:** Instantaneous snapshots of the near jet DNS simulation using the GRI3.0 and GRI2.11 detailed mechanism. The upper side of each picture shows the temperature field in [K]. The lower side presents the velocity field in [m/s]. Axial and radial distances have been made non-dimensional using the fuel jet diameter  $D_j$ .

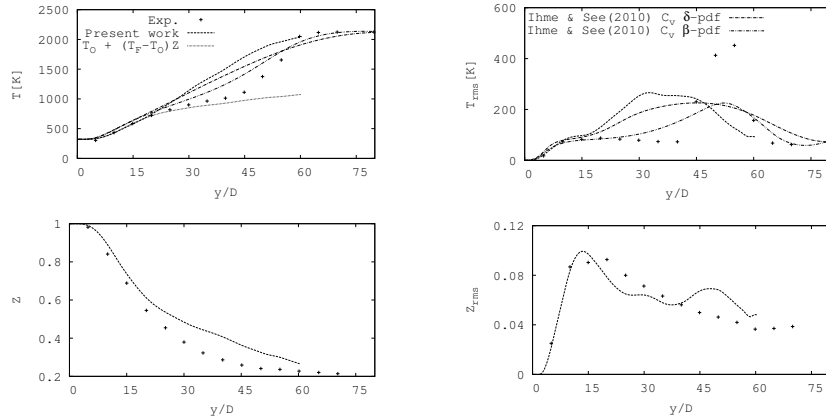


**Figure 4.21:** Axial profiles of temperature (top) and mixture fraction (bottom). Experimental results from Cabra et al.[15] and LES results from hme and See [20] are also plotted. For the latter, two profiles are plotted corresponding to results obtained using different *pdf* for the progress-variable variance  $C_v$ .

simulation shows excellent agreement up to that point. Beyond, heat released from combustion enters into play and increases the temperature further. Compared to previous LES results, the present results show a similar trend to those obtained when a  $\delta$ -*pdf* was assumed for the progress-variable variance. Results from Domingo et al. [9] also showed a dependence on the modelling of the progress-variable variance. This could indicate that the FPV model sets one flamelet in each control volume, where instead there should be more. However, no significant differences were observed when results from the present mesh were compared to previous results using a coarser mesh.

The experimental measurements of the velocity of Gordon [38] indicate that the fuel jet is self-similar. In Fig. 4.22, normalised velocity profiles at different axial locations are shown together with a mean normalised experimental profile. Good agreement is observed between numerical computations and experimental measurements.

In the UFPV model an important parameter is the stoichiometric scalar dissipation rate, which characterises the strain applied to the flamelet. In addition, the progress-variable acts as a tracker of the evolution of the chemical reaction, which can be related to a flamelet time-scale. Fig. 4.23 shows the axial evolution of these two quantities compared against LES results from Ihme and See [20]. It can be observed that the temporally and azimuthally averaged scalar dissipation rate conditioned on the stoichiometric mixture fraction is higher than the LES one. Regarding the lagrangian

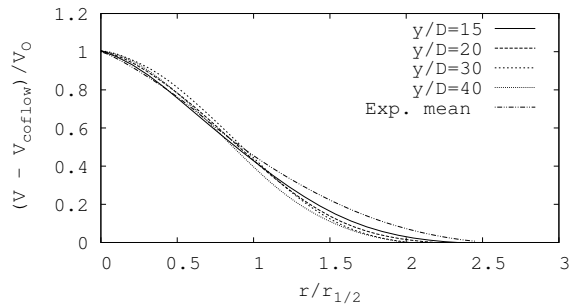


**Figure 4.22:** Normalised radial velocity profiles. Velocity is normalised using the excess velocity at the centreline  $V_O = V(r = 0) - V_{coflow}$  and the radial position is normalised using the half radius  $r_{1/2}$ , defined as the radial position where  $(V_r - V_{coflow}) = V_O/2$ .

flamelet time, it is computed as

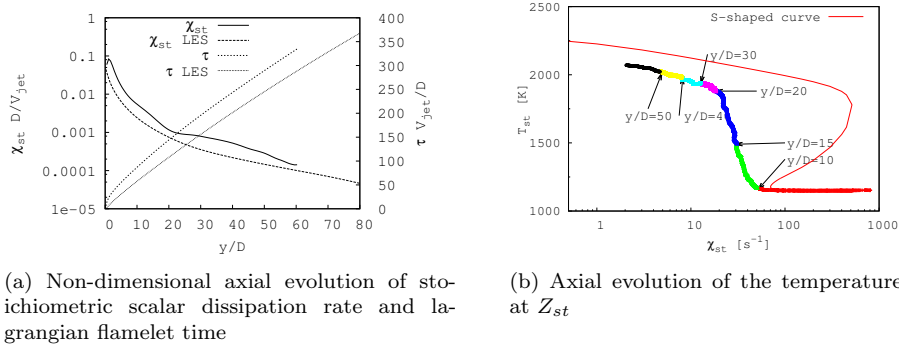
$$\tau(y) = \int_0^y \frac{1}{\langle V_{st}(\zeta) \rangle} d\zeta \quad (4.21)$$

where  $\langle V_{st} \rangle = \langle V | \{Z = Z_{st}\} \rangle$  is the axial velocity conditioned on the stoichiometric mixture fraction. Present computations show a marked increase in its value which implies that at the stoichiometric mixture fraction surface the axial velocities are lower. Hence, flow residence times are higher in the present computations, which could account in part for the shorter ignition distance.

In Fig. 4.23b is also shown the evolution of the temperature conditioned on the stoichiometric mixture fraction. It can clearly be seen the transient evolution of the flamelets in composition space. Previously, when a suitable definition for the progress-variable was sought, it was stated that there were overlapping regions at low  $\chi_{st}$  close to the stable branch. Taking into account the axial evolution shown in the figure, it can be seen that the influence of this non-bijective regions is limited.

## 4.5 Conclusions

The definition of the progress-variable has been shown to be sensitive to the case considered as well as the diffusion mode. Common definitions have been considered, and it has been argued the convenience of increasing the number of considered species and/or the use of unequal weights among the species used to define the progress-variable. Minor species, which required large coefficients, have been shown to be capable of ensuring monotonically varying progress-variables. Improvements have



(a) Non-dimensional axial evolution of stoichiometric scalar dissipation rate and lagrangian flamelet time

(b) Axial evolution of the temperature at  $Z_{st}$ **Figure 4.23:** Axial evolution of derived quantities. Results denoted by LES are taken from Ihme and See [20].

been proposed for unsteady and radiation FPV model for two different flames, for cases using either Fickian or differential diffusion models. Lower success was had for the steady FPV. The presented alternatives were obtained manually and a more systematic approach would lead to better definitions. An automated method, such as the one presented by Ihme et al [10], could provide a suitable definition. The presented results provide an insight on the effect of different species in the progress-variable definition.

The definition of the progress-variable accounting for secondary equilibrium species, such as  $H_2$  and  $CO$ , may help in improving the monotonic growth at the stable branch of the S-shaped curve. However, at the unstable branch they may have the opposite effect, since the burned mixture is not close to its equilibrium values, specially at low stoichiometric scalar dissipation rates. No fully monotonic definition has been found for the steady FPV model for the DLR FLame.  $CD2$  has been argued to be better fitted for the present case. The unsteady variant with the differential diffusion model showed overlapping regions near the stable burning solution at low and intermediate  $\chi_{st}$ . These were the result of a narrower transient process compared to the Fickian one, which causes a build-up of reaction products. Regarding the FPV model with radiation, a complex evolution of the progress-variable has been found, which required adjusting several coefficients of the progress-variable definition in order to obtain bijective functions for both diffusion models. Different definitions were required for each diffusion model. However, the reaction rates for these progress-variable definitions were not always positive. Overall, both diffusion model and combustion model, steady, unsteady or radiation, have a large impact on the progress-variable definition to be used.

The stabilization mechanism for the DLR Flame A has been shown to be greatly dependent on the inclusion of differential diffusion effects, which increased the burning region in the flamelet space compared to the Fickian one: increased stable temperatures, increased extinction scalar dissipation rate and reduced ignition temperatures.

Regarding the self-igniting case, namely the Cabra Flame, an unsteady Flamelet/Progress-Variable has been used to model it. Prior to the numerical simulations in physical space, the flamelet database has been analysed considering the effects of chemical mechanism and differential diffusion. It has been shown that of the two chemical mechanisms studied, the GRI3.0 shows a shorter ignition delay when computing flamelet solutions compared to the GRI2.11. Afterwards, it has been shown that this shorter ignition delay manifests in a shorter ignition distance when numerical simulations were carried out in physical space. Concerning the definition of the progress-variable, it has been shown that differential diffusion is in general not a critical issue. However, during the induction phase, significant differences are observed. In order to account for this different path, a new definition of the progress-variable is proposed. This new definition is mostly monotonic. However, at low  $\chi_{st}$  there remain non-monotonic regions, which are shown to have a limited effect on the simulations since ignition takes place close to  $\chi_i$ .

Concerning the DNS simulations, a deviation from the reported experimental observations is observed. The flame ignites at shorter distances. However, good agreement in the non-reacting zones is observed. Since the flame ignites too early, numerical profiles deviate from the experimental ones at higher axial distances. It has been shown that the present results show a similar trend as the LES results from Ihme and See [20] when a  $\delta - pdf$  was used, which could indicate that the flamelet database is representing different states through one single flamelet. Concerning derived quantities, and specifically the stoichiometric scalar dissipation rate, a similar trend was observed compared to reported results from LES simulations. However, the lagrangian flamelet time showed higher values compared to LES results, indicating lower velocities at the stoichiometric mixture fraction surface. Similarly, as reported from experiments, the computed velocity profiles show that the flame is self similar.

## References

- [1] T. Poinsot and D. Veynante. *Theoretical and Numerical Combustion*. R.T. Edwards Inc., 2005.
- [2] N. Peters. *Turbulent Combustion*. Cambridge University Press, 2000.
- [3] H. Pitsch and N. Peters. A consistent flamelet formulation for non-premixed combustion considering differential diffusion effects. *Combustion and Flame*, 114:26–40, 1998.

- [4] C.D Pierce and P. Moin. Progress-variable approach for large-eddy simulation of non-premixed turbulent combustion. *Journal of Fluid Mechanics*, 504:73–97, 2004.
- [5] H. Pitsch and M. Ihme. An unsteady flamelet/progress variable method for les of nonpremixed turbulent combustion. In *Proceedings of the 43rd Aerospace Sciences Meeting and Exhibit*, 2005.
- [6] M. Ihme, C.M. Cha, and H. Pitsch. Prediction of local extinction and re-ignition effects in non-premixed turbulent combustion using a flamelet/progress variable approach. *Combustion and Flame*, 30(1):793–800, 2005.
- [7] M. Ihme and H. Pitsch. Prediction of extinction and reignition in nonpremixed turbulent flames using a flamelet/progress variable model 2. Application in LES of Sandia flames D and E. *Combustion and Flame*, 155(1-2):90–107, 2008.
- [8] a. W. Vreman, J. a. Oijen, L. P. H. Goey, and R. J. M. Bastiaans. Subgrid scale modeling in large-eddy simulation of turbulent combustion using premixed flamelet chemistry. *Flow, Turbulence and combustion*, 82(4):511–535, 2008.
- [9] P. Domingo, L. Vervisch, and D. Veynante. Large-eddy simulation of a lifted methane jet flame in a vitiated coflow. *Combustion and Flame*, 152(3):415–432, 2008.
- [10] M. Ihme, L. Shunn, and J. Zhang. Regularization of reaction progress variable for application to flamelet-based combustion models. *Journal of Computational Physics*, 231(23):7715–7721, 2012.
- [11] R. Hilbert, F. Tap, H. El-Rabii, and D. Thévenin. Impact of detailed chemistry and transport models on turbulent combustion simulations. *Progress in Energy and Combustion Science*, 30:61–117, 2004.
- [12] K. W. Lee and D. H. Choi. Prediction of NO in turbulent diffusion flames using eulerian particle flamelet model. *Combustion Theory And Modelling*, 12(5):905–927, 2008.
- [13] W. Meier, R.S. Barlow, Y.-L. Chen, and J.-Y. Chen. Raman/Rayleigh/LIF measurements in a turbulent CH<sub>4</sub>/H<sub>2</sub>/N<sub>2</sub> jet diffusion flame: Experimental techniques and turbulence-chemistry interaction. *Combustion and Flame*, 123:326–343, 2000.
- [14] V. Bergmann, W. Meier, D. Wolff, and W. Stricker. Application of spontaneous Raman and Rayleigh scattering and 2D LIF for the characterization of a turbulent CH<sub>4</sub>/H<sub>2</sub>/N<sub>2</sub> jet diffusion flame. *Applied Physics B-Lasers And Optics*, 66:489–502, 1998.

- [15] R. Cabra, J. Chen, R. Dibble, A. Karpetis, and R Barlow. Lifted methane-air jet flames in a vitiated coflow. *Combustion and Flame*, 143(4):491–506, 2005.
- [16] D. Carbonell. *Numerical studies of diffusion flames. Special emphasis on flamelet concept and soot formation.* PhD thesis, Polytechnic University of Catalonia, Terrassa, Spain, 2010.
- [17] J.S. Kim and F.A. Williams. Structures of flow and mixture-fraction fields for counterflow diffusion flames with small stoichiometric mixture fractions. *SIAM Journal On Applied Mathematics*, 53:1551–1566, 1993.
- [18] H. Pitsch, M. Chen, and N. Peters. Unsteady flamelet modeling of turbulent hydrogen-air diffusion flames. *Twenty-Seventh Symposium (International) on Combustion*, pages 1057–1064, 1998.
- [19] H. Pitsch. Improved pollutant predictions in large-eddy simulations of turbulent non-premixed combustion by considering scalar dissipation rate fluctuations. *Proceedings of the Combustion Institute*, 29:1971–1978, 2002.
- [20] M. Ihme and Y.C. See. Prediction of autoignition in a lifted methane/air flame using an unsteady flamelet/progress variable model. *Combustion and Flame*, 157(10):1850–1862, 2010.
- [21] H. Pitsch. Modeling of radiation and nitric oxide formation in turbulent non-premixed flames using a flamelet/progress variable formulation. *Physics of Fluids*, 20(5):055110, 2008.
- [22] R.S. Barlow, J.H. Karpetis A.N., Frank, and J.-Y. Chen. Scalar profiles and NO formation in laminar opposed-flow partially premixed methane/air flames. *Combustion and Flame*, 127(3):2102–2118, 2001.
- [23] J. a. van Oijen and L. P. H. de Goey. Modelling of premixed counterflow flames using the flamelet-generated manifold method. *Combustion Theory And Modelling*, 6(3):463–478, 2002.
- [24] E. Giacomazzi, F.R. Picchia, and N. Arcidiacono. A review of chemical diffusion: Criticism and limits of simplified methods for diffusion coefficient calculation. *Combustion Theory And Modelling*, 12:135–158, 2008.
- [25] O. Lehmkuhl, C.D. Pérez Segarra, R. Borrell, M. Soria, and A. Oliva. Termodfluids: A new parallel unstructured CFD code for the simulation of turbulent industrial problems on low cost PC cluster. *Proceedings of the Parallel CFD Conference*, pages 1–8, 2007.

- [26] L.F. Shampine, B.P. Sommeijer, and J.G. Verwer. IRKC: An IMEX solver for stiff diffusion-reaction PDE's. *Journal of Computational and Applied Mathematics*, 196:485–497, 2006.
- [27] W.L. Grosshandler. RADCAL: A narrow-band model for radiation calculations in a combustion environment. Technical Note 1402, NIST, 1993.
- [28] R.W.C.P. Verstappen and A.E.P. Veldman. Symmetry-preserving discretization of turbulent flow. *Journal of Computational Physics*, 187:343–368, 2003.
- [29] M. S. Darwish and F. H. Moukalled. Normalized variable and space formulation methodology for high-resolution schemes. *Numerical Heat Transfer, Part B: Fundamentals*, 26:76–96, 1994.
- [30] H. Pitsch. Unsteady flamelet modelling of differential diffusion in turbulent jet diffusion flames. *Combustion and Flame*, 123:358–374, 2000.
- [31] F. Nicoud and F. Ducros. Subgrid-scale stress modeling based on the square of the velocity gradient tensor. *Flow, Turbulence and combustion*, 62:183–200, 1999.
- [32] C.D. Pierce and P. Moin. A dynamic model for subgrid-scale variance and dissipation rate of a conserved scalar. *Physics of Fluids*, 10:3041, 1998.
- [33] M. Ihme and H. Pitsch. Modeling of radiation and nitric oxide formation in turbulent nonpremixed flames using a flamelet/progress variable formulation. *Numerical Heat Transfer, Part B: Fundamentals*, 26:76–96, 1994.
- [34] W. L. Chan, H. Kolla, J. H. Chen, and M. Ihme. Assessment of model assumptions and budget terms of the unsteady flamelet equations for a turbulent reacting jet-in-cross-flow. *Combustion and Flame*, 161(10):2601–2613, 2014.
- [35] J. Michel, O. Colin, C. Angelberger, and D. Veynante. Using the tabulated diffusion flamelet model adf-pcm to simulate a lifted methane-air jet flame. *Combustion and Flame*, 156(7):1318–1331, 2009.
- [36] M. Ihme and H. Pitsch. Prediction of extinction and reignition in nonpremixed turbulent flames using a flamelet/progress variable model 1. A priori study and presumed PDF closure. *Combustion and Flame*, 155(1-2):70–89, 2008.
- [37] E. Knudsen, E.S. Richardson, E.M. Doran, N. Pitsch, and J.H. Chen. Modeling scalar dissipation and scalar variance in large eddy simulation: Algebraic and transport equation closures. *Physics of Fluids*, 24:055103, 2012.

- [38] R.L. Gordon. *A numerical and experimental investigation of autoignition*. PhD thesis, University of Sidney, 2008.
- [39] L. Vervisch and P. Poinsot. Direct numerical simulation of non-premixed turbulent flames. *Annual Review of Fluid Mechanics*, 30:655–691, 1998.

# Large Eddy Simulation of a shear stabilised turbulent diffusion flame using a Flamelet/Progress-Variable model.

Main contents of this chapter have been presented at international conferences::

J. Ventosa, O. Lehmkuhl, C.D. Pérez-Segarra, J. Muela, A. Oliva. *Comparative study of subfilter scalar dissipation rate and mixture fraction variance models*. In Proceedings of the 11th World Congress on Computational Mechanics (WCCM XI); 5th European Conference on Computational Mechanics (ECCM V); 6th European Conference on Computational Fluid Dynamics (ECFD VI) pp.5239 - 5248. Barcelona, Spain, July 2014.

J. Ventosa, O. Lehmkuhl, C.D. Pérez-Segarra, A. Oliva. *Assessment of subfilter scalar dissipation rate and mixture fraction variance models*. In Proceedings of the iTi Conference 2014, Bertinoro, Italy, September 2014.

**Abstract.** A common approach to simulate diffusion flames with Large Eddy Simulation (LES) models is to use a flamelet approach coupled with a probability density function assumption, which require the characterisation of mixing at length scales shorter than the mesh, which is described by the mixture fraction variance  $Z_v$  and subgrid scalar dissipation rate  $\chi_{sgs}$ . Four different models for evaluating them are assessed in the context of a Flamelet/Progress-Variable (FPV) model. First, the Local Equilibrium model. Second, a model using a transport equation for the variance. Lastly, two models using the variance statistical definition  $Z_v = \widetilde{Z}^2 - \tilde{Z}^2$ , together with either a transport equation for the squared mixture fraction  $\widetilde{Z}^2$  or a transport equation for the filtered squared mixture fraction gradient  $|\nabla \widetilde{Z}|^2$ . The effect of the different models is assessed using a flame stabilised within a shear layer. A simple turbulent jet  $CH_4/H_2/N_2$  diffusion flame is used due to its simple flow and geometry configuration. Additionally, it is evidenced that correct characterisation of subgrid mixing is critical in the description of the stabilisation mechanism. It is shown

that the model using a transport equation for the variance and the model using the variance definition are not equivalent at the discrete level, even though they are equal at the continuous level. Furthermore, the effect of the FPV model variant, steady, unsteady or radiation, results in a different interaction with the mixing model. The subgrid mixing model is shown to be critical for steady and unsteady models. The radiation model, which only contains a subset of the flamelet space, overshadows the effect of subgrid mixing.

## 5.1 Introduction

In non-premixed combustion, the flamelet regime has been widely studied since it is found in many technological designs. It is characterised by chemical reactions taking place in thin laminar layers embedded within turbulent flow structures[1]. Therefore, the smallest eddies do not penetrate the reaction layer of the flame. Hence, through an appropriate coordinate transformation to a mixture fraction space [1] the combustion process may be split into a transport process and a diffusion-chemistry process. The former requires solving the Navier-Stokes equations, and the latter process reduces to a set of diffusion-reaction equations in mixture fraction space, where there appears the scalar dissipation rate. The latter introduces flow effects from physical space into the flamelet equations.

The mixing process in diffusion flames is usually modelled through a passive scalar, the mixture fraction  $Z$ . In turbulent flows, due to the large span of spatial scales involved, models are introduced to reduce the computational effort required. Both Reynolds Averaged Navier-Stokes (RANS) and Large Eddy Simulation (LES) models split the phenomenon of interest into a resolved and an unresolved part. Particularly, in LES the splitting is performed by means of a spatial filtering. A usual approach is to use the computational mesh as filter. Therefore, in LES the resolved mixture fraction describes mixing at the filter or grid level, and mixing at the subfilter level is characterised by two interconnected quantities, the mixture fraction variance  $Z_v$  and the subgrid scalar dissipation rate  $\chi_{sgs}$ . The resolved mixture fraction is readily available as solution of a transport equation. However both  $Z_v$  and  $\chi_{sgs}$  require modelling.

Solutions of the diffusion-reaction flamelet equations are laminar quantities and are parametrised as a function of laminar variables. Since the focus is on flames in turbulent flows, solution variables of the flamelet equations must be restated into Favre averaged quantities. As turbulent quantities, they can be represented using statistical distributions, particularly through probability density functions (*pdf*). On the one hand, transported probability density function methods were proposed in order to compute these *pdf* [2]. However, with large chemical mechanisms and in conjunction with LES, the method becomes expensive. Furthermore, the diffusion process becomes an unclosed term and has to be modelled. On the other hand, models using presumed *pdf* have been used successfully in many applications, even though the statistical distribution of a given parameter had to be assumed beforehand.

Flamelet models used to simulate turbulent flames commonly rely on the  $\beta$ -*pdf* to describe turbulence-chemistry interactions at the subfilter level. This *pdf* is defined as a function of the first moment, the mean, and the second central moment, the variance. Consequently, mixing at the subgrid level is characterised by the mixture fraction variance. A further quantity of interest which appears in the modelling of the mixture fraction variance is the subgrid scalar dissipation rate.

The evaluation of the subgrid mixture fraction variance and the subfilter scalar dissipation rate is a critical issue in combustion models using a presumed *pdf* approach, such as Flamelet models and Conditional Moment Closure (CMC) models. In premixed flames with Presumed Conditional Moment (PCM) models, the variance of the progress-variable represents a similar challenge. Both parameters model scalar mixing at the subgrid level, which in turn controls the combustion process. Therefore, accurate description of the subgrid mixing is critical as the Reynolds number is increased. The first proposed models to evaluate both quantities were based on a local equilibrium hypothesis, where production and destruction of variance at the subfilter level were assumed to cancel out. The proposed scale similarity model for the mixture fraction variance [3], although being computationally efficient, was found to produce erroneous estimations of the scalar mixing in technically relevant flow configurations [4], thus being not suitable in many cases of industrial interest. In the past, several models have been proposed to account for deviations from local equilibrium. One option in order to take into account non-equilibrium effects is to construct a transport equation for the variance itself (VTE). Alternatively, being the variance an statistical quantity, it can be computed through its definition,  $\tilde{Z}_v = \tilde{Z}^2 - \tilde{Z}^2$ . In turn, this requires the computation of the second moment of the mixture fraction,  $\tilde{Z}^2$ . A transport equation is then usually employed (STE). Nonetheless, in both cases closure for the subfilter dissipation rate is required. Algebraic expressions relating the subgrid variance with the subfilter dissipation through a turbulent time-scale have been proposed [4, 5]. Alternatively, closure for the scalar dissipation rate can also be performed solving a transport equation for the filtered squared gradient of the mixture fraction [6]. Each approach involves different equations using different closures. Furthermore, these two quantities, subgrid variance and subgrid scalar dissipation rate, are parameters of the flamelet database. Thus, differences in their predictions will imply different retrieved values from the flamelet database, and will lead to different flame dynamics.

In the present work the DLR simple-jet [7, 8] is selected as study case because its stabilisation mechanism is through the shear layer between fuel and oxidiser coflow streams. Hence, mixing is a critical aspect to be modelled. Other stabilisation mechanisms for turbulent flows at high Reynolds numbers are the use of pilot flames, recirculation and bluff-bodies, among others. However, since the focus of the present study is the modelling of subgrid mixing these other mechanisms overshadow the role of mixing.

The DLR simple-jet features a fuel jet surrounded by a coflowing stream of oxidiser. The fuel is a mixture of  $CH_4$  and  $H_2$  diluted in  $N_2$ . Hydrogen was added to the fuel in order to increase the burning rate and aid in the stabilisation [7]. Experimentally this flame is attached to the fuel nozzle rim. The stabilisation mechanism for this flame is then mostly due to diffusion through the shear layer between the two reactant

streams. The case will serve to analyse the effect of several subgrid models on the flame predictions.

Due to its canonical geometry and configuration, this flame has been extensively used to validate several combustion models. Pitsch [9] used the classical unsteady flamelet model to study differential diffusion effects in this flame. Emami and Eshghinejad Fard [10] used this flame to study a flamelet approach with Artificial Neural Networks. Lindsted and Ozarovsky [11] used a *pdf* model, Vogiatzaki [12] applied a Multiple Mapping Conditioning (MMC) model and Wang and Pope [13] tested a LES/*pdf* model coupled with a Flamelet/Progress-variable (FPV) model. Fairweather and Woolley [14] used a first order CMC model to study several chemical mechanisms. Lee and Choi [15, 16] used an Eulerian Particle Flamelet model (EPFM) to study NO emissions. Ihme et al. [17, 18] performed a LES simulation using a Flamelet/Progress-Variabile (FPV) model to study combustion generated noise.

Most of the aforementioned studies were conducted using Reynolds Averaged Navier-Stokes (RANS) models, where the turbulent viscosity is usually higher than the molecular one, or with PDF methods, where mixing itself requires closure. In LES this is not the case, where molecular transport can play a significant role as turbulent and molecular diffusivities can be of the same order. Furthermore, in combustion phenomena molecular transport is enhanced due to the exothermicity of chemical reactions [19]. Both Wang and Pope [13] and Ihme et al. [17] reported LES simulations using a FPV model, where a single flamelet was used in the former and only the steady burning solutions were included in the latter [18].

The aim of this chapter is to evaluate several subgrid mixing models in the context of a diffusion flame. Three variants of the Flamelet/Progress-Variable model are used: steady, unsteady and including radiation. The described models for subgrid variance and subgrid scalar dissipation rate are used and their effect in predicted profiles and flame stabilisation compared. Thus, the study focuses on different implementations of the subgrid mixing closure and their effect on the flame predictions. It is shown that incorrect capture of subgrid mixing results in flame lift-off, even though experimentally an attached flame was reported. Furthermore, the thermal effects of the flame on the shear layer are discussed.

The chapter is organized as follows: first, the mathematical formulation for the LES model, the combustion model and subgrid closures are presented. The experimental case and computational domain are then described. Afterwards, results using the different FPV variants and subgrid closures are presented.

## 5.2 Mathematical model

### 5.2.1 LES model

Large Eddy Simulation describes the motion of the large scales of the flow, whereas the small scales are modelled. Scale splitting is performed by means of a low-pass filter,

$$\overline{\rho\phi} = \int_{\Omega} \rho\phi G(\mathbf{x}, \xi) d\xi \quad (5.1)$$

In grid based, implicit filtering the filter kernel  $G(\mathbf{x}, \xi)$  becomes a top-hat filter with size  $\Delta = (h_i)^{1/3}$ , where  $h_i$  is the mesh spacing in the  $i$ -direction. Additionally, for variable density flows, the filtered quantities are density weighted, or Favre filtered. Favre filtered quantities can be related to Reynolds filtered quantities through  $\tilde{\rho}\tilde{\phi} = \overline{\rho\phi}$ . Therefore, applying the filtering operation to the low-Mach Navier-Stokes equations, the equation of mass and momentum conservation become

$$\frac{\partial \overline{\rho}}{\partial t} + \frac{\partial \overline{\rho}\tilde{u}_j}{\partial x_j} = 0 \quad (5.2)$$

$$\frac{\partial \overline{\rho}\tilde{u}_i}{\partial t} + \frac{\partial \overline{\rho}\tilde{u}_j \tilde{u}_i}{\partial x_j} = -\frac{\partial \overline{p}}{\partial x_i} + \frac{\partial}{\partial x_j} ((\tilde{\mu} + \mu_t)\tilde{\sigma}_{ij}) + \overline{\rho}g_i \quad (5.3)$$

where  $\overline{\rho}$ ,  $\overline{p}$  and  $\tilde{u}_i$  represent the filtered density, the filtered dynamic pressure and the Favre filtered velocity, respectively. The diffusive fluxes, including the rate of strain and the deviatoric part, are  $\tilde{\sigma}_{ij} = \left( \frac{\partial \tilde{u}_i}{\partial x_j} + \frac{\partial \tilde{u}_j}{\partial x_i} - \frac{2}{3} \delta_{ij} \frac{\partial \tilde{u}_k}{\partial x_k} \right)$ . Turbulent subgrid fluxes have been modelled through an eddy-diffusivity assumption, where the turbulent subgrid viscosity  $\mu_t$  is closed by means of the Wall-Adapting Local Eddy diffusivity (WALE) model [20] in the context of a Variational Multiscale Model [21]. The choice of subgrid turbulence model is discussed along with the model for the subgrid scalar turbulent diffusivity in Sec. 5.4.1.

Thermochemical properties, such as the density and molecular diffusivities, are provided by the combustion model, and are discussed in the following.

### 5.2.2 Flamelet/Progress-Variable (FPV) model

In the flamelet regime, chemically active layers are thinner than the size of the Kolmogorov scale. Therefore, it is justified to assume that turbulent eddies do not penetrate the reaction zone. Thus, the flame can be considered to exist in a quasi-laminar flow field within those eddies [1]. Consequently, the flame can be considered as an ensemble of laminar flames surrounded by turbulent structures, capable only of wrinkling and straining the flame.

Hence, defining a new coordinate system described by the mixture fraction and applying a coordinate transformation to the species and energy equations, as described by Pitsch and Peters [22], the flamelet equations are obtained

$$\rho \frac{\partial \phi}{\partial t} = \rho \frac{\chi_Z}{2} \frac{\partial^2 \phi}{\partial Z^2} + S_\phi \quad (5.4)$$

where  $\phi$  denotes species mass fractions and temperature,  $S_\phi$  includes the equation's source term and other additional terms and  $\chi_Z = 2D_z \left( \frac{\partial Z}{\partial x_i} \frac{\partial Z}{\partial x_i} \right)$  is the scalar dissipation rate. The latter introduces flow effects from the transport process into the diffusion-chemistry process.

The scalar dissipation rate dependence on the mixture fraction distribution in physical space precludes solving the flamelet equations in a preprocessing stage. Nonetheless, through an analogy between diffusion flames in the flamelet regime and counterflow flames [1], the scalar dissipation rate can be described through an analytical expression in mixture fraction space

$$\chi_Z(Z) = \chi_{st} \frac{f(Z)}{f(Z_{st})} \quad (5.5)$$

$$f(Z) = \exp(-2[\text{erfc}^{-1}(2Z)]^2) \quad (5.6)$$

where  $\text{erfc}^{-1}$  is the inverse of the complementary error function. Furthermore, this expression was also derived from the analysis of unsteady mixing layers [1].

Flamelet modelling of diffusion flames offers a dimensionality reduction by mapping the multicomponent diffusion-reaction process, the flame problem, into a limited set of transported scalars. Solutions of one-dimensional flamelets in their steady state form can be expressed as a state relation

$$\phi = \xi_\phi(Z, \chi_{st}) \quad (5.7)$$

where  $\chi_{st}$  is the scalar dissipation rate at the stoichiometric mixture fraction. Plotting the stoichiometric temperature as a function of the stoichiometric scalar dissipation rate the S-shaped curve is obtained, Fig.5.1.

The upper branch of this curve represents the stable burning state, the middle one the unstable burning solution and the lower one the extinguished state or pure mixing. The turning point between the upper and lower branch corresponds to the quenching scalar dissipation  $\chi_q$ . Although with Eq. (5.4) all solutions of the S-shaped curve can be obtained by setting  $Z$  and  $\chi_{st}$ , Eq. (5.7) does not offer a unique representation of the curve. Hence, only one branch can be represented. Applications of the flamelet model typically represents only the stable burning branch and the stable non-burning solution for  $\chi_{st} > \chi_q$ . This shortcoming of flamelet models can be overcome introducing a new flamelet parameter  $\Lambda = c|Z_{st}|$ , as proposed by Pierce and Moin [23], where the progress-variable  $c$  is usually defined as the summation of

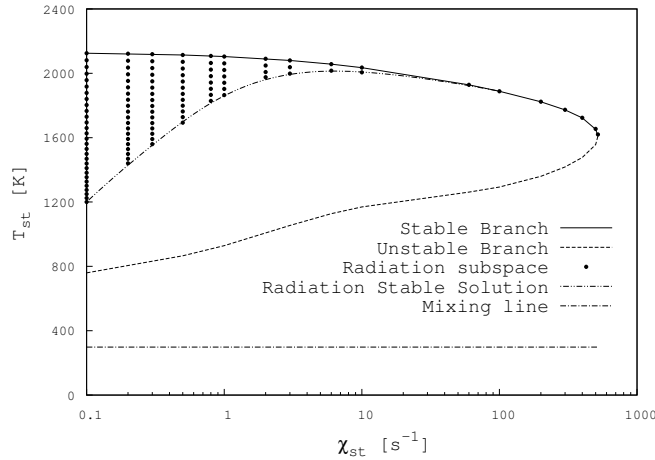


**Figure 5.1:** S-shaped curve for the DLR Flame. Dotted region represents the radiation accessible flamelet subspace.

several species mass fractions. Using this parameter the full S-shape curve can be uniquely represented by a state relation

$$\phi = \zeta_\phi(Z, \Lambda) \quad (5.8)$$

Therefore, the FPV combustion model uses a unique set of parameters to represent all possible flame states, defined by a mixture fraction  $Z$  and a flamelet parameter  $\Lambda$ . Therefore, once  $Z$  and  $\Lambda$  are computed, Eq. (5.8) can be used to retrieve any flamelet solution. It is possible to solve a transport equation for  $\Lambda$ . However, it is more convenient to solve a transport equation for the progress-variable itself, because in turbulent flames the transport equation for  $\Lambda$  contains several terms which are difficult to model. Since the progress-variable can be recovered using the state relation Eq. 5.8, the flamelet parameter  $\Lambda$  can be expressed as a function of the progress-variable,  $\Lambda = \zeta_c^{-1}(Z, c)$ . This implies that there exists a bijective relation between the progress-variable and the progress-variable parameter. Introducing it in Eq. 5.8, a state relation can be defined relating the flamelet scalars to  $Z$  and  $c$  (for steady cases)

$$\phi = F_\phi(Z, c) \quad (5.9)$$

For LES simulations, this state relation must be recast for Favre-filtered quantities.

Then, turbulent quantities are expressed through statistical distributions

$$\tilde{\phi} = \int \int \zeta_\phi(Z, \Lambda) \tilde{P}(Z, \Lambda) dZ d\Lambda \quad (5.10)$$

where  $\tilde{P}(Z, \Lambda)$  denotes the Favre joint *pdf* of  $Z$  and  $\Lambda$ . Assuming that the flamelet parameter  $\Lambda$  is statistically independent with respect to the mixture fraction  $Z$ , then the joint *pdf* is reduced to its marginal *pdf*,  $\tilde{P}(Z, \Lambda) = \tilde{P}(Z)\tilde{P}(\Lambda)$ . The marginal *pdf* of the mixture fraction is modelled using a  $\beta$ -*pdf* [24]. Additionally, the marginal *pdf* of  $\Lambda$  is assumed to be described by a  $\delta$ -*pdf* function [23, 25]. Therefore,

$$\tilde{P}(Z, \Lambda) = \beta(Z; \tilde{Z}, Z_v) \delta(\Lambda - \Lambda^*) \quad (5.11)$$

The  $\beta$ -*pdf* introduces the mixture fraction variance  $Z_v$  as a parameter of the state relation.

With the definition of the *pdf* to model turbulent effects on the laminar flamelet library, a turbulent flamelet library can be constructed. Recasting the turbulent flamelet library as performed previously for the laminar case, all thermochemical variables from the steady state solution of the flamelet equations can be stated as a function of three parameters,  $\tilde{Z}$ ,  $\tilde{c}$  and  $Z_v$

$$\tilde{\phi} = \tilde{\zeta}_\phi(\tilde{Z}, Z_v, \tilde{\Lambda}) \rightarrow \tilde{\phi} = \tilde{F}_\phi(\tilde{Z}, Z_v, \tilde{c}) \quad (5.12)$$

In order to retrieve the data from the database, the Favre filtered mixture fraction  $\tilde{Z}$ , its subfilter variance  $Z_v$  and progress variable  $\tilde{c}$  are computed in physical space. Both mixture fraction and progress-variable are transported quantities in physical space

$$\bar{\rho} \frac{\partial \tilde{Z}}{\partial t} + \bar{\rho} \tilde{u}_j \frac{\partial \tilde{Z}}{\partial x_j} = \frac{\partial}{\partial x_j} \left( \bar{\rho} (\tilde{D}_Z + D_{Z,t}) \frac{\partial \tilde{Z}}{\partial x_j} \right) \quad (5.13)$$

$$\bar{\rho} \frac{\partial \tilde{c}}{\partial t} + \bar{\rho} \tilde{u}_j \frac{\partial \tilde{c}}{\partial x_j} = \frac{\partial}{\partial x_j} \left( \bar{\rho} (\tilde{D}_c + D_{c,t}) \frac{\partial \tilde{c}}{\partial x_j} \right) + \tilde{w}_c \quad (5.14)$$

where  $\tilde{D}_Z$  and  $\tilde{D}_c$  are the mixture fraction and progress-variable molecular diffusivities, respectively. Analogously,  $D_{Z,t}$  and  $D_{c,t}$  are the turbulent diffusivities, which are computed using a constant Schmidt number  $Sc_t = 0.4$ . The progress-variable reaction rate  $\tilde{w}_c$  is defined as the summation of the reaction rates of the species defining the progress-variable. The mixture fraction variance is not readily available and requires modelling. Several closures are discussed in the following section.

Extensions of the steady FPV model have been published to include either the transient term of the flamelet equations or to account for heat losses due to radiation. On the one hand, Pitsch and Ihme [25] introduced  $\chi_{st}$  as an additional parameter to

account for unsteady effects. On the other hand, Ihme and Pitsch [26] used the enthalpy to account for radiation heat losses. Following a similar procedure as described for the steady database, solutions of the flamelets equations can be expressed as state equations. The thermochemical database accessed during numerical simulations for each variant reads

$$\tilde{\phi} = F_{\phi}^{SFPV}(\tilde{Z}, Z_v, \tilde{c}) \quad (5.15a)$$

$$\tilde{\phi} = F_{\phi}^{UFPV}(\tilde{Z}, Z_v, \tilde{c}, \chi_{st}) \quad (5.15b)$$

$$\tilde{\phi} = F_{\phi}^{RFPV}(\tilde{Z}, Z_v, \tilde{c}, \tilde{h}) \quad (5.15c)$$

where  $\tilde{\phi}$  represents the different variables retrieved from the flamelet database, such as the density  $\tilde{\rho}$ , the progress-variable reaction rate  $\tilde{w}_c$ , the molecular mixture fraction diffusivity  $\tilde{D}_Z$ , etc.

The steady FPV (SFPV) model represents the curve defined by the stable burning, unstable burning and non-burning branches, depicted in Fig. 5.1. The unsteady FPV (UFPV) model is able to represent all states in the flamelet subspace, including steady solutions and the transient solutions between them. For the radiation FPV (RFPV), the radiation subspace is depicted in the figure by the dotted region, which represents the region where radiation effects are significant. The reader is referred to references [23, 25, 26] for details on the generation of the databases.

A last aspect to define is the form of the progress-variable. It is a tracking quantity which, together with the mixture fraction, must uniquely define the thermochemical state. It is usually defined as a linear summation, or in some cases a weighted summation, of several species. In the present case, a linear combination of  $CO$ ,  $CO_2$ ,  $H_2$  and  $H_2O$  is used when steady FPV database is employed,  $c = Y_{CO} + Y_{CO_2} + Y_{H_2} + Y_{H_2O}$ , as suggested by Ihme [17]. A slightly modified definition is taken when the unsteady FPV database is used,  $c = Y_{CO} + Y_{CO_2} + Y_{H_2} + Y_{H_2O} + 5Y_{C_2H_2}$ . The GRI 3.0 mechanism [27] is used to generate the chemical database. Differential diffusion effects have been considered in the solution of the flamelet equations.

### Subgrid Closures

The variance, or second central moment, which is required to retrieve solutions from the FPV database, is defined in terms of a probability density function [28]

$$Z_v = \tilde{Z}^2 - \tilde{Z}^2 \quad (5.16)$$

where  $Z_v$  denotes the subfilter mixture fraction variance. To compute it, there are two possibilities. Either a transport equation for the variance itself [28] is used (VTE)

$$\bar{\rho} \frac{\partial Z_v}{\partial t} + \bar{\rho} \tilde{u} \frac{\partial Z_v}{\partial x_i} = \frac{\partial}{\partial x_i} \left( \bar{\rho} (\tilde{D}_Z + D_{t,Z}) \frac{\partial Z_v}{\partial x_i} \right) + 2\bar{\rho} (\tilde{D}_Z + D_{t,Z}) \frac{\partial \tilde{Z}}{\partial x_i} \frac{\partial \tilde{Z}}{\partial x_i} - \bar{\rho} \tilde{\chi}_Z \quad (5.17)$$

or a transport equation for the second moment of the mixture fraction  $\widetilde{Z}^2$  (STE) [6]

$$\bar{\rho} \frac{\partial \widetilde{Z}^2}{\partial t} + \bar{\rho} \tilde{u} \frac{\partial \widetilde{Z}^2}{\partial x_i} = \frac{\partial}{\partial x_i} \left( \bar{\rho} (\tilde{D}_Z + D_{t,Z}) \frac{\partial \widetilde{Z}^2}{\partial x_i} \right) - \bar{\rho} \tilde{\chi}_Z \quad (5.18)$$

A further parameter is here introduced to characterise the mixing state, the filtered scalar dissipation rate  $\tilde{\chi}_Z$ . In both cases closure for the scalar dissipation rate is required

$$\tilde{\chi}_Z = 2\tilde{D}_Z \frac{\widetilde{\partial Z}}{\partial x_i} \frac{\widetilde{\partial Z}}{\partial x_i} = 2\tilde{D}_Z \frac{\partial \widetilde{Z}}{\partial x_i} \frac{\partial \widetilde{Z}}{\partial x_i} + \chi_{Z,sgs} \quad (5.19)$$

where  $\chi_{Z,sgs} = 2\tilde{D}_Z \left( \frac{\widetilde{\partial Z}}{\partial x_i} \frac{\widetilde{\partial Z}}{\partial x_i} - \frac{\partial \widetilde{Z}}{\partial x_i} \frac{\partial \widetilde{Z}}{\partial x_i} \right)$  is the subfilter dissipation rate.

Even though the VTE and STE models are equivalent at the continuous level through Eq. (5.16), Kemenov et al. [29] and Kaul et al. [30] showed that they are not exactly equivalent at the discrete level. For example, the effect of the squared gradient is opposite between the two models. In the STE model  $2\tilde{D}_Z \frac{\partial \widetilde{Z}}{\partial x_i} \frac{\partial \widetilde{Z}}{\partial x_i}$  is a dissipation term and in the VTE model  $2D_{t,Z} \frac{\partial \widetilde{Z}}{\partial x_i} \frac{\partial \widetilde{Z}}{\partial x_i}$  is a production term. Therefore, numerical errors in the computation of the gradient or differences in the mixture fraction field will have a different impact in each model.

In order to close the model for  $Z_v$ , closure for  $\chi_{sgs}$  is required. In Eq. (5.17), if production and destruction of the mixture fraction variance at the small scales are assumed to be in equilibrium [3, 31], denoted as the Local Equilibrium Assumption (LEA), the scalar dissipation rate becomes

$$\tilde{\chi}_Z = 2(\tilde{D}_Z + D_{t,Z}) \frac{\partial \widetilde{Z}}{\partial x_i} \frac{\partial \widetilde{Z}}{\partial x_i} \quad (5.20)$$

However, with the LEA the mixture fraction variance requires a model as Eq. (5.17) with this assumption is just the transport equation of a passive scalar. Hence, a scale similarity model [3] for the mixture fraction variance may be used

$$\bar{\rho} Z_v = C_{var} \Delta^2 \bar{\rho} |\nabla \widetilde{Z}| \quad (5.21)$$

where  $C_{var}$  is here calculated using the *Leonard term Expansion Dynamic model* (LED) [32]. Within the dynamic evaluation, a top-hat test filter with filter size  $\hat{\Delta} = 2\Delta$  is used.

If non-equilibrium effects are to be considered, Eq. (5.20) cannot be used. Thus, alternative closures for the subfilter dissipation rate have to be used. Models using either an algebraic closure or a transport equation for the filtered gradient of the mixture fraction have been proposed. On the one hand, the subgrid variance can be

related to the subfilter dissipation rate through a turbulent mixing time-scale [4, 5], the algebraic approach,

$$\chi_{Z,sgs} = \frac{C_Z}{\tau} Z_v = C_Z \frac{\nu_t}{\Delta^2} Z_v \quad (5.22)$$

$$\frac{1}{\tau} = \frac{\varepsilon_{sgs}}{k_{sgs}} \approx \frac{\nu_t}{\Delta^2} \quad (5.23)$$

where  $\tau$  is a turbulent (mixing) time-scale,  $k_{sgs}$  and  $\varepsilon_{sgs}$  are the subgrid turbulent kinetic energy and dissipation, respectively. The turbulent viscosity  $\nu_t$  is used to model the latter. The model constant is of the form  $C_Z = C_{\chi,Z}(C_\varepsilon/C_u)$ , where  $C_{\chi,Z} = 2$  is a constant relating mechanical and scalar time-scales and  $(C_\varepsilon/C_u) = 2$  is related to the energy spectra [5]. Nevertheless, the effect of the constant is afterwards investigated. In the context of RANS models, a similar functional relation between  $\chi_{sgs}$  and  $Z_v$  was proposed. The time-scale is related to the ratio of kinetic energy and kinetic energy dissipation and the constant takes a value of 2 [1].

On the other hand, closure for the scalar dissipation rate  $\tilde{\chi}_Z$  can be achieved by constructing a transport equation for the filtered squared gradient  $\widetilde{|\nabla Z|^2}$  [6], here denoted as SDR-TE. Evaluation of the SDR-TE requires modelling several unclosed terms and the evaluation of computationally expensive terms.

$$\begin{aligned} \frac{D}{Dt} \left( \bar{\rho} \widetilde{|\nabla Z|^2} \right) &= \frac{\partial}{\partial x_i} \left( \bar{\rho} (\widetilde{D_Z} + D_{t,Z}) \frac{\partial \widetilde{|\nabla Z|^2}}{\partial x_i} \right) \\ &\quad - 2\bar{\rho} \left( \frac{\partial \widetilde{u}_i}{\partial x_j} \frac{\partial \widetilde{Z}}{\partial x_i} \frac{\partial \widetilde{Z}}{\partial x_j} \right) - 2\bar{\rho} \widetilde{D_Z} \left( \frac{\partial^2 \widetilde{Z}}{\partial x_i \partial x_j} \right) \\ &\quad - \frac{2}{\bar{\rho}} \frac{\partial \bar{\rho}}{\partial x_i} \frac{\partial \widetilde{Z}}{\partial x_i} \left( \frac{\partial}{\partial x_j} \left( \bar{\rho} \widetilde{D_Z} \frac{\partial \widetilde{Z}}{\partial x_j} \right) \right) \\ &\quad + 2 \frac{\partial \bar{\rho} \widetilde{D_Z}}{\partial x_i} \frac{\partial \widetilde{Z}}{\partial x_i} \left( \frac{\partial^2 \widetilde{Z}}{\partial x_j^2} \right) + 2 \frac{\partial \widetilde{Z}}{\partial x_i} \frac{\partial \widetilde{Z}}{\partial x_j} \left( \frac{\partial^2 \bar{\rho} \widetilde{D_Z}}{\partial x_i \partial x_j} \right) \\ &\quad + C_{prd} \bar{\rho} \frac{32\nu_t}{\Delta^2} \left( \widetilde{|\nabla Z|^2} - |\nabla \widetilde{Z}|^2 \right) \\ &\quad - 12C_{var} \bar{\rho} \frac{\widetilde{D_Z}}{Z_v} \left( \widetilde{|\nabla Z|^2} - |\nabla \widetilde{Z}|^2 \right)^2 \end{aligned} \quad (5.24)$$

where  $C_{prd} = 1$  is a model constant and  $C_{var}$  is dynamically evaluated using the LED model, as performed for the equilibrium model Eq. (5.21).

Summarizing, the four closures used in the following are listed in Table 5.1

	$Z_v$	$\chi_{sgs}$
Equilibrium Model	Eq. (5.21)	Eq. (5.20)
VTE	Eq. (5.17)	Eq. (5.22)
STE	Eq. (5.16), Eq. (5.18)	Eq. (5.22)
SDR-TE	Eq. (5.16), Eq. (5.18)	Eq. (5.24)

**Table 5.1:** List of subgrid mixing closures and the equations involved in each model.

### 5.2.3 Numerical method

The set of equations for the conservation of mass Eq. (5.2), momentum (Eq. (5.3)) and transport of the mixture fraction (Eq. (5.13)) and progress-variable (Eq. (5.14)) are solved using a finite-volume approach. Particularly, 3D collocated meshes, either structured or unstructured. In order to preserve kinetic energy, a Symmetry-Preserving scheme [33] is used in the construction of the discrete convective term of the momentum equation. For the scalar convective terms, a SMART scheme is used [34]. A second order centred difference scheme is used to construct the discrete diffusive term for all transported quantities. Temporal integration is performed using a linear multi-step method, as described in Chapter 2, with a second order Adams-Bashforth scheme in the predictor step and a Crank-Nicholson scheme in the corrector step. The pressure-velocity coupling is solved through a Fractional Step method. The Poisson equation is solved by means of FFT-based Poisson Solver by Borrell et al. [35], due to the use of an axysymmetric mesh with one circulating direction, as described in the next section.

Numerical computations are performed using the general purpose unstructured and parallel object-oriented CFD code TermoFluids [36].

## 5.3 Turbulent diffusion $CH_4/H_2/N_2$ flame - DLR A flame

The case of study is the axisymmetric jet flame denoted as DLR Flame A [7, 8], which was a standard flame used in the third “International Workshop on Measurement and Computation of Turbulent Nonpremixed Flames” (TNF Workshop) [37]. It consists of a  $D = 8\text{mm}$  wide fuel jet with a thinned rim at the exit. The inner fuel jet is composed of 33.2%  $H_2$ , 22.1%  $CH_4$ , and 44.7%  $N_2$  by volume and the outer jet is regular air with 20.1%  $O_2$ . The fuel jet exit bulk velocity is fixed to  $V_b = 42.15\text{m/s}$ , resulting in a Reynolds number of  $Re_b = 15,200$ . The jet was mounted concentrically to the coflow nozzle, which had a diameter of 140mm and provided air at  $0.3\text{m/s}$ . Both fuel and coflow air were at 300K. The stoichiometric mixture fraction is  $Z_{st} = 0.167$ .

Regarding the computational mesh, two grids have been used, a fine and a coarse one. The former is a structured collocated mesh concentrated near the central jet with 95x645x32 control volumes (CV) in the radial, axial and azimuthal directions respectively. Mesh sizes were compared against the Kolmogorov scale for this case, and ratios ranging between 15 and 20 were found in the regions of interest, thus ensuring that the analysis was performed in the inertial range. The coarse mesh was an unstructured mesh which featured around 250 kCV, using 16 planes in the azimuthal direction. Unless otherwise stated, reported results correspond to the finer mesh.

Inflow conditions for the fuel jet are taken from a fully developed turbulent pipe flow simulated in a preprocessing stage with  $Re_b$ ,  $V_b$  and  $D$  at the jet inflow temperature.

## 5.4 Results and discussion

The current flame, as reported experimentally, shows low levels of extinction and reignition and is attached to the flame nozzle rim indicating that the flame is rapidly ignited. Therefore, mainly the steady FPV is used. The unsteady and radiation variants serve to assess the effect of the model choice on the subgrid quantities.

The flamelet database is discretised using 100x25x100 points for the mixture fraction, its variance and the progress-variable, respectively. For the unsteady variant 13 different transient flamelets were considered. The radiation variant, due to computational limitations, used 75x25x75x65 points in  $\tilde{Z}, Z_v, \tilde{c}$  and  $\tilde{h}$  directions.

Differential diffusion effects are taken into account when building the flamelet database. For the present case, accounting for differential diffusion effects results in a significant increase in the extinction stoichiometric scalar dissipation rate  $\chi_q$ , as shown in *Chapter 4*. Since no stabilisation mechanism is used, use of Fickian diffusion results in the flame lifting-off and stabilising downstream of the fuel nozzle. When radiation heat losses are included, an Optically Thin Model (OTM) is used [38, 39].

### 5.4.1 Turbulent fluxes closure

First, the turbulent eddy diffusivity model used is assessed. Closures for the Reynolds stress tensor have been extensively studied [40, 41] and new models are still nowadays being postulated [20, 42]. Regarding the unresolved fluxes for the scalars, such as the temperature or the mixture fraction, usually a turbulent Prandtl, Schmidt or Lewis number is assumed. These non-dimensional numbers are either constant or dynamically computed in a similar way as the Dynamic Eddy Viscosity model (DEV) [41, 43]. Thus, there is wide range of closure combinations. Three different eddy viscosity models for the Reynolds stress tensor are tested: The Dynamic Eddy Viscosity (DEV) [41], which is based on a strain invariant, the Wall-Adapting Local Eddy-viscosity (WALE) [20], which is based on strain and rotational invariants, and

the QR [42], based on two strain invariants.

When  $\mu_t$  is computed using a Smagorinsky type eddy viscosity model with a dynamic evaluation of the scalar constant, originally developed for the energy equation, model consistency between momentum and scalars closures is ensured. Use of eddy viscosity models relying on different invariants, as in the WALE and QR models, results in an inconsistency among models, leading to excessive diffusion, as shown in Fig. 5.2, where the radial profiles of the mixture fraction and axial velocity at an axial distance located at 5 nozzle diameters from the fuel jet nozzle ( $y/D = 5$ ) are shown. Results were computed using the coarse mesh. On the one hand, the dynamic model applied to all variables (*sgs4*) shows the best agreement with the experimental data. On the other hand, combinations of the WALE or QR models with either a Schmidt number dynamically evaluated (*sgs1*, *sgs6*) or constant (*sgs3*, *sgs7*) showed higher deviations at the curve tail. Both QR and WALE models coupled with a dynamically evaluated mixture fraction diffusivity show a widened profile. The dynamic model is not applied to the progress-variable when the WALE is used because it was unstable. Either a constant Schmidt (*sgs2*) is used or the mixture fraction turbulent diffusivity is taken ( $D_{c,t} = D_{Z,t}$ ) (*sgs1*). We believe that the dynamic model applied to a non-conserved variable, namely the progress-variable, may be inadequate. If a constant turbulent Schmidt number is used, the WALE model shows a similar behaviour as the dynamic model applied to both the viscosity and diffusivity. Hence, model consistency appears to be important in order to properly evaluate turbulent fluxes and limit the effect of the diffusivity introduced by the turbulence model.

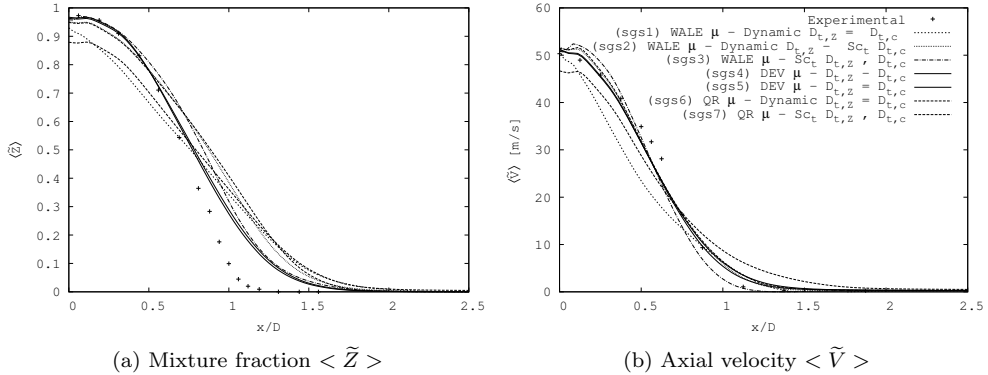


**Figure 5.2:** Time-averaged distributions at  $y/D = 5$  using different combinations of subgrid closures for the unresolved turbulent fluxes. The equal sign in the key ( $= D_{t,c}$ ) indicates that the progress-variable turbulent diffusivity is taken equal to the corresponding one of the mixture fraction. Results correspond the coarse mesh.

Given the just described behaviour, the WALE model with a constant turbulent Schmidt number has been chosen in order to minimize the computational costs, since the WALE model does not require an explicit filtering operation.

#### 5.4.2 Flame stabilisation

The first aspect to analyse is the stabilisation of the flame. Fig. 5.3 shows snapshots of the instantaneous progress-variable using the fine mesh. For each variant of the flamelet model, two different subgrid closures are shown, the equilibrium and SDR-TE ones. It can clearly be seen that neither steady nor unsteady models feature an attached flame. Per contra, the radiation variant does indeed attach to the fuel nozzle rim.

The improvement in the flame stabilisation obtained using the flamelet with radiation is not due to radiation per se. Instead, the range of included solutions into the flamelet database is the main reason. The RFPV only includes solutions close to the burning branch. Analogously, when simulations using the classical steady flamelet were run, a similar behaviour is observed, because the classical steady flamelet model only includes solutions located at the stable burning branch of the S-shaped curve and extinguished solutions for  $\chi_{st} > \chi_q$  [18]. Consequently, all states under the radiation subspace, as in the classical steady flamelet for  $\chi_{st} > \chi_q$ , are projected vertically in the S-shaped curve representation, which results in an always ignited flame. Furthermore, since the parameters used for the RFPV only consider ignited solutions and no solution past  $\chi_q$  is included, the model cannot account for extinction events. Hence, the described projection in flamelet subspace overshadows the effect of the subgrid mixing model in the flame stabilisation.

Regarding the unsteady model, it is observed that it behaves similarly to the steady model. It is suspected that the lack of improvement of the unsteady model is twofold. First, experiments reported an attached flame and low local extinction. Therefore, the numerical simulation should rapidly be accessing solutions close to the stable burning branch. Second, the region under the unstable branch that is stored in the FPV database does not greatly differ between steady and unsteady solutions, as the reaction rate goes rapidly to zero. The essential difference between steady and unsteady models with the radiation model is the available subspace of flamelets solutions. It is suspected that the subgrid progress-variable fluctuations, which are neglected in the present study since a  $\delta - pdf$  is used, may play a similar role as the mixture fraction subgrid fluctuations, characterised through the mixture fraction variance. Comparing between closures for the subgrid mixing, it is observed that the stabilisation distance is dependent on the chosen model. Further details are presented afterwards. Similar conclusions are drawn from the other subgrid closures. Therefore, subgrid mixing modelling is a key element.

Previous studies using the DLR flame A did not report such modelling difficulties. Reported simulations using LES with flamelet modelling used a limited number of

flamelet solutions, one flamelet in the study of Wang and Pope [13] and only the upper steady branch solutions by Ihme [18]. In the latter a similar behaviour to the one here encountered, flame lift-off, is reported. Several studies can be found in the literature in the context of RANS simulations: an Eulerian Particle Flamelet model [14], *pdf* models [11] and MMC [12]. Hence, stabilisation was either shadowed through a limited combustion subspace or through turbulence modelling.

In the next section, focus is placed on the subgrid modelling of the mixture fraction variance. A  $\delta - \text{pdf}$  is retained for the progress-variable in order to limit the number of model closures combinations. At the end, based on the results obtained for the mixture fraction variance, a discussion regarding the progress-variance fluctuations is presented.

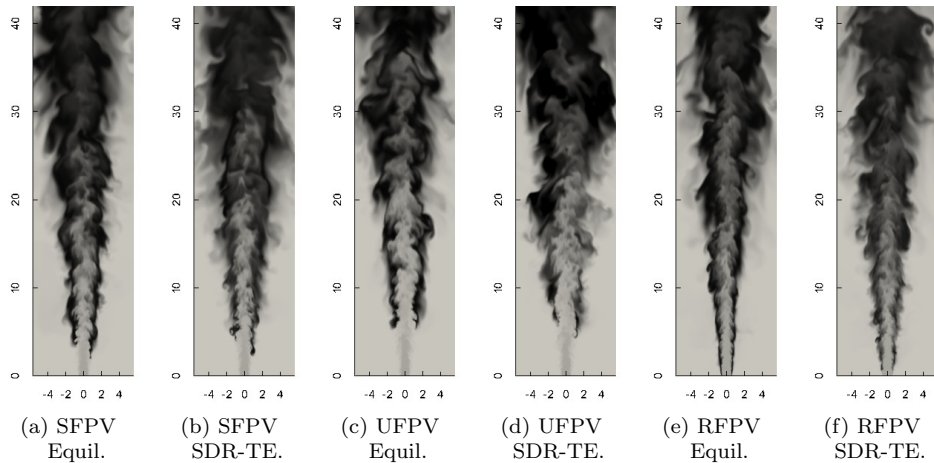
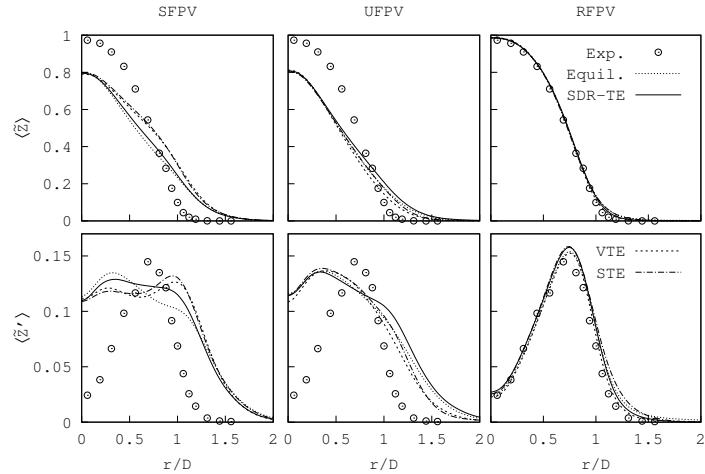


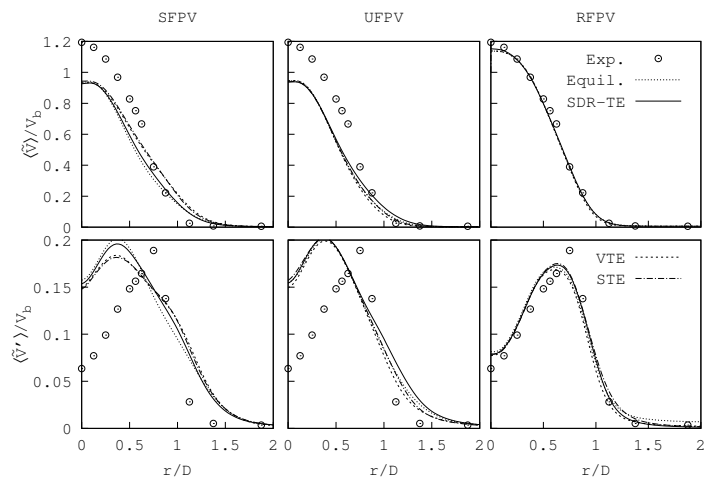
**Figure 5.3:** Snapshot of the instantaneous progress-variable.

Before proceeding to the analysis of the different subgrid models, the effect of the flame lift-off on the fuel jet is shown. In Fig. 5.4 are shown radial profiles of the mixture fraction and axial velocity at  $y/D = 5$  using the different variants of the FPV model and the four subgrid mixing closures. Radial profiles for two quantities are shown, the resolved mixture fraction  $\langle \tilde{Z} \rangle$ , its resolved root mean square (rms)  $\langle \tilde{Z}' \rangle = (\langle \tilde{Z}^2 \rangle - \langle \tilde{Z} \rangle)^{1/2}$ , and the resolved axial velocity  $\langle V \rangle$  and its turbulent intensity  $\langle \tilde{V}' \rangle = (\langle \tilde{V}^2 \rangle - \langle \tilde{V} \rangle)^{1/2}$ . Temporal averaging is denoted by  $\langle \cdot \rangle$ . Profiles are compared against experimental data [7, 8].

Due to the flame lift-off, there is a region between the fuel inlet and the flame base where the shear layer between reactant streams is not affected by the flame. It can be seen that at  $y/D = 5$  both core jet mixture fraction and core velocity



(a) Mixture fraction



(b) Axial velocity

**Figure 5.4:** Radial profiles at  $y/D = 5$ . Results obtained using the steady (SFPV), unsteady (UFPV) and radiation (RFPV) variants of the Flamelet/Progress-Variable model. Dots show data from the reported experiments [7, 8].

are noticeable lower than the experimental ones for the steady and unsteady FPV variants. As reported by Clemens and Paul [44], the strong density gradients induced by flames cause a shear layer thickness reduction, which results in the jet potential core extending over longer distances. Therefore, since in the simulation the jet is not surrounded by the flame, the jet experiences higher shear and the core velocity and scalars are reduced. Profiles obtained using the radiation variant show good agreement with the experimental data. The subgrid mixing model accounts for small differences in this regard. As it can be seen, both steady and unsteady FPV models predict larger fluctuations than the experimental ones.

Fig. 5.5 shows the snapshots of the instantaneous mixture fraction and density using the three variants of the FPV model. Comparing the figures, the effect of the flame is clearly noticeable. As described, the flame interface reduces the turbulent fluctuations at the shear layer, and extends the potential core.

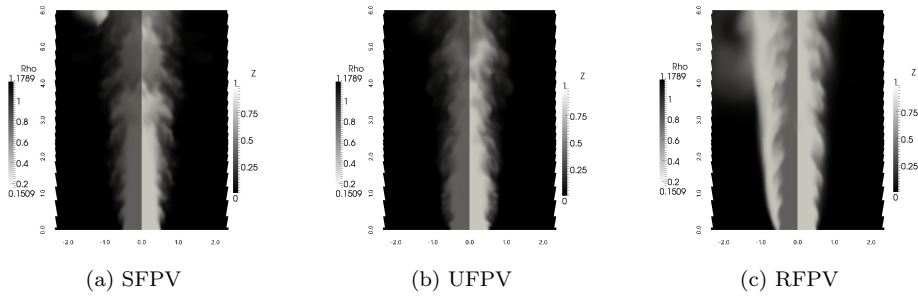


**Figure 5.5:** Snapshots of the density (left) and mixture fraction (right) near jet fields using the steady, unsteady and radiation FPV models. Subgrid mixing is modelled using the equilibrium model. Distances are made non-dimensional using the jet diameter  $D_j$ .

#### 5.4.3 Effect of the subgrid mixing closures

Since the reported levels of local extinction are low for the flame at  $Re=15800$  [7, 8], and in order to include most of the S-shaped solutions, but still limit the effect of the flame lift-off, a slightly modified steady FPV approach is used in the following. The mixing line solution of the SFPV model is taken out from the database. The result is that extinguishing flamelets are projected towards the lowest flamelet solution included into the database. During numerical computations, two main quantities of extinguishing/extinguished flamelets are affected, the reaction rate of the progress-variable and densities. On the one hand, the effect on the reaction rate is not significant, since at the lowest included flamelet the reaction rate is almost zero.

On the other hand, the density change is significant, as there is a 300-400K temperature difference between the pure mixing flamelet and the included flamelet with the smallest  $\chi_{st}$  at the unstable branch. This density decrease is the aimed effect when the pure mixing solution is not included. It will result in an interface between reactant streams. This interface will mimic the effect of thermal expansion and dilatation produced by the flame as if it was stabilised at the fuel nozzle rim. Consequently, turbulent fluctuations are reduced. Results using the radiation variant are presented alongside the modified SFPV ones in order to assess the effect of the subgrid closures when the flame is attached to the nozzle rim. In this case, the reactant streams are fully separated by the flame, and there is a strong density gradient at the shear layer between streams.

#### **Effect on the resolved fields.**

First are presented the time-averaged LES quantities computed using the four subgrid closures listed in Table 5.1. Radial profiles using the modified SFPV flamelet database at four axial locations,  $y/D = 5, 10, 20$  and  $40$  are shown in Fig. 5.6. Results for the STE and VTE models are shown using  $\nu_t$  and  $D_{Z,t}$  as time-scales. In Fig. 5.7 the corresponding results using the radiation variant of the FPV model are presented.

In general, good agreement is seen for all models. The modification in the SFPV database shows a dramatic improvement over the results in Fig. 5.4. Focusing on the mixture fraction, it can be seen that the mean experimental profiles are correctly captured using both variants of the FPV model. Minor differences are observed at the tail of the curve. Regarding mixture fraction fluctuations, at  $y/D = 5$  close to the axis, all mixing models result in an over-prediction of the rms with the modified SPFV. Differently, the RPFV model results in a better description of the fluctuations. Again, the difference is attributable to the flame lift-off. The differences caused by the time-scale in the VTE and STE models are discussed afterwards. Nonetheless, the STE model is seen to deviate significantly from the experimental results.

Considering the velocities, similar trends to the mixture fraction are observed. The modified SFPV model predicts higher fluctuations and a reduced core jet velocity compared to the RPFV model. In general, once the flame is attached, the subgrid mixing model shows a lower effect on the converged statistics. Since the flame causes a laminarization of the shear layer, fluctuations are less pronounced.

Radial profiles of the progress-variable using the modified SPFV model, presented in Fig. 5.8, reveal significant differences between the different models. Close to the jet nozzle, the mixing models play a substantial role in the correct description of the flame. Furthermore, the equilibrium model exhibits an almost linear distribution, indicating that the mixture is not ignited and a mixing process is taking place up to this axial location. At intermediate locations, at  $y/D = 10$  and  $20$ , most models show good agreement with the reference data. Besides the differences due to the time-scales in VTE and STE models, minor differences can be observed close to the jet centre and

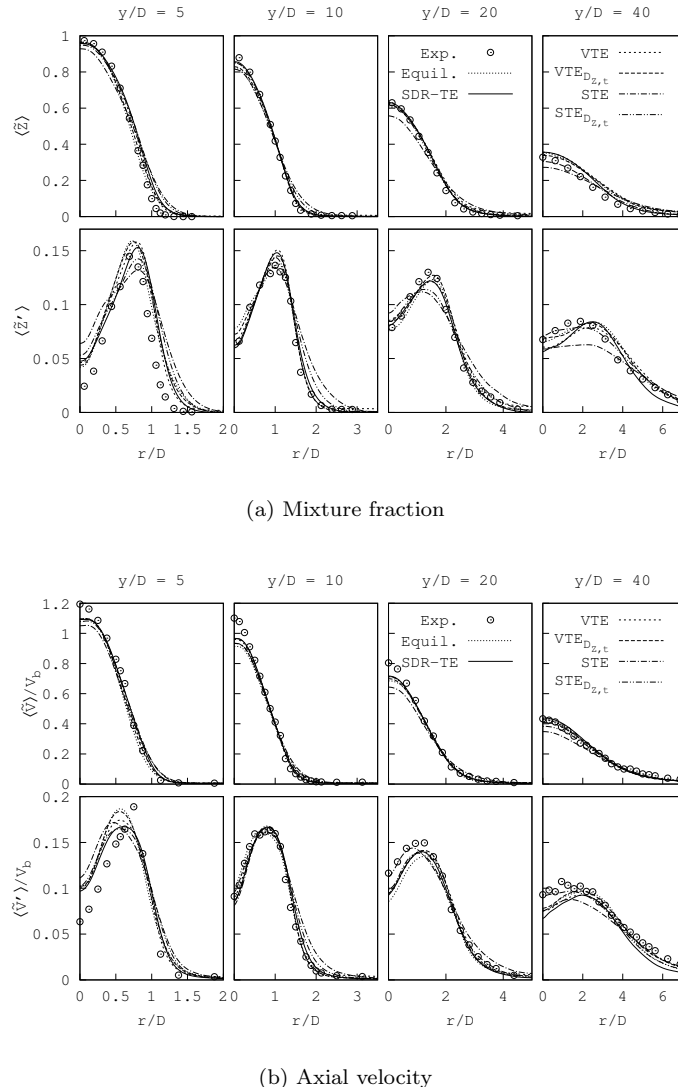


**Figure 5.6:** Radial profiles at four axial locations. Results obtained using the modified steady FPV model. Dots show data from the reported experiments [7, 8]. VTE and STE models are shown using two magnitudes for the time-scale, the turbulent viscosity and the turbulent mixture fraction diffusivity  $D_{Z,t}$ .

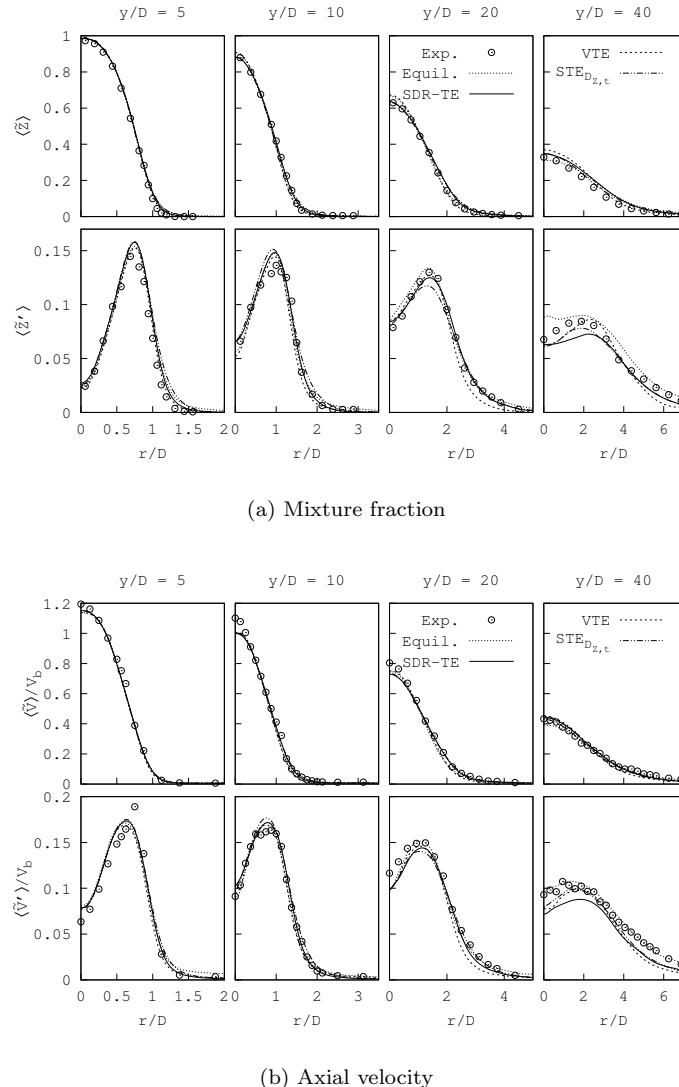


**Figure 5.7:** Radial profiles at four axial locations. Results obtained using the radiation FPV model. Dots show data from the reported experiments [7, 8].

at the curve tail, past the flame front. Further downstream, reaction end products ( $CO/CO_2/H_2/H_2O$ ) are overestimated. Nonetheless, trends are in general correctly

captured.

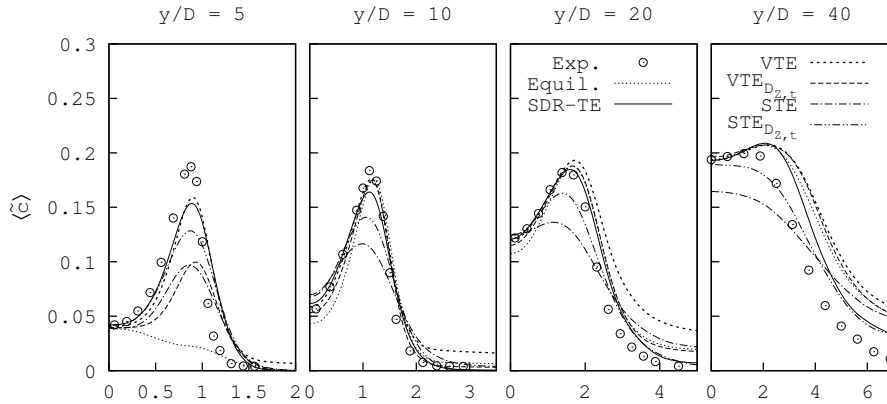


**Figure 5.8:** Radial distributions of the progress-variable using the modified steady FPV model, defined as a linear summation of  $CO$ ,  $CO_2$ ,  $H_2$  and  $H_2O$ . See Fig. 5.6 for further explanation.

Regarding the radiation variant, better agreement is found for the progress variable, shown in Fig. 5.9, as expected from the previous discussion. Interestingly, close to the fuel nozzle, although the shape of the profiles is correctly captured, the peak value is not. Further downstream, at  $y/D = 20$  much better agreement is found. Furthermore, at  $y/D = 40$  the over-prediction of the main combustion products predicted by the steady model is greatly reduced with the inclusion of radiation. Hence, radiation is significant at downstream axial locations. Still, differences due to the subgrid model are noticeable. For example, the equilibrium model shows a broadened profile of combustion products.

#### Turbulent time-scale in VTE and STE models

The choice of time-scale for both VTE and STE models in Eq. (5.22), or change in the model constant, has a significant effect. This constant is directly related to the destruction of variance at the subgrid level in Eq. (5.17). The STE model does not directly take into account production and destruction of variance at the subgrid level, but in Eq. (5.18)  $\chi_{sgs}$  and  $2\tilde{D}_Z \frac{\partial \tilde{Z}}{\partial x_i} \frac{\partial \tilde{Z}}{\partial x_i}$  are two dissipation terms. Therefore, taking into account the results in Fig. 5.8, it may be inferred that the STE model predicts a higher production of subgrid variance and thus the need for a higher constant in the dissipation term. In the VTE,  $\chi_{sgs}$  is also a dissipation source term. However, it has a competing effect with  $2D_{Z,t} \frac{\partial \tilde{Z}}{\partial x_i} \frac{\partial \tilde{Z}}{\partial x_i}$ , which is a production term. Therefore,

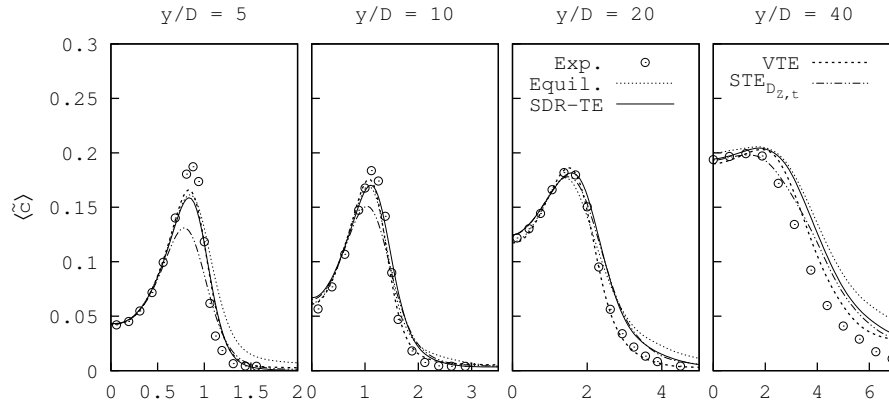


**Figure 5.9:** Radial distributions of the progress-variable using the radiation FPV model, defined as a linear summation of  $CO$ ,  $CO_2$ ,  $H_2$  and  $H_2O$ . See Fig. 5.7 for further explanation.

differences in the mixture fraction gradients can lead to different effects of the  $\chi_{sgs}$  closure in each subgrid mixing model. For example, it can be seen in Fig. 5.8 that the VTE with  $\nu_t$  overestimates the progress-variable at  $y/D = 20$  and 40 while the STE underestimates it. When the time-scale is changed, the profiles match better the experimental data. A downward correction for the VTE is observed whereas an upward correction for the STE is seen. However, focusing on the radial profiles at  $y/D = 5$ , it is observed that the VTE model seems to favour a lower value of the constant, whereas the STE model profiles matches better the experimental ones if a higher value is taken. Therefore, for the VTE model a dynamic evaluation of the constant would be required, as proposed by [4]. The STE shows a unique trend regarding the constant.

Since in the present study a constant turbulent Schmidt number has been used, this shift may be seen as an increase of the constant used in the algebraic relation  $C_Z$ . The value of this constant ( $C_Z$ ) was obtained from analysis of the turbulent spectra and LES filter widths [5]. Furthermore, in the context of RANS simulations a value of two has been usually used [1]. However, higher values for this constant have also been reported [45] when the STE model was used, which is consistent with the present findings.

Results using the RPFV model also showed the described trends, albeit not so clear as in the SFPV model. Therefore, the time-scale discussion is omitted from the RPFV cases.

### Stabilisation distance

The incorrect capture of the progress-variable profiles near the jet nozzle is directly related to the location of the chemically reactive zones. Fig. 5.10 shows the both azimuthal and time averaged progress-variable reaction rate,  $\langle \dot{w}_c \rangle$ , where it can be seen that for all the considered models the flame lifts-off and stabilises at a certain distance from the nozzle jet. Only results using the modified SPFV are shown, since the RFPV resulted in all cases in an attached flame. This lift-off is not observed experimentally. Concerning the effect of the different subgrid mixing models, the Equilibrium model predicts the largest stabilisation distance. In contrast, models accounting for subgrid production and destruction predict shorter distances. The VTE and SDR-TE models show the shortest distances. The VTE predicts a thin and elongated reaction zone, whereas the SDR-TE results in a more compact and thicker reaction zone.

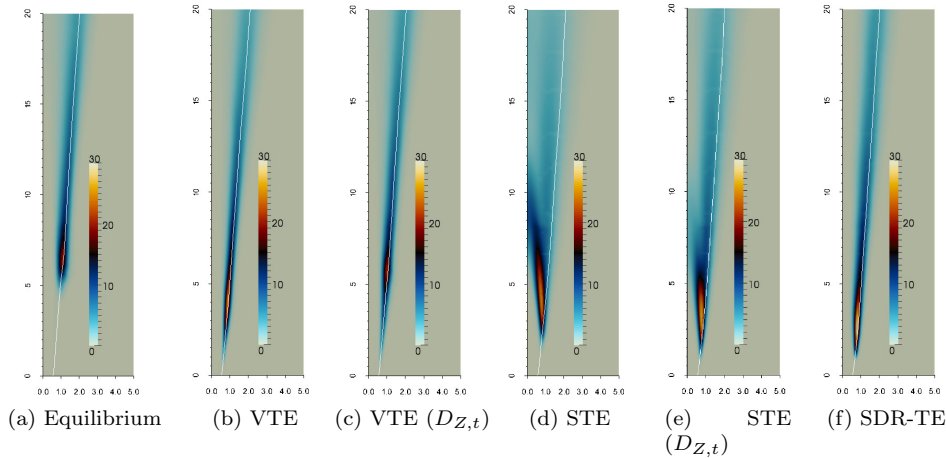


**Figure 5.10:** Azimuthal and time-averaged progress-variable reaction rate,  $\langle \dot{w}_c \rangle$  in  $[kg/m^3]$ . VTE and STE models computed using  $\nu_t$  as time-scale. The white line marks the  $Z_{st}$  iso-contour.

A close inspection at the reaction rate distribution for the STE model, it can bee noticed a misalignment between the reaction rate and the stoichiometric mixture fraction, leaning towards the rich side of the flame. If the turbulent time-scale is made proportional to the turbulent mixture fraction diffusivity  $D_{t,Z}$ , instead of the turbulent diffusivity  $\nu_t$ , this misalignment decreases. Oppositely, for the VTE model, the increase in the time-scale results in the reaction zone of the flame being located at higher axial distances.

Despite the flame being detached from the nozzle flow, once the flame is ignited the profiles obtained match closely the experimental ones. At  $y/D = 5$  in Fig. 5.8 the value of the computed progress-variable is lower than the experimental ones. However, at  $y/D = 10$ , the numerical profiles closely match the experimental ones. Furthermore, at  $y/D = 40$ , there is an overshoot in the numerical profiles with respect to the experimental ones, which is reduced once radiation is accounted for.

Comparing the results of the modified steady FPV model and the “full” one, using for example Fig. 5.10a, Fig. 5.10f, Fig. 5.3a and Fig. 5.3b, it can be seen that the stabilisation distance is only slightly modified by the change in flamelet database. However, the predictions of the velocity and scalars profiles are noticeable improved. As stated, the reason for the minor differences in the progress-variable is that at the lowest included flamelet solution, the reaction rates are almost insignificant. Inspecting the velocity profiles at  $y/D = 5$  with the modified steady and the radiation FPV models, it can be seen that the peak velocity is still better predicted by the latter model, which evidences the effect of the flame on the shear layer and turbulent fluctuations.

#### **Subgrid scalar dissipation rate and mixture fraction variance**

In order to understand the effect of the subgrid models in the stabilisation distance, the mixture fraction variance and subgrid scalar dissipation rate are analysed, as the progress-variable increase is directly dependent to the reaction rate, which in turn depends on  $Z_v$ . It is in the near field of the jet that subgrid effects are higher. Thus their effect on the resolved quantities is more noticeable. The averaged conditional mixture fraction variance  $\langle Z_v \rangle | \langle Z \rangle$  at  $y/D = 5$  is shown in Fig. 5.11a. Surprisingly,  $Z_v$  profiles are rather similar between the Equilibrium model and both variants of the VTE model. The difference in ignition length is explained by the difference in magnitude and the differences in radial distribution. In Fig. 5.6, the resolved rms are not significantly different, but the subgrid part is consistently and significantly higher for the Equilibrium model than for the VTE between the nozzle and  $y/D = 5$ . Therefore, the VTE involves lower subgrid mixing at each control volume, which in turn results in a higher reaction rate for mixture fractions close the stoichiometric one, as depicted in Fig. 5.11b. Thus, the lower reaction rate values for the Equilibrium model, due to the higher predicted subgrid mixing, result in a larger stabilisation distance.

Comparing the subgrid variance predicted by the VTE and STE models, it can be seen that predicted variances with the latter are significantly higher. Kemenov and Pope [29] also reported a similar behaviour when comparing the subgrid variance predictions in a piloted diffusion flame. It was reported that differences in  $Z_v$  could be caused by differences in the gradient field. It is here also argued that these differences can also arise from numerical sources. On the one hand, the mixture fraction gradient calculation plays a different role in each model as previously explained. On the other

hand, in Eq. (5.16), numerical errors from computing the square of the resolved mixture fraction and the subtraction of two similar values can introduce undesired numerical effects. Besides, regarding the increase in the time-scale the the opposite effect between the STE and VTE models can be observed in Fig. 5.11a. In the VTE model, using  $D_{Z,t}$  results in an increase of  $Z_v$  and for the STE results in a decrease.

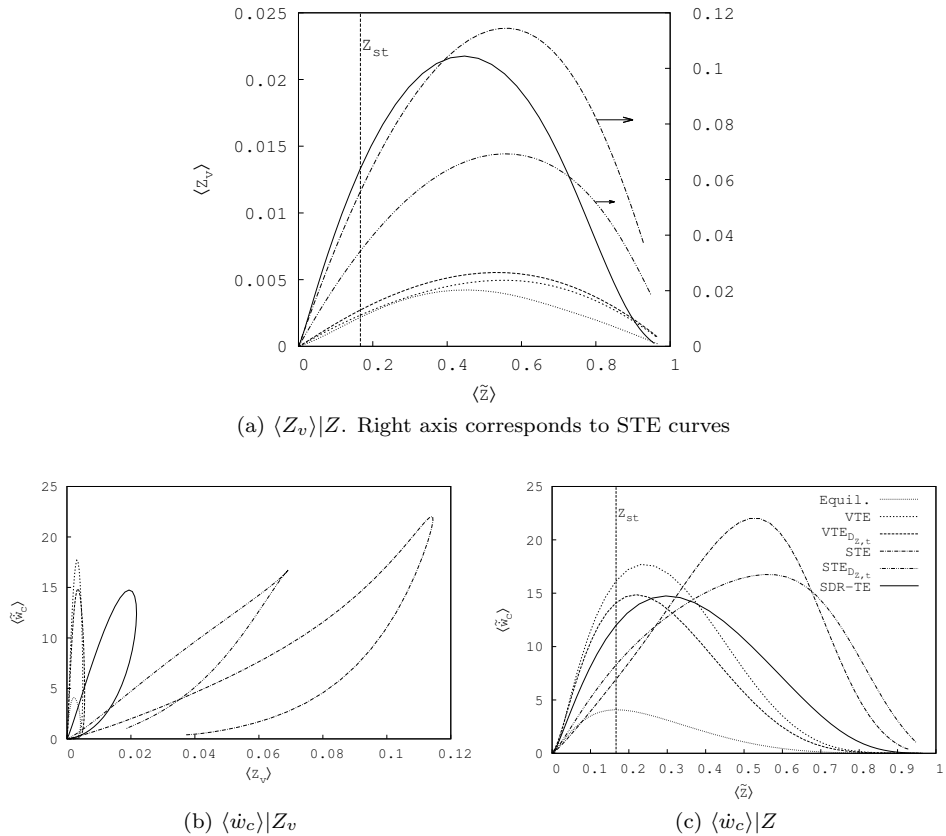


**Figure 5.11:** Conditional  $\langle Z_v \rangle$  and  $\langle \dot{w}_c \rangle$  at  $y/D = 5$  for the modified steady FPV model.

Considering the SDR-TE model, it can be seen that it predicts intermediate values of  $Z_v$ , between those of VTE and STE models. Fig. 5.11b shows the progress-variable reaction rate as a function of the mixture fraction variance, depicting the difference in magnitude due to the variance. The displacement of the reaction rate peak experienced by the STE model, shown in Fig. 5.11c, from the stoichiometric mixture

fraction to higher mixture fractions may be attributed to the predicted high variance. The same effect may be argued for the deviation seen in Fig. 5.10. Regarding the deviation of the reaction rate location for the STE model, it may be argued that even higher values for the constant could be used because i) the change in time-scale only partially corrected the deviation of the reaction rate from the stoichiometric mixture fraction, ii) the SDR-TE model, with lower levels of subgrid variance, showed an improved flame location. Therefore, an increase of the constant could decrease the levels of subgrid variance while improving the flame location.

The former discussion may be extended to axial distances closer to the fuel nozzle. Therefore, to correctly characterise the stabilisation of the present flame it is necessary to accurately represent mixing at the subgrid level.

Although not directly related to the steady or radiation flamelet databases, the scalar dissipation rate affects indirectly most of the models, with the exception of the Equilibrium model. Fig. 5.12 shows the conditional scalar dissipation rate and its resolved and subgrid parts at  $y/D = 5$ .

In Fig. 5.12a, conditional scalar dissipation rates are shown alongside analytical profiles of the scalar dissipation rate in mixture fraction space. For each mixing model, a curve corresponding to the stoichiometric scalar dissipation rate, using Eq. (5.5) is plotted. Additionally, analytical profiles following a scalar dissipation rate functional dependence on  $Z$  based on a one dimensional mixing layer are shown [9, 46]

$$\chi = \chi_{st} \frac{Z^2 \ln(Z)}{Z_{st}^2 \ln(Z_{st})} \quad (5.25)$$

In Fig. 5.12 these curves are denoted as “(ln)”. Most of the models show good agreement with the functional form of Eq. (5.5). However, the STE model shows a better agreement with Eq. (5.25). Furthermore, the displacement of the peak in Fig. 5.12c is due to the subgrid part as the resolved part, shown in Fig. 5.12b, shows a profile centred around  $Z = 0.5$ , similar to the profiles obtained using Eq. (5.5). At higher axial locations, as the resolved part dominates over the subgrid part,  $\tilde{\chi}_Z$  profiles match better those computed using Eq. (5.5). Besides,  $\chi_{sgs}$  corresponding to both variants of the VTE model, can be seen to be smaller than for the STE, which is consistent with the small values of the variance presented, since these two quantities are related through Eq. (5.22), and  $\chi_{sgs}$  is a dissipation term in Eq. (5.17).

The  $\tilde{\chi}_Z$  profile with the SDR-TE model shows a strange turn close to the fuel mixture fraction boundary in Fig. 5.12a, which corresponds to the axial axis around which the mesh is extruded. Some grid properties, such as the aspect ratio of the control volumes located near the axis, are noticeably different to those surrounding them. Therefore, computation of gradients may be affected. As the SDR-TE model requires computing several gradients and second derivatives, as well as multiplications among them, numerical errors may arise in this region. However, the effect is limited,

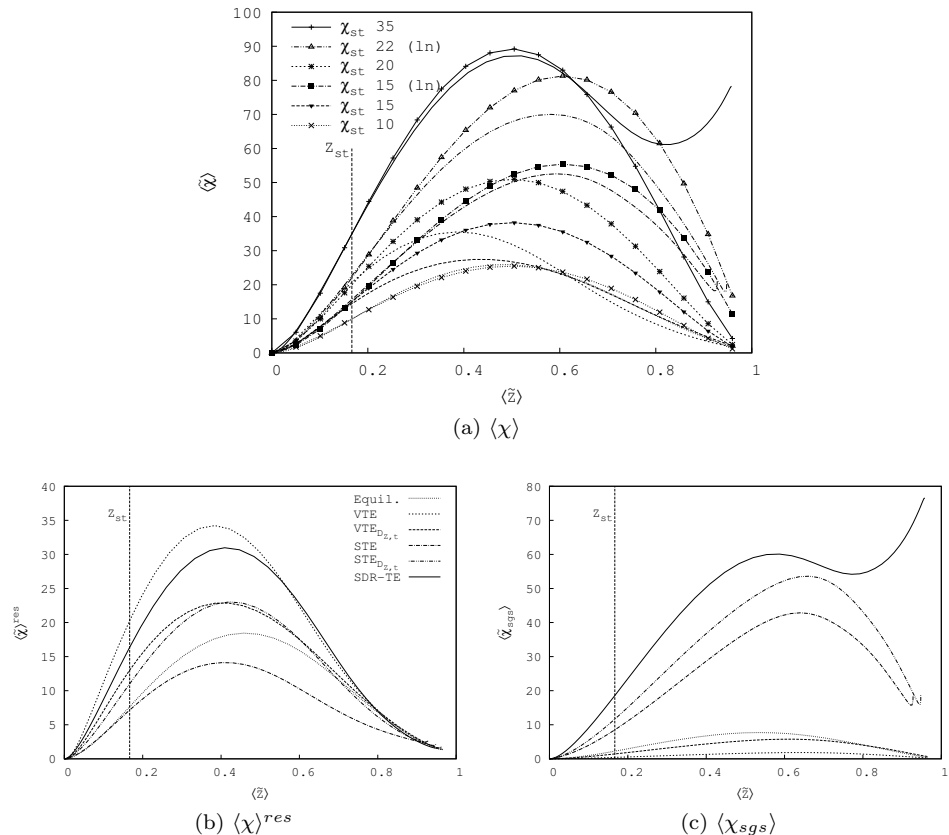


**Figure 5.12:** Conditional Scalar dissipation rate at  $y/D = 5$  for the modified steady FPV model. Lines with points labeled as  $\chi_{st}$  show the analytically scalar dissipation rate distribution using Eq. (5.5) and Eq. (5.25). The latter is labelled as *ln*. Each  $\chi_{st}$  curve line-style matches the line-style of a scalar dissipation rate model. Thus, indicating the  $\chi_{st}$  at  $y/D = 5$  for each model.

as the profiles for the solution variables ( $\tilde{Z}, \tilde{c}, \tilde{V}$ ) are in general in good agreement with the reference data. Nonetheless, it may be seen from Fig. 5.12c that the strange behaviour is caused by the subgrid part of the scalar dissipation rate.

It has been shown that the mixture fraction variance for the STE was higher than the VTE, and that it could be related to the computed gradients. The conditional distribution of the scalar dissipation rate shown in Fig. 5.12 also depicts higher gradients for the STE than for the VTE.

Considering the time-scale for VTE and STE models, in Fig. 5.12 it can also be seen the opposite effect of increasing the time-scale, or alternatively the constant. For the STE it implies an increase in the scalar dissipation rate, whereas for the VTE it results in a decrease. Furthermore, using  $D_{Z,t}$  as time-scale results in a similar resolved scalar dissipation rate for both STE and VTE. However, the subgrid part is still different.

In general, regarding the predicted scalar dissipation rate, differences between the subgrid part of the scalar dissipation rate are more pronounced than their resolved counterpart. Given the stabilisation distances for each mixing model, there appears to be a correlation between the shortest predicted distance and the magnitude of the scalar dissipation rate, which would indicate that the SDR-TE model would be in better agreement with the experimental results, while the other models underestimate the scalar dissipation rate.

The mixture fraction variances obtained using the radiation FPV are shown in Fig. 5.13. The most notable difference is the reduction in the variance predicted by the STE model. With the RPFV, and thus an attached flame, the thermal expansion induced by the flame results in lower fluctuations. Oppositely, the SDR-TE model predicts slightly higher  $Z_v$ . It is interesting to note that STE and SDR-TE converge to similar predicted subgrid variances. Both VTE and Equilibrium models do not show significant changes, which may be caused by the low values of  $Z_v$  already predicted. Regarding the reaction rate, shown in Fig. 5.13b, it can be seen that the reduction in  $Z_v$  results in a correction of the misalignment in the STE model. For the Equilibrium model, since the flame is ignited from the nozzle jet rim, the progress-variable is already higher at this axial distance which leads to higher reaction rates.

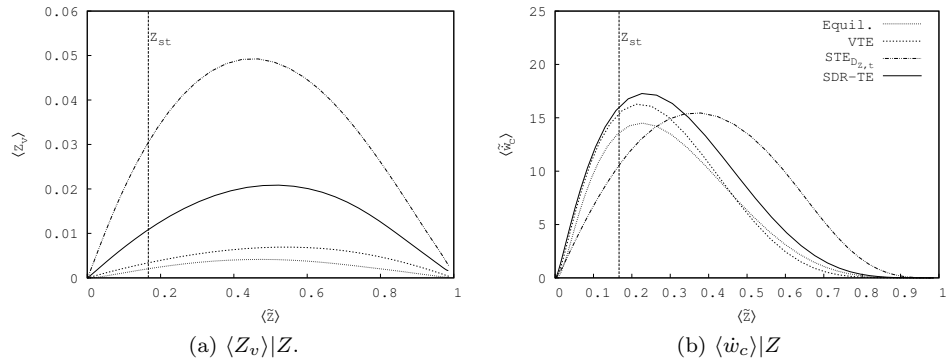


**Figure 5.13:** Conditional  $\langle Z_v \rangle$  and  $\langle \dot{w}_c \rangle$  at  $y/D = 5$  for the radiation FPV model.

Concerning the scalar dissipation rate, shown in Fig. 5.14, it can be observed that

subgrid mixing models tend to two different solutions. The difference is exclusively caused by the subgrid part. It is worth noting that STE and VTE predictions also differ regarding the subgrid scalar dissipation rate. Although STE and VTE are equal at the continuous level, at the discrete level subgrid magnitudes diverge. Nonetheless, primary magnitudes, such as the mixture fraction, the velocities and even the resolved part of the scalar dissipation rate do not show this difference. Regarding the subgrid scalar dissipation rate, again it can be observed that for the SDR-TE model and the STE, their conditional distributions are in better agreement with the logarithmic distribution of  $\chi_Z(Z)$  Eq. (5.25). On the other hand, VTE and Equilibrium models are in better agreement with Eq. (5.5).

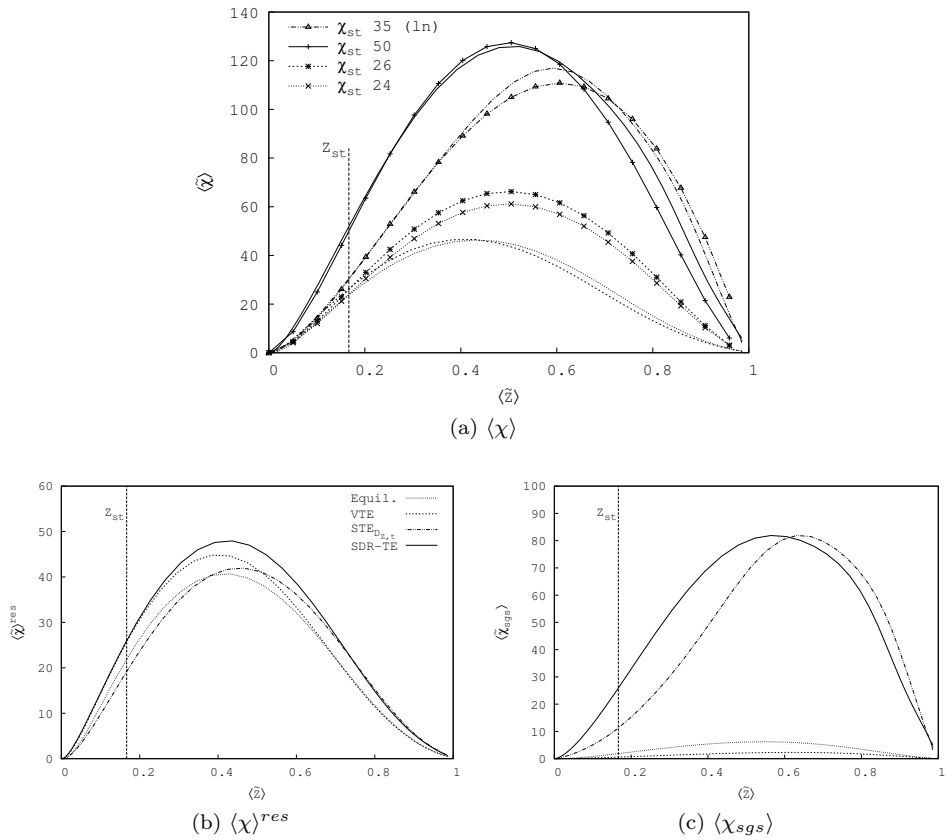


**Figure 5.14:** Conditional Scalar dissipation rate at  $y/D = 5$  for the radiation FPV model. See Fig. 5.12 for further details.

### Progress-variable fluctuations

The previous discussion was centred around the modelling of subgrid mixing through models for the mixture fraction variance and subgrid scalar dissipation rate. The choice of a  $\delta - pdf$  for the progress-variable meant that only effects of its mean value were considered, and its fluctuations were overlooked. The  $\delta - pdf$  has been a common approach in several studies where good agreement with the reference data was reported [4, 6, 17, 23]. However, there are several factors which point towards the need of including the fluctuations of the progress-variable in order to correctly describe the flame stabilisation.

First, results using a coarse mesh resulted in an attached flame. The use of a  $\delta - pdf$  implies that a single flamelet is used to represent the flame state in a control volume. This could indicate that in the coarse mesh, the database is accessed at flamelets at higher progress-variable values, which in turn resulted in higher reaction rates.

Second, resolved progress-variable rms at  $y/D = 5$ , shown in Fig. 5.15, are of the same order of the mixture fraction ones, although slightly lower in magnitude. Given the noticeable effect of the subgrid mixture fraction variance modelling, it is expected that fluctuations of the progress-variable would also have a role in the stabilisation. Furthermore, it can be seen in the figure that neither of the models describe correctly the resolved rms. Interestingly, the rms predicted by the SPFV model are of the same order as the experimental ones, even though the flame lift-off and the reduction of the potential region of the jet. For the modified SFPV and the RFPV variants a reduction of the predicted rms can be observed, which can be related to the effects caused by the presence of the flame. Furthermore, the progress-variable was underestimated, which could account for the reduced rms values. In general the shape of the rms are correctly captured. However, the Equilibrium model mostly results in a single peak curve. The other models do show a dual peak.

Third, as previously stated, the radiation FPV model projects vertically the solutions under the unstable branch of the S-shaped curve towards the upper branch. The resulting rapid ignition and attachment, which is similar to the experiments, points towards the presence of burning flamelets near the flame nozzle, which influence the not ignited ones. The  $\delta - pdf$  cannot account for this effect as it only considers mean values.

With these arguments, if a statistical distribution for the progress-variable was used, each control volume would be represented by more than one single flamelet solution. Then, fluctuations of the progress-variable would broaden the number of flamelets used to represent the state of a single control volume, which could probably lead to higher reaction rates at lower values of the progress-variable. In the literature, either  $\beta - pdf$  or a Statistically Most Likely Distribution (SMLD) [47] have been proposed and used with different degrees of success.

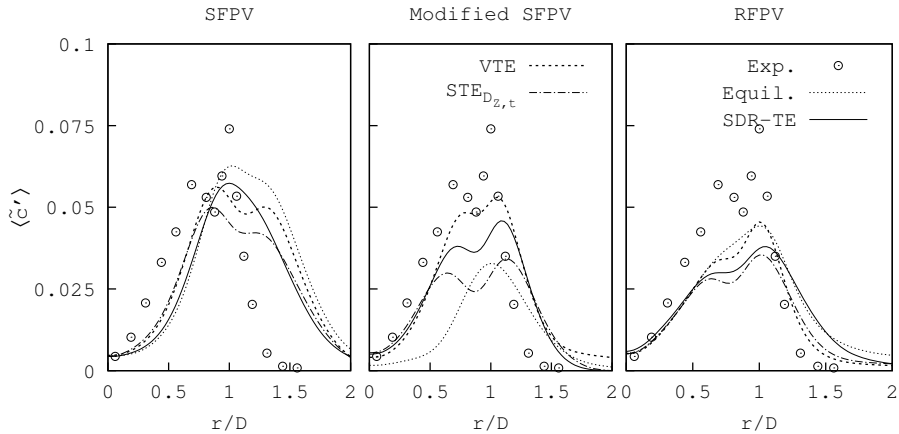


**Figure 5.15:** Radial distributions at  $y/D = 5$  of the resolved progress-variable rms using the steady (SFPV), the Modified SFPV and radiation (RFPV) models. Experimental rms are linear summation of  $CO$ ,  $CO_2$ ,  $H_2$  and  $H_2O$ .

## 5.5 Conclusions

The effect of subgrid mixing in the stabilisation of a  $CH_4/H_2/N_2$  jet flame has been studied using a Flamelet/Progress-Variable model. The studied flame does not feature any auxiliary method to aid its stabilisation. Therefore, diffusion, or mixing, process has been shown to be key in its stabilisation.

Assumed *pdfs* are used in the FPV model to represent statistical distributions of the solution quantities. The subgrid mixture fraction variance is a parameter of the *pdf* and has to be modelled during numerical simulations. Similarly, the subgrid scalar dissipation rate also has to be closed as it indirectly affects the subgrid variance. Four subgrid models have been presented in order to describe the subgrid mixture fraction variance and subgrid scalar dissipation rate: i) an equilibrium model, ii) a variance transport model (VTE), iii) a second moment transport model (STE) and iv) a model using a transport equation for the filtered squared mixture fraction gradient (SDR-TE).

A flame lift-off resulted when the FPV model in its steady and unsteady form were used. Only the radiation variant resulted in an attached flame. For this model, it has been argued that the reason for the flame attachment was not due to the inclusion of radiation in the computations, rather the limited flamelet subspace considered for this case. Nonetheless, it served to show that a limited combustion model may overshadow subgrid diffusion effects. Since the radiation model only contained solutions close to

the burning branch, and could not describe extinction phenomena, it resulted in an attached flame. In this case, the diffusion model played a secondary role.

Comparing the solutions between lifted-off and attached flames, the effect of the density change produced by the flame has been shown. A laminarization of the shear layer is caused by the heat release of the flame. When the flame has lifted-off, fluctuations at the shear layer were higher which resulted in a reduction of the fuel jet potential core.

In order to consider most of the flamelet subspace while limiting the effect of the flame lift-off, a modified steady FPV model has been used. In it, the pure mixing solution of the flamelet solutions was removed. Thus, in flamelet space, solutions under the unstable branch of the S-shaped curve were projected to the flamelet solution with the lowest included scalar dissipation rate. Nonetheless, the effect of this modification had little effect in the stabilisation distances while it greatly improved the model predictions for the core jet.

The subgrid models have been shown to be the key element in describing the flame stabilisation location. The Equilibrium model, which assumed a production and destruction equilibrium of the variance at the subgrid level, predicted the longest distances. Regarding the other three models, they improved the predictions noticeably. The SDR-TE model showed the best agreement with the experimental data. However, the model requires the computation of several computationally costly terms, which reduces its viability and is more prone to numerical errors, as observed in the computation of the scalar dissipation rate close to the jet axis. VTE and STE models offer a compromise between computational cost and accuracy, compared to the Equilibrium model. Although, both STE and VTE models are equivalent at the continuous level, it has been shown that predictions between both models differ. Furthermore, the STE model showed a significant deviation of the reaction rate from the stoichiometric mixture fraction, which was not found in the other models. The model constant had an important effect in improving the results. When a larger constant was used, results for the STE improved while the VTE showed a mixed behaviour, improving at some points and deteriorating at others. Besides, the conditional scalar dissipation rate predicted by the STE model showed a different shape than the VTE. The difference is mainly due to the subgrid part.

Results with the radiation FPV showed lower sensitivity to the diffusion model. Nonetheless, at higher axial locations, the Equilibrium model resulted in a slightly wider radial profile of the progress-variable, indicating a wider flame. Besides, comparing the results of the adiabatic and radiation simulations, at  $y/D = 40$  it is found that radiation is important as the adiabatic computations predict too much combustion end products ( $CO/CO_2/H_2/H_2O$ ).

Finally, it has been argued that an extended *pdf* for the progress-variable should be used in order to correctly predict the mixing and ignition processes near the fuel

jet nozzle. Other common approaches found in the literature are a  $\beta - pdf$  or a Statistically Most Likely Distribution (SMLD), which will be studied in the future.

In closing, the VTE with  $\nu_t$  and STE with  $D_{Z,t}$  models offer a good approach in including non-equilibrium effects. On the other hand, the Equilibrium model showed limited success. Oppositely, the SDR-TE model showed good agreement in general, although minor discrepancies were found when the RFPV model was used. Nonetheless, the computational costs make its possible applications limited to canonical cases. The STE model subgrid predictions were in fairly agreement with the ones from the SDR-TE model. However, the resolved quantities showed noticeable deviations from the experimental data. Therefore, the VTE shows the best compromise between accuracy and computational cost.

## References

- [1] N. Peters. *Turbulent Combustion*. Cambridge University Press, 2000.
- [2] S.B. Pope. Pdf methods for turbulence reactive flows. *Progress in Energy and Combustion Science*, 11:119–192, 1985.
- [3] C.D. Pierce and P. Moin. A dynamic model for subgrid-scale variance and dissipation rate of a conserved scalar. *Physics of Fluids*, 10:3041, 1998.
- [4] C.M. Kaul, V. Raman, E. Knudsen, E.S. Richardson, and J.H. Chen. Large eddy simulation of a lifted ethylene flame using a dynamic nonequilibrium model for subfilter scalar variance and dissipation rate. *Proceedings of the Combustion Institute*, 34(1):1289–1297, 2013.
- [5] M. Ihme and H. Pitsch. Prediction of extinction and reignition in nonpremixed turbulent flames using a flamelet/progress variable model 2. Application in LES of Sandia flames D and E. *Combustion and Flame*, 155(1-2):90–107, 2008.
- [6] E. Knudsen, E.S. Richardson, E.M. Doran, N. Pitsch, and J.H. Chen. Modeling scalar dissipation and scalar variance in large eddy simulation: Algebraic and transport equation closures. *Physics of Fluids*, 24:055103, 2012.
- [7] W. Meier, R.S. Barlow, Y.-L. Chen, and J.-Y. Chen. Raman/Rayleigh/LIF measurements in a turbulent CH<sub>4</sub>/H<sub>2</sub>/N<sub>2</sub> jet diffusion flame: Experimental techniques and turbulence-chemistry interaction. *Combustion and Flame*, 123:326–343, 2000.
- [8] V. Bergmann, W. Meier, D. Wolff, and W. Stricker. Application of spontaneous Raman and Rayleigh scattering and 2D LIF for the characterization of a turbulent CH<sub>4</sub>/H<sub>2</sub>/N<sub>2</sub> jet diffusion flame. *Applied Physics B-Lasers And Optics*, 66:489–502, 1998.

- [9] H. Pitsch. Unsteady flamelet modelling of differential diffusion in turbulent jet diffusion flames. *Combustion and Flame*, 123:358–374, 2000.
- [10] M.D. Emami and A. Eshghinejad Fard. Laminar flamelet modeling of a turbulent CH<sub>4</sub>/H<sub>2</sub>/N<sub>2</sub> jet diffusion flame using artificial neural networks. *Applied Mathematical Modelling*, 36(5):2082–2093, 2012.
- [11] R.P. Lindstedt and H.C. Ozarovsky. Joint scalar transported pdf modeling of nonpiloted turbulent diffusion flames. *Combustion and Flame*, 143:471–490, 2005.
- [12] K. Vogiatzaki, A. Kronenburg, M.J. Cleary, and J.H. Kent. Multiple mapping conditioning of turbulent jet diffusion flames. *Proceedings of the Combustion Institute*, 32(2):1679–1685, 2009.
- [13] H. Wang and S.B. Pope. Large eddy simulation/probability density function modeling of a turbulent CH<sub>4</sub>/H<sub>2</sub>/N<sub>2</sub> jet flame. *Proceedings of the Combustion Institute*, 33:1319–1330, 2011.
- [14] M. Fairweather and R.M. Woolley. First-order conditional moment closure modeling of turbulent, nonpremixed methane flames. *Combustion and Flame*, 138:3–19, 2004.
- [15] K. W. Lee and D. H. Choi. Prediction of NO in turbulent diffusion flames using eulerian particle flamelet model. *Combustion Theory And Modelling*, 12(5):905–927, 2008.
- [16] K. W. Lee and D. H. Choi. Analysis of NO formation in high temperature diluted air combustion in a coaxial jet flame using an unsteady flamelet model. *International Journal Of Heat And Mass Transfer*, 52(5-6):1412–1420, 2009.
- [17] M. Ihme, H. Pitsch, and D. Bodony. Radiation of noise in turbulent non-premixed flames. *Proceedings of the Combustion Institute*, 32(1):1545–1553, 2009.
- [18] M. Ihme. *Pollutant formation and noise emission in turbulent non-premixed flames*. PhD thesis, Standford University, Stanford, United States of America, 2007.
- [19] A. Kemenov, K and S.B. Pope. Molecular diffusion effects in les of a piloted methane-air flame. *Combustion and Flame*, 158(2):240–254, 2011.
- [20] F. Nicoud and F. Ducros. Subgrid-scale stress modeling based on the square of the velocity gradient tensor. *Flow, Turbulence and combustion*, 62:183–200, 1999.

- [21] O. Lehmkuhl. *Numerical resolution of turbulent flows on complex geometries*. PhD thesis, Polytechnic University of Catalonia, Terrassa, Spain, 2012.
- [22] H. Pitsch and N. Peters. A consistent flamelet formulation for non-premixed combustion considering differential diffusion effects. *Combustion and Flame*, 114:26–40, 1998.
- [23] C.D Pierce and P. Moin. Progress-variable approach for large-eddy simulation of non-premixed turbulent combustion. *Journal of Fluid Mechanics*, 504:73–97, 2004.
- [24] C. Wall, B.J. Boersma, and P. Moin. An evaluation of the assumed beta probability density function subgrid-scale model for large eddy simulation of non-premixed, turbulent combustion with heat release. *Physics of Fluids*, 12:2522, 2000.
- [25] H. Pitsch and M. Ihme. An unsteady flamelet/progress variable method for les of nonpremixed turbulent combustion. In *Proceedings of the 43rd Aerospace Sciences Meeting and Exhibit*, 2005.
- [26] H. Pitsch. Modeling of radiation and nitric oxide formation in turbulent non-premixed flames using a flamelet/progress variable formulation. *Physics of Fluids*, 20(5):055110, 2008.
- [27] C.T. Bowman, M. Frenklach, G. Smith, B. Gardiner, and et al. <http://www.me.berkeley.edu/gri-mech/releases.html>, 2012.
- [28] C. Jiménez, F. Ducros, B. Cuenot, and B. Bédat. Subgrid scale variance and dissipation of a scalar field in large eddy simulations. *Physics of Fluids*, 13(6):1748, 2001.
- [29] A. Kemenov, K. H. Wang, and S.B. Pope. Modelling effects of subgrid-scale mixture fraction variance in les of a piloted diffusion flame. *Combustion Theory And Modelling*, 16(4):611–638, 2012.
- [30] C.M. Kaul, V. Raman, Balarac G., and Pitsch H. Numerical errors in the computation of subfilter scalar variance in large eddy simulations. *Physics of Fluids*, 21:055102, 2009.
- [31] G. Balarac, H. Pitsch, and V. Raman. Modeling of the subfilter scalar dissipation rate using the concept of optimal estimators. *Physics of Fluids*, 20:091701, 2008.
- [32] G. Balarac, H. Pitsch, and V. Raman. Development of a dynamic model for the subfilter scalar variance using the concept of optimal estimators. *Physics of Fluids*, 20:035114, 2008.

- [33] R.W.C.P. Verstappen and A.E.P. Veldman. Symmetry-preserving discretization of turbulent flow. *Journal of Computational Physics*, 187:343–368, 2003.
- [34] M. S. Darwish and F. H. Moukalled. Normalized variable and space formulation methodology for high-resolution schemes. *Numerical Heat Transfer, Part B: Fundamentals*, 26:76–96, 1994.
- [35] R. Borrell, O. Lehmkuhl, F.X. Trias, G. Oyarzún, and A. Oliva. FFT-based poisson solver for large scale numerical simulations of incompressible flows. In *Proceedings of the 23rd Parallel Computational Fluid Dynamics*, 2011.
- [36] O. Lehmkuhl, C.D. Pérez Segarra, R. Borrell, M. Soria, and A. Oliva. Termofluids: A new parallel unstructured CFD code for the simulation of turbulent industrial problems on low cost PC cluster. *Proceedings of the Parallel CFD Conference*, pages 1–8, 2007.
- [37] <http://www.sandia.gov/TNF/DataArch/DLRflames.html>, 2012.
- [38] R.S. Barlow, J.H. Karpetis A.N., Frank, and J.-Y. Chen. Scalar profiles and NO formation in laminar opposed-flow partially premixed methane/air flames. *Combustion and Flame*, 127(3):2102–2118, 2001.
- [39] D. Carbonell. *Numerical studies of diffusion flames. Special emphasis on flamelet concept and soot formation.* PhD thesis, Polytechnic University of Catalonia, Terrassa, Spain, 2010.
- [40] P. Sagaut. *Large Eddy Simulation for Incompressible Flows. An Introduction.* Springer-Verlag, 1980.
- [41] M. Germano, U. Piomelli, P. Moin, and W. Cabot. A dynamic subgrid-scale eddy viscosity model. *Physics of Fluids*, 3(7):1760–1765, 1991.
- [42] R. Verstappen. When does eddy viscosity damp subfilter scales sufficiently? In *Quality and Reliability of Large-Eddy Simulations II, volume 16 of ERCOFTAC Series*, volume 16, pages 421–430. M.V. Salvetti, B. Geurts, J. Meyers, and P. Sagaut, editors, 2010.
- [43] P. Moin, W. Squires, W. Cabot, and S. Lee. A dynamic subgrid-scale model for compressible turbulence and scalar transport. *Physics of Fluids*, 3(11):2746–2757, 1991.
- [44] N.T. Clemens and P.H. Paul. Effects of heat release on the near field flow structure of hydrogen jet diffusion flames. *Combustion and Flame*, 102(3):271–284, 1995.

- [45] M. Mueller and H. Pitsch. Les model for sooting turbulent nonpremixed flames. *Combustion and Flame*, 159(6):2166–2180, 2012.
- [46] H. Pitsch, M. Chen, and N. Peters. Unsteady flamelet modeling of turbulent hydrogen-air diffusion flames. *Twenty-Seventh Symposium (International) on Combustion*, pages 1057–1064, 1998.
- [47] M. Ihme and H. Pitsch. Prediction of extinction and reignition in nonpremixed turbulent flames using a flamelet/progress variable model 1. A priori study and presumed PDF closure. *Combustion and Flame*, 155(1-2):70–89, 2008.



# Conclusions

The work developed in this thesis aimed at developing methods and techniques for the simulation of combustion phenomena using Computational Fluid Dynamics (CFD). Specifically, the main target has been turbulent diffusion jet flames in the flamelet regime. Therefore, the different aspects required to perform the simulation of such flames have been described. Although each chapter contains its own conclusions section, a brief review is here presented for the sake of completeness.

In first place, in *Chapter 1* the basic equations which describe chemically reacting flows are introduced. A basic description of chemical kinetics is given. Transport terms and coefficients for multicomponent flows are introduced. Subsequently, combustion regimes are defined, premixed and non-premixed. Then, an introduction to turbulent reacting flows is performed. It is argued that Large Eddy Simulation (LES) offers a good approach due to its transient nature. Additionally, modelling challenges are stated. In LES the large scales of the flow are solved, whereas the small ones are modelled. Since chemical reactions occur at the molecular level, an important modelling effort is required. Due to the non-linearity of the chemical reaction term it is argued that direct closure is not viable [1]. Different combustion models are presented and discussed. Among them, the Eddy Dissipation Concept, the Conditional Moment Closure, the transported Probability Density Function and the flamelet model are mainly discussed. The latter is argued to be suitable for many designs of industrial and academic interest. Hence, it has been the focus of the present thesis.

The remainder chapters deal with different methods required to perform simulations of turbulent diffusion flames. Briefly, in *Chapter 2* is presented a temporal integration scheme and spatial discretisation schemes suitable for variable density flows. In *Chapter 3* a combustion model, specifically a flamelet model, is presented. The model is described in its laminar and turbulent forms. Then, in *Chapter 4* the parameters of the combustion model are analysed. Finally, in *Chapter 5* different models to describe mixing at the subgrid level are studied. In the following are summarised the main findings of each chapter.

*Chapter 2* presents a transient algorithm for variable density flows. Focus is placed on the use of unstructured meshes. Different discretisation schemes are studied. Specifically, a first order upwind scheme, a second order centred scheme and a high order upwind scheme, namely the QUICK scheme. For the latter, a new approach is presented to define upwind and downwind nodes on unstructured meshes. In the chapter it is shown that due to the use of unstructured meshes, the accuracy of high order schemes is reduced. Additionally, the symmetry-preserving scheme is used for the convective term in the momentum equations. This scheme was developed in the context of incompressible flows and the reason for using it is justified by its property of preserving kinetic energy at the discrete level [2]. In the chapter it is shown that this scheme is also suitable to be applied to variable density flows in the low Mach regime.

Moreover, the study considered two different types of spatial variable arrangement applied to unstructured meshes: collocated and staggered schemes. It is described that the collocated scheme places all variables at the cell centres, whereas the staggered scheme uses displaced meshes where velocities are evaluated, leaving the pressure located at the cell centres. The shift of the velocities results in the staggered scheme not suffering from the odd-even decoupling found in collocated schemes. In the collocated scheme, following Felten and Lund [3] a velocity interpolation is applied to minimises the errors in the conservation of kinetic energy, plus a mass correction to avert the odd-even decoupling. Concerning the staggered discretisation, the formulation by Perot [4] is applied. The cell centred velocity reconstruction, which is a critical aspect of this formulation, is analysed. It is found that the first-order reconstruction method performs correctly on structured meshes. When unstructured meshes are considered, a convergence of the results could be observed. However discrepancies with the reference results was observed. A new approach developed by Jofre et al. [5], here extended to variable density flows, showed better behaviour, even though with a higher computational cost.

The described temporal algorithm and spatial schemes are used to study two different cases: a non-reacting and a reacting case. The former case consists of a differentially heated cavity under a large temperature difference. The test served to study the different spatial schemes described. The latter case, the chemically reacting one, is a transient auto-igniting case which served to study the transient behaviour of the temporal algorithm. The effect of the different interpolation schemes on the auto-ignition length is evaluated.

Once a suitable algorithm for variable density flows in either laminar or turbulent regime is set, a suitable combustion model for laminar and turbulent flames is described in *Chapter 3*. The flamelet model introduces a split in the combustion process, resulting in a reaction-diffusion problem, which defines the flame structure, and

a transport problem, which describes the flame motion in a flow. Through this split, the flame structure may be preprocessed and stored in a flamelet library to be used during CFD simulations. In the chapter it is argued that the classical flamelet, which uses the mixture fraction and the stoichiometric scalar dissipation rate as parameters, cannot fully represent the whole flamelet subspace unless an interactive strategy is adopted. However, if the latter approach is taken, then the flamelet model cannot be fully preprocessed. Thus, the computational load during CFD simulations increases. Then, the Flamelet/Progress-Variable (FPV) model developed by Pierce and Moin [6] is presented, which is capable of unambiguously representing the flamelet subspace while still computing all flamelet solutions in a preprocessing stage. The two main parameters used are the mixture fraction, which is a measure of the mixing process, and the progress-variable, which represents the reaction progress. Different variants of the FPV model are presented: steady, unsteady and including radiation, each one using a different set of parameters to represent a different subset of the flamelet subspace. Furthermore, it is shown that including radiation heat losses precludes accounting for ignition and extinction events due to the accessible flamelet subspace.

In the chapter, algorithms are presented to solve the flamelet equations in mixture fraction space. It is argued that high order numerical schemes are required in order to efficiently obtain accurate solutions. Furthermore, numerical algorithms for the solution of the steady flamelet equations have been presented, namely a Gauss-Seidel and a Newton-Raphson. Concerning transient flamelets, an Implicit-Explicit Runge-Kutta-Chebyshev (IMEX RKC) method [7] is used. The method combines explicit evaluation of non-stiff terms with implicit evaluation of stiff terms, namely the reaction rate. The procedure for computing igniting and extinguishing flamelets is described. Similarly, flamelets under radiation heat losses are computed using the transient method described for unsteady flamelets.

The last part of the chapter is concerned with the extension of the flamelet model to turbulent cases. Solution variables in turbulent CFD cases of variable density flows are Favre filtered. Hence, the flamelet database has to be restated into Favre filtered quantities. Probability density functions (*pdf*) are introduced to describe the interaction between chemistry and turbulence. It is argued that the general approach of computing the *pdf* during CFD simulations is computationally demanding. Therefore, the approach taken here is to presume the shape of the statistical distributions. Several *pdf* shapes are discussed and the choice for each variable argued. The mixture fraction statistical distribution is assumed to follow a  $\beta - \text{pdf}$ , which is described by the mean and the variance. For the other quantities, progress-variable, stoichiometric scalar dissipation rate and enthalpy, a  $\delta - \text{pdf}$  is taken, which is described only by the mean value.

Lastly, the flamelet database generation process and its subsequent interaction with the CFD code is detailed.

The flamelet databases introduced in *Chapter 3* use a set of parameters to retrieve data. Hence, each parameter must be properly defined. The mixture fraction and the scalar dissipation rate have unambiguous definitions. However, the progress-variable is an open parameter. Dependencies on combustion regime, premixed or non-premixed, chemical mechanism and fuel composition have been reported in the literature [8]. In *Chapter 4* it is evidenced a further dependency on the diffusion model. It is shown that definitions which are found suitable when Fickian diffusion is assumed are not always suitable when differential diffusion is accounted for. In the study, two representative definitions for the progress-variable are analysed. Besides, in the chapter it is also illustrated that the flamelet subspace of ignited solutions is affected when differential diffusion is taken into account. Two diffusion flames are studied, one having a fuel mixture of methane and hydrogen and a second one being a self-igniting methane flame issuing into a vitiated coflow.

Concerning the methane/hydrogen flame, namely the DLR flame A [9, 10], it has been shown that accounting for differential diffusion causes a significant modification of the ignited flamelet subspace, leading to the flame being able to withstand higher strain. Furthermore, ignited flamelets are found at lower temperatures. It is shown that the two definitions considered featured non-bijective regions which made these definitions unsuitable as parameters for the flamelet databases. Using additional species and modified weights suitable definitions are proposed which minimise the overlapping regions. Although, non-bijective regions still remained, it has been argued that their effect on the solution is limited. Furthermore, it has been evidenced that the progress-variable definition is dependent on the considered FPV variant. Suitable definitions have been found for each variant.

Regarding the self-igniting case [11], it has been argued that differential diffusion plays a minor role. However, in the induction phase the reaction paths differ depending on the considered diffusion model. Additionally, significant differences between two detailed chemical mechanisms are found. The GRI3.0 is shown to result in shorter ignition delay times, compared to the GRI2.11, which cause shorter flame stabilisation distances during CFD simulations. Numerical simulations in physical space showed a divergence between current simulations and experimental measurements. Comparing current numerical results with numerical results from the literature [12] revealed that current results had lower velocities at the stoichiometric mixture fraction surface. This difference in velocities surrounding the fuel jet may account for the ignition distance differences. Nonetheless, profiles in non-reacting regions show good agreement with experimental data.

Overall, in *Chapter 4*, it has been shown that both diffusion model and combustion model, steady, unsteady or radiation, have a large impact on the progress-variable definition to be used.

In *Chapter 5* the study is focused on the modelling of subgrid mixing. The FPV model is generally used in conjunction with assumed *pdfs* to represent the interaction of turbulence and chemistry. Commonly used *pdfs* are defined through the first moment, the mean, and the second central moment (the variance). The former is directly computed during CFD simulations. However, the mixture fraction variance, which represents mixing at the subgrid level, has to be modelled. Similarly, the subgrid scalar dissipation rate also has to be closed as it indirectly affects the subgrid variance. Hence, four subgrid models are studied in order to describe the subgrid mixture fraction variance and subgrid scalar dissipation rate: i) an equilibrium model, ii) a variance transport model (VTE), iii) a second moment transport model (STE) and iv) a model using a transport equation for the filtered squared mixture fraction gradient (SDR-TE).

Regarding the FPV variant, it is found that both steady and unsteady variants feature a lifted flame, even though the flame is experimentally attached to the fuel jet nozzle. When the classical flamelet and radiation variants are considered, an attached flame is observed. The rationale is that both only consider solutions close to the stable burning branch for scalar dissipation rates lower than the extinction one. Thus, the flamelet model forces the flame stabilisation. If a minor modification to the steady FPV model is applied, the effect of the subgrid model can be evidenced. The different subgrid models considered have been shown to be a key element in describing the flame stabilisation location. The Equilibrium model, which assumed an equilibrium between production and destruction of the variance at the subgrid level, predicted the longest distance. Results improve noticeably when the other models are used. The SDR-TE model shows the best agreement with the experimental data. However, the model requires evaluating several computationally expensive terms, which reduces its viability and is more prone to numerical errors. VTE and STE models offer a compromise between computational cost and accuracy. Additionally, it is shown that although these two models are equivalent at the continuous level, numerical predictions between both models differ. Furthermore, the STE model showed a significant deviation of the reaction rate from the stoichiometric mixture fraction, which was not found in the other models. The model constant value, used in the subgrid scalar dissipation rate, has an important effect in improving the results. When a larger constant is used, results for the STE improve while the VTE shows a mixed behaviour, improving at some points and deteriorating at others.

Besides, the conditional scalar dissipation rate predicted by the STE model shows a different shape than the VTE. It is shown that the difference is mainly due to the subgrid part.

Considering the results obtained it is argued that the VTE model using the subgrid viscosity offered a good compromise between accuracy and computational cost.

Overall the work presented in this thesis has covered the aspects required for solving turbulent diffusion flames: i) a numerical algorithm for spatial and temporal discretisation of transport equations have been described and studied; ii) a combustion model, in most of its variants, has been presented and used to study different flames. Regarding the combustion model, studies have been centred on the parameters controlling the database of flame solutions and on models describing the interaction between turbulence and chemistry.

## Future Work

The work developed in this thesis can be regarded as a first step into the simulation of combustion processes using LES methods at the *Centre Tecnològic de Transferència de Calor* (CTTC). The model presented has been tested against canonical flame configurations. Nonetheless, the implementation is suitable to be used in studies of more complex configurations. Some limitations of the model have been already pointed out in the thesis. Additionally, there are areas where the present work could be expanded.

A first aspect is to complete the current state of the unsteady Flamelet/Progress-Variate model by introducing the variance of the progress-variable [12, 13]. The results of this thesis also suggest that including the fluctuations of the progress-variable in the flamelet database may correct the flame lift-off observed in the DLR flame A simulations. Furthermore, accounting for the variance of the progress-variable has been reported to be important for self-igniting cases.

An issue that arose during the development of the flamelet model with radiation and the unsteady one is memory usage, specifically RAM. As new parameters are added the flamelet database grows significantly. In *Chapter 3* it is stated that the size of the radiation flamelet database had to use fewer points in order to fit into RAM. Analogously, if the progress-variable variance is to be added to the unsteady FPV model, thus having a five parameter database, the number of database points will increase considerably unless the number of entries per parameter is reduced. An alternative strategy would be to load a single instance of the flamelet database in a shared memory pool, instead of having each processing unit its own copy of the database, so that several processing units share one single database. Similarly, strategies where the database is selectively loaded could also be considered [14]. However, this would require active load and unload of memory during simulations. Furthermore, it could happen that some processing units required most of the database. Hence, the memory limit could still be reached if still only by one processing unit. Another strategy could be to use polynomial functions to represent the flamelet subspace and to store the coefficients in the database instead of the actual values [15, 16].

Another aspect to consider is the combustion regime. The present work has been centred around diffusion flames. Premixed flames, where reactants are already mixed when they reach the combustion chamber, have the potential of reducing pollutant emissions and increasing the combustion efficiency [1]. However, there are safety issues to be considered when operating in the premixed regime. Since reactants are already mixed prior to the combustion chamber, an uncontrolled temperature increase before reaching the combustion may start the chemical reaction. Advanced simulation techniques which are becoming increasingly accurate and reliable allow to explore new configurations where before there was too much uncertainty. On the one hand, models for premixed flames using a transport equation for a progress-variable, similar to the one presented in this thesis, such as the Presumed Conditional Model (PCM) [13, 17] together with a flamelet database generated using freely propagating flames or burner stabilised flames [18] are a natural extension. On the other hand, models where the flame surface position is advected, usually referred as  $G$  equation [19], could also be of interest due to the expertise at the CTTC in similar methods applied to multiphase flows [20]. A further step is to couple such a premixed flamelet model with the currently developed diffusion flamelet model in order to simulate flames in the partially-premixed regime [21]. Partially premixed flames are of interest because they present characteristics of both regimes, which can be used to the advantage of the designer. Then, in order to access the flamelet database corresponding to the actual burning regime, it is important to properly identify it during simulations. The Burning Index (BI) or Flame Index (FI) is commonly used in this regard, measuring the alignment of reactants. If they are aligned combustion is taking place in the premixed regime. Otherwise, combustion is happening in the diffusion regime.

An important aspect in combustion are pollutant emissions. In the present thesis a model for  $NO_x$  has been introduced, but no account for soot has been taken. In the literature different models may be encountered. Additionally, previous works in the CTTC used a soot model in a flamelet model [22]. The study was limited to laminar cases. Starting from here, soot would have to be introduced into the flamelet code and a proper  $pdf$  would have to be defined to account for the interaction between turbulence and soot [23]. Since soot is composed by a large set of particles formed through pyrolysis, specific models are required to model their transport.

Related to pollutants is the modelling of radiation. In the current thesis, radiation has been deemed as a secondary effect and as such a reduced model, namely an Optically Thin Model (OTM), has been used. The shortcomings of this model are well known and it is acknowledged that more complex models are required. However, the computational requirements of radiation hinder this evolution. Nonetheless, as stated in the *Introduction*, several works regarding radiation have been published by the CTTC group [24–26], where the Radiatiave Transfer Equation (RTE) is solved. Hence, by using advanced radiation models the turbulence radiation interactions (TRI) could

be accounted for.

Additionally, using a similar approach as the one used for radiation flamelet, a flamelet model which could account for heat losses in general, such as wall heat losses, could be developed. In confined flames heat losses to walls is a critical issue due to the high temperatures.

## References

- [1] T. Poinsot and D. Veynante. *Theoretical and Numerical Combustion*. R.T. Edwards Inc., 2005.
- [2] R.W.C.P. Verstappen and A.E.P. Veldman. Symmetry-preserving discretization of turbulent flow. *Journal of Computational Physics*, 187:343–368, 2003.
- [3] F.N. Felten and T.S. Lund. Kinetic energy conservation issues associated with the collocated mesh scheme for incompressible. *Journal of Computational Physics*, 215:465–484, 2006.
- [4] B. Perot. Conservation properties of unstructured staggered mesh schemes. *Journal of Computational Physics*, 159:58–89, 2000.
- [5] Ll. Jofre, O. Lehmkuhl, J. Ventosa, F. Xavier Trias, and A. Oliva. Conservation properties of unstructured finite-volume mesh schemes for the Navier-Stokes equations. *Numerical Heat Transfer, Part B: Fundamentals*, 65(1):53–79, 2013.
- [6] C.D Pierce and P. Moin. Progress-variable approach for large-eddy simulation of non-premixed turbulent combustion. *Journal of Fluid Mechanics*, 504:73–97, 2004.
- [7] L.F. Shampine, B.P. Sommeijer, and J.G. Verwer. IRKC: An IMEX solver for stiff diffusion-reaction PDE’s. *Journal of Computational and Applied Mathematics*, 196:485–497, 2006.
- [8] M. Ihme, L. Shunn, and J. Zhang. Regularization of reaction progress variable for application to flamelet-based combustion models. *Journal of Computational Physics*, 231(23):7715–7721, 2012.
- [9] W. Meier, R.S. Barlow, Y.-L. Chen, and J.-Y. Chen. Raman/Rayleigh/LIF measurements in a turbulent CH<sub>4</sub>/H<sub>2</sub>/N<sub>2</sub> jet diffusion flame: Experimental techniques and turbulence-chemistry interaction. *Combustion and Flame*, 123:326–343, 2000.

- [10] V. Bergmann, W. Meier, D. Wolff, and W. Stricker. Application of spontaneous Raman and Rayleigh scattering and 2D LIF for the characterization of a turbulent CH<sub>4</sub>/H<sub>2</sub>/N<sub>2</sub> jet diffusion flame. *Applied Physics B-Lasers And Optics*, 66:489–502, 1998.
- [11] R. Cabra, J. Chen, R. Dibble, A. Karpetis, and R Barlow. Lifted methane-air jet flames in a vitiated coflow. *Combustion and Flame*, 143(4):491–506, 2005.
- [12] M. Ihme and Y.C. See. Prediction of autoignition in a lifted methane/air flame using an unsteady flamelet/progress variable model. *Combustion and Flame*, 157(10):1850–1862, 2010.
- [13] P. Domingo, L. Vervisch, and D. Veynante. Large-eddy simulation of a lifted methane jet flame in a vitiated coflow. *Combustion and Flame*, 152(3):415–432, 2008.
- [14] S. Weise, D. Messig, B. Meyer, and C. Hasse. An abstraction layer for efficient memory management of tabulated chemistry and flamelet solutions. *Combustion Theory And Modelling*, 17:411–430, 2013.
- [15] D. Veynante, B. Fiorina, P. Domingo, and L. Vervisch. Using self-similar properties of turbulent premixed flames to downsize chemical table. *Combustion Theory And Modelling*, 12(6):1055–1088, 2008.
- [16] G. Ribert, O. Gicquel, N. Darabiha, and D. Veynante. Tabulation of complex chemistry based on self-similar behavior of laminar premixed flames. *Combustion and Flame*, 146(4):649–664, 2006.
- [17] J. Galpin and C. Angelberger. Large-eddy simulation of h<sub>2</sub>-air auto-ignition using tabulated detailed chemistry. *Journal of Turbulence*, 9(13):1–21, 2008.
- [18] B. Fiorina, R. Baron, O. Gicquel, D. Thevenin, and S. Carpentier. Modelling non-adiabatic partially premixed flames using flame-prolongation of ildm. *Combustion Theory And Modelling*, 7(3):449–470, 2003.
- [19] N. Peters. *Turbulent Combustion*. Cambridge University Press, 2000.
- [20] N. Balcázar. *Numerical Simulation of Multiphase Flows: Level-Set Techniques*. PhD thesis, Polytechnic University of Catalonia, Terrassa, Spain, 2006.
- [21] E. Knudsen and H. Pitsch. Capabilities and limitations of multi-regime flamelet combustion models. *Combustion and Flame*, 159:242–264, 2012.
- [22] D. Carbonell. *Numerical studies of diffusion flames. Special emphasis on flamelet concept and soot formation*. PhD thesis, Polytechnic University of Catalonia, Terrassa, Spain, 2010.

- [23] M. Mueller and H. Pitsch. Les model for sooting turbulent nonpremixed flames. *Combustion and Flame*, 159(6):2166–2180, 2012.
- [24] G. Colomer. *Numerical methods for radiative heat transfer*. PhD thesis, Polytechnic University of Catalonia, Terrassa, Spain, 2006.
- [25] G. Colomer, F.X. Trias, R. Borrell, and I. Rodriguez. Parallel algorithms for sn transport sweeps on unstructured meshes. *Journal of Computational Physics*, 232(1):118–135, 2013.
- [26] R. Capdevila, O. Lehmkuhl, O. Colomer, and C.D. Pérez-Segarra. Study of turbulent natural convection in a tall differentially heated cavity filled with either non-participating, participating grey and participating semigrey media. *Journal of Physics: Conference Series*, 395(1):012155, 2013.

---

## Appendix A

# Projection method in the Fractional Step for Low Mach algorithms

In *Chapter 2* a Fractional Step method is described to solve the pressure-velocity coupling in the Navier-Stokes equations. The Fractional Step method relies on a projection to solve this coupling. In incompressible flows, the velocity is projected to a divergence free space due to the incompressible constraint. In variable density flows in the low Mach regime there are two possibilities. On the one hand, in the *momentum projection* method, the mass flux ( $\rho u$ ) is projected, which results in a constant coefficient Poisson equation of the form

$$\frac{1}{\Delta t} \left( \frac{\partial}{\partial x_i} (\rho u_i) - \frac{\partial}{\partial x_i} (\rho \hat{u}_i) \right) = - \frac{\partial}{\partial x_i} \left( \frac{\partial p}{\partial x_i} \right) \quad (\text{A.1})$$

where  $\hat{u}$  is the pseudo-velocity. On the other hand, the *velocity projection* method projects the velocity ( $u$ ) and results in a variable coefficient Poisson equation

$$\frac{1}{\Delta t} \left( \frac{\partial u_i}{\partial x_i} - \frac{\partial \hat{u}_i}{\partial x_i} \right) = - \frac{\partial}{\partial x_i} \left( \frac{1}{\rho} \frac{\partial p}{\partial x_i} \right) \quad (\text{A.2})$$

The former approach, the *momentum projection*, requires evaluating mass divergence at the next step, which is unknown. Nonetheless, using the continuity equation, mass divergence is computed through the temporal derivative of the density. In the latter approach, the *velocity projection*, the velocity divergence has to be computed. As shown in *Chapter 2*, when variable density flows are considered, specifically in the low Mach regime, the velocity divergence is constrained by heat and mass transfer. If, for the sake of brevity, a flow at constant pressure composed of a single substance and only under thermal gradients is considered, the velocity divergence is

$$\frac{\partial u_i}{\partial x_i} = \frac{R}{c_p P_o} \left[ - \frac{\partial}{\partial x_j} \left( \kappa \frac{\partial T}{\partial x_j} \right) \right] \quad (\text{A.3})$$

where  $R, c_p, P_o, \kappa$  and  $T$  are the ideal gas constant, the heat capacity, the thermodynamic pressure, the heat conductivity and the temperature, respectively. Hence, Eq. (A.3) can be used to compute the velocity divergence when the *velocity projection* method is considered.

Analysis of the velocity divergence constraint reveals that in the limit of inviscid flows, which also includes flows at high Reynolds numbers, low Mach algorithms behave in general similarly to incompressible ones.

Still, the actual projection chosen for the Poisson equation introduces a difference. Of the two projection methods, the *velocity projection* collapses to the incompressible limit for inviscid flows, since the velocity divergence goes to zero and the Poisson equation takes the same form as in incompressible cases. Contrarily, the *momentum projection* does not directly enforce the incompressible limit. Hence, algorithms with a *velocity projection* do converge to the incompressible limit, whereas *momentum projection* ones do not.

Consequently, in regions where negligible heat and mass transfer occurs, a low Mach flow should behave similarly to an incompressible one. *Velocity projection* methods ensure this convergence, whereas the *momentum projection* algorithms do not explicitly enforce the incompressible limit. “Only” mass conservation is imposed. Thus, a null mass divergence can be achieved through a non-null velocity divergence balanced out through density gradients. In *velocity projection* methods, in temporally constant density regions, the null velocity divergence condition implies null density gradients.

However, for numerical simulations, *velocity projection* algorithms require computing energy and mass transport in order to evaluate the velocity divergence. This does not represent a great issue in cases where energy and mass are directly solved. However, for cases where surrogate scalars are used, i.e. a mas fraction and a progress-variable for diffusion flamelets as presented in this thesis, this approach requires solving for additional equations. Hence, the method becomes expensive compared to *momentum projection* algorithms, where only the density derivative is required, which is a straightforward computation, even though certain stability issues arise, as detailed in *Chapter 2*. Furthermore, the latter Poisson equation has constant coefficients, thus allowing for preprocessing the matrix.

Summarising, *velocity projection* methods are an interesting approach in cases where heat and mass transport are directly solved and iterative solvers are used, such as the Conjugate-Gradient (CG). On the other hand, when surrogate scalars are used or solvers which require preprocessing the matrix of the Poisson equation, *momentum projection* algorithms offer a computational advantage.

---

## Appendix B

### A note on software development

All studies performed in the framework of the present thesis have made use of numerical methods implemented into computational software libraries. As stated throughout the thesis, most simulations have been performed using the TermoFluids [1] parallel and object-oriented code as a base CFD code. All methods used in the thesis have been implemented on top of this base code. Hence, different libraries and sublibraries have been developed. Besides the functions and routines required for solving the different transport equations, three main software libraries have been developed, among others. First, a finite differences code for the solution of the flamelet equations, as described in *Chapter 3*. The second one is related to the evaluation of thermophysical properties. Third, a sublibrary for the evaluation of convective and diffusive operators. A brief summary of the latter two is presented in the following.

An important library required for multicomponent and variable density flows is a library for evaluating these properties. Hence, together with Dr. Lluis Jofré, a library for computing the properties of mixtures and substances was developed. This library features a hierachic design, going from a global element such as a *Mixture* down to the mathematical expression which defines a thermodynamic property. Hence, the most global element is a *Mixture*, which is basically a combination of several *Substances*. One substance can be abstracted as a collection of different *Properties*, i.e. viscosity, heat capacity, etc. Furthermore, each property is defined through a mathematical expression which enables its computation, termed here as *Calculate*.

The library also sets a unified interface to input external parameters and to retrieve substance data. Furthermore, several standard methods are already defined to handle typical mixtures and substances. Nonetheless, the library is flexible enough to allow full customization of the internal structure of each abstraction level. With this design, all sorts of physical substances and mixtures can be represented. Additionally, since the present thesis focused on chemically reacting flows, functions for the evaluation of chemical kinetics have also been implemented.

In any CFD code one of the core elements is the evaluation of convective and diffusive terms, as all transport equations contain at least one of them. These are two terms which are evaluated for each considered equation and at each time-step. Therefore, fast routines are required for efficient computations. Besides, not always the same numerical scheme for the convective or diffusive term of each transport equation is used. Hence, flexible functions are required to allow selecting different numerical schemes depending on the specific needs. Combining both criteria is a complex process, as increasing the generality of a code is usually equivalent to reduced performance due to increased overhead.

Evaluation of convective and diffusive terms require using geometrical information and flow information, basically the transported quantity, thermophysic properties and mass fluxes. The devised solution, developed with the help of Mr. Aleix Báez, makes use of C++ capabilities of object-oriented programming and inheritance. A diamond inheritance structure is implemented in order to handle the combination of different numerical schemes. At the top is placed a virtual class which defines the interface of the class. Then, it branches into two families of subclasses: the family defining the convective operator, here denoted as *CEq*, and the family for the diffusive operator, denoted as *DEq*. It is at this level where geometrical data related to the operators is stored. Furthermore, geometrical data is stored in compact form in order to minimise memory usage and to have all necessary information placed close together in memory. Additionally, these classes can also be used to either evaluate a convective or diffusive term. Finally, *Equations* classes, which basically represent a combination of a convective and diffusive term, can be constructed by inheriting from both a *CEq* and a *DEq*, without having to rewrite a routine for the storage of the geometrical data. The bottom of the diamond structure represents the common use of this sublibrary as in general transport equations have both convective and diffusive terms.

## References

- [1] O. Lehmkuhl, C.D. Pérez Segarra, R. Borrell, M. Soria, and A. Oliva. Termofluids: A new parallel unstructured CFD code for the simulation of turbulent industrial problems on low cost PC cluster. *Proceedings of the Parallel CFD Conference*, pages 1–8, 2007.

---

## Appendix C

### Main publications in the context of this thesis

#### International Journal Papers:

- J. Ventosa-Molina, J. Chiva, O. Lehmkuhl, J. Muela, C.D. Pérez-Segarra, A. Oliva. Numerical assessment of conservative unstructured discretisations for Low-Mach flows. Submitted to *Journal of Computational Physics*, 2015.

#### International Conference Papers:

- J. Ventosa, J. Chiva, O. Lehmkuhl, C.D. Pérez-Segarra. Modelization of the Low-Mach Navier Stokes equations in unstructured meshes. In Proceedings of the *7th International Conference on Computational Heat and Mass Transfer ICCHMT 2011*, pp. 1-8., Istanbul, Turkey, July 2011.
- J. Rigola, O. Lehmkuhl, J. Ventosa, C.D. Pérez-Segarra, A. Oliva. Numerical simulation of the turbulent fluid flow through valves based on low mach models. In Proceedings of the *2012 Compressor/Refrigeration & Air Conditioning/ High Performance Buildings Conferences* pp. 1375 (1-8), Purdue 2012.
- J. Ventosa, J. Chiva, O. Lehmkuhl, C.D. Pérez-Segarra, A. Oliva. Low Mach Navier-Stokes equations on unstructured meshes. In Proceedings of the *Conference on Modelling Fluid Flow CMFF'12: the 15th event of International Conference Series on Fluid Flow Technologies*, pp. 979 - 986, Budapest 2012.
- L. Jofre, O. Lehmkuhl, J. Ventosa, A. Oliva. Conservation properties and accuracy of unstructured mesh schemes for the Navier Stokes equations. In Proceedings of the *7th International Symposium on Turbulence, Heat and Mass Transfer*, pp. 1 - 12, ISBN 978-1-56700-301-7 Begell House, Palermo, Italy, 2012.

- J. Muela, O. Lehmkuhl, J. Ventosa, A. Oliva. Study of the autoignition of a hydrogen jet in a turbulent co-flow of heated air using LES modelling. In Proceedings of the *6th European Combustion Meeting*, Lund, Sweden, 2013.
- J. Ventosa, O. Lehmkuhl, C.D. Pérez-Segarra, A. Oliva. Large eddy simulation of a turbulent jet diffusion flame using the Flamelet-Progress Variable model. In Proceedings of the *6th European Combustion Meeting*, Lund, Sweden, 2013.
- J. Muela, J. Ventosa, O. Lehmkuhl, A. Oliva. Large eddy simulation of hydrogen autoignition in a preheated turbulent co-flow. In Proceedings of the *Eighth Mediterranean Combustion Symposium*, Çeşme, Turkey, 2013.
- J. Muela, J. Ventosa, O. Lehmkuhl, C.D. Pérez-Segarra, A. Oliva. Large eddy simulation of a turbulent jet diffusion flame using unstructured meshes. In Proceedings of the *Eighth Mediterranean Combustion Symposium*, 2013.
- J. Ventosa, O. Lehmkuhl, C.D. Pérez-Segarra, J. Muela, A. Oliva. Comparative study of subfilter scalar dissipation rate and mixture fraction variance models. In Proceedings of the *11th World Congress on Computational Mechanics (WCCM XI); 5th European Conference on Computational Mechanics (ECCM V); 6th European Conference on Computational Fluid Dynamics (ECFD VI)*, pp. 5239-5248, Barcelona, Spain, 2014.
- J. Ventosa, O. Lehmkuhl, C.D. Pérez-Segarra, A. Oliva. Assessment of subfilter scalar dissipation rate and mixture fraction variance models. In Proceedings of the *iTi Conference 2014* Bertinoro, Italy, September 2014.
- J. Ventosa-Molina, O. Lehmkuhl, C.D. Pérez-Segarra and A. Oliva. Towards a Direct Numerical Simulation of a lifted  $CH_4$ -air diffusion flame. In Proceedings of the *8th International Symposium on Turbulence, Heat and Mass Transfer*, Sarajevo, Bosnia and Herzegovina, September 2015.